

Flow and Transport Modelling of Fractured Aquifers based on a Geostatistical Approach

Von der Fakultät Bau- und Umweltingenieurwissenschaften der
Universität Stuttgart zur Erlangung der Würde eines
Doktor-Ingenieurs (Dr.-Ing.) genehmigte Abhandlung

Vorgelegt von
Anongnart Assteerawatt
aus Bangkok, Thailand

Hauptberichter: Prof. Dr.-Ing Rainer Helmig
Mitberichter: Prof. Dr. rer. nat. Dr.-Ing. habil. András Bárdossy
Prof. Dr.-Ing Reinhard Hinkelmann

Tag der mündlichen Prüfung: 21. Juli 2008

Institut für Wasserbau der Universität Stuttgart
2008

Heft 176 Flow and Transport Modelling
of Fractured Aquifers based on
a Geostatistical Approach

von
Dr.-Ing.
Anongnart Assteerawatt

D93 Flow and Transport Modelling of Fractured Aquifers based on a Geostatistical Approach

Titelaufnahme der Deutschen Bibliothek

Assteerawatt, Anongnart:
Flow and Transport Modelling of Fractured Aquifers based on a Geostatistical Approach / von Anongnart Assteerawatt. Institut für Wasserbau, Universität Stuttgart. - Stuttgart: Inst. für Wasserbau, 2008

(Mitteilungen / Institut für Wasserbau, Universität Stuttgart: H. 176)
Zugl.: Stuttgart, Univ., Diss., 2008)
ISBN 978-3-933761-80-4

NE: Institut für Wasserbau <Stuttgart>: Mitteilungen

Gegen Vervielfältigung und Übersetzung bestehen keine Einwände, es wird lediglich um Quellenangabe gebeten.

Herausgegeben 2008 vom Eigenverlag des Instituts für Wasserbau
Druck: Document Center S. Kästl, Ostfildern

Acknowledgement

First of all, I would like to thank my main supervisor Prof. Rainer Helmig for giving me an opportunity to do my research at the Institute of Hydraulic Engineering (IWS), University Stuttgart. His valuable discussions, guidance, support and individual characters have motivated and encouraged me throughout my time here. I also would like to express my grateful gratitude to my co-supervisors Prof. András Bárdossy and Prof. Reinhard Hinkelmann.

Furthermore, I would like to thank to Håkon Hægland from the University of Bergen for the collaboration in the development of the streamline tracing in a fracture-matrix system. I would also like to acknowledge Philipp Haas for his help on German translation of the summary of my work.

Many thanks go also to all colleagues at IWS, particularly the Hydrosys whose fruitful academic discussions as well as cheerful non-scientific activities create uniquely special and memorable working environment. Special thanks to Prudence Lawday for proofreading my dissertation and for help on my administrative documents here.

I extend my thanks to all my Thai friends for being accompanied throughout the time in Germany. Finally, I am extremely thankful to my family, especially my parents and my sisters, for their mental support and endless encouragement.

Contents

List of Figures	ii
List of Tables	vii
Nomenclature	viii
Abstract	xi
Zusammenfassung	xiii
1 Introduction	1
1.1 Motivation	1
1.2 Objectives	2
1.3 Structure of the Work	3
2 From Nature to Conceptual Models	5
2.1 Geometrical Characteristics of Fractured Aquifers	5
2.1.1 Fracture orientation	7
2.1.2 Fracture aperture	8
2.1.3 Fracture size and fracture trace	9
2.1.4 Fracture density	10
2.1.5 Fracture space	10
2.2 Model Concepts for Fracture Aquifers	11
2.2.1 Scales and representative elementary volume (REV)	11
2.2.2 Continuum model approach	12
2.2.3 Discrete model approach	13
2.2.4 Scales of consideration	15
3 Stochastic Characteristics of Fracture Networks	18
3.1 Statistics	18
3.1.1 Univariate statistics and bivariate statistics	18
3.1.2 Probability distribution and random variables	19
3.2 Geostatistics	22
3.2.1 Stationary process	23
3.2.2 Variogram models	24

3.3	Statistical Analysis of Fracture Characteristics	26
3.3.1	Fracture orientation	26
3.3.2	Fracture aperture	27
3.3.3	Fracture size and fracture trace	27
3.3.4	Fracture space	29
3.4	Geostatistical Analysis of Fracture Characteristics	29
4	Generation of Fracture Network: Geostatistical Approach	30
4.1	General Concept of Fracture Network Generation	30
4.2	Description of the Study Site	31
4.3	Analysis of Spatial Characteristics of Pliezhausen Block	32
4.4	Geostatistical Fracture Generation	42
4.4.1	Global optimization technique: simulated annealing	42
4.4.2	Indicator-field generation	44
4.4.3	Fracture-network generation	46
5	Mathematical and Numerical Model	51
5.1	Formulation of Flow and Transport Equations	51
5.1.1	Flow process	51
5.1.2	Transport process	55
5.2	Discretization of Flow and Transport Equations	57
5.3	Streamline Tracing	61
5.4	Flux Recovery for Streamline Simulation	64
6	Comparison of Geostatistical and Statistical Fracture Generation	68
6.1	Description of Study Cases	68
6.2	Structure of Fracture Network	76
6.3	Flow and Transport in Fracture-Matrix System	81
6.3.1	Model set-up	81
6.3.2	Parameters characterizing system behavior	83
6.3.3	Mesh size analysis	84
6.3.4	Comparison of study cases	88
7	Comparison of Streamline Simulation and Advective-Diffusive Transport	94
7.1	Mass Transport in Streamlines	94
7.2	Comparison Study in Preliminary Test Cases	96
7.2.1	Group A: Homogeneous and heterogeneous domains	96
7.2.2	Group B: Single fracture	100
7.2.3	Group C: Systematically distributed fractures	102
7.3	Comparison Study in Complex Fracture Networks	104
8	Conclusion and Outlook	108

List of Figures

1	Verfahren einer modifizierten Scanline-Technik zur Erzeugung eines Indikatorfeldes aus einer Oberflächenkartierung.	xvi
2	Illustration der Nachbarschafts-Richtungen mit den Ziffern 0 bis 7. . .	xvii
3	Die gescannte Ansicht des Feldversuchsblocks von Nordwesten (a) und Südosten (b) (modifiziert nach Dietrich et al. [2005]).	xviii
4	Standardisierte experimentelle Variogramme der fünf Außenseiten. . .	xix
5	Nachbarschaftsparameter der fünf Außenseiten.	xx
6	Kluftzellen-Dichte der fünf Außenseiten.	xx
2.1	Determination of a fracture orientation: azimuth, strike and dip (modified after Dietrich et al. [2005]).	7
2.2	Determination of polar coordinates of a unit normal vector of a fracture surface.	8
2.3	Fracture-orientation-distribution diagram from a Pliezhausen block (after Dietrich et al. [2005]).	8
2.4	Two opposite fracture surfaces of a single fracture intersecting a core sample of ca. 20 cm diameter (in cooperation with the Institute for Robotics and Process Control, Technical University of Braunschweig, Germany) (after Silberhorn-Hemminger [2002]).	9
2.5	Illustration of fracture spaces from a scanline survey.	10
2.6	Sketch of the scales (modified after Silberhorn-Hemminger [2002]). . .	11
2.7	Definition of the REV for a porous medium and a fractured system (modified after Bear [1993]).	12
2.8	Sketch of the relation between model concepts and scales of the investigated domain (modified after Silberhorn-Hemminger [2002] and Dietrich et al. [2005]).	17
3.1	Cumulative distribution function (a) and probability distribution function (b) in an interval $(a, b]$	20
3.2	Different probability distributions of a random variable: uniform, normal, log-normal, exponential and Erlang distribution.	22
3.3	Two different indicator fields of the same mean and variance.	22
3.4	Variogram models: nugget model, spherical model, exponential model and Gaussian model.	25

3.5	Sketch of the cone of confidence with the spherical aperture ω (after Dietrich et al. [2005]).	27
4.1	View of the study site Pliezhausen block: a) a view from the south-east direction and b) a part of vertical exposed wall (modified after Dietrich et al. [2005]).	32
4.2	Procedure of a modified scanline technique for evaluating an indicator field from a fracture-trace map.	33
4.3	View of the Pliezhausen block from the north-west and the south-east (modified after Dietrich et al. [2005]).	34
4.4	Fracture-trace maps of the five exposed walls obtained from the Pliezhausen block.	35
4.5	Horizontal-scanline indicator fields of the five exposed walls, the scanline distance $d = 0.10\text{m}$ and the segment length $l = 0.10\text{m}$	36
4.6	Vertical-scanline indicator fields of the five exposed walls, the scanline distance $d = 0.20\text{m}$ and the segment length $l = 0.10\text{m}$	37
4.7	Standardized experimental variograms of the horizontal-scanline indicator fields, the scanline distance $d = 0.10\text{m}$ and the segment length $l = 0.10\text{m}$	38
4.8	Standardized experimental variograms of the vertical-scanline indicator fields, the scanline distance $d = 0.20\text{m}$ and the segment length $l = 0.10\text{m}$	39
4.9	Variogram models of the average of the standardized experimental variograms of the horizontal- and the vertical-scanline indicator fields.	39
4.10	Illustration of the neighborhood directions in connection with the digits 0 to 7.	40
4.11	Neighborhoods of the horizontal-scanline indicator fields, the scanline distance $d = 0.10\text{m}$ and the segment length $l = 0.10\text{m}$	40
4.12	Neighborhoods of the vertical-scanline indicator fields, the scanline distance $d = 0.20\text{m}$ and the segment length $l = 0.10\text{m}$	41
4.13	Fracture-cell density from the horizontal-scanline indicator fields, the scanline distance $d = 0.10\text{m}$ and the segment length $l = 0.10\text{m}$	41
4.14	Probability of accepting changes (p) related to the objective function ($\Delta O = O(C_2) - O(C_1)$) at different temperature steps (T1,T2,T3 and T4).	43
4.15	Algorithm of indicator-field generation.	45
4.16	The generated and the target indicator fields.	46
4.17	Algorithm of the fracture generator FRAC3D (modified after Silberhorn-Hemminger [2002]).	47
4.18	Algorithm of fracture-network generation.	49
4.19	Fracture trace on a cross-section from one realization of a fractured system.	50

5.1	Velocity distribution of a laminar flow between two parallel plates. . .	53
5.2	A schematic of model concepts for a fracture aperture.	54
5.3	Dispersion at the microscopic scale.	55
5.4	Finite Element (FE) and Finite Volume (FV) mesh.	58
5.5	Illustration of a) Ansatz function and b) weighting function of a Box method.	59
5.6	Pollock tracing for a unit square.	62
5.7	Transformation of an unstructured grid and edge fluxes from a physical space \mathcal{P} to a reference space \mathcal{R}	63
5.8	Integration points and interior points of a control volume where fluxes and interior fluxes are evaluated.	65
5.9	Five cases of extended fractures in a discrete fracture model: a) single fracture ending in a control volume; b) single fracture passing through a control volume; c) two fractures passing through a control volume; d) two fractures combining case a) and b); e) two fractures like case a).	65
5.10	Flux recovery for a control volume of a fracture-matrix system. . . .	67
6.1	Objective functions depending on temperature steps from realizations of different maximum fracture sizes.	69
6.2	Five exposed walls from one realization generated by SFG-A.	71
6.3	Five exposed walls from one realization generated by SFG-B.	72
6.4	Five exposed walls from one realization generated by GFG-A.	73
6.5	Five exposed walls from one realization generated by GFG-B.	74
6.6	Five exposed walls from one realization generated by GFG-C.	75
6.7	Comparison of cumulative distribution functions of the average trace length from five study cases.	76
6.8	Comparison of cumulative distribution functions of the average fracture distance from the five study cases.	77
6.9	Comparison of the average standardized experimental variograms from the five study cases.	78
6.10	Comparison of the average fracture neighborhood from the five study cases.	78
6.11	Comparison of the average matrix neighborhood from the five study cases.	79
6.12	Neighborhoods of one realization of GFG-A from vertical-scanline indicator fields with a segment length of 0.10 m and a distance of 0.20 m.	79
6.13	Neighborhoods of one realization of GFG-B from vertical-scanline indicator fields with a segment length of 0.10 m and a distance of 0.20 m.	79
6.14	Comparison of average fracture-cell density from the five study cases.	80

6.15	Boundary conditions for flow and transport simulations.	82
6.16	A schematic of concentration distributions related to the skewness evaluated from the breakthrough curves.	84
6.17	Discretized domain of different mesh sizes of a south-west exposed wall from a scanned outcrop.	85
6.18	Comparison of breakthrough curves from different discretization meshes: 0.01, 0.02, 0.05, 0.10 and 0.20 m of a scanned south-west exposed wall.	86
6.19	Concentration distribution of the south-west walls at times 200, 32000 and 116000 s from mesh sizes 0.02 and 0.20 m.	87
6.20	Average and extreme values (min./max.) of flow and transport simulations of the south-west wall of five study cases compared with the results obtained from the field outcrop simulation (dashed line).	89
6.21	Comparison of breakthrough curves of the south-west walls from twenty-five realizations of five study cases.	90
6.22	Comparison of accumulated breakthrough curves of the south-west walls from twenty-five realizations of five study cases.	91
7.1	Mass transport in a streamtube as a block.	95
7.2	Breakthrough curve from STR and ADT.	96
7.3	A domain of two cases of Group A.	97
7.4	Discretized domain of different mesh sizes of homogeneous and heterogeneous domain.	98
7.5	Numerical results of ADT and STR for two cases of Group A: a) homogeneous and b) heterogeneous.	99
7.6	A domain of two cases of Group B.	100
7.7	Numerical results of ADT and STR for two cases of Group B: a) long fracture and b) short fracture.	101
7.8	A domain of two cases of Group C.	102
7.9	Numerical results of ADT and STR for two cases of Group C: a) test1 and b) test2.	103
7.10	Comparison of average accumulated breakthrough curves of the south-west walls of five study cases.	105
7.11	Comparison of average breakthrough curves of the south-west walls of five study cases.	106
7.12	Average and extreme values (min./max.) obtained from the streamline tracing and the advective-dispersive transport of the south-west wall of five study cases.	107

List of Tables

2.1	Total porosity, effective porosity and hydraulic conductivity of selected hard rocks (after Dietrich et al. [2005]).	6
4.1	Statistics of fracture geometries obtained from the Pliezhausen block (modified after Silberhorn-Hemminger [2002]).	32
6.1	Parameters of fracture network generation for five study cases.	70
6.2	Domain and fluid properties for all simulations.	82
6.3	Parameters characterized of flow and transport simulations of the scanned south-west wall of different mesh sizes.	85
6.4	Results of flow and transport simulations of the south-west wall obtained from the scanned wall and from average values of five study cases.	88

Nomenclature

The following table shows the significant symbols used in this work. Local notations are explained in the text.

Symbol	Definition	Unit
Latin Letters:		
A	cross-sectional area	$[m^2]$
A	geological coordinate Azimuth	$[degree]$
$AccBTC$	accumulated breakthrough curve	$[kg]$
BTC	breakthrough curve	$[kg/s]$
Cov	covariance of random variable	
D	geological coordinate Dip	$[degree]$
\mathbf{D}	hydrodynamic dispersion tensor	$[m^2/s]$
D_d	dispersion coefficient	$[m^2/s]$
D_e	diffusion coefficient of electrolytes	$[m^2/s]$
D_m	molecular diffusion	$[m^2/s]$
E	population mean or expected value	
H	fracture-cell density	
I	indicator variable of indicator field	
J	mass flux	$[kg/(m^2 s)]$
\mathbf{J}	Jacobian transformation matrix	$[-]$
\mathbf{K}	permeability tensor	$[m^2]$
N	Ansatz function	$[-]$
N_f	fracture neighborhood	
N_m	matrix neighborhood	
O	objective function	
P	investigated parameter	
Q	volumetric flux	$[m^3/s]$
Re	Reynolds number	$[-]$

SV	standardized value	
TOF	time of flight of a streamline	
Var	variance of random variable	
W	weighting function	
Z	random variable	
b	distance between two plates	$[m]$
c	concentration of a tracer	$[kg/m^3]$
d_3	fracture density	$[m^2/m^3]$
d	length dimension of porous media	$[m]$
dl	length of a patch boundary	$[m]$
f	flux over a unit-length face	$[m^3/(m\ s)]$
g	gravitational constant	$[m/s^2]$
h	piezometric head	$[m]$
k	hydraulic conductivity	$[m/s]$
\mathbf{k}	hydraulic conductivity tensor	$[m/s]$
l	length of core sample	$[m]$
l	trace length	$[m]$
m	mass flux	$[kg/s]$
n	number of fractures intersecting core sample	
n	number of neighboring nodes	
\mathbf{n}	outward normal vector	
\mathbf{n}_m	outward unit-normal vector	
p	probability of occurrence	
p	pressure	$[Pa]$
\mathbf{q}_m	Darcy velocity of matrix subcontrol volume	$[m/s]$
s	standard deviation	
s^2	variance	
t	time	$[s]$
t	travel time	$[s]$
\bar{t}	effective travel time	$[s]$
x	variable	
\bar{x}	mean of variable	
z	elevation	$[m]$

Greek Letters:

Γ	boundary of a control volume	
Ω	control volume	
α	cooling factor	
α	dispersion length	[m]
γ	skewness	
γ	variogram	
γ_s	standardized experimental variogram	
ε	residuum	
θ	acute angle of fracture and core sample	[degree]
θ	polar coordinate	[degree]
κ	concentration parameter	
μ	dynamic viscosity	[Pa s]
μ	population mean	
μ	temporal moment	
ϕ	total porosity	[-]
ϕ	polar coordinate	[degree]
ρ	fluid density	[kg/m ³]
σ	standard deviation of variable	
σ^2	variance of variable	
τ	pseudo time-of-flight	[s]
ν	kinematic viscosity	[m ² /s]
ω	spherical aperture	

Subscripts:

<i>a</i>	advective
<i>c</i>	central
<i>en</i>	enter
<i>ex</i>	exit
<i>i</i>	index
<i>j</i>	nodal index
<i>l</i>	longitudinal
<i>max</i>	maximum
<i>r</i>	realization
<i>s</i>	seepage
<i>sw</i>	scanned south-west wall
<i>t</i>	transversal
<i>x</i>	Cartesian coordinate in x-axis
<i>y</i>	Cartesian coordinate in y-axis

Abstract

Aquifer-analogue studies established in the petroleum reservoir have been widely used for characterizing fractured aquifer systems because detailed analysis can be performed practically and characteristics of fractured systems obtained on this scale can be upscaled to fractured systems on field scales (Dietrich et al. [2005]). A discrete model approach is an attractive alternative compared with a continuum model approach for aquifer analogue studies because there is no a priori assumption that a fractured system behaves as a continuum, and the effect of individual fractures can be explicitly investigated. However, a generation of a “representative” fracture network remains a challenging task when the discrete model is applied (National Research Council [1996]). In a case where a fracture network is embedded in a porous matrix, known as a fracture-matrix system, the numerical study of flow and transport processes requires a full two- or three-dimensional description of the fractures and the surrounding matrix. This causes a rise in computational demand for the numerical study of the flow and transport behavior of such a fractured system.

The overall purpose of this work is to improve the study of flow and transport processes in a fracture-matrix system on an analogue scale by using a discrete fracture model. An important prerequisite for this is the generation of a “representative” fracture network. Subsequently, an alternative approach to advective-dispersive transport which requires high computational demand for simulating transport in a fracture-matrix system has to be considered. In the first part of this work, a geostatistical fracture generation (GFG) which integrates statistical geometries and spatial characteristics has been developed and the technique for evaluating spatial characteristics in terms of a standardized variogram, neighborhoods, a fracture-cell density and a variance has been presented. In the following part, streamline tracing (STR) in a fracture-matrix system has been introduced as an alternative to advective-dispersive transport (ADT).

The comparative study of geostatistical fracture generation (GFG) and statistical fracture generation (SFG) shows that the spatial characteristics of a fracture network observed from the field as well as the flow and transport behavior of a fracture-matrix system (such as discharge, peak arrival time and mean effective time) are better represented by the results of GFG than those of SFG. Hence, integrating the spatial characteristics and the statistical geometries in GFG have improved the discrete fracture generation and the fractured system behavior can be better predicted.

Furthermore, the transport behavior in terms of an accumulated breakthrough curve (AccBTC) and a breakthrough curve (BTC) of fracture-matrix systems are investigated by using streamline tracing (STR) and compared with the results obtained by using advective-dispersive transport (ADT). STR shows significant reduction in computation time and clearly less numerical diffusion in comparison with ADT. In the cases considering a single fracture and systematically distributed fractures in a porous matrix, the effect of fast flow in fractures and slow flow in matrix, which is obviously noticed in STR, is smeared out due to the numerical diffusion in ADT. In complex fracture-matrix systems, numerical diffusion in ADT delays plume migration, whereas purely advective transport in STR leads to fast solute transport. As a result, the difference between the AccBTCs and the BTCs from the two approaches are clearly distinguished. Further investigations involving comparisons with experimental or field studies have to be carried out in order to validate the results of the two approaches.

Zusammenfassung

Einleitung

In vielen Ländern weltweit liefern geklüftete Festgestein-Systeme wichtige natürliche Rohstoffe wie Erdöl, Erdgas, Wasser oder geothermische Energie. Schon seit fast zwanzig Jahren wird auch vermehrt die Eignung solcher geklüfteter Systeme als Zwischen-/Endlager für radioaktive Nuklearabfälle untersucht (Bodvarsson und Tsang [1999], Poteri et al. [2002] und Cacas et al. [1990a]). Aufgrund dieser Rohstoffförderung und der möglichen Anwendbarkeit wird in jüngster Zeit intensiv am Verständnis, der Charakterisierung und letztendlich an der Vorhersage des Verhaltens solcher geklüfteter Systeme geforscht.

Zur Charakterisierung geklüfteter Aquifer-Systeme wurden im großen Umfang Aquiferanalog-Untersuchungen angewendet. Bei solchen Analog-Untersuchungen werden detaillierte praktische Analysen an geklüfteten Systemen durchgeführt, wie zum Beispiel Bohrkern-Analysen, hydraulische Messungen oder Untersuchungen an freiliegenden Felsoberflächen. Die so auf einer analogen Skala gewonnenen Strömungs- und Transporteigenschaften können dann auf großflächige Systeme übertragen werden (Dietrich et al. [2005]). Auf einer großflächigen Skala wird ein geklüftetes System vereinfacht als Equikontinuum oder als Doppelkontinuum unter Annahme eines repräsentativen Elementarvolumens (representative elementary volume, REV) (Bear [1972]) angesehen, auf einer analogen Skala ist jedoch die Annahme eines geklüfteten Systems als Kontinuum fragwürdig. In Long et al. [1982] wird gezeigt, dass geklüftete Systeme, abhängig von deren charakteristischen Eigenschaften (beispielsweise Dichte und Orientierung) nicht immer als Kontinuum angesehen werden können. Bei den Aquiferanalog-Untersuchungen ist ein diskretes Modell eine attraktive Alternative, weil das System dabei nicht als Kontinuum angenommen wird und somit Effekte aufgrund einzelner Klüfte explizit untersucht werden können. Die in letzter Zeit immer weiter gestiegenen Rechengeschwindigkeiten machen mittlerweile den sehr hohen Rechenaufwand, der bislang das Haupthindernis eines diskreten Ansatzes war, auf der analogen Skala realisierbar. Allerdings bleibt bei der Annäherung mit einem diskreten Modell die Generierung eines "repräsentativen" Kluftnetzwerks ein kritischer Schritt (National Research Council [1996]). Generell basiert die Generierung eines Kluftnetzwerks auf beobachteten geometrischen Kluftparameter und kann wie in die

Kategorien deterministische Kluftgenerierung (deterministic fracture generation, DFG) und statistische Kluftgenerierung (statistical fracture generation, SFG) unterteilt werden. Die geometrischen Eigenschaften eines Kluftnetzwerks (z.B. Kluftgröße, Durchlässigkeit und Orientierung) sind bei der DFG für einzelne Klüfte exakt bestimmt, während sie bei der SFG durch statistische Verteilungsfunktionen repräsentiert sind (Long [1983], Dverstorp und Andersson [1989] und Casas et al. [1990b]). Allerdings benötigt einerseits die DFG zur Beschreibung eines natürlichen geklüfteten Systems eine große Menge an Kluftgeometrie, andererseits scheitert die SFG oft an der Erfassung der räumlichen Variabilität und der Konnektivität der Kluftgeometrie. Diese Konnektivität hängt mit den Querverbindungen der Strömungspfade untereinander ab, die meist die Strömungs- und Transportprozesse dominieren (Berkowitz [2002]).

Diese Arbeit befasst sich mit geklüfteten porösen Medien beziehungsweise mit Kluft-Matrix-Systemen (fracture-matrix system, FMS) auf einer analogen Skala. Die numerische Untersuchung von Strömungs- und Transportprozessen in einem Kluft-Matrix-System, in dem das Kluftnetzwerk von einer porösen Matrix umgeben ist, unterscheidet sich stark von der Untersuchung bei geklüftetem Felsgestein mit undurchlässiger umgebender Matrix, weil in ersterem Fall die Vereinfachung durch Transformation von verbundenen Strömungspfaden in Klüfte in einen eindimensionalen Fluss, wie sie in Tsang und Tsang [1987] eingeführt wird, nicht erlaubt ist. Das bedeutet, dass eine komplette zwei- oder dreidimensionale Beschreibung der Klüfte und der umgebenden Matrix notwendig ist (Therrien und Sudicky [1996], Marýsaronka et al. [2005] und Reichenberger et al. [2006]). Des Weiteren kann das Verhalten eines Kluft-Matrix-Systems durch Betrachtung gemittelter Charakteristiken, die man mit verschiedenen Realisierungen stochastisch generierter Kluftnetzwerke erzeugen kann, repräsentiert werden. Diese Aspekte bedeuten für die numerische Untersuchung von Kluft-Matrix-Systemen einen rechen-technischen Mehraufwand.

Hauptaufgabe dieser Arbeit ist die Verbesserung der Untersuchung von Kluft-Matrix-Systemen durch Anwendung diskreter Modelle. Eine wichtige Voraussetzung dafür ist die Generierung eines "repräsentativen" Kluftnetzwerkes. Anschließend soll eine alternative Methode entwickelt werden, für den weniger Rechenzeit nötig ist als für den advektiv-dispersiven Transport.

In Bogdanov et al. [2003] wird die Notwendigkeit der Betrachtung untereinander verbundener Klüfte hinsichtlich der Perkolationsschwelle demonstriert, wobei man sich auf deren Einfluss auf die effektive Permeabilität geklüfteter poröser Medien konzentriert. Durch Anwendung einer modifizierten Scanline-Technik auf einer analogen Skala entdeckte Silberhorn-Hemminger [2002] die räumliche Beziehung von Kluftspuren in freiliegenden Felsen. Aufgrund dieser Fakten wurde in der vorliegenden Studie eine geostatistische Kluftgenerierung entwickelt (geostatistical fracture generation, GFG), die sowohl die statistischen Geometrien als auch die

räumlichen Charakteristiken in Betracht zieht. Diese räumlichen Charakteristiken für das Kluftnetzwerk werden direkt aus freiliegenden Felswänden bestimmt.

Auf einer großflächigen Skala betrachtet, bei der Klüfte und Matrix wie zwei wechselwirkende Kontinua behandelt werden, wurden vielversprechende Ergebnisse von Huang et al. [2004] und Al-Huthali und Datta-Guppa [2004] unter Anwendung von "Streamline-Tracing" präsentiert. Deren Ergebnisse zeigten eine gute Übereinstimmung mit Ergebnissen aus einer gitterbasierten Simulation finiter Differenzen bei einer deutlichen Reduktion der Rechenzeit. Deshalb wurde im Rahmen dieser Arbeit ein "Streamline-Tracing" für ein diskretes Kluft-Matrix-System in Zusammenarbeit mit dem mathematischen Institut der Universität Bergen (Haegland et al. [2008]) entwickelt.

In den folgenden Abschnitten wird zunächst die Methodik der Quantifizierung der räumlichen Charakteristik freiliegender Felswände vorgestellt und die geostatistische Kluftgenerierung (GFG) basierend auf den statistischen Geometrien und der analysierten räumlichen Charakteristik eingeführt. Anschließend werden die Strömungs- und Transportgleichungen sowie das "Streamline-Tracing" in einem Kluft-Matrix-System beschrieben. Zum Schluss wird eine vergleichende Studie an Kluft-Matrix-Systemen durchgeführt, wobei die Kluftnetzwerke mittels GFG und SFG generiert werden. Schließlich werden der advektiv-dispersive Transport und das "Streamline-Tracing" verglichen, wobei die Aufmerksamkeit auf dem Transportverhalten der berechneten Ergebnisse liegt.

Analyse der räumlichen Charakteristik

Die räumliche Charakteristik eines Kluftnetzwerks kann mit Hilfe von Oberflächenkartierungen an freiliegenden Felswänden durch Anwendung einer *modifizierten Scanline-Technik* (modified scanline technique, MS) quantifiziert werden (Dietrich et al. [2005] und Silberhorn-Hemminger [2002]).

Abbildung 1 illustriert die Vorgehensweise bei der MS. Zunächst wird ein Satz paralleler und gleichmäßig verteilter Scanlines über die Oberflächenkartierung gelegt, wobei die Richtung der Scanlines senkrecht zur Hauptrichtung der Kluftspuren angeordnet ist. Die Scanlines werden dann in Segmente gleicher Länge l unterteilt. Dann wird entlang jeder Scanline die Existenz von Schnittpunkten zwischen den Kluftspuren und dem jeweiligen Scanline-Segment erfasst und durch eine Indikatorvariable $I(\mathbf{x})$ beschrieben:

$$I(\mathbf{x}) = \begin{cases} 1 & \text{Kluftspur und Scanline schneiden sich ("Kluftzelle"),} \\ 0 & \text{Kluftspur und Scanline schneiden sich nicht ("Matrixzelle").} \end{cases} \quad (1)$$

Hier ist \mathbf{x} die Mittelpunktskoordinate eines Scanline-Segments. Dadurch wird die Oberflächenkartierung auf ein Indikatorfeld übertragen. Der Abstand d zwischen den Scanlines und das Scanline-Segment l werden abhängig von der Größe der Oberflächenkartierung und der Charakteristik der Kluftspuren definiert. Dabei sollten mehrere unterschiedliche Scanline-Abstände und Scanline-Segmente untersucht werden, um geeignete Werte zu finden (Dietrich et al. [2005]).

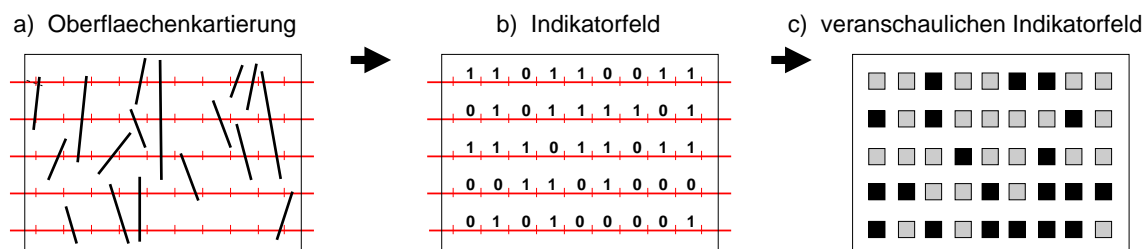


Abbildung 1: Verfahren einer modifizierten Scanline-Technik zur Erzeugung eines Indikatorfeldes aus einer Oberflächenkartierung.

Die räumliche Variabilität wird mit Hilfe verschiedener Parameter aus dem Indikatorfeld analysiert. Der erste Parameter ist ein standardisiertes experimentelles Variogramm, das ein Maß für den Mittelwert der Wertzunahme zwischen zwei Punkten ist und gleichzeitig die Variabilität des Indikatorfeldes bezüglich der Varianz σ^2 berücksichtigt:

$$\gamma_s(\mathbf{h}) = \frac{1}{2\sigma^2} \left(\frac{1}{n_h} \sum_{\alpha=1}^{n_h} [I(\mathbf{x}_\alpha + \mathbf{h}) - I(\mathbf{x}_\alpha)]^2 \right), \quad (2)$$

wobei der Abstandsvektor \mathbf{h} senkrecht zur Scanline-Richtung gemessen wird und n_h die Gesamtzahl von Variablenpaaren mit Abstand \mathbf{h} ist. Die Varianz eines Indikatorfeldes mit zwei möglichen Werten 0 und 1 wird mit dem Bernoullischen Gesetz beschrieben:

$$\sigma^2 = p(1-p), \quad \text{wobei} \quad p = \frac{1}{n} \sum_{\alpha=1}^n I(\mathbf{x}_\alpha). \quad (3)$$

Der Term p wird als "Treffer-Wahrscheinlichkeit" bezeichnet und n ist die Gesamtzahl der Zellen.

Zusätzlich zum standardisierten Variogramm werden auch die als Nachbarschaftsparameter bezeichneten Bildrekonstruktions-Parameter in Betracht gezogen, die die räumliche Konnektivität der Kluftspuren im Verhältnis zu den angrenzenden Zellen charakterisieren.

Die Kluftspuren-Nachbarschaftsparameter N_f und die Matrix-Nachbarschaftsparameter N_m werden aus den acht angrenzenden Zellen bestimmt nach:

$$N_f(k) = \frac{1}{n_f} \sum_{\alpha=1}^n [I(\mathbf{x}_\alpha^k)] \quad \text{wenn } I(\mathbf{x}_\alpha) = 1, \quad (4)$$

$$N_m(k) = \frac{1}{n_f} \sum_{\alpha=1}^n [I(\mathbf{x}_\alpha^k)] \quad \text{wenn } I(\mathbf{x}_\alpha) = 0. \quad (5)$$

Hier ist n die Gesamtzahl der Zellen, n_f die Gesamtzahl der Kluftspur-Zellen und \mathbf{x}_α^k ist die angrenzende Zelle in der Richtung k von \mathbf{x}_α . Die Richtungen k werden durch die Ziffern 0 bis 7 (Abbildung 2) gekennzeichnet.

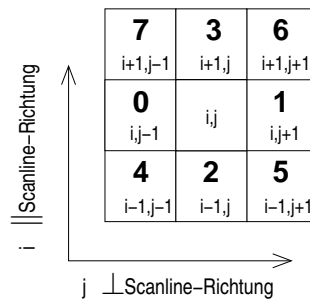


Abbildung 2: Illustration der Nachbarschafts-Richtungen mit den Ziffern 0 bis 7.

Der nächste als Kluftzellen-Dichte H bezeichnete Parameter ist das Verhältnis der Zahl der Kluftzellen zur Gesamtzahl der Zellen entlang jeder horizontalen Scanline:

$$H(z) = \frac{1}{n_z} \sum_{\alpha=1}^{n_z} [I(\mathbf{x}_\alpha)] . \quad (6)$$

Dabei ist n_z die Gesamtzahl der Zellen entlang jeder Scanline bezüglich der z -Koordinate.

Forschungsobjekt für diese Arbeit war ein etwa $8 \text{ m} \times 10 \text{ m} \times 2 \text{ m}$ großer Sandsteinblock in der Gegend von Pliezhausen in Deutschland. Der Block ist durch eine hohe Kluftdichte sowie eine hohe Matrixporosität und -permeabilität gekennzeichnet. Mittels stereofotogrammetrischer Vermessung wurden fünf offenliegende Seiten kartiert: Die Nord-, die Ost-, die Südost-, die Südwest- sowie die Westseite (siehe Abbildung 3). In der Abbildung erkennt man drei Kluft-Hauptgruppen, eine mit beinahe horizontaler und zwei mit beinahe vertikaler Ausrichtung. Allerdings sind an den freiliegenden Wänden nur zwei Hauptrichtungen der Kluftspuren zu erkennen, nämlich eine horizontale und eine vertikale. Die Scanlines müssen senkrecht zur Hauptrichtung der Kluftspuren sein, deshalb werden zwei Scanline-Richtungen benötigt. Aus jeder freiliegenden Seite werden je zwei Indikatorfelder ermittelt:

das erste mit Hilfe der horizontalen Scanline zur Auswertung der vertikalen Kluftspuren, das zweite mit Hilfe der vertikalen Scanline zur Auswertung der horizontalen Kluftspuren.

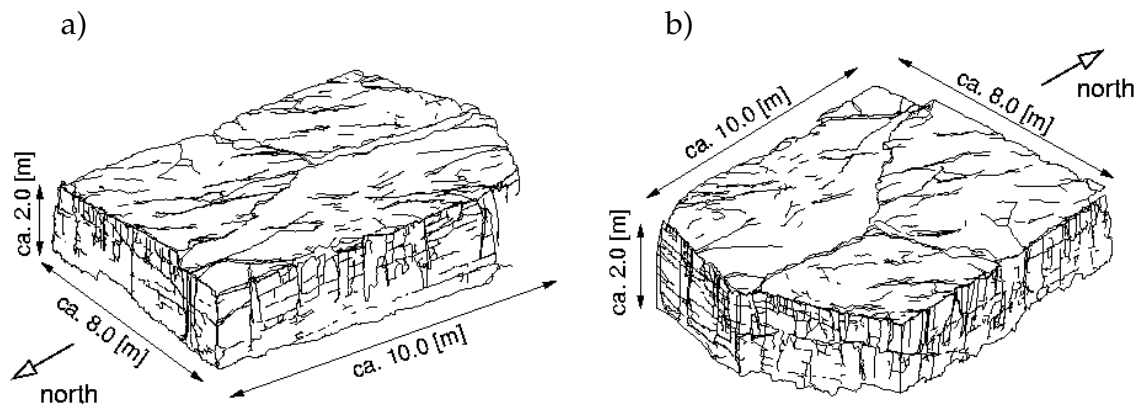


Abbildung 3: Die gescannte Ansicht des Feldversuchsblocks von Nordwesten (a) und Südosten (b) (modifiziert nach Dietrich et al. [2005]).

Eine Segmentlänge von $l = 0,10$ m und ein Scanline-Abstand von $d = 0,10$ m (für die horizontale Scanline) und $d = 0,20$ m (für die vertikale Scanline) wurden für diese Studie nach Dietrich et al. [2005] ausgewählt. Die räumliche Charakteristik des Kluftnetzwerks wird aus der Oberflächenkartierung der fünf Außenseiten ermittelt. Wie man in den Abbildungen 4a und 4b sehen kann, erhöhen sich die standardisierten Variogramme in den vertikalen und horizontalen Scanline-Richtungen innerhalb eines spezifischen Abstands h , der so genannten Korrelationslänge oder auch Korrelationsbereich, und erreichen dann einen konstanten Wert, den so genannten Schwellenwert. Die Mittelwerte der standardisierten experimentellen Variogramme der fünf Außenseiten werden mit dem Variogramm-Modell von VARIOWIN (Panatier [1996]) gefittet. Die gemittelten Daten zeigen eine optimale Anpassung an eine Kombination aus exponentiellen Modellen und Nugget-Variogramm-Modellen (Chilés und Delfiner [1999]):

$$\gamma_s(\mathbf{h}) = \sigma_1^2 + \sigma_2^2 \left(1 - e^{\left(-\frac{h}{a}\right)} \right) \quad \text{für } a > 0. \quad (7)$$

Die Werte der Parameter σ_1^2 , σ_2^2 und a betragen 0,14, 0,86 und 0,80 für die horizontalen Scanline-Indikatorfelder und 0,48, 0,52 und 1,67 für die vertikalen Scanline-Indikatorfelder, siehe Abbildungen 4c und 4d. Hierbei ist wegen der Normalisierung der experimentellen Variogramme auf ihre Varianzen die Summe über σ_1^2 und σ_2^2 gleich 1.

Die Nachbarschaftsparameter N_f und N_m der fünf Außenseiten für die vertikalen und die horizontalen Scanlines werden in der Abbildung 5 gezeigt. Aufgrund der

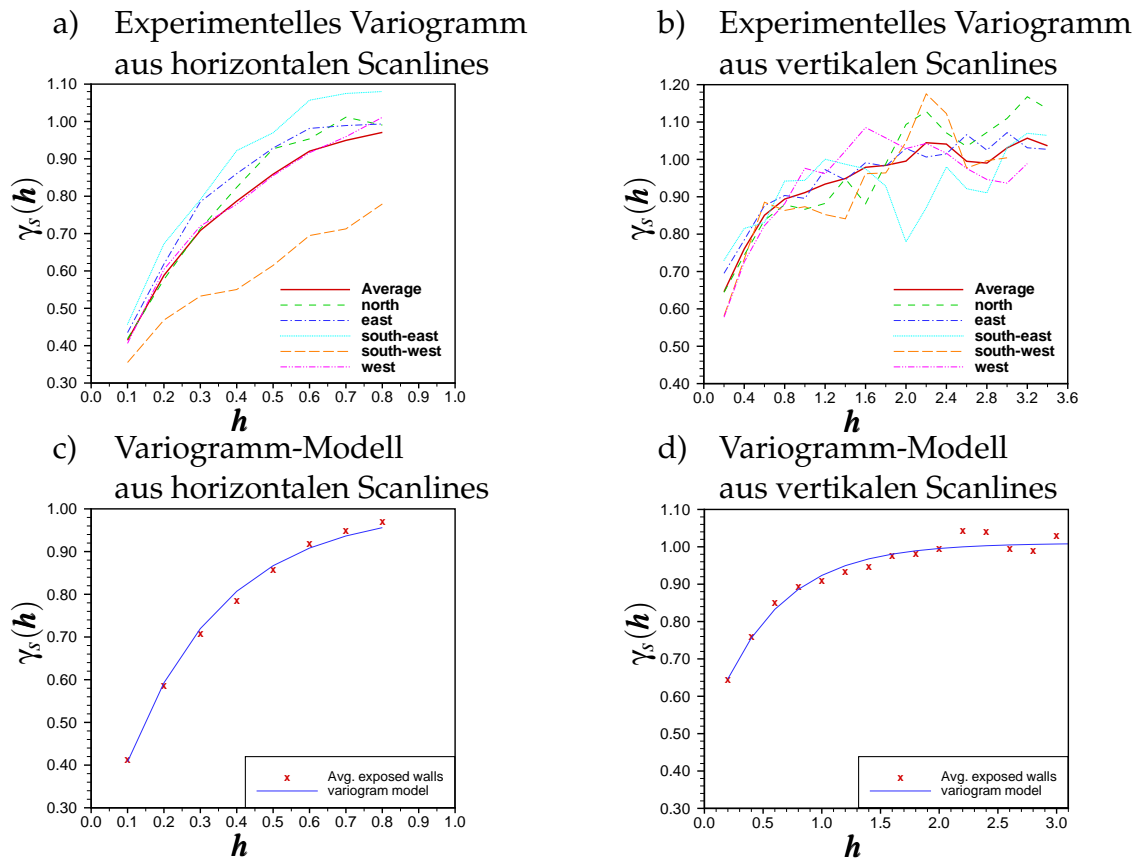


Abbildung 4: Standardisierte experimentelle Variogramme der fünf Außenseiten.

zugeordneten Werte in Gleichung (1) bedeuten die großen Werte der Nachbarschaftsparameter eine große Zahl von Kluftzellen. Wie zu erwarten war, beobachtet man hohe N_f in der Kluftspur-Richtung ($k = 2, 3$), weil in Kluft-Richtung die benachbarten Zellen einer Kluftzelle die Tendenz haben, ebenfalls Kluftzellen zu sein. Die N_m sind deutlich niedriger in Richtung der Kluftspuren, was bedeutet, dass benachbarte Zellen einer Matrixzelle dazu tendieren, eher Matrix- als Kluftzellen zu sein. Die Werte der Nachbarschaftsparameter in den anderen Richtungen hängen mit der Zahl der Kluft- und Matrixzellen in diesen Richtungen zusammen. Wenn eine zentrale Zelle eine Kluftzelle ist und eine benachbarte Zelle in einer Nicht-Kluftspurrichtung ($k \neq 2, 3$) ebenfalls eine Kluftzelle ist, kann das auf die Existenz einer Kluftspur in dieser Richtung hinweisen, wodurch die Konnektivität der Kluftspuren in Beziehung zu den Werten der Nachbarschaftsparameter steht.

In Abbildung 6 zeigen die Ergebnisse für die fünf Außenseiten eine deutliche Zunahme der Anzahl der Kluftzellen mit zunehmendem vertikalen Abstand z , was auf Verwitterungsprozesse am oberen Teil der Außenseiten hinweist.

Die in Gleichung (3) ausgedrückte Varianz wird als einer der räumlichen Parameter in die GFG integriert, um indirekt die Anzahl der Kluftzellen und Matrixzellen

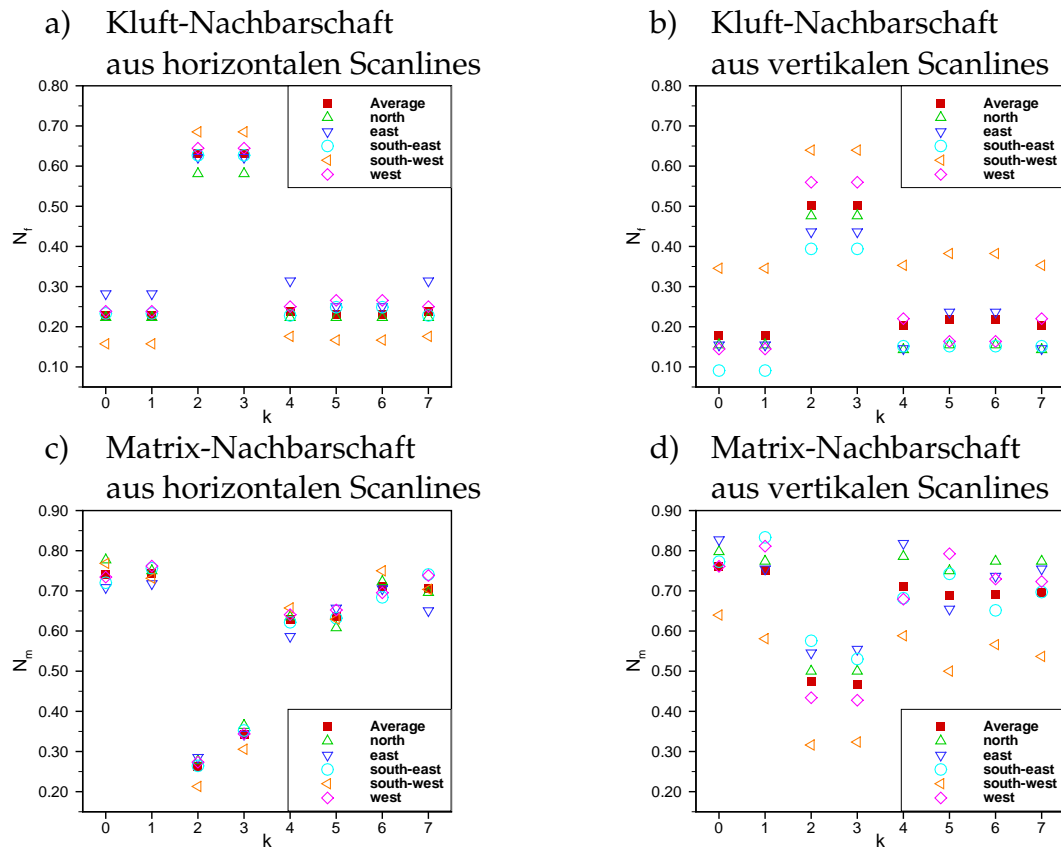


Abbildung 5: Nachbarschaftsparameter der fünf Außenseiten.

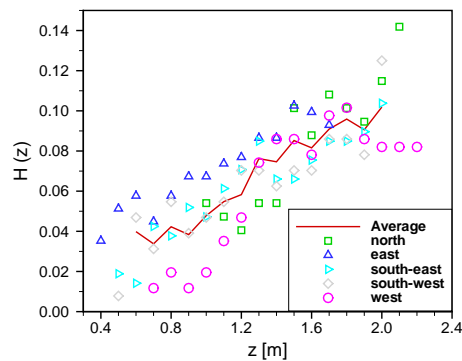


Abbildung 6: Kluftzellen-Dichte der fünf Außenseiten.

zu kontrollieren. Die Mittelwerte der Varianzen, die aus den Indikatorfeldern der horizontalen und vertikalen Scanlines berechnet wurden, betragen 0,167 beziehungsweise 0,181.

Die räumlichen Parameter, die aus den Außenseiten ermittelt wurden, werden als räumliche Charakteristik des Kluftnetzwerks betrachtet. Im nächsten Abschnitt wird die geostatistische Kluftgenerierung (GFG) durchgeführt, wobei die räumliche

Charakteristik und statistische Geometrie des Kluftnetzwerks einbezogen werden.

Geostatistische Kluftgenerierung (GFG)

Der Erfolg des sogenannten *Simulated Annealing* (SA) als globale Optimierungsmethode bei der Integration mehrerer Charakteristiken diskreter Klüften (Baafi und Schofield [1997] und Tran et al. [2006]) sowie dessen Flexibilität bei der Einbeziehung zusätzlicher Informationen (falls nötig) machen es zu einer attraktiven Methode bei der Kluftnetzwerk-Generierung. Dabei startet das SA in einem Anfangszustand und wird zufällig in einen neuen Zustand überführt. Dieser neue Zustand wird akzeptiert, wenn die Veränderung entweder die Zielfunktion erniedrigt oder erhöht. Die Wahrscheinlichkeit der Akzeptanz des Zustands beträgt:

$$p = \begin{cases} 1 & \text{wenn } O(C_2) \leq O(C_1) \\ e^{\left(-\frac{O(C_2)-O(C_1)}{T}\right)} & \text{wenn } O(C_2) > O(C_1) . \end{cases} \quad (8)$$

Der als Temperatur bezeichnete, konstante Parameter T wird zur Beeinflussung der Akzeptanz des neuen Zustands verwendet. $O(C_1)$ und $O(C_2)$ sind jeweils die Zielfunktionen des aktuellen und des neuen Zustands. Für jede Temperatur wird eine Störungsrechnung über sehr viele Iterationen M durchgeführt und danach die Temperatur erniedrigt. Die Temperatur T wird dabei linear auf eine neue Temperatur T_{new} mit dem Kühlfaktor α , $T_{new} = \alpha T$ erniedrigt. Mit abnehmender Temperatur T verringert sich auch die Wahrscheinlichkeit, dass Zustandsänderungen, die hohe Werte der Zielfunktion zur Folge haben, akzeptiert werden. Dadurch kann das Problem konvergieren.

In dieser Studie berücksichtigt die GFG die statistische Geometrie und die räumliche Charakteristik der Indikatorfelder. Der Anfangszustand des Kluftnetzwerks wird aufgrund der statistischen Kluftgeometrien (Orientierung, Kluftgröße und Kluftdichte) erzeugt. Indem man in einem erzeugten Gebiet mehrere untersuchte Querschnitte definiert, können aus diesen die räumlichen Parameter ermittelt werden. Die Zielfunktion der GFG ist definiert als die Summe der normalisierten Differenzen zwischen den räumlichen Charakteristiken des Ziel-Kluftnetzwerks ($\hat{\gamma}_s(\mathbf{h})$, $\hat{N}_f(j)$, $\hat{N}_m(j)$, $\hat{H}(z)$ und $\hat{\sigma}^2$) und des erzeugten Kluftnetzwerks im Zustand k

$(\gamma_s^k(\mathbf{h}), N_f^k(j), N_m^k(j), H^k(z))$ und $\sigma^{2,k}$) für alle N_e untersuchten Querschnitte:

$$\begin{aligned}
O(k) = & \sum_{i=1}^{N_e} (w_1 \sum_{j=1}^{n_{\gamma_s}} \frac{|\hat{\gamma}_s(\mathbf{h}_j) - \gamma_s^k(\mathbf{h}_j)|}{\hat{\gamma}_s(\mathbf{h}_j)} + w_2 \sum_{j=0}^7 \frac{|\hat{N}_f(j) - N_f^k(j)|}{\hat{N}_f(j)} \\
& + w_3 \sum_{j=0}^7 \frac{|\hat{N}_m(j) - N_m^k(j)|}{\hat{N}_m(j)} + w_4 \sum_{j=1}^{n_H} \frac{|\hat{H}(z_j) - H^k(z_j)|}{\hat{H}(z_j)} \\
& + w_5 \frac{|\hat{\sigma}^2 - \sigma^{2,k}|}{\hat{\sigma}^2}), \tag{9}
\end{aligned}$$

wobei die Gewichtungsfunktion w_i immer positive Werte liefert. Durch die Einführung der Gewichtungsfunktion kann der Einfluss jedes räumlichen Parameters kontrolliert werden. Nach Berechnung der Zielfunktion eines aktuellen Zustands wird das Kluftnetzwerk in eine neue Konfiguration überführt und eine neue Zielfunktion berechnet. Die beiden Zielfunktionen werden verglichen und das neue Kluftnetzwerk wird nach den Akzeptanzkriterien in Gleichung (8) akzeptiert. Das Kluftnetzwerk wird bei jedem Iterationsschritt durch Hinzufügen oder Entfernen einer Kluft oder durch zufällige Auswahl einer Kluft und Änderung ihrer Geometrien (Ort, Orientierung oder Form) verändert. Diese Veränderung des Kluftnetzwerks wird unter der Bedingung durchgeführt, dass sich die Kluftdichte nicht um mehr als 15% ändert. Die Störungsrechnung wird mit M Iterationen durchgeführt und die Temperatur T wird dann mit dem Kühlfaktor α reduziert. Schließlich bricht das SA ab, sobald die Zielfunktion nach einigen Temperaturschritten nicht mehr verbessert oder wenn die Minimumtemperatur T_{stop} erreicht wird. Die Konfiguration mit der minimalen Zielfunktion wird als die Lösung betrachtet, die der räumlichen Charakteristik des Ziel-Kluftnetzwerks am nächsten kommt. Außerdem kann das Kluftnetzwerk von der GFG manchmal unter Einbeziehung nur der Kluftorientierung und Kluftdichte, aber ohne Einbeziehung der Kluftgröße erzeugt werden. Die Klüfte werden zufällig erzeugt und ihre Größen werden limitiert durch eine definierte Maximalgröße, die man aus Beobachtungen der Kluftspuren an den freiliegenden Felswänden annähern kann. Durch Veränderung der maximalen Polygongröße und Vergleichen der Zielfunktionen wird diejenige maximale Kluftgröße ausgewählt, die die minimale Zielfunktion liefert. Diese zusätzliche Option der GFG könnte im Falle einer starken Verzerrung oder großen Unsicherheit der statistischen Verteilung der Kluftspuren hilfreich sein, um die Kluftgrößen-Verteilung zu bestimmen.

Das Hauptproblem bei der Anwendung des SA ist, dass es keine offensichtliche Analogie zur Definition der Anfangstemperatur T_0 , der Zahl der Iterationen M und des Kühlfaktors α für die Temperaturschritte gibt. Nach Bárdossy [1998] wird der Wert der Anfangstemperatur T_0 derart gewählt, dass die anfängliche Akzeptanz

eines neuen Zustands ungefähr 0,80 und der Kühlfaktor konstant 0,90 für alle Temperaturschritte ist. Als Zahl der Iterationen M definiert man die Hälfte der Anzahl der Klüfte, um eine hohe Wahrscheinlichkeit zu gewährleisten, dass generierte Klüfte in den Austausch-Prozess involviert werden. Die Störungsrechnung des SA wird dann solange wiederholt, bis es die Abbruchkriterien erfüllt.

Grundlegende Gleichungen für Strömungs- und Transportsimulationen und “Streamline-Tracing”

Strömungs- und Transportsimulation und “Streamline-Tracing” werden unter Verwendung des numerischen Modells MUFTE-UG (MUltiphase Flow, Transport and Energy Model - Unstructured Grids, Multiphasenströmungs-, Transport- und Energie-Modell - unstrukturierte Gitter) durchgeführt (Helmig et al. [1998] und Bastian et al. [1997]). Eine Diskretisierungs-Technik, genannt Knoten-zentrierte Finite-Volumen-Methode (vertex centered finite volume method) oder Box-Methode (Box method) wird für die Simulationen angewendet. Dabei wird ein Gebiet zunächst durch ein Finite-Element-Gitter (FE) diskretisiert, wobei Strömungsvariablen und Matriceigenschaften in jedem Element als konstant angenommen werden. In einem zweidimensionalen Gebiet wird dann ein Finite-Volumen-Gitter (FV) konstruiert, indem die Schwerpunkte der Elemente mit den Kantenmittelpunkten verbunden werden. Klüfte in einem Gebiet werden durch eine niedrigerdimensionale Näherung beschrieben, beispielsweise als eindimensionale Linie in einem zweidimensionalen Gebiet, und das Gebiet wird dann durch ein unstrukturiertes Netz mittels ART (Fuchs [1999]) diskretisiert.

Zur Vereinfachung wird eine stationäre Strömung eines inkompressiblen Einphasensystems in einer undeformierbaren Matrix betrachtet und Quellen-/Senken-Terme werden vernachlässigt. Aufgrund der Massenerhaltung in einem Kontrollvolumen kann die Kontinuitätsgleichung als

$$\nabla \cdot \mathbf{v} = 0 \quad (10)$$

beschrieben werden. Hierbei ist die Geschwindigkeit \mathbf{v} nach Darcys Gesetz als Funktion des Drucks p und des Permeabilitätstensors \mathbf{K} definiert und Gravitationseffekte werden vernachlässigt:

$$\mathbf{v} = -\frac{\mathbf{K}}{\mu} \nabla p, \quad (11)$$

wobei μ die Viskosität des Fluids und ρ die Fluidichte ist. Für eine Kluft ist die Permeabilität nach dem Konzept der parallelen Platten gegeben:

$$K = \frac{b^2}{12}. \quad (12)$$

Beim advektiv-dispersiven Transport (ADT) werden die Transportprozesse für einen konservativen Tracer hauptsächlich von drei Prozessen bestimmt: *Advektion*, *Diffusion* und *Dispersion*. Die grundlegende Gleichung des ADTs erhält man über die Erhaltung des Massenflusses durch die Grenzen eines Kontrollvolumens zu

$$\frac{\partial c}{\partial t} + \nabla \cdot (\mathbf{v}_s c - \mathbf{D} \nabla c) = 0, \quad (13)$$

wobei c die Konzentration eines konservativen Tracers ist. Die Sicker- oder Teilchengeschwindigkeit \mathbf{v}_s , ist definiert als:

$$\mathbf{v}_s = \frac{1}{\phi_e} \mathbf{v}. \quad (14)$$

Hierbei bezeichnet ϕ_e die effektive Porosität, d.h. die Porosität ohne "dead-end-Poren", die nicht zum aktiv durchströmten Aquiferbereich gehören. Ein hydrodynamischer Dispersionstensor \mathbf{D} wird als Summe der Dispersion \mathbf{D}_d und der molekularen Diffusion D_m eingeführt.

Im Gegensatz zum ADT betrachtet das "Streamline-Tracing" nur den advektiven Transport. Die Vorgehensweise beim "Streamline-Tracing" kann wie folgt zusammengefasst werden:

- Berechnung des Geschwindigkeitsfeldes aus einem Druckfeld, das wiederum das Ergebnis einer Strömungssimulation ist.
- Ausweiten der Klüfte je nach ihrer Öffnungsweite; Aufstellen einer Volumenbilanz an jedem Kontrollvolumen eines FV-Gitters zur Gewinnung der Volumenflüsse an allen inneren Grenzflächen.
- Verfolgung der Streamlines auf dem unstrukturierten Gitter unter Anwendung einer Erweiterung der Pollock-Methode.
- Berechnung einer kumulativen Durchbruchkurve und einer Durchbruchkurve anhand der Time-of-Flight-Methode der Streamlines.

Vergleich der geostatistischen und der statistischen Klüftgenerierung

Im Folgenden werden geostatistische (GFG) und statistische (SFG) Klüftgenerierung miteinander verglichen. Dabei werden zwei Fälle für die SFG (SFG-A und SFG-B) und drei Fälle für die GFG (GFG-A, GFG-B und GFG-C) in Betracht gezogen. Die beiden Fälle bei der SFG werden anhand zweier verschiedener Annahmen bei der Definition der Klüftgrößen bereitgestellt. Bei der SFG-A werden rechteckige

Klüfte angenommen, um deren Größe direkt durch die Kluftspur-Verteilung definiert zu haben. Länge und Breite der horizontalen Klüfte werden dabei durch die horizontale Spurverteilung beschrieben. Höhe und Breite der vertikalen Klüfte sind jeweils durch die vertikale und die horizontale Spurverteilung gegeben. Bei der SFG-B wird die Kluftgrößenverteilung solange angepasst, bis die gleiche Kluftspurverteilung wie im Feldversuchsblock erreicht wird. In beiden Fällen der SFG wird, nachdem man ein Kluftnetzwerk mit den spezifischen Kluftgeometrien (Kluftgröße, -orientierung und -dichte) erhalten hat, der Kluftabstand optimiert, sodass er mit dem am Feldversuchsblock beobachteten Wert übereinstimmt. In den ersten beiden Fällen der GFG werden die Anfangskonfigurationen des Kluftnetzwerks aus den beiden Fällen der SFG ohne Optimierung des Kluftabstands verwendet, also GFG-A aus SFG-A und GFG-B aus SFG-B. Im dritten Fall der GFG (GFG-C) wird die Anfangskonfiguration zufällig anhand der Kluftorientierung, Kluftdichte und der definierten maximalen Kluftgröße generiert. Durch Variation der maximalen Kluftgröße und Vergleich der Zielfunktionen findet man die minimale Zielfunktion anhand von Simulationen mit einer maximalen Kluftgröße von $0,9\text{ m} \times 1,8\text{ m}$ für vertikale Klüfte und $0,5\text{ m} \times 1,2\text{ m}$ für horizontale Klüfte. Nachdem man das Initial-Kluftnetzwerk für die GFG erhalten hat, werden die räumlichen Charakteristiken (das standardisierte experimentelle Variogramm, die Nachbarschaftsparameter, die Kluftzellen-Dichte und die Varianzen) optimiert, sodass sie mit den Werten des Feldversuchsblocks übereinstimmen.

Vom stochastischen Gesichtspunkt ist es möglich, vielfache Realisationen von Kluftnetzwerken zu generieren, wobei jede Realisation spezifische Eigenschaften beschreibt. Allerdings kann keine einzelne Realisation mit dem realen System exakt übereinstimmen. Das Verhalten des geklüfteten Systems kann aus der Mittelung der Gesamtheit vorhergesagt werden, die man aber nur erhält, wenn die Zahl der Realisierungen groß genug ist. In dieser Arbeit wird beabsichtigt, die Charakteristiken und das Verhalten eines geklüfteten Systems zu verstehen, nicht aber es vorherzusagen. Daher werden fünfundzwanzig Realisationen (fünf für jeden der oben genannten Fälle) generiert. Um die verschiedenen Fälle zu vergleichen, werden die Parameter jedes Falls durch Mittelung für jede der fünf freiliegenden Seiten des Feldversuchsblocks ermittelt, und zwar für jede einzelne Realisation und nochmal für alle fünf Realisationen.

Kluftnetzwerk-Struktur

Die räumlichen Strukturen von Kluftnetzwerken nach den fünf oben genannten Fällen, wie die Kluftspurverteilung, die Kluftgrößenverteilung und die räumlichen Charakteristiken (standardisiertes experimentelles Variogramm, Nachbarschaftsparameter und Kluftzellen-Dichte) wurden mit den Messwerten vom Feldversuchsblock bei Pliezhausen verglichen.

- Die Kluftgröße konnte aus der Kluftspur unter sorgfältiger Vorgehensweise angenähert werden. Der direkte Transfer der Kluftspurverteilung zeigt eine Unterschätzung der Kluftgröße (in der SFG-A). Die Kluftgröße wird besser angenähert, wenn die Größe solange modifiziert wird, bis die Kluftspurverteilung mit dem Wert des Feldversuchsblocks übereinstimmt (bei der SFG-B). Bei Optimierung der räumlichen Charakteristik in der GFG-A und GFG-B ändert sich die Kluftspurverteilung leicht.
- Bei der statistischen Kluftgenerierung (SFG) wird der Kluftabstand optimiert, daher zeigen die SFG-A und SFG-B gute Übereinstimmung mit den Daten vom Feldversuchsblock. Obwohl die Kluftabstände bei der geostatistischen Kluftgenerierung (GFG) nicht berücksichtigt werden, reproduzieren auch die Ergebnisse der drei GFG-Fälle die Gesamtheit der Abstände.
- Bei der GFG werden die räumlichen Charakteristiken in Betracht gezogen, nicht aber bei der SFG. Deshalb repräsentieren die drei GFG-Fälle fast alle räumlichen Charakteristiken mit Ausnahme der Nachbarschaftsparameter aus der vertikalen Scanline-Richtung, die richtungsabhängig ist. Die beiden Fälle bei der SFG zeigen statistisch, dass sie von den räumlichen Charakteristiken nur die Nachbarschaftsparameter in der Klufttrichtung reproduzieren, nicht aber das standardisierte Variogramm und die Kluftzellen-Dichte.

Strömungs- und Transportverhalten eines Kluft-Matrix-Systems

Für alle fünf oben genannten Testfälle wurde deren Strömungs- und Transportverhalten hinsichtlich der Mittelwerte des Gesamt-Volumenstroms Q sowie der Charakteristiken einer Durchbruchkurve (breakthrough curve, BTC) (der maximale Massenfluss \dot{m}_p , die Ankunftszeit des maximalen Massenflusses t_p , die mittlere Aufenthaltszeit \bar{t} , die Varianz σ^2 und die Schiefe γ) mit den Werten der gemessenen Südwest-Außenseite des Feldversuchsblocks verglichen. Die bei den drei GFG-Fällen erhaltenen Werte für Q , t_p und \bar{t} sind deutlich näher an denen des Feldversuchsblocks als jene der beiden SFG-Fälle. Das bedeutet, dass untereinander verbundene Strömungspfade, die das Bulk-Verhalten der Flüssigkeitsbewegung beeinflussen, mit der GFG repräsentiert werden können, jedoch nicht mit der SFG. Die Verteilung des Tracers der Konzentrationsfahnen wird auch durch bevorzugte Strömungspfade beeinflusst. Ein schneller Transport in verbundenen Pfaden und ein langsamer Transport in der Matrix resultiert in einem Doppelkontinuum-Verhalten, was man an Durchbruchkurven mit langen Ausläufern erkennt. Das Transportverhalten wird von der GFG besser reproduziert als von der SFG. Diejenigen Variablen, die einen weiten Bereich von Extremwerten (Min. und Max.) zeigen, wie beispielsweise der maximale Massenfluss \dot{m}_p und die Varianz σ^2 , benötigen mehr Realisationen um brauchbare Mittelwerte bei den einzelnen Testfällen zu bekommen.

Kluftnetzwerke, die mit der geostatistischen Kluftgenerierung erzeugt werden, erfassen das Strömungs- und Transportverhalten eines Kluft-Matrix-Systems offensichtlich besser als solche, die mittels der statistischen Kluftgenerierung erzeugt werden. Indem die räumlichen Charakteristiken und die statistischen Geometrien in die GFG integriert werden, können auch untereinander verbundene Strömungskanäle, die die Strömungs- und Transportprozesse beeinflussen, repräsentiert werden. Keines der Kluftnetzwerke aus den drei verschiedenen Fällen der GFG erfasst das Verhalten des Feldversuchsblocks deutlich besser als das jeweils andere. Dies könnte daher rühren, dass das Verhalten des Kluft-Matrix-Systems eher von den räumlichen Charakteristiken als von den Kluftgrößen beeinflusst wird, die ja den Unterschied zwischen diesen drei Fällen darstellen.

Zusätzlich kann der Einfluss numerischer Diffusion durch Vergleich der BTCs der gescannten Südwestseite des Feldversuchsblock bei verschiedenen Gittergrößen beobachtet werden. Sobald die Gittergröße kleiner wird, nehmen die Varianzen der Kurven zu und der Maximalwert nimmt ab. Das ist das Resultat einer physikalischen Diffusion aufgrund der starken Heterogenität zwischen Klüften und Matrix. Bei einem feinen Gitter wird ein injizierter Tracer, sobald er die Klüfte erreicht, rasch innerhalb der Klüfte transportiert. Die Lösung, die in der Matrix bleibt, benötigt eine längere Zeit um aus dem geklüfteten Matrix-System transportiert zu werden. Andererseits werden bei einem groben Gitter die Effekte der schnellen Strömung in den Klüften und der langsamen Strömung in der Matrix über den zur Strömungsrichtung senkrechten Querschnitt wegen der numerischen Diffusion verwischt, und das Kluft-Matrix-System tendiert zum Verhalten eines homogenen Systems. Somit ist eine feine Gittergröße nötig, um die Genauigkeit des numerischen Schemas zu garantieren, die Rechenzeit wird hierdurch allerdings erhöht.

Vergleich von Streamline-Simulation und advektiv-diffusivem Transport

Die Hauptvorteile des Streamline-Tracings (STR) sind seine schnelle Rechenzeit und das Nicht-Vorhandensein numerischer Diffusion, allerdings wird bei diesem Ansatz nur der advektive Transport berücksichtigt. Die Anwendbarkeit der STR zur Untersuchung des Transport-Verhaltens eines Kluft-Matrix-Systems wird durch Vergleich der Ergebnisse bezüglich einer mittels ADT erhaltenen Durchbruchkurve und einer kumulativen Durchbruchkurve untersucht. Zunächst wird eine Vergleichsstudie für vorläufige Testfälle ausgeführt, um grundlegende Kenntnisse der Charakteristik der STR im Vergleich mit dem advektiv-dispersiven Transport (ADT) zu erhalten. Dann wird das STR an Kluft-Matrix-Systemen aus den fünf Testfällen, die im vorherigen Abschnitt generiert wurden, durchgeführt und deren Ergebnisse mit denen der ADT verglichen.

Vorläufige Testfälle

Die vorläufigen Testfälle werden in der Weise angesetzt, dass sie einen großen Bereich der Gebietscharakteristik abdecken: Gruppe A enthält homogene und heterogene poröse Medien, Gruppe B betrachtet eine einzelne Kluft in einer porösen Matrix und Gruppe C konzentriert sich auf systematisch verteilte Klüfte in einer porösen Matrix.

Die Effekte schneller Strömungen in einem hochpermeablen Bereich oder in Klüften und langsamer Strömungen in einer Matrix werden durch die numerische Diffusion beim ADT in allen Testfällen verwischt. Die numerische Diffusion in Strömungsrichtung induziert eine Aufweitung der Konzentrationsfahne, deshalb zeigen die Ergebnisse des ADT eine anfänglich geringere Durchbruchzeit und einen geringeren maximalen Massenfluss als die des STR, das keine numerische Diffusion hat. Die schnellen und langsamen Strömungen in heterogenen, porösen Medien und Kluft-Matrix-Systemen mit einem Doppelkontinuum-Verhalten werden aufgrund des Auftretens zweier Maxima der BTCs mit dem STR besser beschrieben als mit dem ADT. Etwas unterschiedliche Werte der AccBTCs findet man beim STR, weil das Streamline-Tracing vom Geschwindigkeitsfeld abhängt, das man aus einer Strömungssimulation erhält und es ist (in der Nähe einer Kluft) lokal gitterabhängig.

Komplexe Kluftnetzwerke

Bei den komplexen Kluft-Matrix-Systemen der fünf Testfälle zeigt numerische Diffusion beim ADT das Wandern von Konzentrationsfahnen, während der rein advective Transport beim STR einen schnellen Transport des Tracers aufweist. Das hat zur Folge, dass der Unterschied zwischen den AccBTCs und BTCs aus den beiden Ansätzen in allen Testfällen des Kluft-Matrix-Systems klar zu erkennen ist. Die physikalische Dispersion aufgrund des schnellen und langsamen Transport manifestiert sich in langen Ausläufern der BTC sowohl beim STR als auch beim ADT und manifestiert sich auch in der Schiefe, die einen positiven Wert zeigt. Die Schiefe aus dem STR zeigt höhere Werte als die aus dem ADT, was eine größere physikalische Dispersion andeutet. Zur weiteren Überprüfung der Ergebnisse des ADT und STR sollten weitere Vergleiche mit experimentellen bzw. Feld-Studien durchgeführt werden.

Ausblick

Ein mit Hilfe der geostatistischen Kluftgenerierung erzeugtes Kluftnetzwerk repräsentiert die räumlichen Charakteristiken und die Geometrien des Kluftnetzwerks eines Feldversuchsblocks, weshalb man auch das Strömungs- und Transportverhalten des Kluft-Matrix-Systems erfassen kann. Auch das Streamline-Tracing, wie es in dieser Arbeit eingeführt wurde, ist eine vielversprechende Alternative, weil sein geringerer Rechenaufwand die numerische Simulation von Transportprozessen für etliche Realisationen und auf einer größeren Skala erlaubt. Dennoch sind weitere Studien auf diesem Gebiet nötig, um einige offene Fragen zu beantworten:

- Strömungs- und Transportverhalten eines zweidimensionalen Querschnitts eines Kluft-Matrix-Systems können in den Fällen erfasst werden, bei denen das Kluftnetzwerk mit Hilfe der geostatistischen Kluftgenerierung erzeugt wird. Die Untersuchung der Strömungs- und Transportprozesse muss auf ein dreidimensionales Kluft-Matrix-System erweitert werden, weil dann die Konnektivität der Klüfte komplexer ist. Die Einbeziehung dieses Effekts könnte zusätzlichen Aufwand zur Verbesserung der geostatistischen Kluftgenerierung notwendig machen. Weiterhin benötigt eine numerische Studie eines Strömungs- und Transportprozesses in einem dreidimensionalen Kluft-Matrix-System einen geeigneten Netzgenerator, der robust sein sollte und effektiv viele stochastisch generierte, in eine Matrix eingebettete Klüfte vernetzen sollte.
- In dieser Arbeit funktioniert das Streamline-Tracing gut, während der advektiv-dispersive Transport Probleme mit der numerischen Diffusion zeigt, die in manchen Fällen sogar die physikalische Dispersion dominiert. Da das Streamline-Tracing für stark advektiv dominierte Probleme geeignet ist, muss der Anwendungsbereich des Streamline-Tracings über den Vergleich der Ergebnisse mit denen eines experimentellen Setup definiert werden. Das Verhältnis zwischen Advektion und Dispersion (Peclet-Zahl) könnte als Maß verwendet werden.
- Die geostatistische Kluftgenerierung zeigte vielversprechende Ergebnisse auf einer analogen Skala und ihr Konzept neigt dazu, skalenunabhängig zu sein. Die Anwendbarkeit der geostatistischen Kluftgenerierung auf einer großen Skala sollte genauer untersucht werden.

1 Introduction

1.1 Motivation

For many countries worldwide, fractured rock systems have provided and still provided important natural resources such as petroleum, gas, water and geothermal energy. Recently, the investigation of the suitability of fractured systems as storage/disposal sites for high-level nuclear waste has been carried out in Yucca Mountain, USA (Bodvarsson and Tsang [1999] and Bodvarsson et al. [2003]), in Äspö Hard Rock Laboratory, Sweden (Dverstorp et al. [1992], Poteri et al. [2002]) and in Fanay-Augerès, France (Cacas et al. [1990b], Cacas et al. [1990a]). The resource exploitation and potential utilization have led to extensive studies with the aim of understanding, characterizing and finally predicting the behavior of fractured systems.

Aquifer analogue studies have been widely used for characterizing fractured aquifer systems. In the analogue studies, the detailed analysis of fractured systems such as borehole samplings, hydraulic measurements or exposed wall investigations can be performed practically, and the flow and transport properties obtained on an analogue scale can be upscaled to a large field scale (Dietrich et al. [2005]). On a large reservoir scale, a fractured system can be considered as a single- or double-continuum by assuming a representative elementary volume (REV) (Bear [1972]); however, on an analogue scale, the assumption of a fractured system as a REV is not always valid. Long et al. [1982] showed that considering a fractured system as a continuum depends on the characteristics of the fractured system, e.g. density and orientation. A discrete fracture model is an attractive alternative compared with the continuum model for aquifer analogue studies because there is no a priori assumption that a fractured system behaves as a continuum, and the effect of individual fractures can be explicitly investigated. Two main critics on the discrete model approach are its expensive computation time and its excessive data requirement for generating a fracture network. The increased speed of computers nowadays makes high computational demand, feasible on an analogue scale. A generation of a “representative” fracture network remains a challenging task when the discrete model is applied (National Research Council [1996]). In general, a fracture network generation based on observed fracture geometries can be categorized as: deterministic fracture generation (DFG) and statistical fracture generation (SFG). Geometries of a fracture network (e.g. size, aperture, orientation and location) are determined

exactly for individual fractures in DFG, whereas they are represented by statistical distribution functions in SFG (Long et al. [1982], Long [1983] and Dverstorp and Andersson [1989]). Due to intensive data requirements in DFG, SFG is widely used for a complex fracture network. In the case where dominating fractures are known, a combination of SFG with DFG is required. However, SFG often fails to capture the spatial variability and connectivity of fracture networks, which is related to interconnected flow paths that may dominate flow and transport processes in fractured systems (Berkowitz [2002]).

This work considers a fractured porous medium or a fracture-matrix system (FMS), which refers to a fracture network embedded in a porous matrix. The numerical study of flow and transport processes in such a fractured system differs strongly from the study in a fractured rock, in which a surrounding matrix is impermeable, because the simplification by transforming connected flow paths in fractures to a one-dimensional channel flow as introduced by Tsang and Tsang [1987] is not possible in this case. This means that a full two- or three-dimensional description of the fractures and the surrounding matrix, as presented by Therrien and Sudicky [1996], Marýšcaronka et al. [2005] and Reichenberger et al. [2006], is required. Furthermore, behavior of a fracture-matrix system can be represented by considering average characteristics obtained from several realizations of stochastically generated fracture networks. These aspects cause a rise in computational demand for the numerical study of the flow and transport behavior of a fracture-matrix system.

1.2 Objectives

The overall purpose of this work is to improve the study of a fracture-matrix system on an analogue scale using a discrete fracture model. An important prerequisite for this is the generation of a “representative” fracture network. Subsequently, an alternative approach to advective-dispersive transport in order to overcome the problem of high computational demand required for flow and transport simulations in a fracture-matrix system has to be considered.

Bogdanov et al. [2003] showed the importance of connected fractures in terms of the percolation threshold by considering its influence on the effective permeability of fractured porous media. By performing a modified scanline technique on the analogue scale, Silberhorn-Hemminger [2002] found the spatial dependency of fracture traces on exposed walls. As a result, a geostatistical fracture generation (GFG) is developed by taking into account not only the statistical geometries but also the spatial variability. The spatial characteristics considered in the GFG are determined directly from exposed walls. The flow and transport behavior of a fractured system are investigated in order to compare the geostatistical fracture generation (GFG) and

the statistical fracture generation (SFG), in which statistical geometries are included but not the spatial variability.

On the reservoir scale where fractures and matrix are treated as two interacting continua, promising results from streamline tracing have been presented by Huang et al. [2004] and Al-Huthali and Datta-Gupta [2004]. Their results showed a close agreement with the results from a grid-based finite difference simulation with an obvious reduction in computation time. Therefore, a streamline tracing for a discrete fracture-matrix system is developed in cooperation with the Department of Mathematics, University of Bergen (Haegland et al. [2008]). Further, the flow and transport behavior of a fracture-matrix system obtained from streamline tracing are compared with results from a vertex centered finite volume method (MUFTE-UG (Helmig et al. [1998])) in order to study the difference between the two approaches.

1.3 Structure of the Work

In Chapter 2, the characteristics of natural fractured aquifers in terms of fracture geometries are presented and different model concepts for studying the behavior of complex fractured aquifers are described. Moreover, the application of different conceptual models depending on the scale of the investigated problems are reviewed. The complex geometries of natural fractured systems are analyzed with respect to statistics and geostatistics in Chapter 3. First, an overview of statistics and geostatistics is presented. Then, the application of statistical distribution functions and geostatistical parameters to characterize fracture geometries is discussed.

This work relates to a study of a fractured porous sandstone block by using a discrete fracture-matrix model. In Chapter 4, the possible fracture generation approaches are addressed. Next, the geostatistical fracture generation (GFG), which is based on the fracture geometries and spatial characteristics, is introduced. A method for determining the required spatial characteristics of a fracture network from exposed walls is also presented in this chapter.

The mathematical formulations and the numerical models for studying solute flow and transport in a fracture-matrix system are described in Chapter 5. Here, governing equations for flow and transport processes in a fracture-matrix system are presented and the discretization techniques are explained. Furthermore, the streamline-tracing equations in a fracture-matrix system and the flux-recovery approach, which is a prerequisite of streamline tracing, are introduced.

The two aspects of the objectives lead to two different foci of the study. The first one attempts to improve fracture-network generation by considering both the fracture geometries and the spatial connectivity. In Chapter 6, flow and transport results

from the developed geostatistical fracture generation (GFG) are compared with the results from the statistical fracture generation (SFG). The second one aims to overcome the high computational demand of the transport simulation by using streamline tracing as an alternative approach. The comparative study of the flow and transport behavior of fracture-matrix systems using the advective-dispersive transport and using the streamline tracing are carried out in Chapter 7.

Finally, the main issues are summarized and an outlook including further research suggestion are given in Chapter 8.

2 From Nature to Conceptual Models

A fractured aquifer is a highly complex system due to the heterogeneity between the fractures and the surrounding matrix, and the variation of geological structures. Several model concepts have been developed in recent decades for investigating, understanding and ultimately predicting flow and transport behavior in such a complex system. The objective of the conceptual models is to simplify the complexity of fracture geometries and matrix-pore structures, and to make it possible to represent the relevant physical processes influencing the behavior of fractured aquifers. Selecting a suitable conceptual model depends on the spatial scale of a domain of interest and the characteristics of a fractured aquifer system. This chapter first presents the geometrical characteristics of natural fractured aquifers and then a review of the different model concepts.

2.1 Geometrical Characteristics of Fractured Aquifers

In earth science and hydrogeology, *fracture* is a term often used for all types of generic discontinuities in rocks. Three main classes of rocks can be classified: igneous, sedimentary and metamorphic rock. Igneous rock is formed by crystallization of magma. Sedimentary rock is formed through the deposition of sediments derived from weathered rocks, biogenic activity or precipitation from a solution. Metamorphic rock is the results of the transformation of pre-existing rocks by changes in texture or composition in response to changes in ambient temperature, pressure, volatile content. Different rock origins lead to various rock properties. Generally, metamorphic and igneous rocks have very low porosity and hydraulic conductivity. Sedimentary rock, on the other hand, has higher porosity and varied hydraulic conductivity. The ranges of porosity and hydraulic conductivity for different rock types are presented in Table 2.1. The difference between the total porosity ϕ and the effective porosity ϕ_e is that all the pores in the rocks are included in the total porosity, whereas, only pores contributing to the flow are taken into account in the effective porosity.

A fractured aquifer system is considered a fracture network embedded in a rock matrix. Depending on the different hydraulic properties of rocks, fractured aquifers can be categorized as belonging to one of two types: a fractured rock (FR), in which

Table 2.1: Total porosity, effective porosity and hydraulic conductivity of selected hard rocks (after Dietrich et al. [2005]).

Rock	Total porosity ϕ (%)	Effective porosity ϕ_e (%)	Hydraulic conductivity K (m s^{-1})
Granite	0.1	0.0005	$0.5 \cdot 10^{-12} - 2.0 \cdot 10^{-12}$
Limestone	5 – 15	0.10 – 5	$1.0 \cdot 10^{-09} - 6.0 \cdot 10^{-06}$
Chalk	5 – 44	0.05 – 2	$6.0 \cdot 10^{-09} - 1.4 \cdot 10^{-07}$
Sandstone	5 – 20	0.5 – 10	$3.0 \cdot 10^{-10} - 6.0 \cdot 10^{-06}$
Shale	1 – 10	0.5 – 5	$1.0 \cdot 10^{-13} - 2.0 \cdot 10^{-09}$

the surrounding matrix is considered to be impermeable to flow, and a fractured porous rock or a fracture-matrix system (FMS), in which the matrix is permeable to flow, although less permeable than in fractures by several orders of magnitude. For a FR, flow process occurs only in a fracture network not in the surrounding matrix; therefore, advective and dispersive transport takes place in a fracture network, but only diffusive transport can occur in a surrounding matrix. In contrast, in the case of FMS, flow and transport processes occur in both a fracture network and a matrix rock.

Geometries of the fracture networks, which can be described in terms of orientation, aperture, size and density, are obtained from one-dimensional observations (e.g. boreholes or core samples) or two-dimensional observations (e.g. outcrops or drift walls). The borehole survey is a direct method of characterizing fractures; however, only local information is gained from each sample. Hence, a large number of samples is necessary to quantify the geometries of the fracture networks accurately. Furthermore, by performing a scanline survey and/or an areal survey on exposed rock surfaces (rock outcrops, tunnel walls, or tunnel roofs), an additional two-dimensional information (such as fracture traces) can be obtained. A scanline survey collects only fracture traces intersecting the scanline, and the areal survey, however, collects all fracture traces inside a defined survey area.

On the basis of the geometrical information obtained from observations, different sets of fractures can be classified and their geometries are described by statistical distribution functions. Based on the observed statistical geometries, different sets of fractures can be classified. The description of the geometries of the fracture network is presented briefly in the following.

2.1.1 Fracture orientation

The orientation of natural fractures is described in geological coordinates as an azimuth A or a strike S , and a dip D . The strike S is a direction of a line formed by the intersection of a rock surface (in this case, a planar fracture) with an imaginary horizontal plane. The azimuth A is the angle between the vertical projection of the line of greatest slope of a rock surface onto a horizontal surface and north, typically measured in a clockwise direction from north. The relation between the azimuth and the strike is $A = S + 90^\circ$. The dip D is the magnitude of the inclination of a rock surface from the horizontal plane. The azimuth, the strike and the dip are illustrated in Figure 2.1.

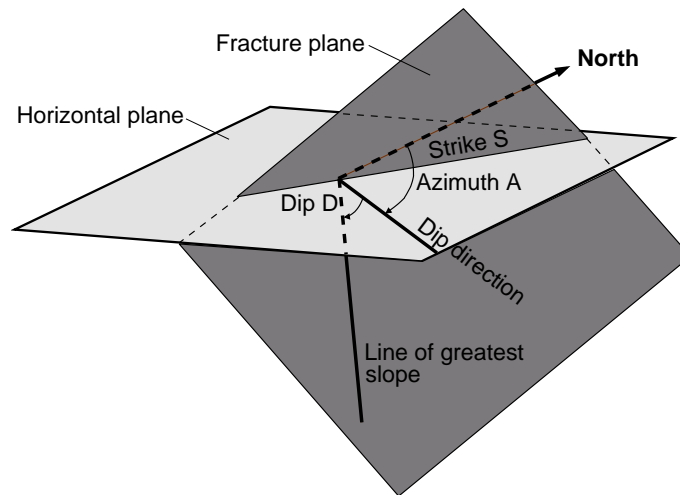


Figure 2.1: Determination of a fracture orientation: azimuth, strike and dip (modified after Dietrich et al. [2005]).

A statistical distribution of a fracture orientation is commonly expressed by a unit normal vector \vec{N} of a fracture plane in polar coordinates (θ, ϕ) , shown in Figure 2.2. Fisher et al. [1993] showed that the spherical polar coordinates is related to the azimuth and the dip as

$$\theta = D + 90^\circ \quad \text{and} \quad \phi = 360^\circ - A. \quad (2.1)$$

With stereographic projection, the fracture orientation in the polar coordinates is mapped on the lower hemisphere and later the sets of fractures together with their main orientations can be analyzed (e.g. Rouleau and Gale [1985], Dietrich et al. [2005]). Figure 2.3 illustrates the orientation distribution of fractures on the lower hemisphere.

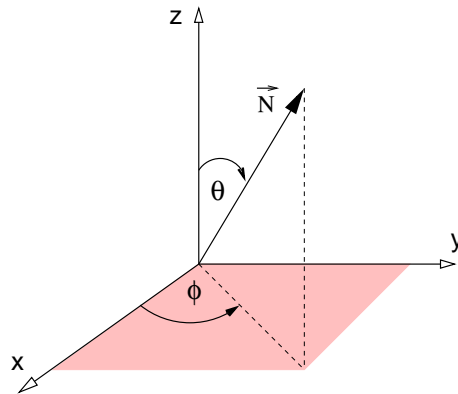


Figure 2.2: Determination of polar coordinates of a unit normal vector of a fracture surface.

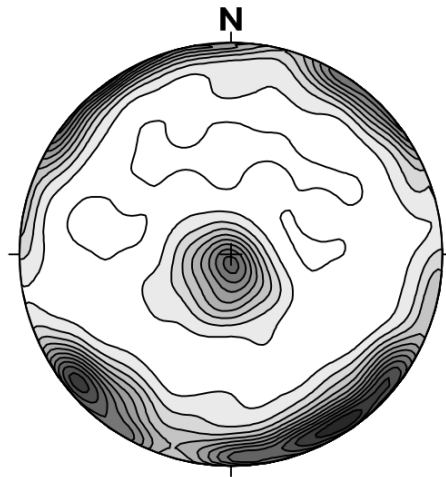


Figure 2.3: Fracture-orientation-distribution diagram from a Pliezhausen block (after Dietrich et al. [2005]).

2.1.2 Fracture aperture

A fracture aperture, defined as the distance between two fracture walls, varies within a single fracture and between fractures of the same set. Figure 2.4 shows roughness of surfaces of two fracture walls from a sample of ca. 20 cm diameter. The strong spatial variation of the fracture surfaces leads to highly varied aperture within these walls. On a larger scale, the spatial variation of the aperture in a single fracture was studied by Lapcevic et al. [1999]. He found that longitudinal and transversal spreading of tracer plume observed in a single fracture within a domain of the size 35 m × 40 m could be approximated by numerical simulations with a single fracture with varying aperture.

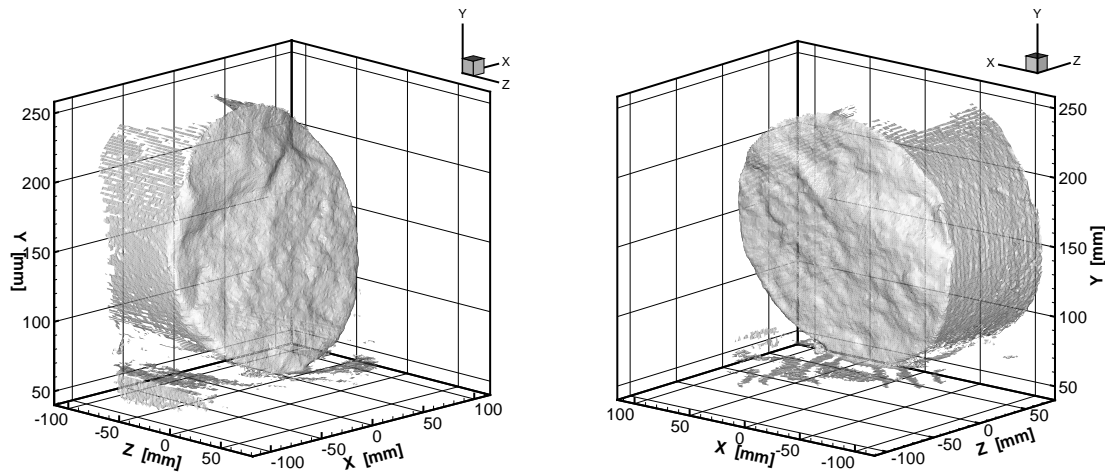


Figure 2.4: Two opposite fracture surfaces of a single fracture intersecting a core sample of ca. 20 cm diameter (in cooperation with the Institute for Robotics and Process Control, Technical University of Braunschweig, Germany) (after Silberhorn-Hemminger [2002]).

The fracture aperture can be obtained from direct measurements (photography), known as a mechanical or a physical aperture, and from hydraulic/pneumatic tests, known as a hydraulic aperture or an effective aperture. The hydraulic aperture is determined from the results of flow tests assuming that the fracture consists of two parallel plates. The mechanical aperture is expected to be larger than the hydraulic aperture since the variation in the aperture of natural fractures forces the flow to be tortuous (Hakami and Larsson [1996]).

2.1.3 Fracture size and fracture trace

A fracture size is one of the most difficult fracture geometries to obtain accurately because it cannot be measured directly from either one-dimensional borehole samples or two-dimensional exposed wall surveys. The fracture size can be approximated from the distribution of fracture traces if the fracture shape is assumed. Different geometrical shapes have been used to describe the fracture shape such as circular disks (Cacas et al. [1990b]), rectangles (Silberhorn-Hemminger [2002]) or polygons (Huseby et al. [2001]). Warburton [1980] presented an analytical method for evaluating the fracture size from the trace length distribution. He assumed that fractures are circular discs and their diameters follow log-normal distribution.

2.1.4 Fracture density

By definition, the volumetric fracture density d_3 is an average area of fractures per unit matrix volume. As mentioned previously, the fracture size (area) cannot be measured directly from observations; hence, the fracture density has to be approximated from accessible information. Chilès and de Marsily [1993] determined the fracture density d_3 from the core sample as

$$d_3 = \frac{1}{l} \sum_{i=1}^n \frac{1}{\sin \theta_i}, \quad (2.2)$$

where θ_i is the acute angle of the fracture and the core axis and n is the number of fractures intersecting the core of length l .

2.1.5 Fracture space

The fracture space is generally defined as the distance between a pair of discontinuities measured along a reference line. Priest [1993] distinguished between three different types of fracture space (see Figure 2.5):

- **Total spacing:** a distance between two directly adjacent fractures measured along a reference line.
- **Set spacing:** a distance between two directly adjacent fractures from the same fracture set measured along a reference line.
- **Normal set spacing:** a distance between two directly adjacent fractures from the same fracture set measured along a reference line that is normal to the mean direction of the fracture set.

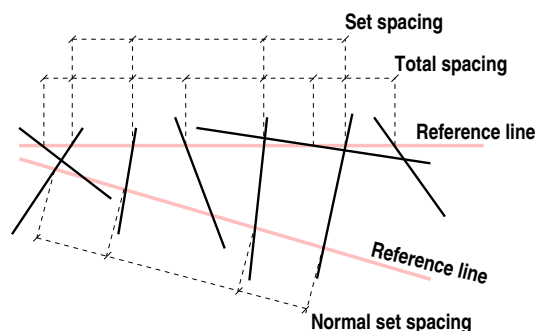


Figure 2.5: Illustration of fracture spaces from a scanline survey.

The fracture space distribution is a parameter indicating a spatial correlation of fractures; however, it shows only a weak spatial correlation (Priest [1993]).

2.2 Model Concepts for Fracture Aquifers

2.2.1 Scales and representative elementary volume (REV)

Relevant processes dominating flow and transport in fractured aquifer systems may differ on different spatial scales of interest. Thus, a physical law that describes the flow and transport processes on one scale may not be appropriate when the processes are upscaled to a larger volume. The overview of the relevant scales is given in Figure 2.6.

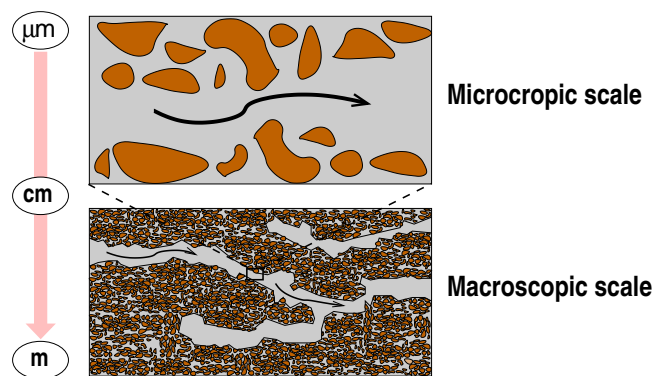


Figure 2.6: Sketch of the scales (modified after Silberhorn-Hemminger [2002]).

- **Microscopic scale:** The level of the pores or grain of the system is considered on the microscopic scale. The fluid motion is described by Navier-Stokes equations. The relevant parameters, i.e. fluid properties, and the exact geometries of the pore spaces are required.
- **Macroscopic scale:** The physical structure and hydraulic behavior on the microscopic scale is averaged over a macroscopic scale by introducing *effective parameters*, such as the porosity for the structure of the pore space in the total volume, the permeability for fluid-grain interaction, the saturation for fluid-fluid interaction and the capillary pressure for fluid interface.

Representative Elementary Volume (REV)

The *effective parameters* on the macroscopic scale can be determined by volume averaging within the representative elementary volume (REV). According to Bear [1972], the size of the REV should be large enough to avoid fluctuations of the parameters, but, it should be small enough to ensure spatial heterogeneity on the macroscopic scale. The range of the REV depends on the type of systems, see Figure 2.7.

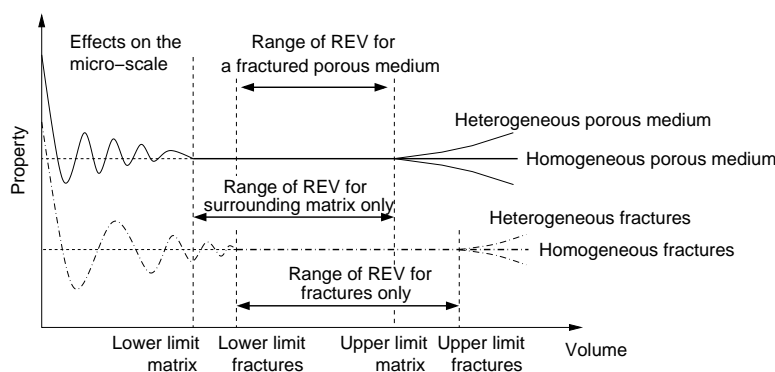


Figure 2.7: Definition of the REV for a porous medium and a fractured system (modified after Bear [1993]).

2.2.2 Continuum model approach

A continuum approach regards a fractured aquifer system as a continuum or continua on a REV scale. Consequently, complex geometries of the fractured aquifer are expressed in terms of the effective parameters, and flow and transport processes are described with continuity equations. There are three main different types of continuum model approach:

- **Single-continuum or equivalent-continuum model:** A fractured aquifer system is adequately considered a homogeneous continuum. That means its properties are averaged and assumed to be constant over the whole domain (e.g. Berkowitz et al. [1988], Pruess et al. [1990]).
- **Double-continuum and multi-continuum model:** Due to the heterogeneity between a high-permeability fractured system and a low-permeability porous matrix or between micro- and macro-fractures, the fractured aquifer is described separately by two interacting continua, known as the double-continuum model. Each continuum can be described by the conservation of mass and the two continua are coupled by exchange terms. Two main concepts of the double-continuum model are *dual porosity* and *dual/double permeability*. In the dual-porosity model introduced by Barenblatt et al. [1960], flow occurs only in a fracture continuum and transfer of fluid (or solute) in a matrix continuum is constrained only with the neighboring fractures (e.g. Bibby [1981], Zimmermann et al. [1993]). In the double-permeability model, flow and solute transport occur in both fracture and matrix continua (e.g. Gerke and van Genuchten [1993a], Gerke and van Genuchten [1993b]). Generally, the dual-porosity model is suitable for fractured rock (FR) and the dual-permeability model for fracture-matrix system (FMS). In a case where fractures of different scale are considered, the double-continuum concept can be extended to include more than two continua; this is known as a multi-continuum model.

- **Stochastic-continuum model:** The stochastic-continuum concept was firstly applied in heterogeneous porous media. Later, Neuman and Depner [1988] and Tsang et al. [1996] introduced this concept to fractured systems. The heterogeneity between fractures and matrix is considered in a single continuum by using geostatistical parameters such as the mean, variance and correlation length to express the hydraulic properties (e.g. hydraulic conductivity and porosity). In the stochastic model developed by Tsang et al. [1996], the fracture zones were distinguished from the matrix by imposing a correlation structure of a high hydraulic conductivity.

The advantage of the continuum approach lies in its simplicity. Complex geometries of a fractured system are ignored, and instead, the effective parameters (e.g. permeability, porosity and exchange terms) are introduced to describe the system behavior. The effective parameters can be obtained from the field measurements (Reimus et al. [2003]). For fractured systems, the application of the continuum approach mainly depends on the existence of a REV on the scale of interest. Long et al. [1982] showed that the fractured systems cannot always be considered a continuum. They behaved more as homogeneous media when the scale of investigated domains was enlarged, the fracture density increased and the fracture orientation was varying rather than constant. The continuum model is a promising approach for large field scales of hundreds of meters up to several kilometers such as in Yucca Mountain (Wu et al. [1999]).

2.2.3 Discrete model approach

In contrast to the single- or multi-continuum model approach, fractures are explicitly determined in a discrete model approach. Consequently, the detailed geometries of fractures such as the orientation, the size, the aperture and the density are required. Complex fracture geometries are simplified by assuming that the spatial variability of the geometries can be represented by statistical distribution functions and/or geostatistical parameters. Deterministic, statistical and geostatistical information on the fracture geometries is obtained from laboratory investigations and field observations.

Two main aspects of utilizing the discrete model approach can be distinguished. One aspect is to have a primary tool to study a fractured aquifer: existing of the REV for characterizing a fractured aquifer as an equivalent continuum or double continua, and determining effective parameters if a continuum can be justified. The second aspect is to have an approach that accounts for and quantifies effects of individual fractures on fluid flow and transport, as well as provides an alternative if a fractured system cannot be assumed as a continuum.

With the discrete model approach, the influence of fracture geometries on the hydraulic behavior can be investigated individually and the preferential flow paths due to high permeability in connected fractures can be represented. Depending on the scale of problems and the characteristics of the fractured aquifers, a different type of the discrete model approach can be applied:

- **Single-fracture model:** A well-defined single fracture is determined. If the fracture surfaces are considered perfectly smooth parallel plates, the flow in a single fracture is described by a parallel plate concept. On the basis of this simplified concept, analytical solutions for a tracer transport can be derived. Tang et al. [1981] proposed the analytical solution considering advection, dispersion, sorption and reaction processes. Later, Yates [1990] and Yates [1992] extended the scope of the study to consider cases with a linear and an exponential dispersion function. However, experimental and numerical investigations of fractures indicate preferential flow paths in a fracture plane, depending on the variation of the fracture aperture (Moreno et al. [1988], Brown et al. [1998] and Jakobs [2004]). Tsang and Tsang [1987], Tsang et al. [1988] proposed a raster model concept to reproduce the variation of the fracture aperture with the statistical distribution function and correlation lengths. The fracture-aperture distribution is approximated by using computer tomography (CT) scanning or by assuming statistical distribution functions.
- **Fracture-network model:** This model approach applies widely for fractured rocks (FR) where fluid flows through the interconnected fractures embedded in an impermeable surrounding rock matrix. The conceptual model for a channeling flow in fractured rock was proposed by Tsang and Tsang [1987]. They assumed one-dimensional flow channel flow through two- or three-dimensional fractured rocks. Approaches for determining the properties of the flow channel are discussed by Tsang et al. [1988]. Cacas et al. [1990b] applied the channeling-flow concept to in-situ observations; simulation results after calibrating the stochastic discrete fracture-network model showed a good agreement with the measurement data. Apart from the channeling-flow concept, fractures can be assumed to be parallel planes with a constant effective aperture (Long and Billaux [1987]) or with variable apertures (Nordqvist et al. [1992]).
- **Fracture-matrix model:** This model applied for the flow occurs in a fracture network and the surrounding matrix, such as in a fracture-matrix system (FMS). A matrix is presented as a continuum and discrete fractures are determined by statistical distribution functions. The applications of the fracture-matrix model are presented in Marýsaronka et al. [2005], Silberhorn-Hemminger [2002], Neunhäuserer [2003] and Reichenberger et al. [2006].

A discrete fracture approach requires much higher computational demand than the continuum approach; therefore, the attempt to use the continuum model has been widely recognized, particularly on a large field scale. However, applying the continuum approach to study fractured systems has to be done with a good understanding of the system behavior. Samardzioska and Popov [2005] compared the equivalent-continuum, the double-permeability and the discrete fracture-matrix models in systematical fractured systems. Flow and transport results from the discrete approach showed good agreement with the equivalent-continuum and the dual permeability only when the fracture network was located parallel to the flow direction. If the rotated fracture network is considered, the fluxes evaluated from the double-permeability model are accurately presented when the channeling effect is taken into account. The accuracy of the transport for the double-permeability model is strongly affected by the accuracy of the assumed exchange term between fractures and matrix.

2.2.4 Scales of consideration

The selection of the suitable model concept depends on the scale of the problems under investigation; these can be classified in the following way (Dietrich et al. [2005] and Bear [1993])

- **The very near field:** Flow and transport processes are considered in a well-defined single fracture. If the surrounding matrix is included, only diffusive transport is considered for the FR, whereas advective and diffusive transport are assumed for the FMS.
- **The near field:** The study domain on this scale is relatively small and contains a relatively small number of fractures. The geometries of the individual fractures can be explicitly determined or stochastically generated based on deterministic or stochastic information obtained from observations.
- **The far field:** It is assumed that flow and transport processes occur simultaneously in two overlapping continua. One continuum is composed of fluid within a fracture network and the other describes fluid within a matrix. Fluid mass and its components may be exchanged between the two continua.
- **The very far field:** The entire fractured system is described as one single continuum, possibly heterogeneous and anisotropic if geological layers and fault zones on a large scale are taken into account.

The application of the model approaches according to the scale of investigated problems is presented in Figure 2.8.

The fractured system considered in this study is a sandstone field block of ca. $8\text{ m} \times 10\text{ m} \times 2\text{ m}$ located at Pliezhausen, Germany (Dietrich et al. [2005]). The field

block is characterized as a fracture-matrix system (FMS) of dense fractures and high matrix porosity and permeability. On this problem scale, the existence of an REV in the fracture-matrix system cannot be guaranteed, therefore, the discrete model concept is an attractive alternative for the study of the field block. In accordance with the characteristics of the sandstone field block, the fracture-matrix model concept is used to describe the fractured system as well-defined fractures embedded in a porous matrix.

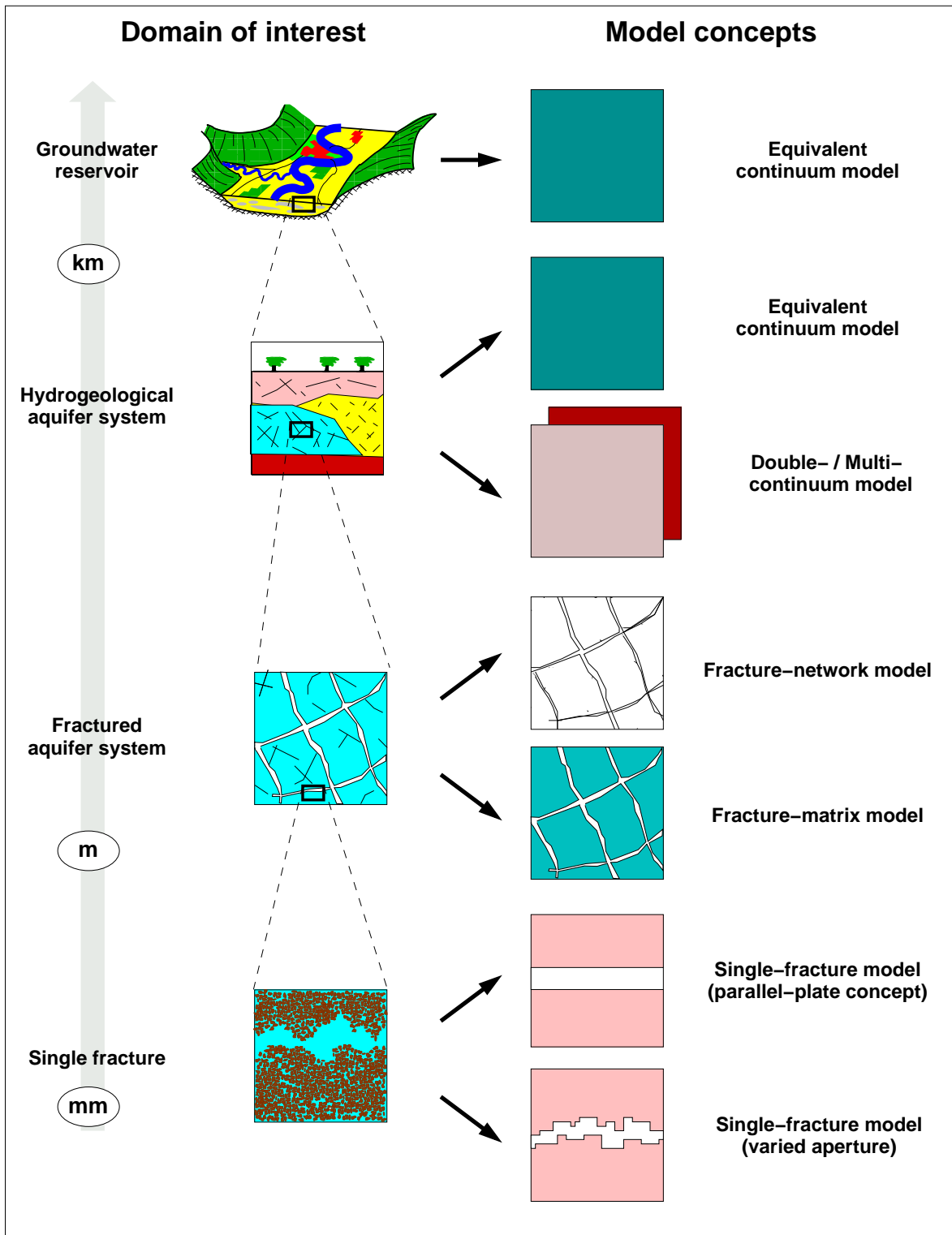


Figure 2.8: Sketch of the relation between model concepts and scales of the investigated domain (modified after Silberhorn-Hemminger [2002] and Dietrich et al. [2005]).

3 Stochastic Characteristics of Fracture Networks

Complex geometries of natural fractured systems must be defined explicitly in a discrete model approach. In most cases, it is not feasible to determine each fracture in the model exactly in the same way as the one in nature. Hence, the complexity of natural fracture geometries is described using statistical distribution functions and/or geostatistical parameters. In this chapter, after the basics of statistics and geostatistics have been presented in Sections 3.1 and 3.2, the analysis of fracture characteristics based on statistics and geostatistics is discussed in Sections 3.3 and 3.4.

3.1 Statistics

Statistics refers to the mathematical study concerning the collection, analysis, interpretation, and presentation of data. It is applicable to a wide variety of academic disciplines ranging from the physical and social sciences to the humanities. The principles of statistics which are relevant to the analysis of fracture geometries are presented in the following.

3.1.1 Univariate statistics and bivariate statistics

Univariate statistics is the branch of statistics devoted to analyzing a data set of a single variable of interest. Typically, the univariate statistics of a data set are the (arithmetic) mean, variance and standard deviation. The mean of variable x from n data points is

$$\bar{x} = \frac{1}{n} \sum_{i=1}^n x_i. \quad (3.1)$$

The variance infers the variability of the values which is expressed as

$$s^2 = \frac{1}{n-1} \sum_{i=1}^n (x_i - \bar{x})^2. \quad (3.2)$$

The spread of data about the mean in the same data unit can be measured by the standard deviation. It is defined as the square root of the variance

$$s = \sqrt{s^2}. \quad (3.3)$$

If a considered data set is a random variable $Z(x)$ to which a probability distribution $f(x)$ is assigned, the statistics of the random variable can be characterized by its moments. The population mean of $Z(x)$, also called expected value $E[Z(x)]$, is defined by taking the first moment

$$E[Z(x)] = \mu = \int_{-\infty}^{+\infty} xf(x)dx. \quad (3.4)$$

The variance is the second central moment of $Z(x)$

$$Var[Z(x)] = \sigma^2 = E[(Z(x) - \mu)^2] = \int_{-\infty}^{+\infty} (x - \mu)^2 f(x)dx. \quad (3.5)$$

In contrast to the univariate statistics, the bivariate statistics relates to the correlation between two random variables $Z(x)$ and $Z(y)$. The correlation is defined by covariance as

$$Cov[Z(x), Z(y)] = E[(Z(x) - \mu_x)(Z(y) - \mu_y)]. \quad (3.6)$$

3.1.2 Probability distribution and random variables

The distribution of a random variable X is determined by the *cumulative distribution function* (cdf), also called the distribution function,

$$F(x) = P(X \leq x), \quad (3.7)$$

which denotes the probability that a random variable X does not exceed any specified value x . The cdf is a monotone-increasing function ranging from 0 to 1. For a continuous random variable X , the cdf $F(x)$ can be described by a *probability distribution function* (pdf) $f(u)$

$$F(x) = \int_{-\infty}^x f(u)du. \quad (3.8)$$

In other words, the pdf can be expressed in terms of the cdf as

$$f(x) = \frac{d}{dx}F(x) = P(x < X \leq x + dx). \quad (3.9)$$

The cdf in an interval $(a, b]$ is defined by the integral of the pdf from a to b

$$P(a < X \leq b) = F(b) - F(a) = \int_a^b f(u)du. \quad (3.10)$$

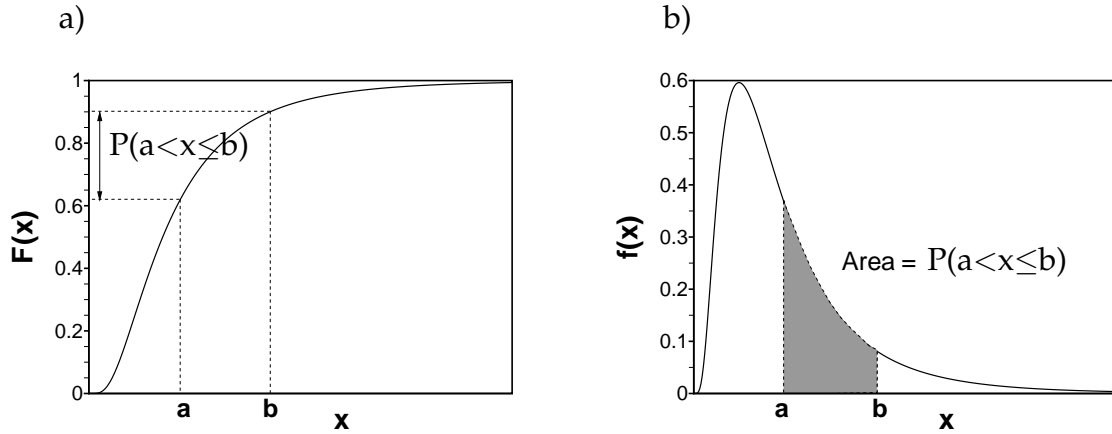


Figure 3.1: Cumulative distribution function (a) and probability distribution function (b) in an interval $(a, b]$.

Figure 3.1 shows the cumulative distribution function and the probability distribution function in an interval $(a, b]$.

In statistics, the probability distributions of the random variable X can be characterized by mathematical functions. Considering the same random variable X at several locations, the distribution of the random variable X in the space is assumed to be the same as the probability distribution of the random variable X at each location. This part only presents the probability distribution functions which are applied to describe the geometries of fractures in space.

- **Poisson distribution function:** It expresses the probability of a number of events occurring in a fixed period of time. These events must be independent of the time since the last event and occur with a known average rate. The Poisson distribution is defined as

$$f(k) = \frac{\lambda^k e^{-\lambda}}{k!}. \quad (3.11)$$

Here k is the number of occurrences of the event during a given interval, and λ is the expected number of occurrences during the given interval.

- **Uniform distribution:** The probability is equally distributed over a specific interval $[a, b]$ as

$$f(x) = \begin{cases} \frac{1}{b-a} & \text{if } a \leq x \leq b, \\ 0 & \text{if } x < a \text{ or } x > b. \end{cases} \quad (3.12)$$

- **Normal distribution or Gaussian distribution:** The importance of the normal distribution is its wide application in natural sciences. Many measurements and physical parameters can be approximated well by the normal distribution, which is given as

$$f(x) = \frac{1}{\sigma\sqrt{2\pi}} e^{-\frac{(x-\mu)^2}{2\sigma^2}}, \quad (3.13)$$

where σ is the standard deviation, and μ is the mean.

- **Log-normal distribution function:** By definition, the log-normal distribution has certain similarities to the normal distribution. A variable is log-normally distributed if the log-transformed variable is normally distributed. The log-normal distribution is defined as

$$f(x) = \frac{1}{x\sigma\sqrt{2\pi}} e^{-\frac{(\ln x - \mu)^2}{2\sigma^2}}, \quad (3.14)$$

where μ and σ are the mean and standard deviation of the logarithm of the variable, respectively. The distribution function is valid for values of $x > 0$.

- **Exponential distribution function:** The exponential distribution is characterized by a probability density function as

$$f(x) = \begin{cases} \lambda e^{-\lambda x} & \text{if } x \geq 0, \\ 0 & \text{if } x < 0, \end{cases} \quad (3.15)$$

with the rate parameter $\lambda > 0$.

- **Erlang distribution function:** The distribution is determined by two parameters: the shape k , which is a positive integer, and the rate $\lambda > 0$:

$$f(x) = \frac{\lambda^k x^{k-1} e^{-\lambda x}}{(k-1)!} \quad \text{for } x > 0. \quad (3.16)$$

When the shape parameter k equals 1, the distribution simplifies to the exponential distribution. This distribution is sometimes called the Erlang- k distribution (e.g. an Erlang-2 distribution is an Erlang distribution with $k = 2$).

An example of different distribution functions in Figure 3.2 shows that a random variable distributes differently depending on its probability distribution.

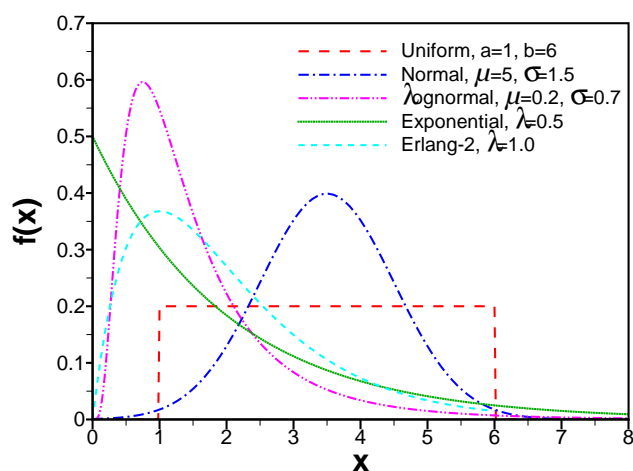


Figure 3.2: Different probability distributions of a random variable: uniform, normal, log-normal, exponential and Erlang distribution.

3.2 Geostatistics

Geostatistics can be regarded as the study of variations of reality in space or time by assuming that variables are spatially or temporally correlated. It was first introduced in 1962 by G. Matheron in order to estimate ore reserves in gold-deposit sites of the Witwatersrand. Nowadays, geostatistics is widely applied in various fields, such as petroleum geology, hydrogeology, hydrology, meteorology, oceanography, geochemistry, and geography.

The difference between geostatistics and statistics can be illustrated with the indicator fields shown in Figure 3.3. Both indicator fields have the same statistic values, such as means and variances; however, the correlation in the space which is related to geostatistics can be observed only in Figure 3.3a, not in Figure 3.3b.

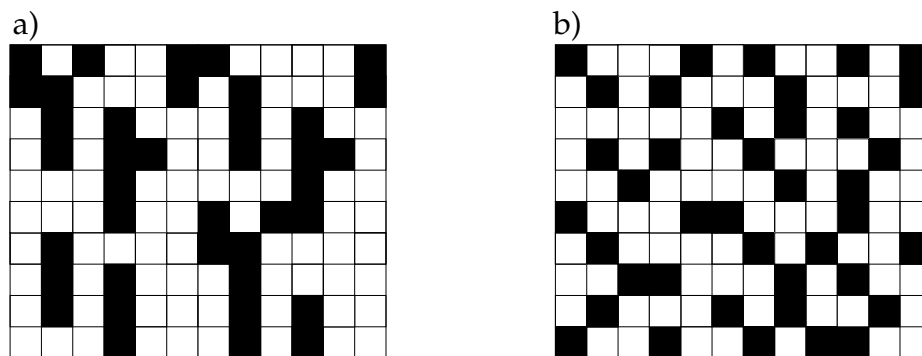


Figure 3.3: Two different indicator fields of the same mean and variance.

In mathematics, the correspondence of regionalized random variables can be characterized with a *stationary process*. Geostatistics relates to the principle of the stationary process and the spatial variation is analyzed using a *variogram*. In this section, a stationary process is briefly explained; later several variogram models and the procedure for calculating an experimental variogram from the field data are presented.

3.2.1 Stationary process

A stationary process is a random process in which none of its statistical properties vary with time. The random process consists of random variables at the location \mathbf{x} in time and has all the properties of random variables, such as mean and variance.

- **Strictly stationary:** A random process is classified as strictly stationary if its joint distributions are identical regardless of the separation vector \mathbf{h}

$$P(Z(\mathbf{x}_1), Z(\mathbf{x}_2), \dots, Z(\mathbf{x}_n)) = P(Z(\mathbf{x}_1 + \mathbf{h}), Z(\mathbf{x}_2 + \mathbf{h}), \dots, Z(\mathbf{x}_n + \mathbf{h})) . \quad (3.17)$$

- **Second-order stationary:** This is a weaker form of the strictly stationary process. A random process is second-order stationary if its mean is constant over the whole domain Ω and its covariance function depends only on the separation \mathbf{h}

$$\begin{aligned} E[Z(\mathbf{x})] &= \mu && \text{for } \mathbf{x} \in \Omega , \\ E[(Z(\mathbf{x} + \mathbf{h}) - \mu)(Z(\mathbf{x}) - \mu)] &= Cov(\mathbf{h}) && \text{for } \mathbf{x}, \mathbf{x} + \mathbf{h} \in \Omega . \end{aligned} \quad (3.18)$$

- **Intrinsic hypothesis:** A random process is said to be intrinsic stationary if its mean is constant and a variance of increment depends only on a shift \mathbf{h} from its origin. The intrinsic hypothesis is characterized by

$$\begin{aligned} E[Z(\mathbf{x})] &= \mu && \text{for } \mathbf{x} \in \Omega , \\ E[(Z(\mathbf{x} + \mathbf{h}) - Z(\mathbf{x}))^2] &= 2\gamma(\mathbf{h}) && \text{for } \mathbf{x}, \mathbf{x} + \mathbf{h} \in \Omega . \end{aligned} \quad (3.19)$$

Theoretically, $2\gamma(\mathbf{h})$ is called the variogram, and $\gamma(\mathbf{h})$ is known as the semivariogram. This work only refers to $\gamma(\mathbf{h})$; thus, the term variogram is used for $\gamma(\mathbf{h})$. The variogram can be related to the covariance by

$$\begin{aligned} \gamma(\mathbf{h}) &= \frac{1}{2}E[(Z(\mathbf{x} + \mathbf{h}) - Z(\mathbf{x}))^2] \\ &= \frac{1}{2}E[((Z(\mathbf{x} + \mathbf{h}) - \mu) - (Z(\mathbf{x}) - \mu))^2] \\ &= \frac{1}{2}(E[(Z(\mathbf{x} + \mathbf{h}) - \mu)^2] + E[(Z(\mathbf{x}) - \mu)^2] - 2E[(Z(\mathbf{x} + \mathbf{h}) - \mu)(Z(\mathbf{x}) - \mu)]) \\ &= Cov(0) - Cov(\mathbf{h}) . \end{aligned} \quad (3.20)$$

The advantage of describing the random process with the intrinsic hypothesis is that the evaluation of the variogram requires no information of its mean, in contrast to the calculation of the covariance function in the second-order stationary. The intrinsic hypothesis can be seen as a limitation of the second-order stationary, which means the second-order stationary implies the intrinsic behavior, but not vice versa.

3.2.2 Variogram models

The constraint of the intrinsic hypothesis is satisfied when a variogram function is a positive-definite function (Pannatier [1996]). Therefore, a few simple mathematical functions which satisfy a positive-definite condition are used as variogram models. The variogram models imply that the adjacent data are more correlated than the remote data, which means the correlation decreases when the separating distance $|\mathbf{h}|$ increases. If the separating distance $|\mathbf{h}|$ is larger than a *range*, the data are no longer correlated and reach a plateau which is called a *sill*. A list of variogram models is presented in the following, where $|\mathbf{h}| \geq 0$ and a constant parameter $a > 0$.

- **Nugget model:**

$$\gamma(\mathbf{h}) = \begin{cases} \sigma^2 & \text{if } |\mathbf{h}| > 0, \\ 0 & \text{if } |\mathbf{h}| = 0. \end{cases} \quad (3.21)$$

The nugget model represents the variability in a small interval which is finer than sample spacing. The abrupt change of the variogram from 0 (at $|\mathbf{h}| = 0$) to σ^2 (at $|\mathbf{h}| > 0$) indicates the variability of the variable over small scales or the measurement error.

- **Spherical model:**

$$\gamma(\mathbf{h}) = \begin{cases} \sigma^2 \left(\frac{3|\mathbf{h}|}{2a} - \frac{1}{2} \left(\frac{|\mathbf{h}|}{a} \right)^3 \right) & \text{if } |\mathbf{h}| \leq a, \\ \sigma^2 & \text{if } |\mathbf{h}| > a. \end{cases} \quad (3.22)$$

The range of the spherical variogram is equal to a and the variance σ^2 or the sill is greater than zero. The curve shows a linear relationship near the origin (see Figure 3.4).

- **Exponential model:**

$$\gamma(\mathbf{h}) = \sigma^2 \left(1 - e^{-\frac{|\mathbf{h}|}{a}} \right) \quad \text{for } a > 0. \quad (3.23)$$

Unlike the spherical variogram, the exponential model has no well-defined range. The value of $3a$ where the variogram reaches 95% of the variance is

used as an approximated range (Deutsch and Journel [1992]). Near the origin, the curve increases rapidly and when $|\mathbf{h}|$ becomes larger it raises more slowly (see Figure 3.4).

- **Gaussian model:**

$$\gamma(\mathbf{h}) = \sigma^2 \left(1 - e\left(-\frac{|\mathbf{h}|^2}{a^2}\right)\right) \quad \text{for } a > 0. \quad (3.24)$$

The curve shows parabolic behavior at the origin (see Figure 3.4). Kitanidis [1997] suggested that in practice a range is defined as $|\mathbf{h}|$ at which the correlation is 0.05.

In order to distinguish different behavior of different variogram models, curves of the variogram models of the same variance/sill and the same range are plotted in Figure 3.4.

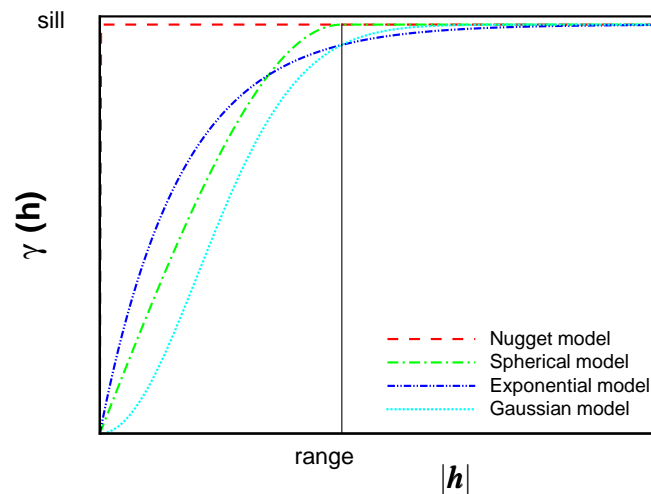


Figure 3.4: Variogram models: nugget model, spherical model, exponential model and Gaussian model.

3.3 Statistical Analysis of Fracture Characteristics

Characterizing geometries of fractured aquifer systems requires a transfer of knowledge from the observations (borehole samplings, measurements on exposed rock surfaces) mostly on a smaller scale to the entire fractured aquifer. Hence, the assumption that the statistical patterns analyzed from observations can (to some extent) represent the fracture geometries of the complete system has been made. The geometries of fractures (e.g. orientation, aperture, size, density) are generally described with the log-normal or the exponential distributions. However, these distributions are found to be scale-dependent. Attempts to determine fracture geometries with distribution functions of no characteristic length scale such as a power law or a fractal geometry, are presented by Odling [1997]. Bonnet et al. [2001] discussed the techniques and guidelines for accurately estimating exponents and fractal dimensions from observations. In the following, an overview of different statistical distributions for describing the fracture geometries mentioned in Section 2.1 is presented.

3.3.1 Fracture orientation

The statistical distribution of fracture orientation is often described by the Fisher distribution (Fisher et al. [1993], Cacas et al. [1990b]) as:

$$f(\theta, \phi) = \frac{\kappa}{4\pi \sinh \kappa} e^{[\kappa (\sin \theta \sin \alpha \cos(\phi-\beta) + \cos \theta \cos \alpha)] \sin \theta} . \quad (3.25)$$

Here, α is the θ -pole coordinate (latitude) of the main orientation \vec{R} , β is the ϕ -pole coordinate (longitude) of the main orientation \vec{R} and κ is the concentration parameter indicating the orientation distribution around the main orientation \vec{R} . For $\kappa \rightarrow \infty$, the orientation distribution is strongly concentrated around \vec{R} . For $\kappa \rightarrow 0$, the orientation is closer to the uniform distribution. For $\kappa \geq 4$, the distribution can be quantified with a cone of spherical aperture ω around \vec{R} which is known as a cone of confidence (see Figure 3.5):

$$\omega = \arcsin \sqrt{2 \frac{1 - 1/n}{\kappa}} . \quad (3.26)$$

Here, n is the sample size. The spherical aperture for the Fisher distribution corresponds to the standard deviation of the Gaussian normal distribution.

The borehole survey introduces a bias in fracture orientation since the fractures that are parallel to the borehole are less likely to be recorded than fractures that are perpendicular to the borehole. The rotation of the borehole during the extraction requires careful analysis of the fracture orientation. Additionally in two-dimensional

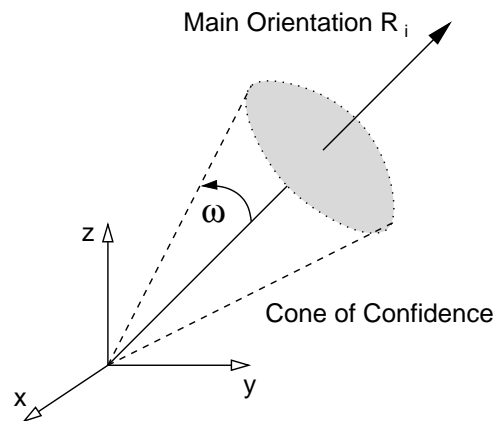


Figure 3.5: Sketch of the cone of confidence with the spherical aperture ω (after Dietrich et al. [2005]).

observation, the fracture orientation is always more or less biased by the sampling direction; e.g. the fractures that have a steep angle to the outcrop tend to be sampled rather than fractures that are parallel to the outcrop. The correction of bias is presented in Munier [2004]. Odling [1997] showed that the fracture orientation in sandstones of areas ranging from 18 to 720 m is scale-independent, which means transferring fracture orientation from an observed scale to a study scale is possible.

3.3.2 Fracture aperture

Regarding numerical studies of flow and transport processes in a single fracture, variable aperture have been described by distribution functions such as log-normal distribution (Snow [1970]) or Gaussian normal distribution (Hakami and Larsson [1996], Lapcevic et al. [1999]). Due to the aperture distribution, the channeling effect can be observed within and between fractures in the fractured rock.

In the case of a fracture-matrix system, as in this study, the heterogeneity between fractures and the porous matrix leads to stronger channeling effects than the channeling effect due to the aperture variation in each fracture. Therefore, preferential flow paths in each fracture are not considered and the fractures are described as a pair of parallel plates at a constant distance; this is known as a parallel plate concept (see Section 5.1 for more details).

3.3.3 Fracture size and fracture trace

Different distribution functions, such as a log-normal distribution (e.g. Priest and Hudson [1981], Baecher [1983], Rouleau and Gale [1985], Dverstorp and Andersson

[1989], Cacas et al. [1990b]) and an exponential distribution (Cruden [1977]), are applied to characterize the fracture traces. Odling [1997] proposed using a power law distribution because it is possible to upscale from observations on a small scale to fractured aquifers on a large scale within the upper and lower cutoffs. The cutoff values existed as a result of a sampling bias. The power law distribution for the fracture trace is given by

$$N(l) = k l^{-a} . \quad (3.27)$$

Here, $N(l)$ is the number of fractures of a length greater than or equal to the constant length l per unit area and a is the fractal dimension. The exponent a is defined by the slope of the log-log graph of $N(l)$ plotted against l . It is generally recognized that the effects of resolution and finite size on a power law population lead to the log-normal-like or exponential-like distributions (Bonnet et al. [2001]).

The areal and scanline survey of fracture traces on exposed walls often introduce four main biases (Bear [1979] and National Research Council [1996]):

- **Censoring:** due to the limited extension of drift walls, one or both terminations of traces are not observable.
- **Truncation:** traces that are shorter than the cut-off length and large traces that do not intersect drift walls are not recorded.
- **Length bias:** small fractures are underestimated, as there is less probability of intersecting smaller fractures than larger fractures.
- **Orientation bias:** fractures aligned parallel to the scanline or parallel to a sampling face are underestimated.

The areal survey causes less length and orientation bias than the scanline survey; however, censoring still remains where the rock surface is of limited extent. Influences of the biases on the distribution of fracture traces are summarized by Baecher [1983]. The possible biases caused by scanline surveys are analyzed by Priest [1993]. Rouleau and Gale [1985] showed that different degrees of censoring, i.e. both ends observable, only one end observable and neither end observable, affected the statistics of the fracture traces (the maximum length, the mean and the standard deviation).

Extrapolations of two-dimensional information of fracture traces to a three-dimensional fracture size have been performed analytically and numerically. Warburton [1980] provided the analytical solutions which derived from the distributions of fracture traces by assuming the circular fractures with a log-normally distributed diameter. In the case of severe bias due to censoring, the reliability of the fracture-trace distribution is ambiguous. Hence, La Pointe et al. [1993] developed a stochastic forward model for estimating the fracture size from the bias trace length information.

3.3.4 Fracture space

Snow [1970] showed that the distribution of fracture frequency along a line can be approximated with the Poisson distribution. Priest and Hudson [1981] and Baecher [1983] showed that the distribution of total spacing for various rock types could be modeled by the exponential distribution function. Priest [1993] expressed mathematically that if the existence of fractures follows the Poisson distribution, which means that fractures occur randomly, the fracture space is determined by an exponential distribution.

3.4 Geostatistical Analysis of Fracture Characteristics

In a hydrogeology field relating to fractured aquifers, geostatistics is used as a tool for analyzing the spatial correlation of the fracture structure observed in the field. When the variogram of the fracture geometries, known as the *experimental variogram*, is calculated, the spatial variability of the fracture properties can be examined. The experimental variogram is defined as

$$\gamma(\mathbf{h}) = \frac{1}{2} \frac{1}{n_h} \sum_{\alpha=0}^n [Z(\mathbf{x} + \mathbf{h}) - Z(\mathbf{x})]^2, \quad (3.28)$$

where $|\mathbf{h}|$ is a separating distance and n_h is the number of pairs of random variables at a distance $|\mathbf{h}|$ apart.

La Pointe and Hudson [1985] showed that the density and the orientation of fractures followed systematic spatial patterns. Further geostatistical investigations were carried out by Long and Billaux [1987]. They generated a two-dimensional heterogeneous fracture network from homogeneous subdomain fracture networks by introducing geostatistics as a tool for predicting the spatial variation of the fracture trace length and the fracture density between subdomains. Desbarats and Bachu [1994] investigated the vertical and horizontal heterogeneities of the hydraulic conductivity of a sandstone aquifer using geostatistics. The investigation additionally considers the upscaling of the hydraulic conductivity from the core scale to the regional scale. Silberhorn-Hemminger [2002] used a modified scanline technique to characterize the spatial variability of the fracture network and the results of experimental variograms showed spatial dependency of fracture traces.

4 Generation of Fracture Network: Geostatistical Approach

When the discrete model approach is applied to study a fractured system, fractures are determined explicitly. The strong influence of fracture structures on the behavior of the fractured system makes the fracture-network generation crucial. This study attempts to develop a fracture network generator that considers both spatial characteristics and statistical fracture geometries. In this chapter, the possible fracture-generation approaches are reviewed. After presenting the statistical geometries and the description of the study site, the method for characterizing the spatial variability of the study site is discussed. Later, the generation of the fracture network based on the analyzed spatial variability and the statistical geometries is introduced.

4.1 General Concept of Fracture Network Generation

Characterizing a fracture network as discrete fracture elements requires geometrical information on fractures, such as the orientation, the aperture, the size, the traces, the density and the space. These fracture geometries are obtained from one- or two-dimensional observations such as borehole surveys, man-made excavations (tunnels or drifts), or outcrops. There are three main concepts for reconstructing discrete fracture networks:

- **Deterministic approach:** Geometries of fractures are exactly determined for each fracture and have to be carefully extrapolated from the one- or two-dimensional geometrical data. This is feasible when only a few (dominant) fractures are considered. However, for a complex fracture network, the deterministic approach demands extensive information on the fracture geometries, in most cases, this is not available.
- **Statistical approach:** Fracture geometries are described using statistical distributions, such as uniform distribution, power law distribution, normal distribution, log-normal distribution, and Fisher distribution (as mentioned in Section 3.3) instead of using individually determined geometries as in the deterministic approach. Statistical fracture generation regardless of spatial correlation was introduced for a two-dimensional case by Long et al. [1982] and was

further developed for a three-dimensional field case by Cacas et al. [1990b]. Statistical generation generally starts with randomly locating the center of a fracture according to the Poisson distribution. Then, the orientation, the size and the aperture are assigned to the fracture on the basis of the statistical distribution functions. The generation of fractures is repeated until the density of the fracture network is reached. Silberhorn-Hemminger [2002] included the optimization of the fracture space distribution in order to integrate the spatial correlation into the statistically generated fracture network.

- **Geostatistical approach:** The effort to integrate spatial correlations of fracture geometries into a generated fracture network has been made in the recent decades. The experimental variogram is a geostatistical tool widely applied for accounting for the spatial variation of the geometries. Long and Billaux [1987] evaluated the experimental variogram of fracture traces from a drift wall and generated a two-dimensional heterogeneous fracture network which contained statistically homogeneous subdomains. This concept was extended by Billaux et al. [1989] to generate a three-dimensional fracture network of circular-disc fractures. Tran et al. [2006] proposed the utilization of conditional global optimization to simulate a two-dimensional discrete fracture network by considering spatial statistics of the fracture density, the fracture size and the fracture orientation.

4.2 Description of the Study Site

The study site is a sandstone field block of ca. $8 \text{ m} \times 10 \text{ m} \times 2 \text{ m}$ located at Pliezhausen, Germany (see Figure 4.1). The Pliezhausen block is characterized as a fracture-matrix system (FMS) of dense fractures and high matrix porosity and permeability. The statistical geometries of the fractured system obtained from the one- and two-dimensional survey are summarized in Table 4.1 (Dietrich et al. [2005]).

In this study site, the spatial variability of fracture geometries cannot be assumed to be homogeneous in a subdomain and varied in a whole domain as presented by Long and Billaux [1987] and Billaux et al. [1989], since relatively large fracture traces upto ca. 2 m are observed on the exposed walls of several meters which means that the assumption of locally constant geometries cannot be fulfilled. Therefore, the spatial variability of the study site are quantified directly from its exposed walls. The approach for evaluating the spatial characteristics and the results are discussed in the next section.

	Distribution Function	Parameters of Distribution Function		
Orientation:	Fisher Dist.	Azimuth (A)	Dip (D)	Spherical Aperture
set1		146°	7°	12.05°
set2		229°	8°	10.20°
set3		201°	85°	11.22°
Fracture Trace:	Erlang-2 Dist.		lambda (λ)	
vertical			-3.933	
horizontal			-5.372	
Fracture Distance:	Exponential Dist.		lambda (λ)	
			-4.565	
Fracture Density:	Uniform Dist.		11.337 m ² /m ³	

Table 4.1: Statistics of fracture geometries obtained from the Pliezhausen block (modified after Silberhorn-Hemminger [2002]).

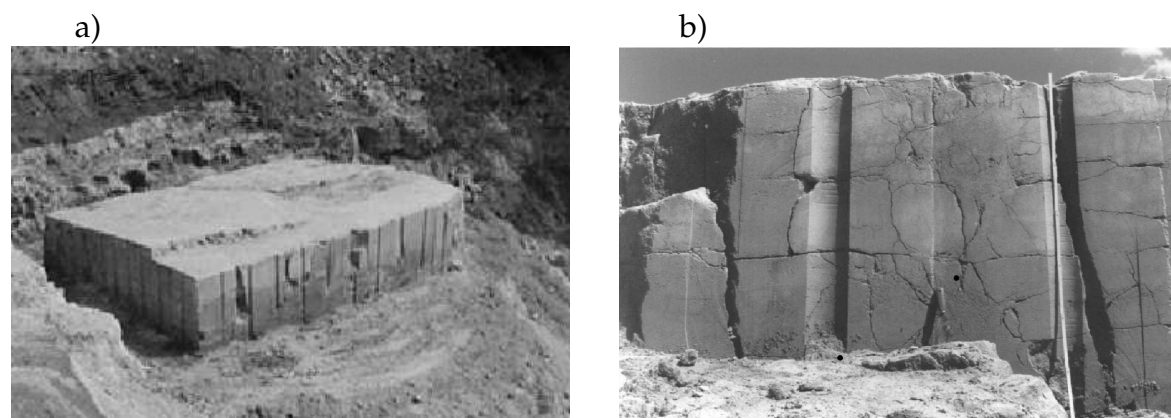


Figure 4.1: View of the study site Pliezhausen block: a) a view from the south-east direction and b) a part of vertical exposed wall (modified after Dietrich et al. [2005]).

4.3 Analysis of Spatial Characteristics of Pliezhausen Block

The spatial structures and the connectivity of the fracture network are parameters that strongly influence the hydraulic behavior of the fractured aquifer systems. However, in the fracture-network generation, these characteristics cannot be represented only by considering the statistics of the fracture geometries. A *modified scanline technique* (MS) which was presented in the work of Silberhorn-Hemminger [2002] and Dietrich et al. [2005] is a tool to quantify the spatial characteristics of

the fracture network. Figure 4.2 illustrates the procedure in the MS for analyzing the spatial characteristics from exposed walls. First, a set of parallel and equally distributed scanlines are overlaid on a fracture-trace map, where the direction of the scanlines is arranged perpendicular to the main orientation of the fracture trace. The scanlines are divided into segments of equal length l . Then, along each scanline, the existence of intersection points between fracture traces and the scanline segment itself are recorded and described with an indicator variable $I(\mathbf{x})$

$$I(\mathbf{x}) = \begin{cases} 1 & \text{intersection "fracture-scanline" exists, called fracture cell,} \\ 0 & \text{no intersection "fracture-scanline" exists, called matrix cell,} \end{cases} \quad (4.1)$$

where \mathbf{x} is a midpoint coordinate of a scanline segment. By following this way, the fracture-trace map is transformed to an indicator field, which can be visualized as two types of cells, a gray cell for a fracture cell and a black cell for a matrix cell. The distance d between scanlines and the scanline segment l are defined depending on the size of the fracture-trace maps and the characteristics of fracture traces. Different scanline distances and scanline segments should be investigated in order to find suitable values for the investigated exposed walls (Dietrich et al. [2005]).

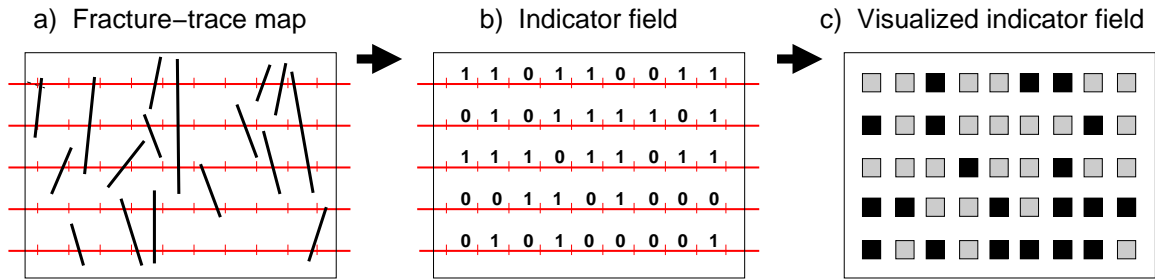


Figure 4.2: Procedure of a modified scanline technique for evaluating an indicator field from a fracture-trace map.

The fracture-trace maps of the surfaces of the Pliezhausen block are recorded by performing stereophotogrammetric shooting, see Figure 4.3. The fracture-trace maps of the five exposed walls: the north, the east, the south-east, the south-west and the west walls are presented in Figure 4.4. Three main fracture sets, a horizontally oriented and two vertically oriented sets, are identified using the stereographic projection (previously presented in Figure 2.3). However, only two main directions of fracture traces are observed on the five exposed walls: one horizontal and one vertical. For the MS, the scanline direction should be arranged perpendicular to the main fracture direction; hence, the horizontal and the vertical fracture-trace sets are analyzed separately. Two indicator fields are obtained from each exposed wall: *horizontal-scanline indicator field*, using a horizontal scanline direction to consider two vertical fracture orientations, and *vertical-scanline indicator field*, using a vertical scanline direction to consider a horizontal fracture orientation. According to Dietrich

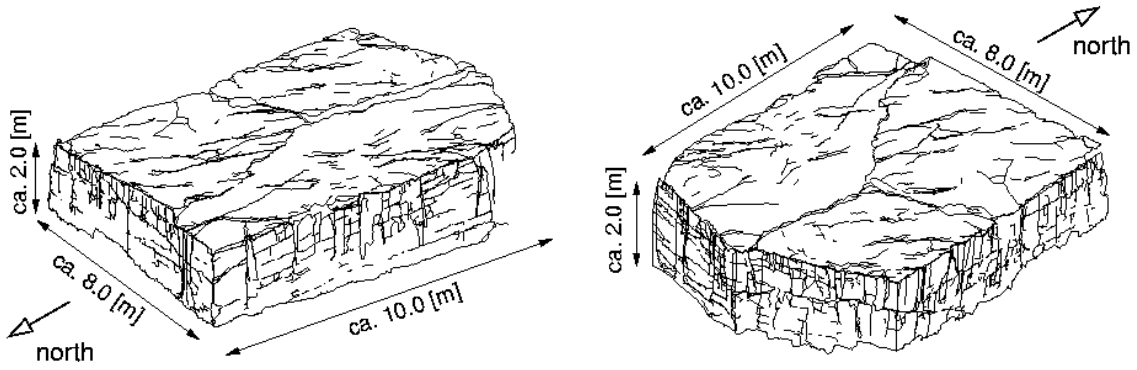


Figure 4.3: View of the Pliezhausen block from the north-west and the south-east (modified after Dietrich et al. [2005]).

et al. [2005], for all five exposed walls, the segment length l and the scanline distance d are selected as $l = 0.10\text{ m}$ and $d = 0.10\text{ m}$ for the horizontal-scanline indicator field (Figures 4.5) and $l = 0.10\text{ m}$ and $d = 0.20\text{ m}$ for the vertical-scanline indicator field (Figures 4.6).

The spatial characteristics are analyzed from the indicator field using different parameters. The first parameter is a standardized variogram, which is selected instead of a variogram because variability of a variable ($I(x)$) can be taken into account by scaling its variogram by its variance σ^2

$$\gamma_s(\mathbf{h}) = \frac{\gamma(\mathbf{h})}{\sigma^2}. \quad (4.2)$$

The variability of indicator fields becomes important when comparing several indicator fields of different variances. The standardized experimental variogram of the indicator field is defined as

$$\gamma_s(\mathbf{h}) = \frac{1}{2\sigma^2} \left(\frac{1}{n_h} \sum_{\alpha=1}^{n_h} [I(\mathbf{x}_\alpha + \mathbf{h}) - I(\mathbf{x}_\alpha)]^2 \right), \quad (4.3)$$

where n_h is the number of pairs of variables at a distance $|\mathbf{h}|$ apart. The distance $|\mathbf{h}|$ is considered perpendicular and parallel to the scanline direction.

The variance of the indicator fields is described according to a Bernoulli trial, which is an experiment whose outcome is random and can be either of two possible outcomes. When considering the indicator fields having two possible outcomes 0 and 1, the variance is described as

$$\sigma^2 = p(1-p), \quad \text{where} \quad p = \frac{1}{n} \sum_{\alpha=1}^n I(\mathbf{x}_\alpha). \quad (4.4)$$

The term p is known as the probability of success and n is the total number of cells.

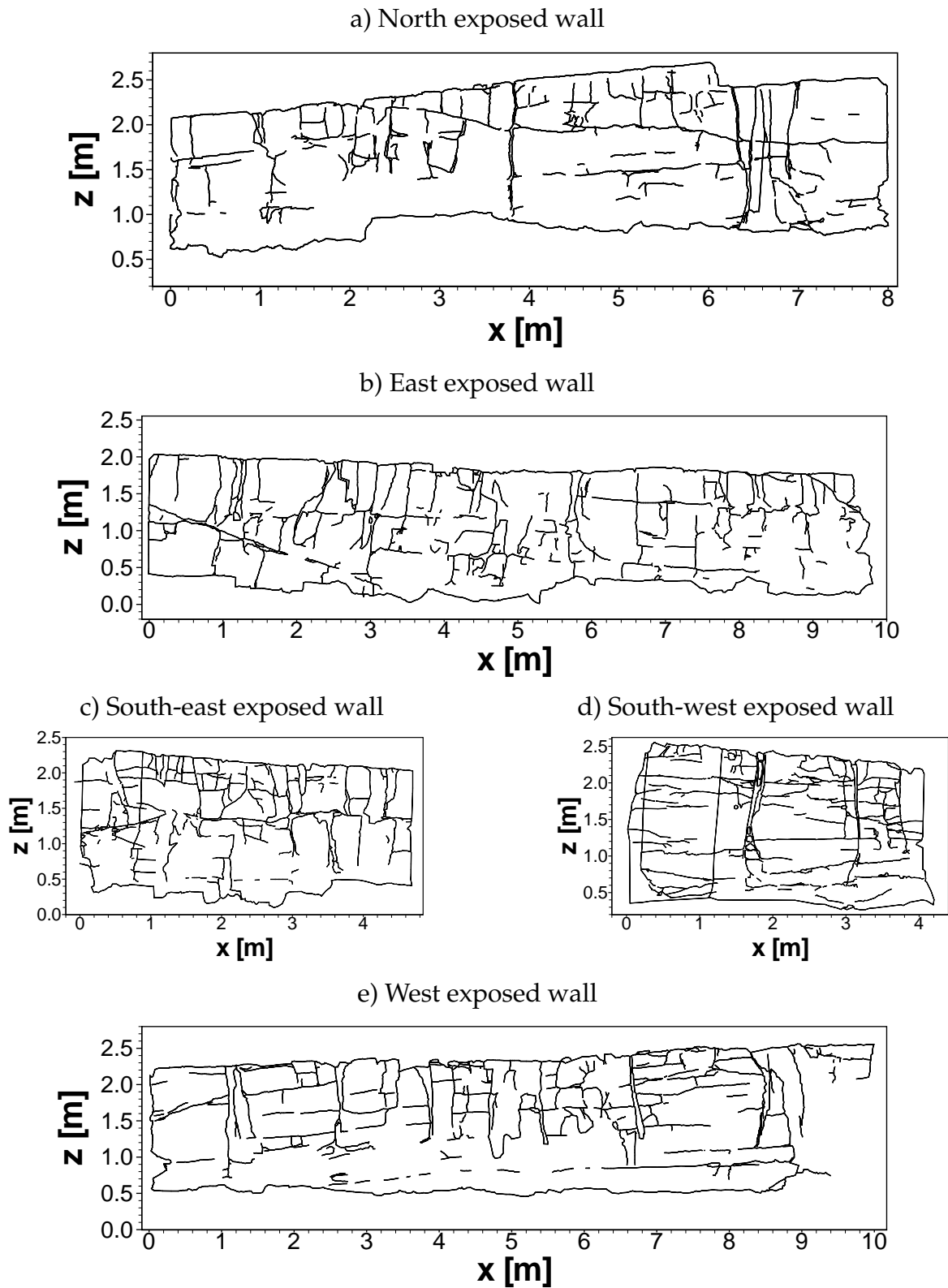


Figure 4.4: Fracture-trace maps of the five exposed walls obtained from the Pliezhausen block.

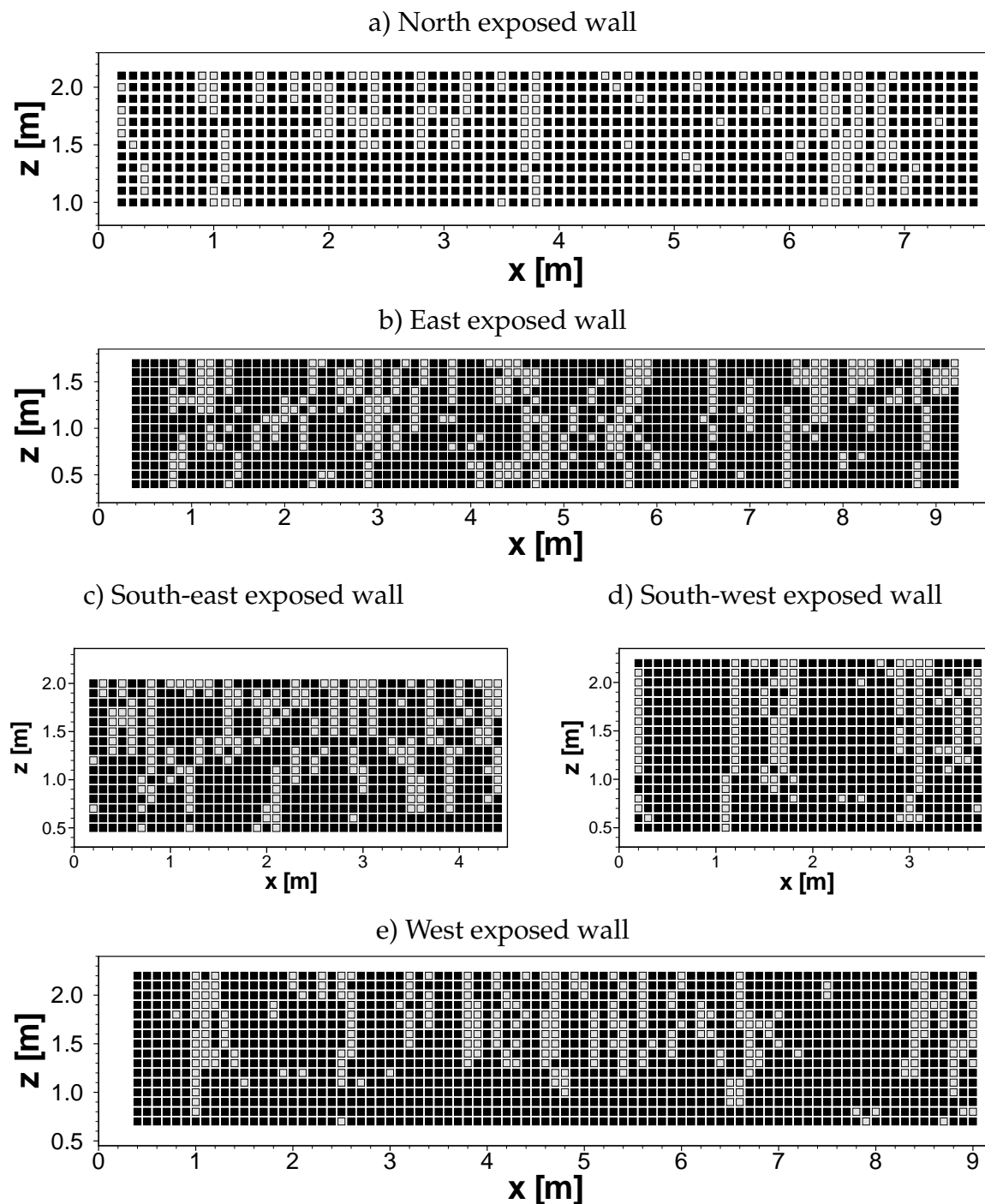


Figure 4.5: Horizontal-scanline indicator fields of the five exposed walls, the scanline distance $d = 0.10$ m and the segment length $l = 0.10$ m.

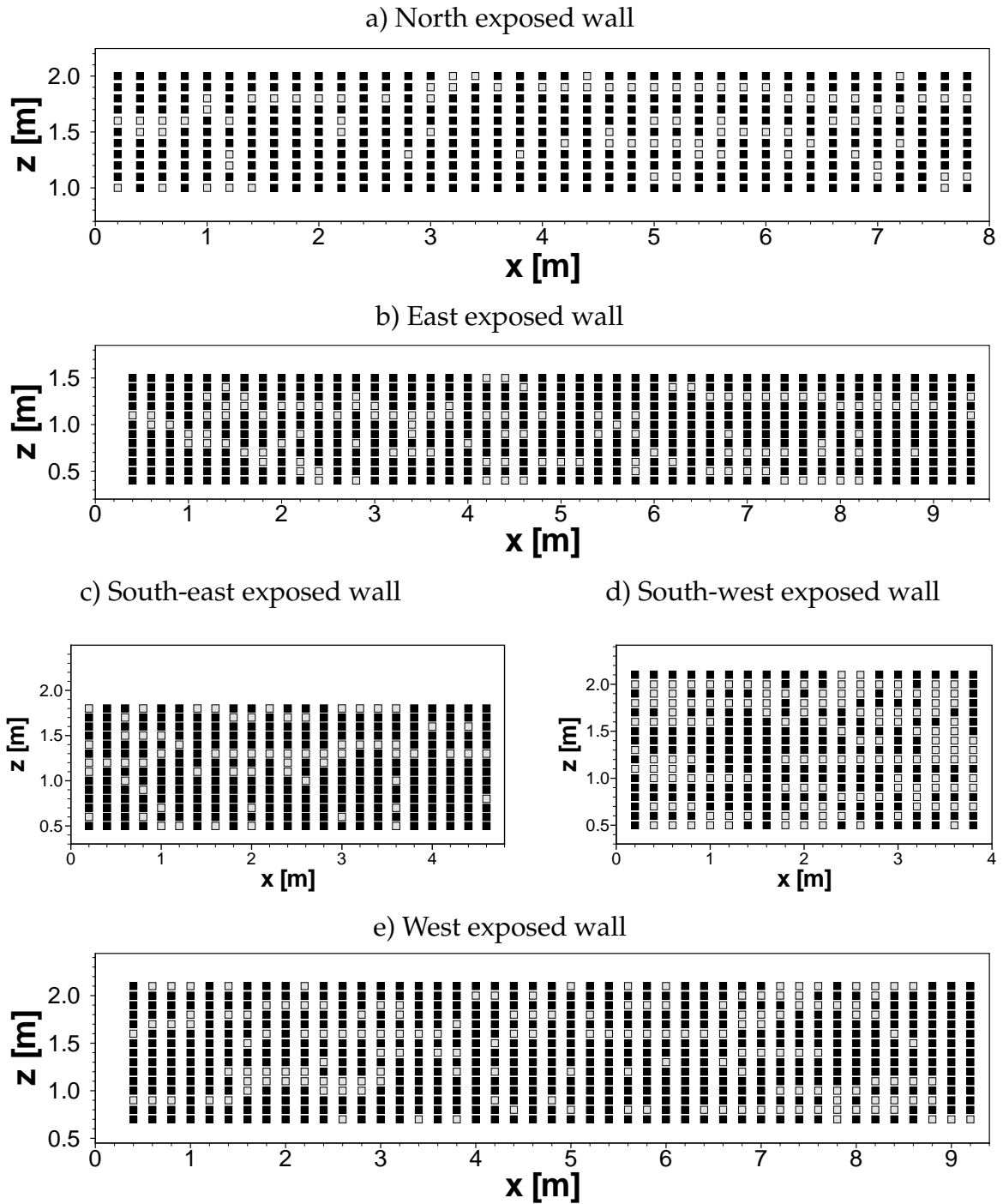


Figure 4.6: Vertical-scanline indicator fields of the five exposed walls, the scanline distance $d = 0.20$ m and the segment length $l = 0.10$ m.

The standardized experimental variograms of the five exposed walls are evaluated from Equation (4.3) for the horizontal- and vertical-scanline indicator fields. When \mathbf{h} is perpendicular to the scanline directions (Figures 4.7a and 4.8a), the curves increase within the correlation length or the range, and later reach a constant value. The range indicating an interval where a spatial dependency exists relates to the fracture-trace length observed on the fracture-trace maps. However, in the parallel cases (Figure 4.7b and 4.8b), the standardized experimental variograms show only a slightly oscillation interpreted as nugget behavior. This implies that there was no correlation between a fracture and the neighboring fractures at the sampling distance $|\mathbf{h}|$ in the direction parallel to the scanline. Hence, the appearance of the fractures can be considered a random process, which is in accordance with the assumption of a Poisson distribution.

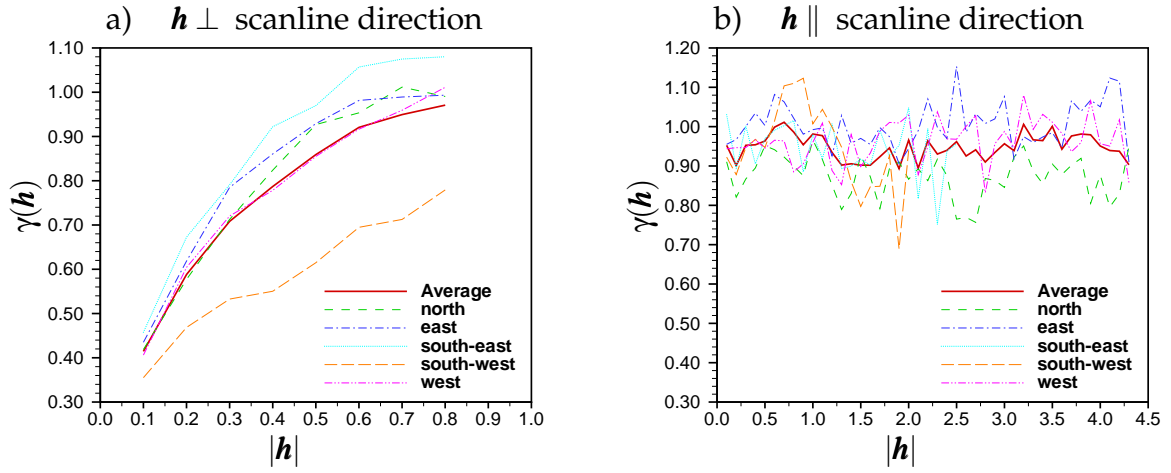


Figure 4.7: Standardized experimental variograms of the horizontal-scanline indicator fields, the scanline distance $d = 0.10\text{m}$ and the segment length $l = 0.10\text{m}$.

The standardized experimental variograms of the five exposed walls for perpendicular cases are averaged and fitted with the variogram model by VARIOWIN (Pannatier [1996]). The average data shows the best fit with a combination of the exponential and the nugget variogram models, which are presented in Section 3.2

$$\gamma(\mathbf{h}) = \sigma_1^2 + \sigma_2^2 \left(1 - e^{\left(-\frac{|\mathbf{h}|}{a}\right)}\right) \quad \text{for } a > 0. \quad (4.5)$$

The parameters σ_1^2 , σ_2^2 and a are 0.14, 0.86 and 0.80 respectively for the horizontal-scanline indicator fields and 0.48, 0.52 and 1.67 respectively for the vertical-scanline indicator fields, see Figure 4.9. In this case due to the normalize of the experimental variograms with their variances the sum of σ_1^2 and σ_2^2 is 1.

In addition to the standardized variogram, image-reconstruction parameters denoted as neighborhoods are considered with the aim of characterizing the spatial

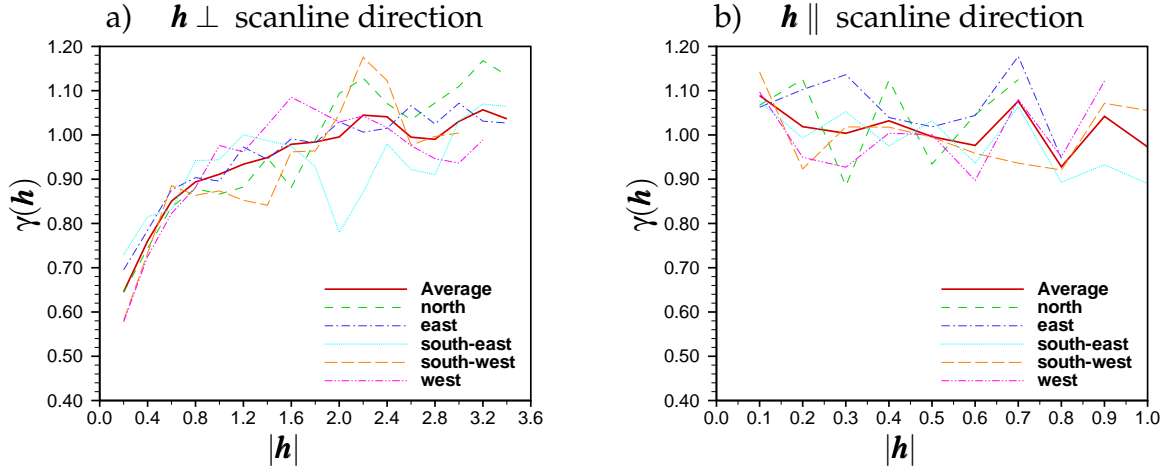


Figure 4.8: Standardized experimental variograms of the vertical-scanline indicator fields, the scanline distance $d = 0.20\text{m}$ and the segment length $l = 0.10\text{m}$.

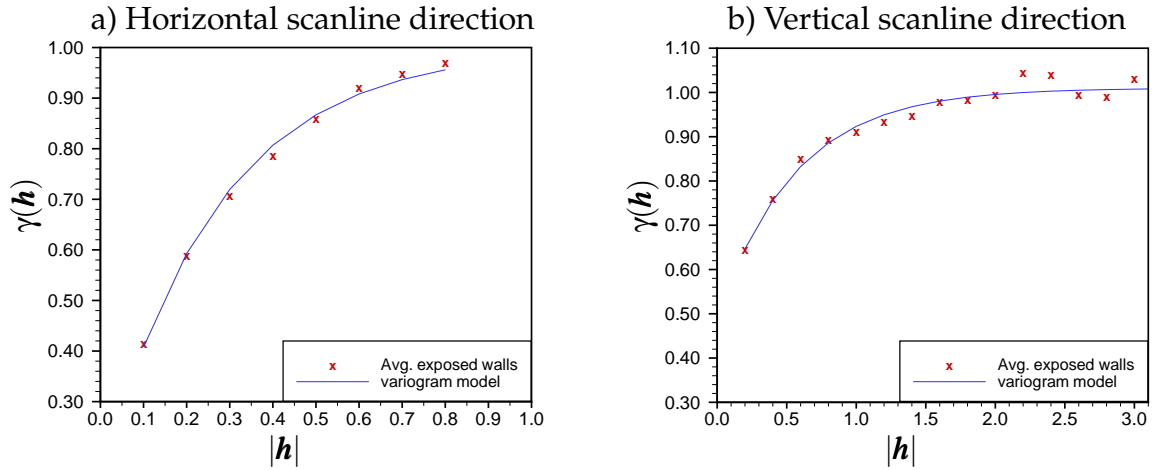


Figure 4.9: Variogram models of the average of the standardized experimental variograms of the horizontal- and the vertical-scanline indicator fields.

connectivity of fracture traces related to adjacent cells. The fracture neighborhood N_f and the matrix neighborhood N_m are determined from eight adjacent cells as

$$N_f(k) = \frac{1}{n_f} \sum_{\alpha=1}^n [I(\mathbf{x}_\alpha^k)] \quad \text{if } I(\mathbf{x}_\alpha) = 1, \quad (4.6)$$

$$N_m(k) = \frac{1}{n_f} \sum_{\alpha=1}^n [I(\mathbf{x}_\alpha^k)] \quad \text{if } I(\mathbf{x}_\alpha) = 0. \quad (4.7)$$

Here, n is the total number of cells, n_f is the total number of fracture cells, \mathbf{x}_α^k is the adjacent cell located at direction k of \mathbf{x}_α . The directions k are represented by the digits 0 to 7 (see Figure 4.10).

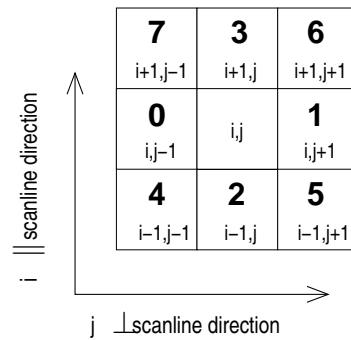


Figure 4.10: Illustration of the neighborhood directions in connection with the digits 0 to 7.

The fracture neighborhood and the matrix neighborhood are evaluated from the horizontal- and the vertical-scanline indicator fields for all the five exposed walls and the results are presented in Figures 4.11 and 4.12 respectively. Due to the values assigned in Equation (4.1), the high values of neighborhoods mean a large number of fracture cells. High N_f are clearly observed in the fracture-trace direction ($k = 2, 3$) as expected because neighboring cells of a fracture cell in the fracture direction have a tendency to be fracture cells. The N_m are significantly lower in the direction of fracture traces. That means neighboring cells of a matrix cell in the fracture direction tend to be a matrix cell rather than a fracture cell. The values of the neighborhoods in the other directions are related to the number of the fracture and the matrix cells found in those directions. If a center cell is a fracture cell and a neighboring cell in a non-fracture-trace direction ($k \neq 2, 3$) is a fracture cell, this could indicate the existence of a fracture trace in that direction. Hence the spatial connectivity of fracture traces is related to the values of the neighborhoods.

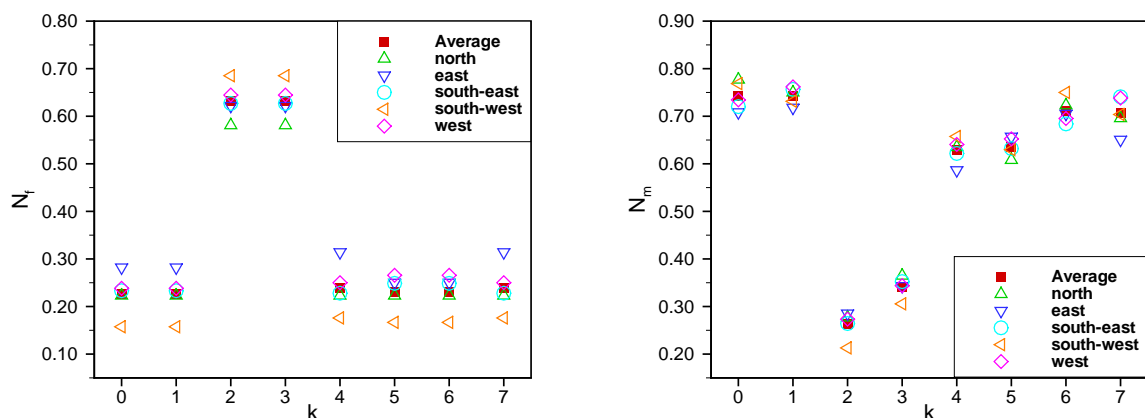


Figure 4.11: Neighborhoods of the horizontal-scanline indicator fields, the scanline distance $d = 0.10\text{m}$ and the segment length $l = 0.10\text{m}$.

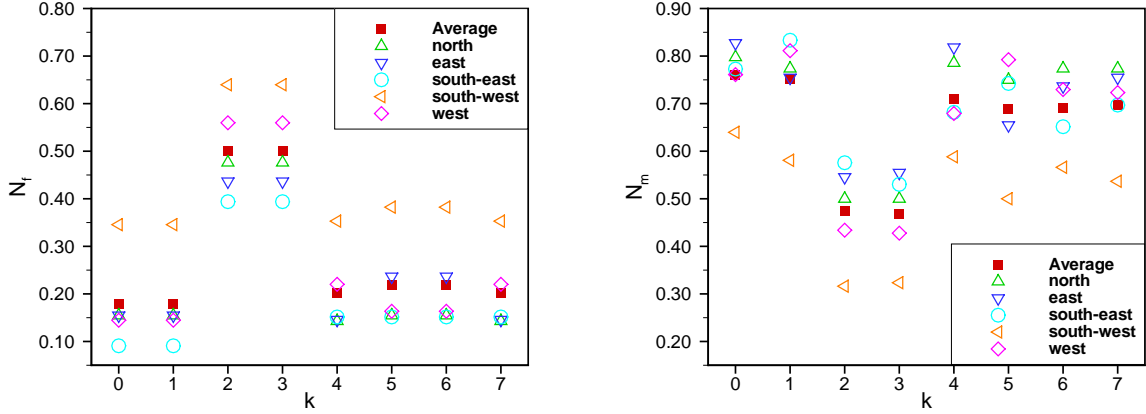


Figure 4.12: Neighborhoods of the vertical-scanline indicator fields, the scanline distance $d = 0.20\text{m}$ and the segment length $l = 0.10\text{m}$.

Due to the weathering process acting on the exposed walls, the greater number of vertical fractures are observed on the top. To represent this fracture structure, a fracture-cell density $H(z)$ defined by the number of fracture cells relative to the total number of cells n_z along each scanline is set up, where z is a z-coordinate of a scanline:

$$H(z) = \frac{1}{n_z} \sum_{\alpha=1}^{n_z} [I(x_\alpha)] . \tag{4.8}$$

The fracture-cell density is only evaluated from the horizontal-scanline indicator field relating to the vertical fracture traces. In Figure 4.13, the results from five exposed walls clearly show an increase of the number of fracture cells with increased vertical distance z , which is in agreement with the observation from the field block.

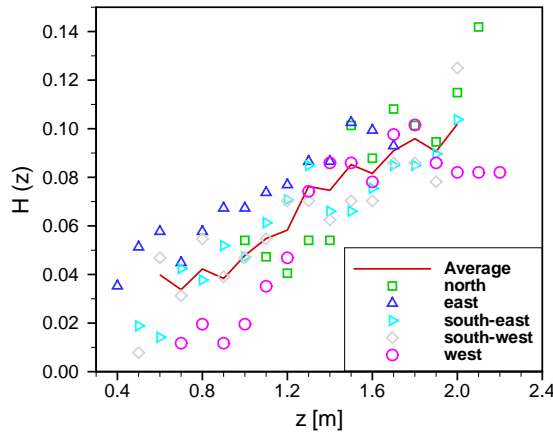


Figure 4.13: Fracture-cell density from the horizontal-scanline indicator fields, the scanline distance $d = 0.10\text{m}$ and the segment length $l = 0.10\text{m}$.

The variance expressed in Equation (4.4) is included as one of the spatial parameters in the GFG in order to indirectly control the number of fracture cells and matrix cells. The average variances evaluated from the horizontal- and vertical-scanline indicator fields are 0.167 and 0.181 respectively.

Evaluating the indicator fields of the Pliezhausen block reveals that all three spatial parameters, the standardized experimental variogram, the neighborhoods and the fracture-cell density, show similar behavior on all exposed walls for both horizontal and vertical scanline directions. Therefore, these parameters together with the variance are further used to describe the spatial characteristics of the Pliezhausen fracture network in the geostatistical fracture generation (GFG).

4.4 Geostatistical Fracture Generation

Geostatistical fracture generation (GFG) developed in this work aims to create a representative fracture network by accounting for both the spatial characteristics of a fracture network and the statistical distribution of fracture geometries. The success of simulated annealing (SA) as a global optimization method in integrating multiple characteristics of discrete fractures (Baafi and Schofield [1997] and Tran et al. [2006]), and its flexibility in incorporating additional information (if needed), make the SA attractive as a methodology for fracture-network generation. In this section, after a review of simulated annealing (SA), the application of the SA to generate two-dimensional indicator fields is presented. Then, the generation of a three-dimensional fracture network by GFG using SA is introduced.

4.4.1 Global optimization technique: simulated annealing

Global optimization has been recognized as an effective tool for handling complex problems in combinatorial optimization. An advantage of the global optimization compared with a local optimization is that the globally best solution can be reached due to its ability to avoid getting trap in local minima. Simulated annealing (SA) is an efficient global optimization technique which can locate a good approximation to the global optimum of a given objective function in a large search space (Aarts and Korst [1989]). The concept of the SA was first introduced by Metropolis et al. [1953] to find the equilibrium configuration of interacting molecules at a given temperature. Later, Kirkpatrick et al. [1983] applied this concept to a general combinatorial optimization problem. The use of the SA in simulation-optimization of methane extraction was presented by Kobayashi [2004]. In spatial-structure-optimization, Deutsch and Cockerham [1994] used the SA for creating stochastic fields of the desired spatial properties (a semivariogram). The successful application of SA in opti-

mizing spatial problems concerning fractured systems has been reported by several authors (Mauldon et al. [1993] Day-Lewis et al. [2000] and Tran [2007]).

In metallurgy, annealing is the technique involving heating, maintaining a suitable temperature, and slowly cooling. If the temperature is decreased slowly enough, the material recrystallizes at (or very close to) its minimum energy state. By analogy, the generalization of the annealing procedure referred to the combinatorial optimization SA is straightforward. The energy for the system and the minimum ground state are analogous to the objective function and the global minimum of the optimization problem respectively. The SA starts at an initial state, and the system is modified randomly to a new state. The new state is accepted if the change decreases the objective function or, if the change increases the objective function, it is accepted with the probability

$$p = \begin{cases} 1 & \text{if } O(C_2) \leq O(C_1) , \\ e^{\left(-\frac{O(C_2)-O(C_1)}{T}\right)} & \text{if } O(C_2) > O(C_1) . \end{cases} \quad (4.9)$$

Here, the constant parameter T called temperature is used for controlling the acceptance of the new state, and $O(C_1)$ and $O(C_2)$ are the objective functions of the current state and the new state respectively. At each temperature, the perturbation is repeated for a large number of iterations M before decreasing the temperature. The temperature T is reduced linearly to a new temperature T_{new} with the cooling factor α , $T_{new} = \alpha T$. When the temperature T becomes lower, the probability of changes which cause higher objective functions being accepted becomes smaller (see Figure 4.14). This allows the problem to converge.

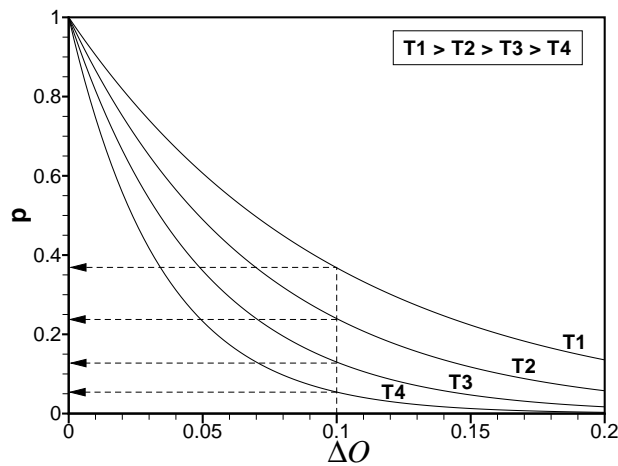


Figure 4.14: Probability of accepting changes (p) related to the objective function ($\Delta O = O(C_2) - O(C_1)$) at different temperature steps (T_1, T_2, T_3 and T_4).

The major difficulty in applying SA is that there is no obvious analogy for defining the initial temperature T_0 , the number of iterations M , and the cooling factor α at each temperature step. In accordance with Bárdossy [1998], the value of the initial temperature T_0 is selected so that the initial acceptance of a new stage is approximately 0.80 and the cooling factor α is 0.90 which remains constant for all temperature steps. The number of iterations M is defined as half of the total number of fractures to ensure a high probability of generated fractures involved in the exchange processes. The perturbation of the SA is repeated until it reaches the stopping criteria; these are that the objective function remains unimproved or the minimum temperature is reached.

4.4.2 Indicator-field generation

The generation of indicator fields is conducted to assess the spatial parameters evaluated in Section 4.3. SA is applied to generate an indicator field which contains the same spatial characteristics as the *target indicator field* evaluated from the fracture-trace map of the exposed wall. This means that the *objective function* of SA is to minimize the difference between the spatial parameters from the target indicator field ($\hat{\gamma}_s(\mathbf{h}), \hat{N}_f(j), \hat{N}_m(j), \hat{H}(z)$) and from the generated indicator field at the state k ($\gamma_s^k(\mathbf{h}), N_f^k(j), N_m^k(j)$ and $H^k(z)$). The objective function of a state k is defined as

$$\begin{aligned}
 O(k) = & w_1 \sum_{j=1}^{n_{\gamma_s}} \frac{|\hat{\gamma}_s(\mathbf{h}_j) - \gamma_s^k(\mathbf{h}_j)|}{\hat{\gamma}_s(\mathbf{h}_j)} + w_2 \sum_{j=0}^7 \frac{|\hat{N}_f(j) - N_f^k(j)|}{\hat{N}_f(j)} \\
 & + w_3 \sum_{j=0}^7 \frac{|\hat{N}_m(j) - N_m^k(j)|}{\hat{N}_m(j)} + w_4 \sum_{j=1}^{n_H} \frac{|\hat{H}(z_j) - H^k(z_j)|}{\hat{H}(z_j)}, \quad (4.10)
 \end{aligned}$$

where w_i is a weighting function, $\sum w_i = 1$. The weighting function is introduced to equalize or to emphasize influences of the spatial parameters on the objective function. The total number of investigated distances of the standardized variogram and the fracture-cell density are n_{γ} and n_H respectively. In the objective function of the indicator-field generation, the parameter variance can be neglected because on the assumption of the same number of fracture and matrix cells, the variance of the generated field is the same as the target field.

The application of SA to generate indicator fields is illustrated in Figure 4.15.

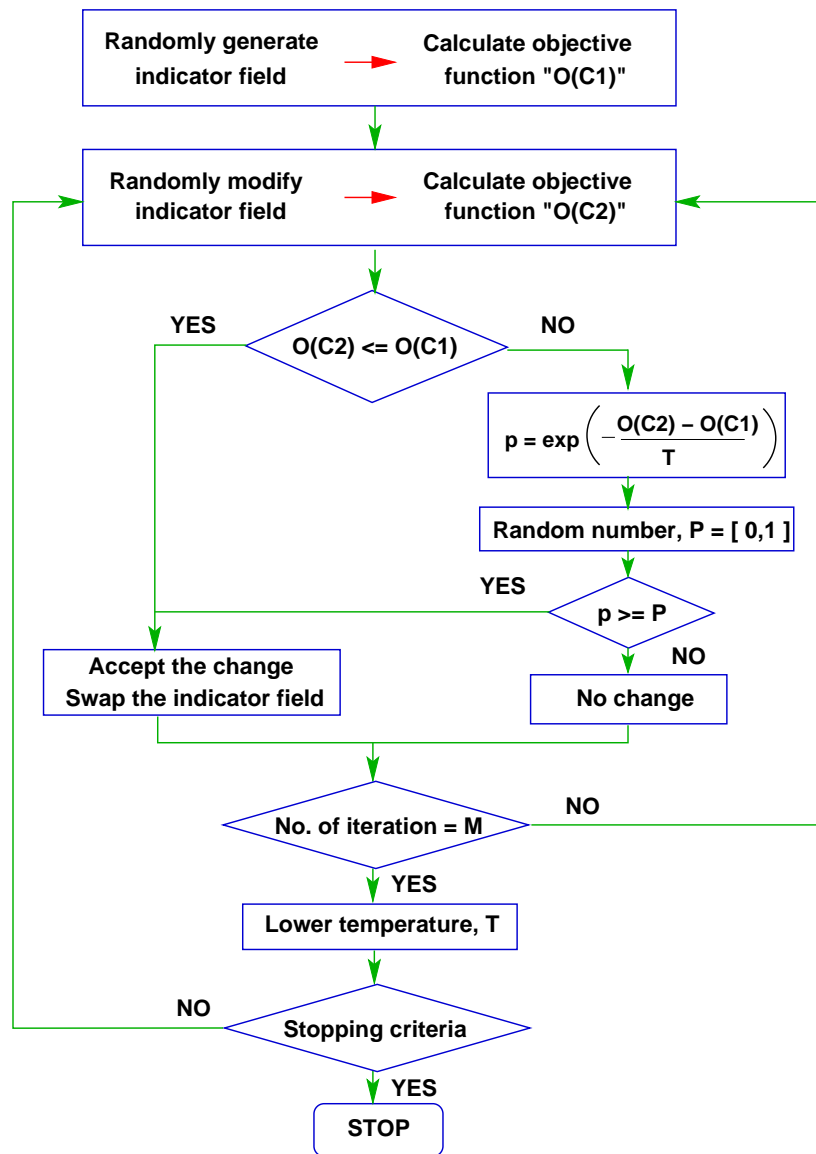


Figure 4.15: Algorithm of indicator-field generation.

First, an indicator field which has the same number of fracture and matrix cells as the target indicator field is arbitrarily generated and is then modified to a new state by exchanging the indicator variable $I(\mathbf{x})$ of two randomly selected cells which have to be a fracture and a matrix cell. The decision to accept the changes is described in Equation (4.9). The indicator field is continually modified until the number of iterations equals the defined iteration steps M and then the temperature T is reduced by a factor of α to the new temperature T_{new} . The procedure is repeated until it reaches the stopping criteria: the objective function remains unimproved after a couple of

temperature steps, or the minimum temperature T_{stop} is reached. The configuration with a minimum objective function is regarded as a result of a realization.

As shown in Figure 4.16, the randomly distributed fracture cells in an initial indicator field (Figure 4.16a) are rearranged successively in the direction of the vertical fracture traces in a final result of a realization (Figure 4.16b) which shows similar characteristics to the target indicator field (Figure 4.16c).

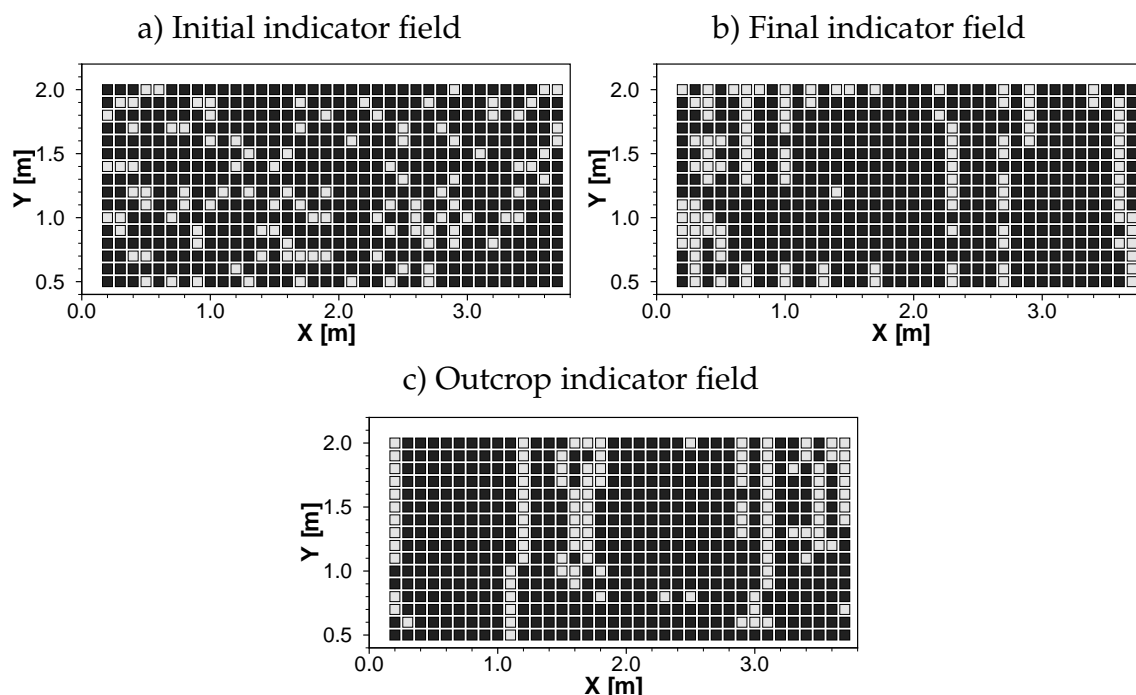


Figure 4.16: The generated and the target indicator fields.

4.4.3 Fracture-network generation

Based on the concept applied in indicator-field generation, geostatistical fracture generation (GFG) is developed. GFG takes into account the statistical geometries and the spatial variability of the indicator fields (the standardized experimental variogram, the neighborhoods, the fracture-cell density and the variance). An initial state of a fracture network is generated based on the statistical geometries; then, fractures are rearranged to achieve the spatial characteristics resembling the target field.

GFG is implemented in the existing three-dimensional fracture generator FRAC3D developed by Silberhorn-Hemminger [2002]. FRAC3D originally offers two different approaches: deterministic fracture generation (DFG) and statistical fracture generation (SFG). In DFG, each fracture in the system is explicitly defined by giving four

corner points. SFG extends the concept described by Long and Billaux [1987] and Wollrath [1990] to create a three-dimensional fracture network from the statistical distribution of fracture geometries (the orientation, the size and the density). Each fracture is assumed to be a rectangular plane. SFG starts by randomly generating a fracture midpoint and assigning a normal vector to a fracture following the distribution of the fracture orientation. Then four corner points are defined according to the fracture size and the normal vector. A new fracture is generated and added to a system until the required fracture density is achieved. Optionally, a reallocation of fractures related to the fracture-space distribution can be carried out. Whereas SFG mainly focuses on the fracture geometries, GFG combines the statistical fracture geometries with the spatial characteristics of the fracture network. The algorithm of FRAC3D is presented in Figure 4.17. In addition to the generation routine, FRAC3D offers the possibility to extract several 2D subplanes (or cross-sections) and a 3D subvolume from the generated domain. Interfaces for the mesh-discretization program ART (Almost Regular Triangulation), developed by Fuchs [1999] and for the flow and transport simulation program MUFTE-UG (MULTiphase Flow, Transport and Energy - Unstructured Grids) are also included in the FRAC3D.

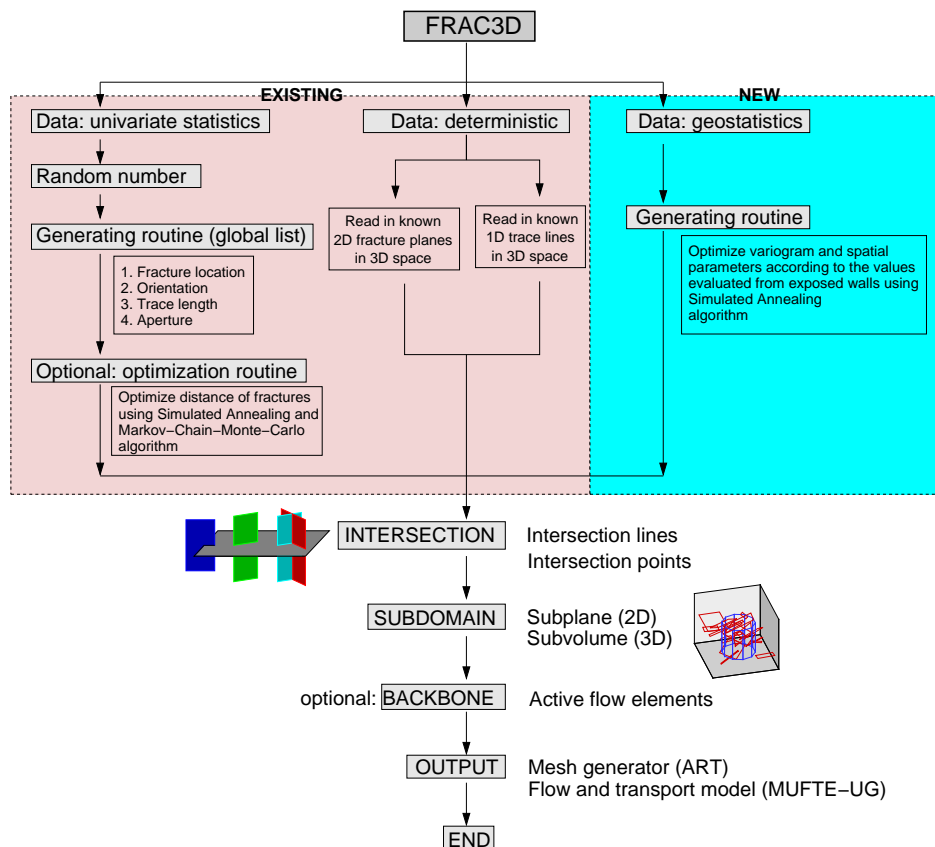


Figure 4.17: Algorithm of the fracture generator FRAC3D (modified after Silberhorn-Hemminger [2002]).

The schematic of GFG using SA is presented in Figure 4.18. An initial state of a fracture network is generated by SFG; therefore, the generated fracture network obeys the statistical geometries. The spatial parameters of a generated domain can be evaluated from the investigated cross-sections which are distributed systematically in the domain. The objective function $O(k)$ of the randomly generated system is defined as the sum of the normalized differences between the spatial parameters of the target fracture network ($\hat{\gamma}_s(\mathbf{h})$, $\hat{N}_f(j)$, $\hat{N}_m(j)$, $\hat{H}(z)$ and $\hat{\sigma}^2$) and of the generated fracture network at the state k ($\gamma_s^k(\mathbf{h})$, $N_f^k(j)$, $N_m^k(j)$, $H^k(z)$ and $\sigma^{2,k}$) from all N_e investigated cross-sections:

$$\begin{aligned}
O(k) = & \sum_{i=1}^{N_e} (w_1 \sum_{j=1}^{n_{\gamma_s}} \frac{|\hat{\gamma}_s(\mathbf{h}_j) - \gamma_s^k(\mathbf{h}_j)|}{\hat{\gamma}_s(\mathbf{h}_j)} + w_2 \sum_{j=0}^7 \frac{|\hat{N}_f(j) - N_f^k(j)|}{\hat{N}_f(j)} \\
& + w_3 \sum_{j=0}^7 \frac{|\hat{N}_m(j) - N_m^k(j)|}{\hat{N}_m(j)} + w_4 \sum_{j=1}^{n_H} \frac{|\hat{H}(z_j) - H^k(z_j)|}{\hat{H}(z_j)} \\
& + w_5 \frac{|\hat{\sigma}^2 - \sigma^{2,k}|}{\hat{\sigma}^2}), \tag{4.11}
\end{aligned}$$

where w_i is the weighting function and $\sum w_i = 1$. The influence of each spatial parameter on the objective function can be controlled by introducing the weighting function. After the objective function of a current state from Equation (4.11) has been evaluated, the generated fracture network is modified to a new configuration and a new objective function is calculated. The results of the two objective functions are compared and the new fracture network is accepted with the acceptance criteria mentioned in Equation (4.9). The fracture network is modified at each iteration step by adding or removing one fracture, or randomly selecting one fracture and changing its geometries (location, orientation or shape). The new location is calculated by shifting a fracture with a randomly generated shifting vector. The new normal vector of a fracture obtained from the fracture-orientation distribution defines the new fracture orientation. All fractures are convex polygons consisting of four to seven edges. The fracture shape is modified by adding/removing the edges (the number of edges is constrained) or moving a corner point. Modifying the fracture network is performed under the condition that the fracture density should not change by more than 15%. The perturbation is carried out for M iterations and then the temperature T is reduced related to the cooling factor α . Finally, SA stops when the objective function remains unimproved after a couple of temperature steps, or the minimum temperature T_{stop} is reached. The configuration with a minimum objective function is regarded as a solution of a realization which has spatial characteristics closest to the target fracture network. Figure 4.19a and 4.19b show a cross-section from one realization at the initial state and the final best solution respectively. The generated fractured network in this case contains two clusters of vertical fractures.

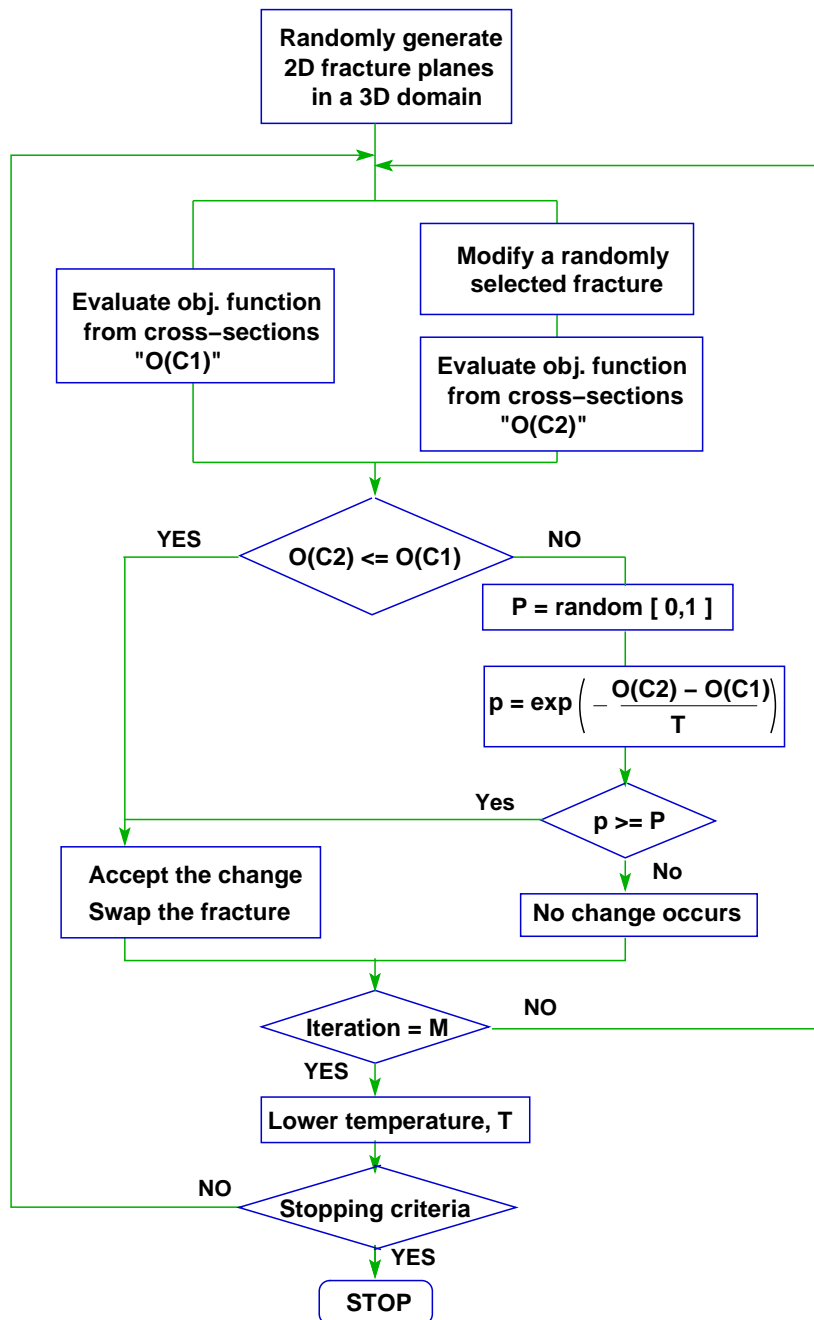


Figure 4.18: Algorithm of fracture-network generation.

Additionally, GFG can generate the fracture network without using the initial state obtained from SFG. The generation approach considers the fracture orientation, the fracture density and a maximum size of a fracture polygon. The fracture orientation and the fracture density are determined by the statistical distribution of the field. A range of maximum fracture sizes can be approximated from fracture traces observed on exposed walls. The objective functions of different maximum fracture sizes are

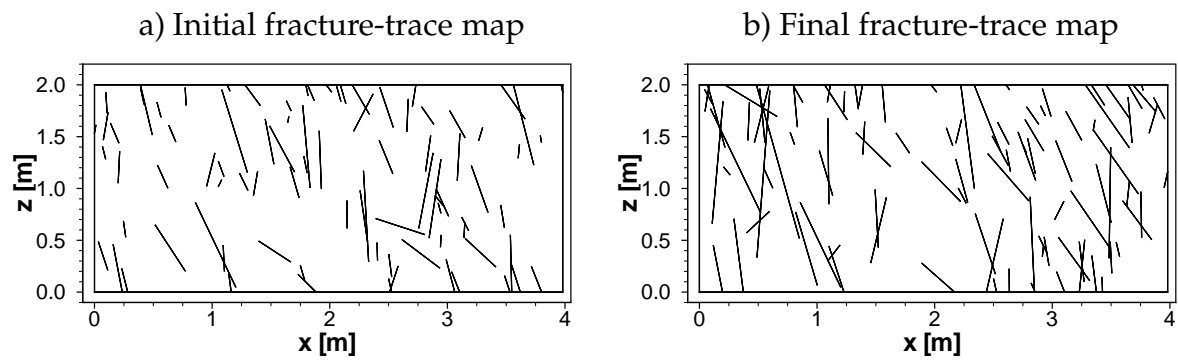


Figure 4.19: Fracture trace on a cross-section from one realization of a fractured system.

compared. Then the maximum size which provides the minimum objective function is selected. This additional option of GFG could be useful if there is severe bias or a strong uncertainty of statistical distribution of the fracture traces.

5 Mathematical and Numerical Model

A discrete fracture-matrix model is selected to represent a natural fracture-matrix system on an analogue scale. The relevant processes of natural systems considered in a conceptual model have to be described by mathematical formulations. However, the complexity of the problem leads to a sophisticated mathematical model that is not possible to be solved analytically. A numerical method is required in this study for solving the sets of equations by discretizing the mathematical formulations in space and in time. In this chapter, the governing equations of the flow and transport processes for a fracture-matrix system are formulated and discretized using a vertex-centered finite volume method or a Box method. Subsequently, a streamline-tracing approach and a flux recovery for a fracture-matrix system are presented.

5.1 Formulation of Flow and Transport Equations

5.1.1 Flow process

Darcy's law

Henry Darcy (1856) conducted a one-dimensional experiment of fully saturated water flow in a vertical homogeneous sand column. He found the relationship between the volumetric flux Q , the cross-sectional area A , the hydraulic gradient $\frac{\Delta h}{L}$ and the hydraulic conductivity k to be

$$Q = -k A \frac{\Delta h}{L} . \quad (5.1)$$

The hydraulic gradient is the difference of the piezometric head h between the two measurement points at a distance L apart. From Equation (5.1), the Darcy velocity v in a one-dimensional column can be expressed by

$$v = -k \frac{\Delta h}{L} . \quad (5.2)$$

Extending Equation (5.2) to describe three-dimensional porous media yields

$$\mathbf{v} = -\mathbf{k} \nabla h, \quad (5.3)$$

in which \mathbf{k} denotes the hydraulic conductivity tensor. Darcy's law is valid in a range of laminar flow where a Reynolds number Re is smaller than 1 (Bear [1972]). The dimensionless Reynolds number determines the ratio of inertial to viscous forces

$$Re = \frac{v d}{\nu}, \quad (5.4)$$

where d is the length dimension, and ν the kinematic viscosity. The length dimension of porous media is generally approximated by the mean grain size (d_{50}).

The hydraulic conductivity \mathbf{k} depends on the properties of both porous medium and fluid

$$\mathbf{k} = \frac{\mathbf{K} \rho g}{\mu}, \quad (5.5)$$

where \mathbf{K} is the permeability tensor, g the gravitational constant, μ the dynamic viscosity of fluid, and ρ the fluid density. Inserting Equation (5.5) into (5.3) and expressing the piezometric head h in terms of the pressure p and the elevation z result in the full formula of the Darcy velocity as

$$\mathbf{v} = -\frac{\mathbf{K} \rho g}{\mu} \nabla \left(\frac{p}{\rho g} + z \right). \quad (5.6)$$

When the gravitational effect is neglected, Equation (5.6) is reduced to

$$\mathbf{v} = -\frac{\mathbf{K}}{\mu} \nabla p. \quad (5.7)$$

Parallel plate concept

A natural fracture is a discontinuity in a rock which is bounded by two rough-wall surfaces. Lomize [1951] introduced a concept which simplified the rough-wall surfaces to two smooth parallel plates, known as the parallel-plate concept (see Figure 5.1).

The velocity distribution of an incompressible fluid within two parallel plates can be derived from the Navier-Stroke equation (Bear [1972]):

$$v_x(z) = -\frac{\rho g}{8\mu} \left(\frac{dh}{dx} \right) (b^2 - 4z^2), \quad (5.8)$$

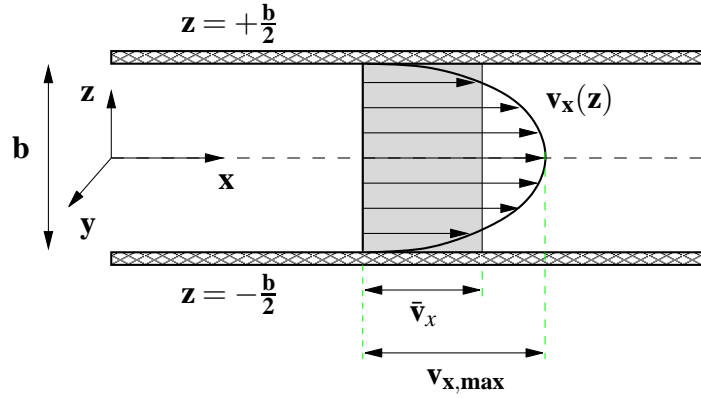


Figure 5.1: Velocity distribution of a laminar flow between two parallel plates.

where b is the distance between two plates. The maximum velocity $v_{x,max}$ at $z = 0$ is

$$v_{x,max} = -\frac{b^2 \rho g}{8\mu} \left(\frac{dh}{dx} \right). \quad (5.9)$$

The mean value of a parabola-shaped profile is equal to two-thirds of the maximum value; hence, the mean velocity \bar{v}_x can be derived from the maximum velocity $v_{x,max}$ in Equation (5.9) as

$$\bar{v}_x = -\frac{b^2 \rho g}{12 \mu} \left(\frac{dh}{dx} \right). \quad (5.10)$$

When Equation (5.10) is compared with Equation (5.6), the permeability of a fracture given by the parallel-plate concept is

$$K = \frac{b^2}{12}. \quad (5.11)$$

The volumetric flux per unit length (in y -axis) Q_u can be determined as the integral of the velocity in Equation (5.8) over the distance between two plates

$$Q_u = \int_{-\frac{b}{2}}^{+\frac{b}{2}} v_x(z) dz, \quad (5.12)$$

which yields

$$Q_u = -\frac{b^3 \rho g}{12 \mu} \left(\frac{dh}{dx} \right). \quad (5.13)$$

If the parallel-plate concept is assumed, the flux Q_u is proportional to the cube of the aperture b , which is known as the *cubic law*. Hence, the predicted flux depends strongly on the approximated value of the fracture aperture b . Witherspoon et al.

[1980] showed that the fracture aperture approximated from hydraulic measurements resulted in an accurate laminar-flow-rate prediction; however, the directly measured aperture showed less success. During recent decades, the application of the parallel-plate concept has been viewed skeptically due to the preferential flow paths arising from varied fracture apertures. Channeling effects have been observed on a scale ranging from laboratory experiments to field measurements (e.g. Lee et al. [2003], Glass et al. [2002], Abelin et al. [1991]). Therefore, a raster-element concept has been developed with the aim of capturing the channeling effects by representing the variation in fracture aperture with a statistical distribution function and a spatial correlation length (Tsang and Tsang [1987], Tsang et al. [1988]). Figure 5.2 illustrates the two different model concepts for a single fracture. The raster-element concept succeeds in simulating a single fracture (Tsang et al. [1988]). However, in a fracture-network model, it is impracticable due to high computational demand.

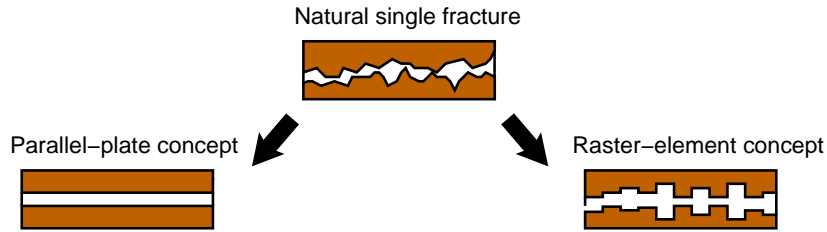


Figure 5.2: A schematic of model concepts for a fracture aperture.

In a fracture-matrix system, the fracture geometries (the orientation, the density and the size) strongly influence the global flow behavior. This could dominate a local effect due to the aperture variation within a single fracture. Therefore, the parallel plate concept, which assigns a constant aperture to each fracture, can be assumed when studying a fracture-matrix system.

Continuity equation

The continuity equation based on mass conservation without source/sink terms can be described as

$$\frac{\partial(\phi\rho)}{\partial t} + \nabla \cdot (\rho\mathbf{v}) = 0, \quad (5.14)$$

which yields

$$\phi \frac{\partial \rho}{\partial t} + \rho \frac{\partial \phi}{\partial t} + \rho \nabla \cdot \mathbf{v} + \mathbf{v} \cdot \nabla \rho = 0, \quad (5.15)$$

where ϕ is the total porosity. When an incompressible single phase in a non-deformable matrix is considered, the continuity equation shown in Equation (5.15)

can be simplified to

$$\nabla \cdot \mathbf{v} = 0. \quad (5.16)$$

The velocity \mathbf{v} is given by Darcy's law in Equation (5.7) as the gravitational effect is neglected. The permeability of fractures is approximated by the parallel plate concept, shown in Equation (5.11).

5.1.2 Transport process

The transport process in this study focuses on conservative tracer transport, which means no interactions such as sorption between the fluid and the matrix and no chemical/biological reactions of the fluid. Therefore, the process is mainly described by three basic mechanisms: *advection*, *diffusion* and *dispersion*.

Advective transport indicates the movement of a tracer with average velocity in a control volume, which can be written in terms of an advective mass flux as

$$\mathbf{J}_a = c \mathbf{v}_s, \quad (5.17)$$

where c is the concentration of a conservative tracer. The seepage velocity or the particle velocity \mathbf{v}_s is defined as

$$\mathbf{v}_s = \frac{1}{\phi_e} \mathbf{v}, \quad (5.18)$$

in which ϕ_e denotes the effective porosity, excluding the dead-end pore.

Dispersion describes the mixing of a tracer due to velocity fluctuation around the average velocity and can be observed on both a microscopic and a macroscopic scale. On the microscopic scale, three main reasons for the velocity differences are (a) friction in the pores, (b) varying pore sizes and (c) varying travel-path lengths (see Figure 5.3). Velocity fluctuation on the macroscopic scale, which leads to macroscopic

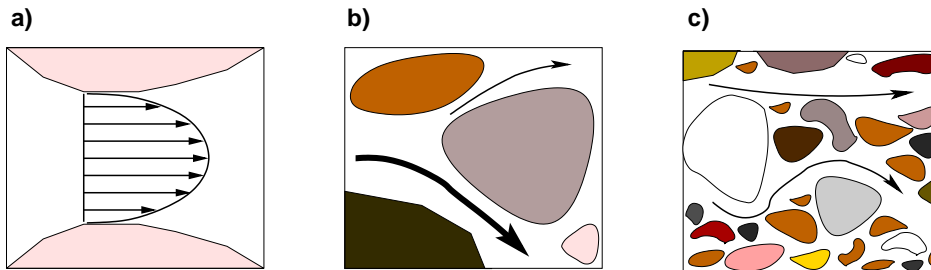


Figure 5.3: Dispersion at the microscopic scale.

dispersion, is due to spatial heterogeneities within matrix porous media on the REV

scale and a contrast in permeability between fractures and the surrounding matrix. Macroscopic dispersion is much higher than dispersion on the microscopic scale. Therefore, dispersion in this study concerns only macroscopic dispersion. The dispersion coefficient D_d depends on the seepage velocity and the dispersion length α . In the one-dimensional case, it is expressed as

$$D_d = \alpha v_s . \quad (5.19)$$

In the two-dimensional case, if the system of coordinate is in alignment with the flow direction, the dispersion leads to a diagonal 2x2 matrix:

$$\mathbf{D}_d = \begin{bmatrix} D_l & 0 \\ 0 & D_t \end{bmatrix} = \begin{bmatrix} \alpha_l v_x & 0 \\ 0 & \alpha_t v_y \end{bmatrix} , \quad (5.20)$$

where α_l and α_t are longitudinal and transversal dispersion lengths respectively. D_l and D_t are longitudinal and transversal dispersion. The dispersion matrix in a general case is expressed as:

$$\mathbf{D}_d = \begin{bmatrix} D_{xx} & D_{xy} \\ D_{yx} & D_{yy} \end{bmatrix} , \quad (5.21)$$

with

$$\begin{aligned} D_{xx} &= \alpha_l \frac{v_x^2}{\|\mathbf{v}_s\|} + \alpha_t \frac{v_y^2}{\|\mathbf{v}_s\|} \\ D_{xy} &= D_{yx} = (\alpha_l - \alpha_t) \frac{v_x v_y}{\|\mathbf{v}_s\|} \\ D_{yy} &= \alpha_l \frac{v_y^2}{\|\mathbf{v}_s\|} + \alpha_t \frac{v_x^2}{\|\mathbf{v}_s\|} . \end{aligned} \quad (5.22)$$

The longitudinal dispersion length is a scale-dependent parameter and is in most cases greater than the transversal dispersion (Maréchal et al. [1992]).

Diffusion is the movement of molecules under the influence of their kinetic activity in the direction of their concentration gradients. Diffusion is independent of the movement of the fluid. Bear [1972] suggested that diffusion in porous media D_m could be approximated from the well known diffusion coefficients of electrolytes in aqueous solutions D_e as

$$D_m = w D_e , \quad (5.23)$$

where the constant coefficient w is smaller than 1 and should be determined empirically.

A hydrodynamic dispersion tensor \mathbf{D} is described as the sum of the dispersion \mathbf{D}_d , which is proportional to the seepage velocity, and the diffusion D_m . The dispersion

part normally dominates hydrodynamic dispersion; however, if the fluid velocity is extremely low, diffusion becomes more important. In a two-dimensional case where the transport direction follows the coordinate axis, the hydrodynamic dispersion is determined as

$$\mathbf{D} = \begin{bmatrix} \alpha_l \|\mathbf{v}_s\| + D_m & 0 \\ 0 & \alpha_t \|\mathbf{v}_s\| + D_m \end{bmatrix}. \quad (5.24)$$

Dispersive and diffusive transport can be described by Fick's law in terms of a mass flux as

$$\mathbf{J}_d = \mathbf{D} \nabla c. \quad (5.25)$$

The governing equation for advective-dispersive transport (ADT) can be derived from the conservation of the mass flux across the boundaries of a control volume as

$$\frac{\partial c}{\partial t} + \nabla \cdot (\mathbf{v}_s c - \mathbf{D} \nabla c) = 0. \quad (5.26)$$

5.2 Discretization of Flow and Transport Equations

Discretization techniques enable the complex differential equations derived in the previous sections to be solved numerically. Three main aspects have to be considered when selecting the discretization scheme for the flow and transport simulations in a fracture-matrix system. First, the complex geometries of a fracture network lead to an unstructured-grid problem. Second, the accuracy of the transport simulation results relies on the precision of the velocity field obtained from the flow calculations. Last, the concentration-front propagation has to be correctly predicted. Therefore, a vertex-centered finite volume method, also called Box method, is preferred as it can be applied to unstructured grids and is locally mass conservative (Reichenberger et al. [2006]). In addition, the numerical techniques applied in the Box method should avoid oscillation and show less numerical diffusion. Several discretization methods for simulating flow and transport processes in fractured porous media are analyzed by Neunhäuserer [2003].

In a discrete fracture model, fractures may either be discretized with the same dimension as the surrounding matrix elements, so called an equi-dimensional approach, or with one dimension less than the matrix, so called a lower-dimensional approach. Fractures in a lower-dimensional approach are described by a one-dimensional line in a two-dimensional domain or a two-dimensional surface in a three-dimensional domain, and they have a virtual width associated with it equal to their aperture. The comparison study of the two discretization approach presented in Neunhäuserer [2003] showed that the flow and transport results revealed

a number of differences locally, however, a non-significant difference globally. In this study, a global solution is the main interest and a fracture aperture is very small compared with the size of a domain, therefore, a lower-dimensional approach is applied for discretizing a fracture-matrix system.

The spatial discretization of the Box method is based on a primary finite element (FE) mesh and a secondary finite volume (FV) mesh. First, a domain is discretized into a FE mesh, where flow variables and matrix properties are assumed to be constant on each element. Next, in a two-dimensional domain, by connecting element barycenters with edge midpoints, a FV mesh is constructed (see Figure 5.4).

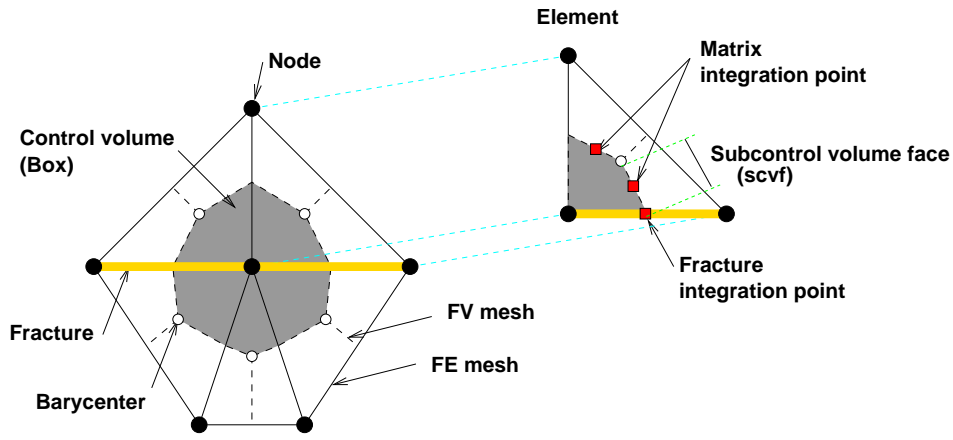


Figure 5.4: Finite Element (FE) and Finite Volume (FV) mesh.

The discrete values of the primary variables or the unknowns u are calculated at nodes or vertices. The primary variables within each element are approximated using nodal values \hat{u}_j and Ansatz functions N_j

$$\tilde{u} = \sum_{j=1}^n N_j \hat{u}_j, \quad (5.27)$$

where n is number of nodes belonging to the element. The Ansatz function N_j is determined as

$$N_j = \begin{cases} 1 & \text{if } i = j, \\ 0 & \text{if } i \neq j, \end{cases} \quad (5.28)$$

which is illustrated in Figure 5.5a for a triangular element.

The approximation of u with \tilde{u} leads to a residuum ε :

$$f(\tilde{u}) = \varepsilon. \quad (5.29)$$

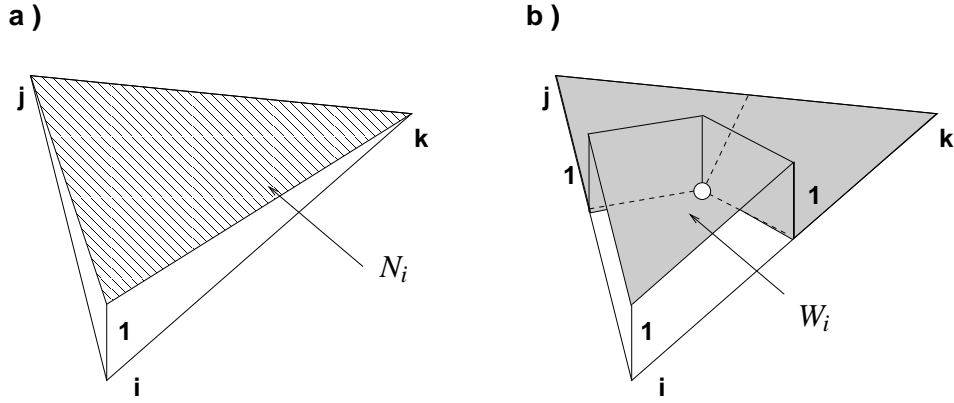


Figure 5.5: Illustration of a) Ansatz function and b) weighting function of a Box method.

After application of the appropriate weighting function W_i , the integral of ε over the whole domain Ω becomes zero; that is known as the principle of weighted residual:

$$\int_{\Omega} W_i \varepsilon d\Omega = \int_{\Omega} W_i f(\tilde{u}) d\Omega = 0. \quad (5.30)$$

For the Box method, W_i is defined as piece-wise constant weighting functions as

$$W_i = \begin{cases} 1 & \text{if } x \in \Omega_i, \\ 0 & \text{if } x \notin \Omega_i, \end{cases} \quad (5.31)$$

where Ω_i is the control volume of node i (see Figure 5.5b).

The continuity equation of the flow process in Equation (5.16) is discretized with the Box method for a control volume Ω_i :

$$\int_{\Omega_i} W_i \nabla \cdot \tilde{\mathbf{v}} d\Omega = 0. \quad (5.32)$$

Applying the Green-Gauss integral rule to Equation (5.32) leads to

$$\int_{\Gamma_i} W_i \tilde{\mathbf{v}} \cdot \mathbf{n} d\Gamma - \int_{\Omega_i} \nabla W_i \cdot \tilde{\mathbf{v}} d\Omega = 0, \quad (5.33)$$

where Γ_i is the boundary of a control volume Ω_i and \mathbf{n} is its outward unit normal vector. The definition of W_i in Equation (5.31) results in ∇W_i becoming zero. Equation (5.33) is simplified to

$$\int_{\Gamma_i} \tilde{\mathbf{v}} \cdot \mathbf{n} d\Gamma = 0. \quad (5.34)$$

Inserting Equation (5.7) into (5.34) yields

$$\int_{\Gamma_i} \frac{\mathbf{K}}{\mu} \nabla(\tilde{p}) \cdot \mathbf{n} d\Gamma = 0. \quad (5.35)$$

Substituting the unknown \tilde{p} with Equation (5.27) leads to

$$\int_{\Gamma_i} \frac{\mathbf{K}}{\mu} \nabla \left(\sum_{j=1}^n N_j \hat{p}_j \right) \cdot \mathbf{n} d\Gamma = 0, \quad (5.36)$$

which can be rewritten as

$$\int_{\Gamma_i} \frac{\mathbf{K}}{\mu} \sum_{j=1}^n (\hat{p}_j \nabla N_j) \cdot \mathbf{n} d\Gamma = 0. \quad (5.37)$$

Here, n is the total number of neighboring nodes of the considered node i . The final discretization for the continuity equation of an incompressible fluid in a non-deformable matrix is shown in Equation (5.37). This can be physically interpreted as the sum of fluxes across the boundary control volume Γ_i equals zero. Each flux is evaluated at the integration point and assumed to be constant over subcontrol volume face (scvf) and the length of the normal vector \mathbf{n} is equal to one.

Following the same principle of weighted residual, the continuity of the transport process in Equation (5.26) is discretized as

$$\int_{\Omega_i} W_i \frac{\partial \tilde{c}}{\partial t} d\Omega + \int_{\Omega_i} W_i \nabla \cdot (\mathbf{v}_s \tilde{c}) d\Omega - \int_{\Omega_i} W_i \nabla \cdot (\mathbf{D} \nabla \tilde{c}) d\Omega = 0. \quad (5.38)$$

Applying the Green-Gauss integral rule to Equation (5.38) yields

$$\underbrace{\int_{\Omega_i} W_i \frac{\partial \tilde{c}}{\partial t} d\Omega}_{\text{storage}} + \underbrace{\int_{\Gamma_i} W_i (\mathbf{v}_s \tilde{c}) \cdot \mathbf{n} d\Gamma}_{\text{advective}} - \underbrace{\int_{\Gamma_i} W_i (\mathbf{D} \nabla \tilde{c}) \cdot \mathbf{n} d\Gamma}_{\text{dispersive/diffusive}} = 0. \quad (5.39)$$

For dispersive/diffusive flux, the concentration \tilde{c} is approximated with the Ansatz functions described in Equation (5.28). However, for advective flux, the fully-upwind method is carried out to avoid oscillation behavior. The concentration \tilde{c} of the advective flux on the scvf between nodes i and j is defined by the concentration at the upstream node:

$$\tilde{c}_{up} = \begin{cases} c_i & \text{if } \mathbf{v}(i, j) > 0, \\ c_j & \text{if } \mathbf{v}(i, j) \leq 0. \end{cases} \quad (5.40)$$

Here, the velocity $\mathbf{v}(i, j)$ is positive if the flow direction is from node i to j . The order of consistency is equal to $O(\Delta x)$ for the advective term and $O(\Delta x^2)$ for the dispersive term (Hinkelmann [2005]). Applying an implicit Euler scheme and approximating the unknown \tilde{c} with the Ansatz function in Equation (5.39) yields

$$\begin{aligned} \frac{1}{\Delta t} \int_{\Omega_i} \sum_{j=1}^n (c_j^{(t+\Delta t)} - c_j^t) W_i N_j d\Omega + \int_{\Gamma_i} W_i (\mathbf{v}_s \tilde{c}_{up})^{(t+\Delta t)} \cdot \mathbf{n} d\Gamma \\ - \int_{\Gamma_i} W_i \sum_{j=1}^n \mathbf{D} \hat{c}_j^{(t+\Delta t)} \nabla N_j \cdot \mathbf{n} d\Gamma = 0. \end{aligned} \quad (5.41)$$

There is no limit to time step size in the implicit Euler and the order of consistency is $O(\Delta t)$ (Hinkelmann [2005]). Using the mass-lumping technique proposed by Huber [1999] for the storage term in Equation (5.41) and defining the weighting function for the advective and dispersive/diffusive terms as in Equation (5.31) leads to

$$\frac{V_i}{\Delta t}(c_i^{(t+\Delta t)} - c_i^t) + \int_{\Gamma_i} (\mathbf{v}_s \tilde{c}_{up})^{(t+\Delta t)} \cdot \mathbf{n} d\Gamma - \int_{\Gamma_i} \sum_{j=1}^n \mathbf{D} \hat{c}_j^{(t+\Delta t)} \nabla N_j \cdot \mathbf{n} d\Gamma = 0. \quad (5.42)$$

5.3 Streamline Tracing

Streamlines are lines that determine flow paths, and are always perpendicular to equipotential lines of a piezometric head. Streamline simulation simplifies the two- and three-dimensional transport problems to one-dimensional problems solving numerically along streamlines. The advantages of streamline tracing are lower computational demand and less numerical diffusion compared with the advective-dispersive transport model (Kinzelbach [1992], Crane and Blunt [1999]). Similar to the governing equation in the transport process, streamline tracing is based on the velocity field determined from the flow simulation.

Pollock's method (Pollock [1988]) is widely used for streamline tracing in a Cartesian coordinate system with a structured grid. It assumes a piece-wise linear approximation of velocity in each coordinate direction within a grid block. When the Pollock's method is carried out in a unit square, the velocity field can be defined by the linear interpolation of the edge fluxes as

$$\mathbf{v}(\mathbf{x}) = \begin{bmatrix} f_{x0}(1-x) + f_{x1}x \\ f_{y0}(1-y) + f_{y1}y \end{bmatrix}, \quad 0 \leq x \leq 1 \quad \text{and} \quad 0 \leq y \leq 1, \quad (5.43)$$

where f_k are fluxes over the unit square faces (see Figure 5.6).

The travel time t along the streamline from location i to j is computed by inserting Equation (5.43) in

$$t = \int_i^j \frac{\phi_e}{v} dx. \quad (5.44)$$

If $f_{x0} \neq f_{x1}$ and $f_{y0} \neq f_{y1}$, solving Equation (5.44) yields two separate expressions:

$$t_x(x_i, x_j) = \frac{\phi_e}{f_{x1} - f_{x0}} \ln \left(\frac{f_{x0} + (f_{x1} - f_{x0})x_j}{f_{x0} + (f_{x1} - f_{x0})x_i} \right), \quad (5.45)$$

$$t_y(y_i, y_j) = \frac{\phi_e}{f_{y1} - f_{y0}} \ln \left(\frac{f_{y0} + (f_{y1} - f_{y0})y_j}{f_{y0} + (f_{y1} - f_{y0})y_i} \right). \quad (5.46)$$

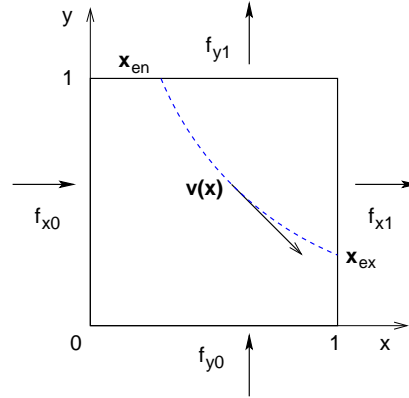


Figure 5.6: Pollock tracing for a unit square.

The time that a particle travels from entry point \mathbf{x}_{en} to exit point \mathbf{x}_{ex} of the grid cell is called the time-of-flight (TOF), which can be determined by calculating the time that the streamline requires to cross the grid boundaries. Inserting $x_j = 0$ and $x_j = 1$ in Equation (5.45) and $y_j = 0$ and $y_j = 1$ in Equation (5.46), and replacing x_i and y_i with \mathbf{x}_{en} yield the times that the streamline requires to cross the left, the right, the bottom and the top boundaries respectively. The TOF is derived from the minimum of the calculated times, which exclude any negative time and the time calculated from the side where the particle enters. By rearranging Equations (5.45) and (5.46) and inserting the TOF in t_{ex} , the exit point \mathbf{x}_{ex} is then given as

$$x_{ex} = \frac{1}{f_{x1} - f_{x0}} \left\{ v_{en,x} \exp \left(\frac{t_{ex}}{\phi_e} (f_{x1} - f_{x0}) \right) - f_{x0} \right\}, \quad (5.47)$$

$$y_{ex} = \frac{1}{f_{y1} - f_{y0}} \left\{ v_{en,y} \exp \left(\frac{t_{ex}}{\phi_e} (f_{y1} - f_{y0}) \right) - f_{y0} \right\}, \quad (5.48)$$

where \mathbf{v}_{en} is a velocity at the entry point \mathbf{x}_{en} calculated from Equation (5.43).

Considering a fracture-matrix system results in a complex domain which can only be discretized precisely with unstructured grids; hence, the streamline method which performs well on unstructured grids is required. The extension of Pollock's method on unstructured grids has proved successful in several studies (e.g. Cordes and Kinzelbach [1992], Prévost et al. [2002], Haegland et al. [2007]). The coordinate together with the velocity in a physical space \mathcal{P} are transformed to a reference space \mathcal{R} (see Figure 5.7).

After the bilinear iso-parametric transformation is applied, the unstructured grid in \mathcal{P} is related to a unit cell in \mathcal{R} as

$$\mathbf{x}(\mathbf{x}') = \sum_{i=1}^4 \mathbf{x}_i N_i(\mathbf{x}'), \quad (5.49)$$

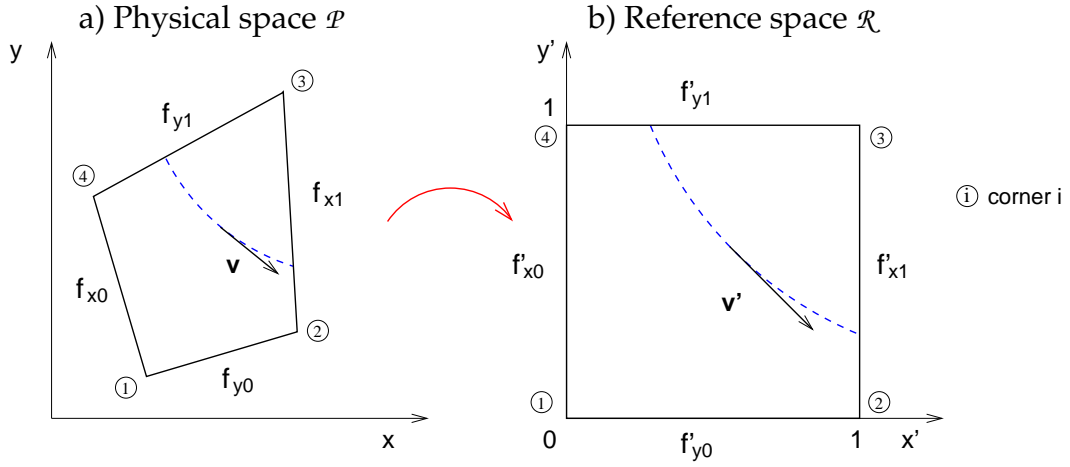


Figure 5.7: Transformation of an unstructured grid and edge fluxes from a physical space \mathcal{P} to a reference space \mathcal{R} .

Here, i are the corner points and the bilinear shape functions N_i are

$$\begin{aligned}
 N_1(\mathbf{x}') &= (1-x')(1-y'), \\
 N_2(\mathbf{x}') &= x'(1-y'), \\
 N_3(\mathbf{x}') &= x'y', \\
 N_4(\mathbf{x}') &= (1-x')y'.
 \end{aligned} \tag{5.50}$$

The velocity in \mathcal{R} at location \mathbf{x}'_i is related to the velocity in \mathcal{P} as (Haegland et al. [2007])

$$\mathbf{v} = \mathbf{J}\mathbf{v}', \tag{5.51}$$

where \mathbf{J} is the Jacobian transformation matrix

$$\mathbf{J} = \begin{bmatrix} \frac{dx}{dx'} & \frac{dx}{dy'} \\ \frac{dy}{dx'} & \frac{dy}{dy'} \end{bmatrix}. \tag{5.52}$$

The transformed velocity is then given by rearranging Equation (5.51)

$$\mathbf{v}' = \mathbf{J}^{-1}\mathbf{v}. \tag{5.53}$$

According to Haegland et al. [2007], the velocity field in \mathcal{R} is related to the linear flux interpolation as

$$\mathbf{v}'_i = \frac{1}{\det \mathbf{J}} \begin{bmatrix} f_{x0}(1-x'_i) + f_{x1}x'_i \\ f_{y0}(1-y'_i) + f_{y1}y'_i \end{bmatrix}. \tag{5.54}$$

By using a pseudo time-of-flight τ in \mathcal{R} as shown in Jimenez et al. [2005], the velocity in Equation (5.54) is rewritten as

$$d\tau = \frac{dt}{\det \mathbf{J}} = \left[\begin{array}{c} \frac{dx'}{f_{x0}(1-x'_i) + f_{x1}x'_i} \\ \frac{dy'}{f_{y0}(1-y'_i) + f_{y1}y'_i} \end{array} \right], \quad (5.55)$$

where t is real time in \mathcal{P} . The actual time-of-flight t_{ex} is then evaluated by integrating Equation (5.55) from \mathbf{x}'_{en} to \mathbf{x}'_{ex} (Haegland et al. [2007]):

$$t_{ex} = \int_0^{t(\tau_{ex})} dt = \int_0^{\tau_{ex}} \det \mathbf{J}(x'(\tau), y'(\tau)) d\tau. \quad (5.56)$$

5.4 Flux Recovery for Streamline Simulation

The precision of streamline tracing strongly depends on the accuracy of the velocity field. Approximating the velocity field from pressure gradients obtained from the flow simulation with the Box method results in discontinuous velocities at element boundaries, where the hydraulic conductivities of neighboring elements are different. Cordes and Kinzelbach [1992] proposed a technique for deriving continuous distribution fluxes of porous media on each subdomain from the Finite Element solutions, which are the hydraulic heads. This technique was extended by Prévost et al. [2002] for the Control-Volume Finite Element scheme on unstructured grids. On the basis of Cordes and Kinzelbach [1992] and Prévost et al. [2002], a flux recovery for a two-dimensional fracture-matrix system has been developed by Haegland et al. [2008]. This approach is applied in this study as a pre-processing of the streamline tracing.

After the flow in a fracture-matrix system using the Box method has been simulated, the pressure head on each node, which results in conservative fluxes on each control volume boundary, is solved. The conservative fluxes are given at the integration points and are constant over subcontrol volume faces (see Figure 5.8a). In streamline tracing, lower-dimensional fractures are extended to equi-dimensional fractures in order to allow velocities in fractures to be in any direction, not only parallel to fractures. Hence, streamlines which enter the fractures can leave at any location on the fracture boundaries. Applying the extended Pollock's method for streamline tracing on subcontrol volumes requires additional continuous fluxes evaluated on matrix and fracture interior points (see Figure 5.8b). These interior fluxes are calculated in the flux recovery approach.

Five possible cases of extended fractures that are likely to occur in a discrete fracture model are considered in this study (see Figure 5.9).

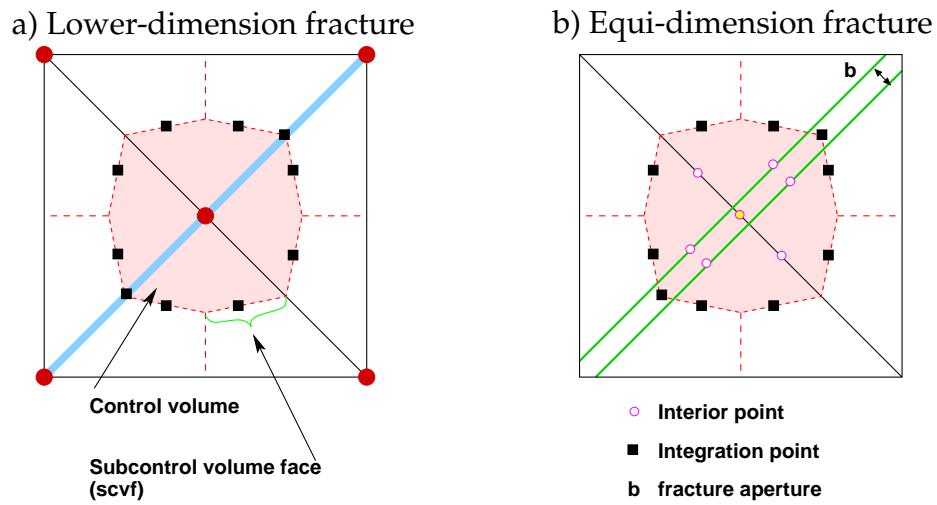


Figure 5.8: Integration points and interior points of a control volume where fluxes and interior fluxes are evaluated.

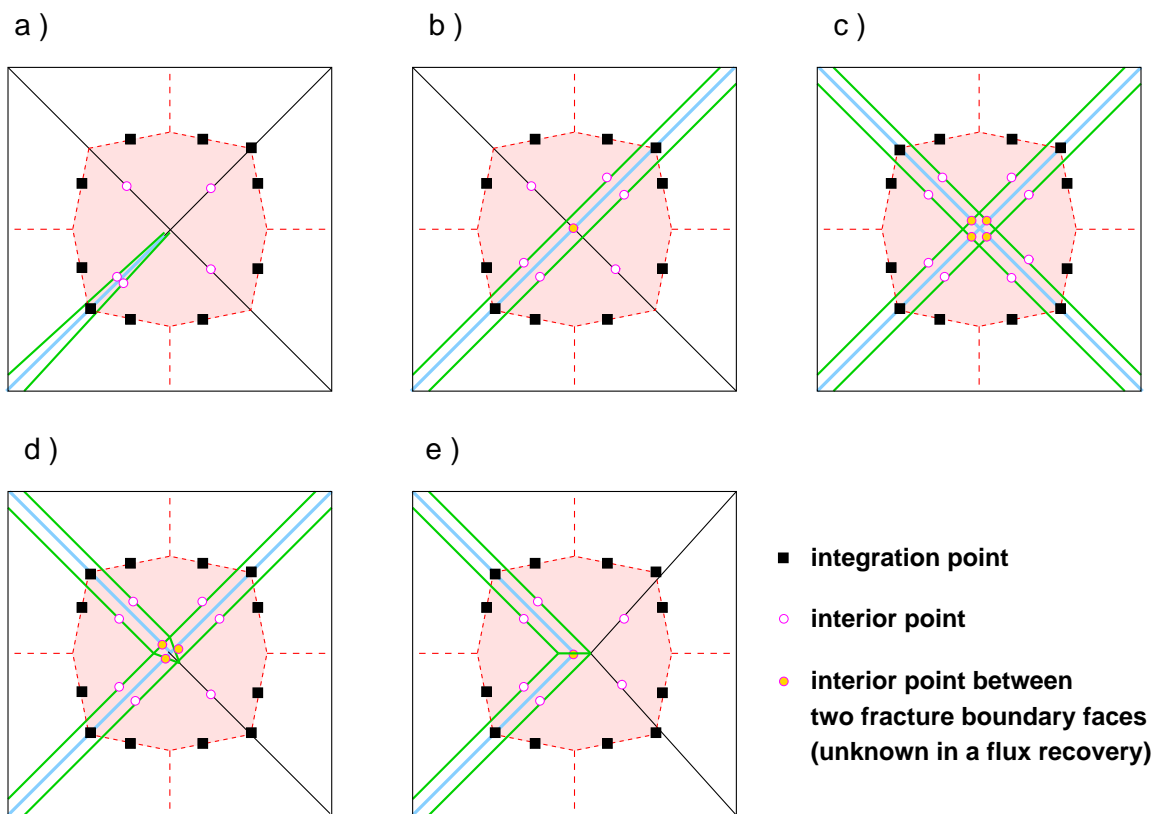


Figure 5.9: Five cases of extended fractures in a discrete fracture model: a) single fracture ending in a control volume; b) single fracture passing through a control volume; c) two fractures passing through a control volume; d) two fractures combining case a) and b); e) two fractures like case a).

By solving the constant Darcy velocities of each matrix subcontrol volume \mathbf{q}_m and the interior fluxes between two fracture boundary faces f_n^{fb} (see Figure 5.10), the interior fluxes can be determined later. The constant Darcy velocities \mathbf{q}_m and the interior fluxes f_n^{fb} must satisfy the following conditions:

- fluxes on a part of a patch boundary equal the sum of the fluxes of the two integration points:

$$\mathbf{q}_m \cdot \mathbf{n}_m dl_m = f_{i,1} + f_{i,2}, \quad (5.57)$$

where \mathbf{n}_m is an outward unit-normal vector of a subcontrol volume m , dl_i is the length of a patch boundary i and flux $f_{i,j}$ is the flux over the subcontrol volume face between node i and j .

- the continuity of the flux on the interior boundary:

$$\mathbf{q}_m \cdot \mathbf{v}_{m,n} dl_{m,n} = \mathbf{q}_n \cdot \mathbf{v}_{m,n} dl_{m,n}, \quad (5.58)$$

where $\mathbf{v}_{m,n}$ is a unit-normal vector of an interior boundary pointing from subcontrol volume m to n and $dl_{m,n}$ is the length of the interior boundary between the subcontrol volume m and n .

- the mass conservation in a fracture:

$$\sum_{m \in F_k} \mathbf{q}_m \cdot \mathbf{v}_{m,k} dl_m + f_k^{fb} + f_k^{fi} = 0, \quad (5.59)$$

where F is the neighboring matrix of a fracture k , $\mathbf{v}_{k,m}$ is the unit-normal vector of an interior boundary pointing from fracture k to subcontrol volume m , f_k^{fb} is the unknown interior flux of fracture k and f_k^{fi} is the flux at the integration point of fracture k .

The closure equation is formulated from the mathematical fact that the curl of the gradient of any scalar field is always zero. First, rearranging the Darcy velocity given in Equation (5.7) leads to

$$\mathbf{K}^{-1} \mathbf{v} = -\frac{1}{\mu} \nabla p. \quad (5.60)$$

Then, taking the curl of Equation (5.60) results in zero

$$\nabla \times \mathbf{K}^{-1} \mathbf{v} = -\frac{1}{\mu} \nabla \times \nabla p = 0. \quad (5.61)$$

From Stokes theorem, an integral of Equation (5.61) can be written as

$$\int_{\Omega_s} \nabla \times \mathbf{K}^{-1} \mathbf{v} d\Omega = \int_{\Gamma_s} \mathbf{K}^{-1} \cdot \mathbf{v} d\Gamma = 0, \quad (5.62)$$

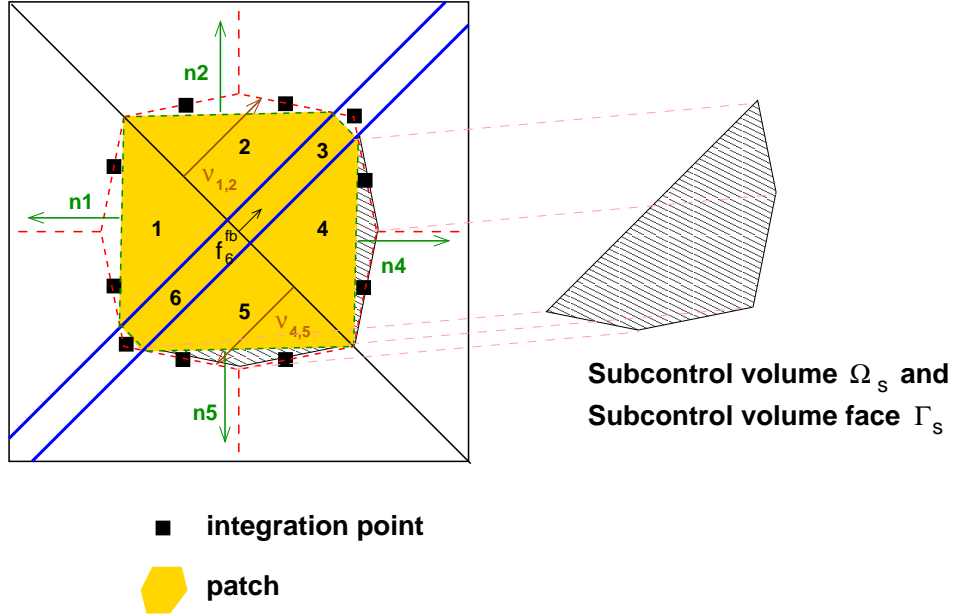


Figure 5.10: Flux recovery for a control volume of a fracture-matrix system.

where a subcontrol volume face Γ_s is defined by a part of the control volume boundary Γ_i which includes matrix subcontrol volume faces and fracture boundary faces (see Figure 5.10).

The velocity along the fracture boundary faces is determined by fluxes on the fracture boundary faces. The velocity of fractures in \mathcal{R} (\mathbf{v}'_f) is given by Equation (5.54) and is related to the velocity in \mathcal{P} as

$$\mathbf{v}_f = \mathbf{J}\mathbf{v}'_f = \frac{\mathbf{J}}{\det \mathbf{J}} \begin{bmatrix} f_{x0}(1-x'_i) + f_{x1}x'_i \\ f_{y0}(1-y'_i) + f_{y1}y'_i \end{bmatrix}. \quad (5.63)$$

Here, the constant Jacobian matrix is given as

$$\mathbf{J} = \begin{bmatrix} x_2 - x_1 & x_4 - x_1 \\ y_2 - y_1 & y_4 - y_1 \end{bmatrix}, \quad (5.64)$$

where x_i and y_i are coordinates at the corner i ($i = 1, \dots, 4$). The value of $\det \mathbf{J}$ is simply equal to the area of the fracture.

More details of flux recovery for a fracture-matrix system are described in Haegland et al. [2008].

6 Comparison of Geostatistical and Statistical Fracture Generation

Fractures have to be defined as discrete elements when a discrete fracture-matrix model is used in order to study a fracture-matrix system. There are two approaches for generating a complex fracture network: statistical fracture generation (SFG) and geostatistical fracture generation (GFG), described in Chapter 4. In this chapter, the application of SFG and GFG on the generation of fracture networks based on the statistical geometries and the spatial characteristics obtained from the Pliezhausen block (Dietrich et al. [2005]) are presented and later the results are compared by considering two different aspects: the structural characteristics of the fracture networks and the flow and transport behavior of the fracture-matrix systems.

6.1 Description of Study Cases

The geometries and spatial characteristics of a fracture network are important information for fracture generation. The detailed fracture geometries and the spatial characteristics of this study, the Pliezhausen field block, are presented in Sections 4.2 and 4.3 respectively. Two different generation approaches are considered in this study: statistical fracture generation (SFG), which is based only on the statistical fracture geometries, and geostatistical fracture generation (GFG), which takes into account both the statistical fracture geometries and the spatial characteristics.

Two study cases of SFG (SFG-A and SFG-B) and three study cases of GFG (GFG-A, GFG-B and GFG-C) are considered. The two cases of SFG are set up according to two different assumptions on defining the fracture size. As the size of fractures cannot be measured directly, it has to be approximated from the fracture trace observed on the exposed walls by assuming the relation between the fracture size and the observed trace length. In SFG-A, rectangular fractures are assumed to have the size directly defined by the fracture-trace distribution. The length and the width of the horizontal fractures are described by the horizontal trace distribution. The height and the width of the vertical fractures are given by the vertical and the horizontal trace distribution respectively. In SFG-B, the fracture-size distribution is adjusted until the same fracture-trace distribution as the field block is achieved. For the two

cases of SFG, after a fracture network of the specified fracture geometries (the size, the orientation and the density) has been obtained, the fracture distance is optimized to match the distribution observed in the field block. In two cases of GFG, an initial configuration of a fracture network is taken from the SFG without optimizing the fracture distance, GFG-A from SFG-A and GFG-B from SFG-B. For the last case of GFG (GFG-C), its initial configuration is randomly generated based on the orientation, the density and the defined maximum fracture size. After a comparison of several values of the maximum fracture size, the value that results in a minimum objective function of the SA is selected. The range of the maximum fracture sizes taken from the trace-length distribution is between 1.0 - 2.0 m high and 0.5 - 1.0 m long (for the vertical fractures) and between 0.5 - 1.2 m wide and 1.2 - 1.8 m long (for horizontal fractures). When the maximum size has been changed and the objective functions calculated from several simulations (from sim7 to sim21) are compared, the minimum objective functions are found in sim20 with a maximum size of 0.9 m \times 1.8 m (for vertical fractures) and 0.5 m \times 1.2 m (for horizontal fractures) as presented in Figure 6.1. After the initial fracture network has been obtained, the global optimization Simulated Annealing (SA) is performed by minimizing the objective function, defined as the divergence between the spatial characteristics of the generated fractured system and the field block. As a result, the generated fracture network can capture the spatial variability of the field block.

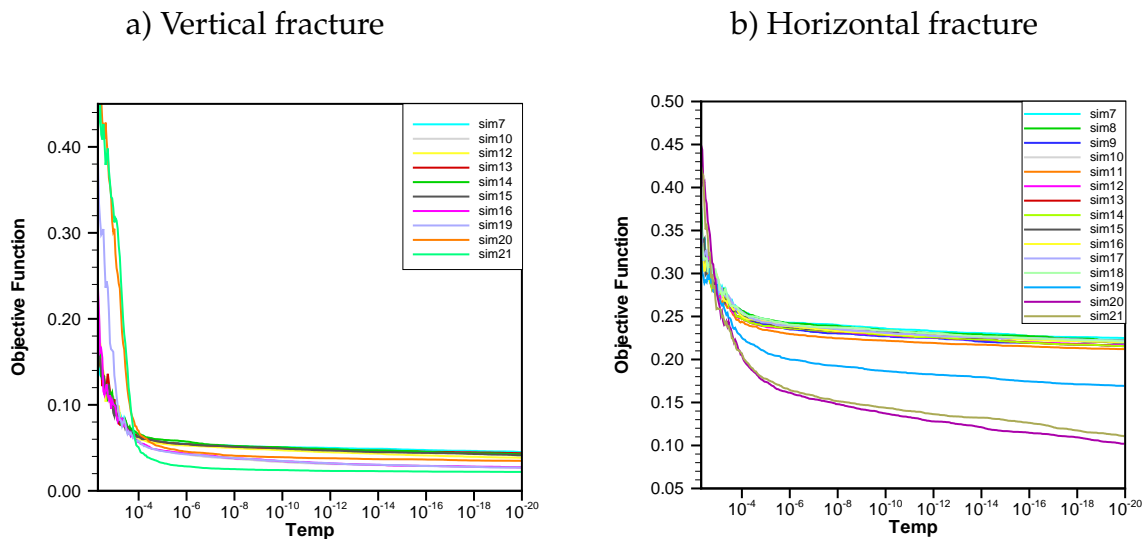


Figure 6.1: Objective functions depending on temperature steps from realizations of different maximum fracture sizes.

The parameters for generating fracture networks of all five study cases are summarized in Table 6.1.

		SFG-A	SFG-B	GFG-A	GFG-B	GFG-C
Orientation:	Fisher Dist.	(Azimuth)		(Dip)		
vertical	set1	146°		7°		
	set2	229°		8°		
horizontal	set3	201°		85°		
Fracture Size:	Erlang-2 Dist.	(lambda)				
vertical	height	-3.933	-1.750	-3.933	-1.750	-
	length	-5.372	-4.281	-5.372	-4.281	-
horizontal	width	-5.372	-4.281	-5.372	-4.281	-
	length	-5.372	-4.281	-5.372	-4.281	-
Max. Fracture Size:	Uniform Dist. [m]					
vertical	height	-	-	-	-	1.8
	length	-	-	-	-	0.9
horizontal	width	-	-	-	-	0.5
	length	-	-	-	-	1.2
Fracture Density:	Uniform Dist. [m ² /m ³]					
vertical		6.3	6.3	6.0	6.0	6.0
horizontal		5.0	5.0	5.3	5.3	5.3
Fracture Distance:	Exponential Dist.	(lambda)				
		-4.565	-4.565	-	-	-
Spatial Characteristic:		(γ, N_f, N_m, H)				
		-	-	Figure 4.7 to Figure 4.13		

Table 6.1: Parameters of fracture network generation for five study cases.

From the stochastic point of view, it is possible to generate multiple realizations of fracture networks. While each realization presents the specified descriptions, no single realization can exactly match the real system. The structure of the natural fracture network and the behavior of the real fracture-matrix system can be predicted from an ensemble average which can be achieved only when the number of realizations is large enough. This work intends to study, rather than to predict, the characteristics and the fracture-matrix behavior of the Pliezhausen block. The number of realizations is thus limited to five realizations for each study case. The structures and the flow and transport behavior of the Pliezhausen block are compared with the five study cases. The average values of the investigated characteristics of each study case is evaluated by averaging over the five exposed walls of each realization and again over all five realizations. The example of five exposed walls taken from one realization of each study case are shown in Figure 6.2 to 6.6.

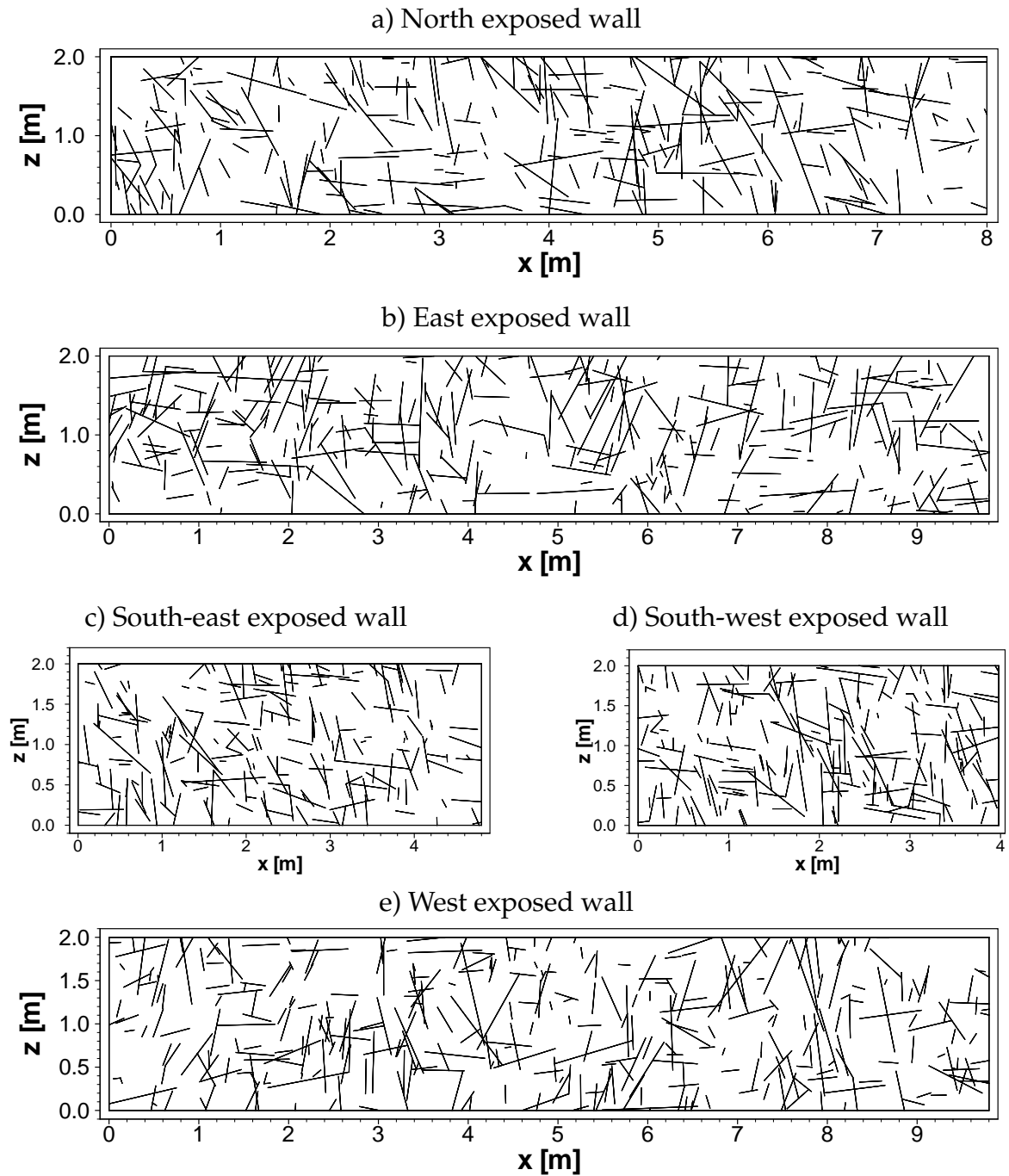


Figure 6.2: Five exposed walls from one realization generated by SFG-A.

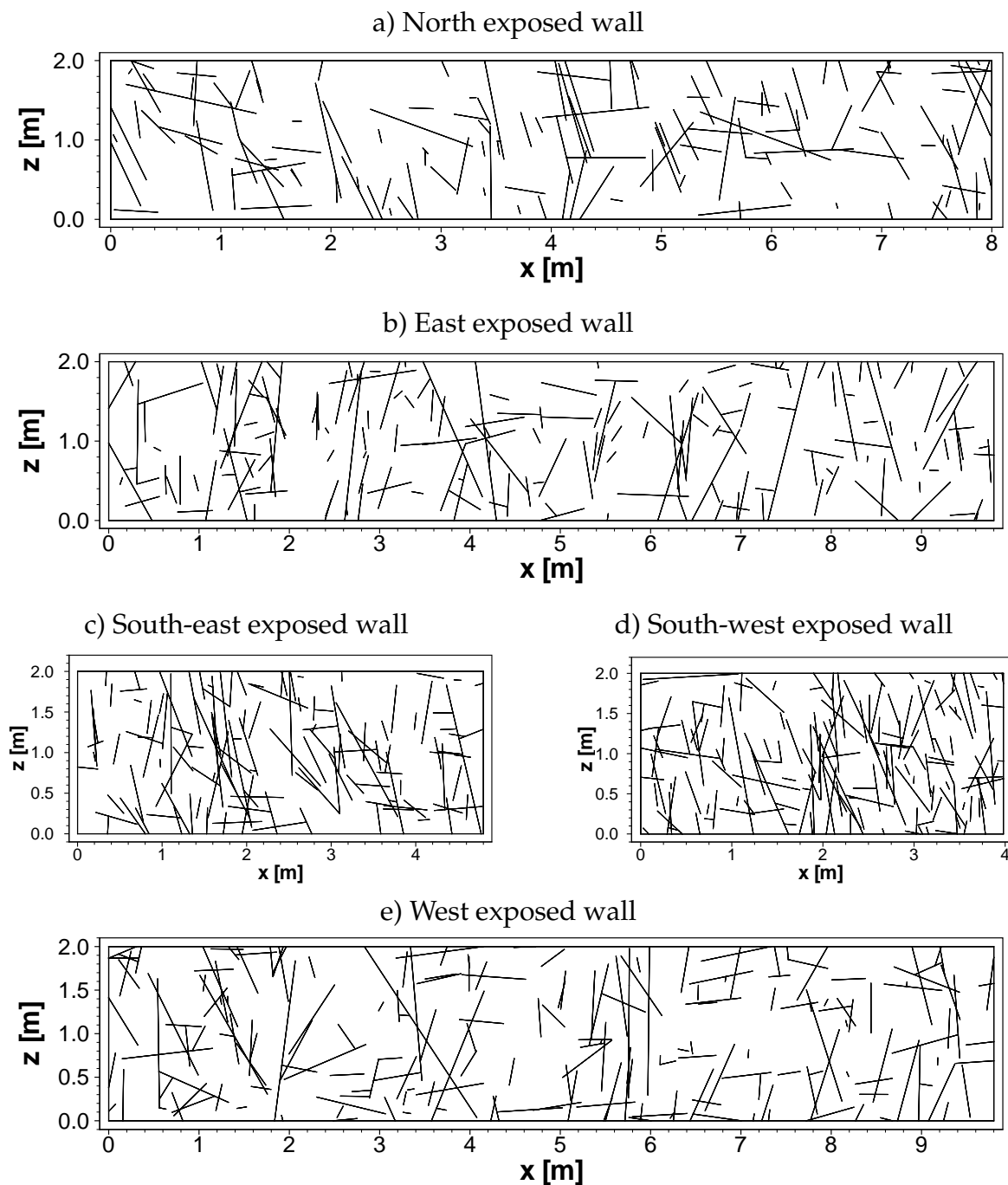


Figure 6.3: Five exposed walls from one realization generated by SFG-B.

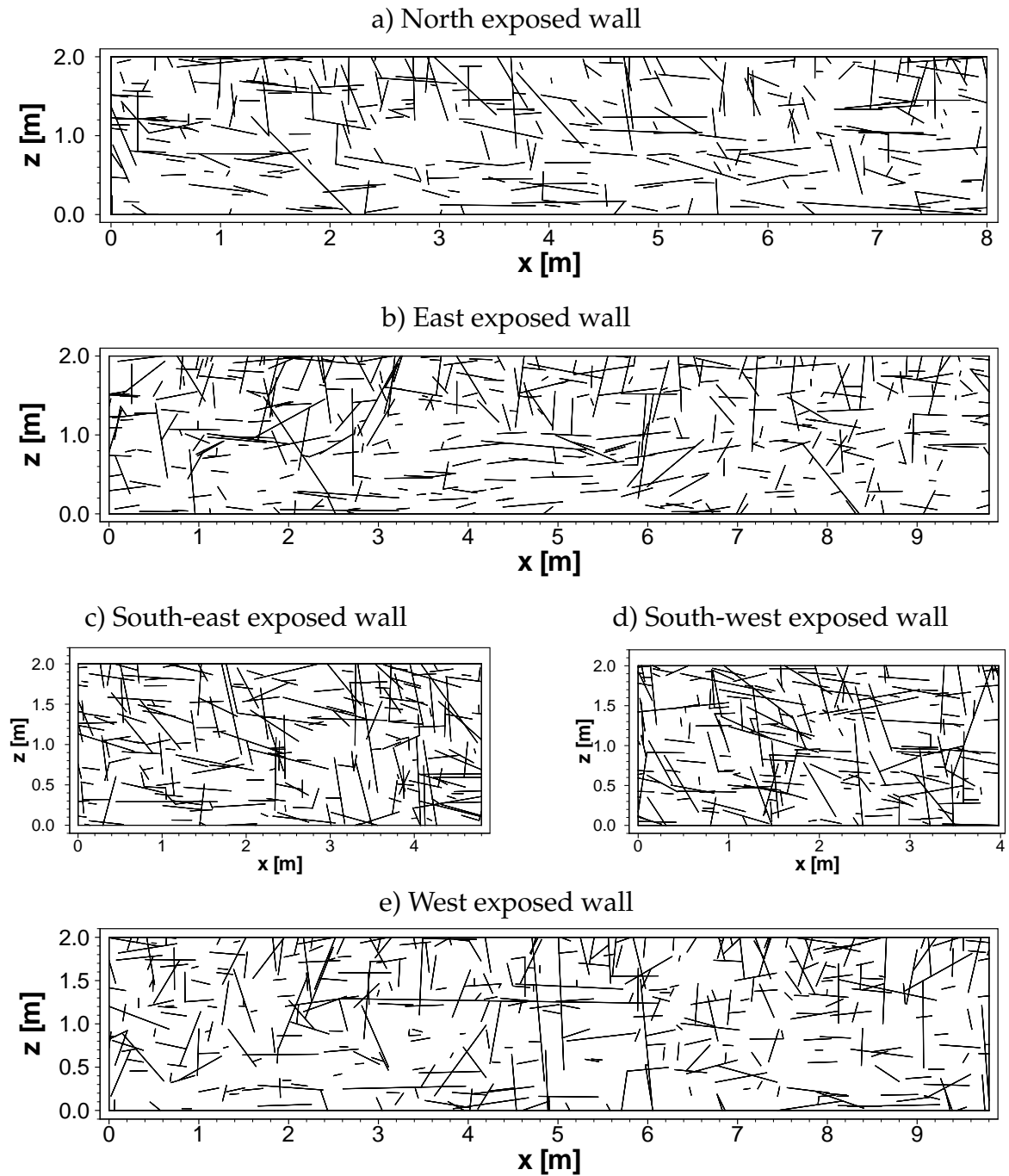


Figure 6.4: Five exposed walls from one realization generated by GFG-A.

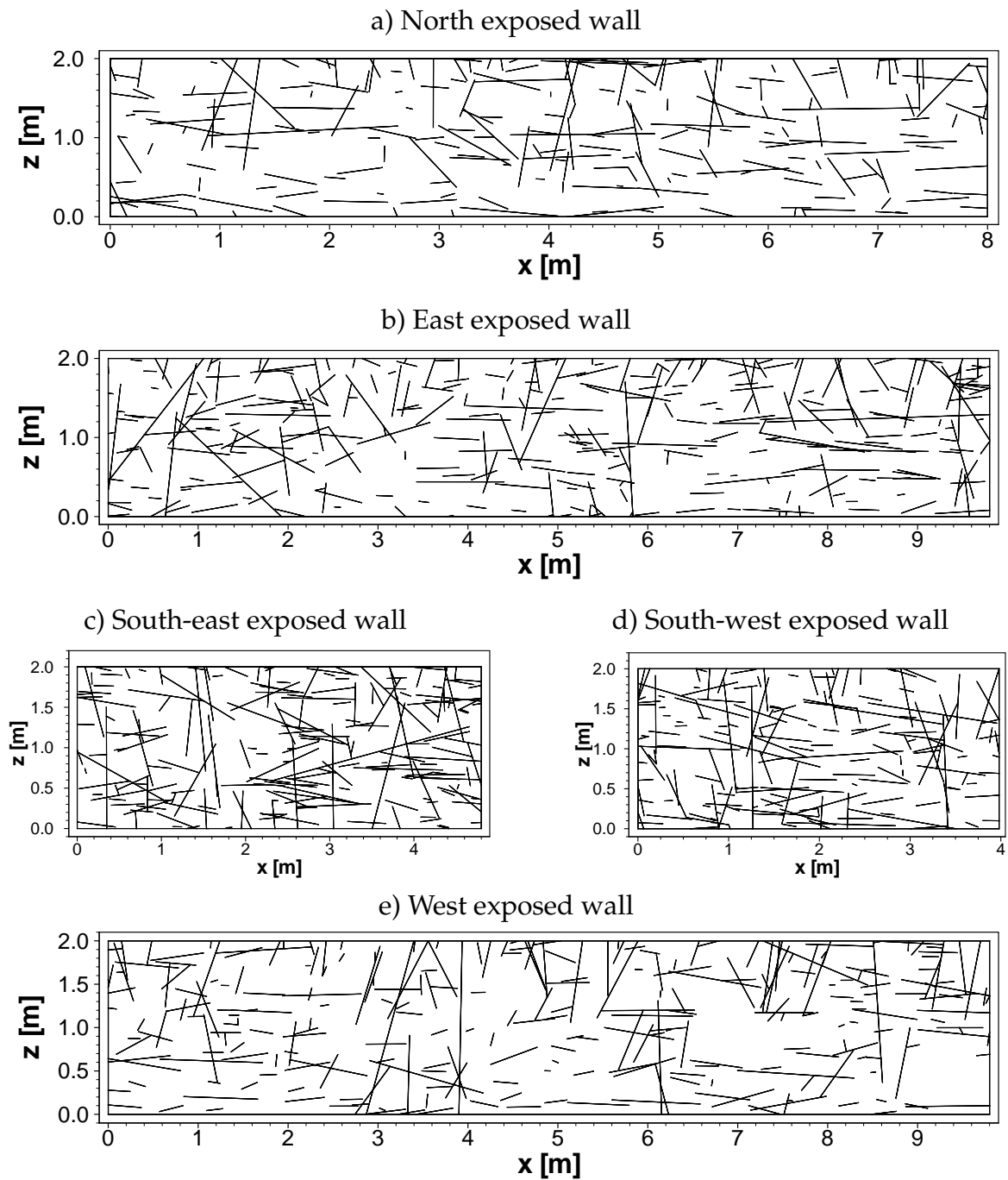


Figure 6.5: Five exposed walls from one realization generated by GFG-B.

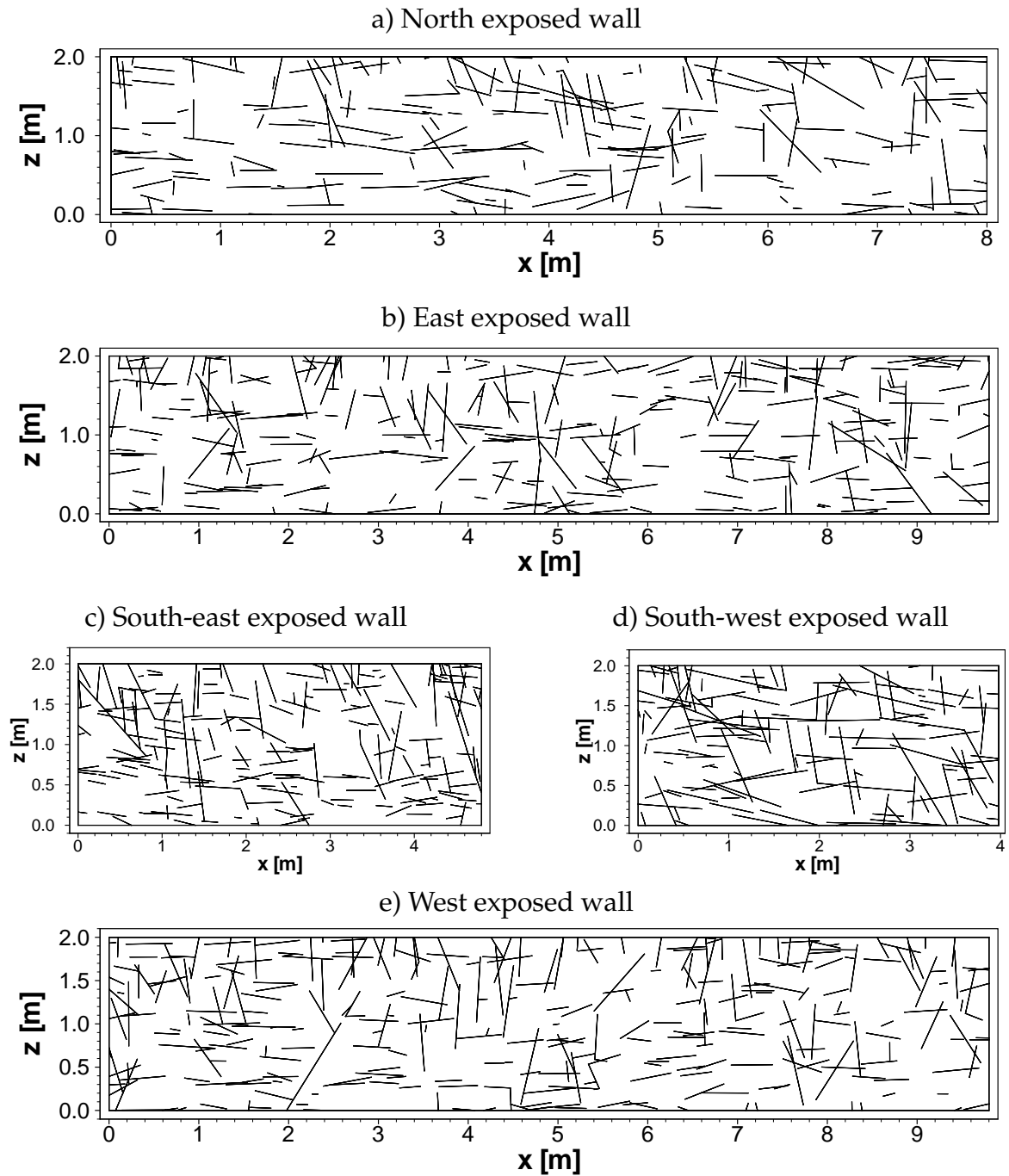


Figure 6.6: Five exposed walls from one realization generated by GFG-C.

6.2 Structure of Fracture Network

The fracture networks generated in the five cases are compared with the field block, focusing on the fracture geometries and the spatial characteristics. The study of the fracture-network structures in this section provides the background and the basic knowledge for understanding the comparative study of the flow and transport behavior of the fracture-matrix system in the next section.

Fracture trace length

The averages of the cumulative distributions $F(x)$ related to the trace length x for the vertical and horizontal trace from the five study cases are presented in Figure 6.7. The trace-length distribution for SFG-A is too short for both vertical and horizontal directions compared with the target value evaluated from the outcrop of the field block. This means that a direct transfer of the length distribution observed in two-dimensional outcrops to the fracture size in the three-dimensional domain leads to an underestimation of the fracture size. SFG-B enlarges the fracture size to fit the fracture-trace distribution of the field block by decreasing the parameter lambda (see Table 6.1); therefore, its fracture-trace distribution shows a good agreement with the field data. Optimizing the spatial characteristics in GFG-A slightly changes the length distribution. In GFG-B the length distribution becomes smaller than SFG-B, which means that the spatial-characteristic optimization in this case results in decreasing the fracture size. The randomly generated fracture polygon without an explicitly defined fracture size in GFG-C is able to represent the fracture-trace distribution for a small fracture trace very well. However, for a large trace length, it shows the highest deviation from the observed field data.

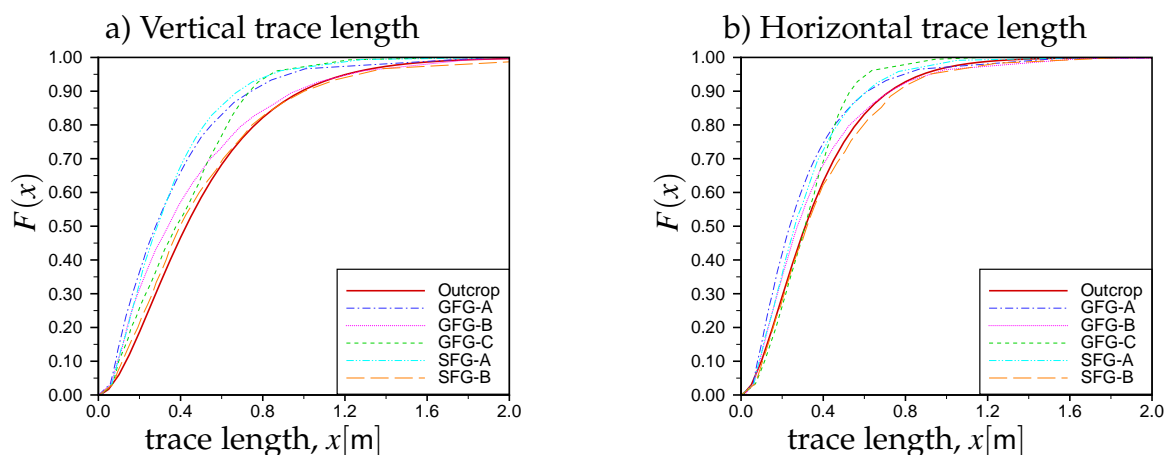


Figure 6.7: Comparison of cumulative distribution functions of the average trace length from five study cases.

Fracture space

The cumulative distributions of the fracture distance of the five study cases are compared with the value from the outcrop of the field block (see Figure 6.8). The location of fractures in SFG is optimized to match the distribution function of the fracture distance, therefore, SFG-A and SFG-B show a close agreement with the observed fracture space from the field block. A slightly larger fracture space of SFG-B compared with SFG-A is due to the fact that, for the same fracture density, the larger fracture size in SFG-B (see Figure 6.7) leads to a lower number of fractures, which means a larger distance between two adjacent fractures. Although the three cases of GFG are not considered the fracture-distance in the generating scheme, the result from GFG-A shows a close agreement with the observed field data. The larger fracture size in GFG-B compared with GFG-A (see Figure 6.7) yields a larger space distribution, which is also observed when SFG-B is compared with SFG-A. The fracture space of GFG-C is close to GFG-B.

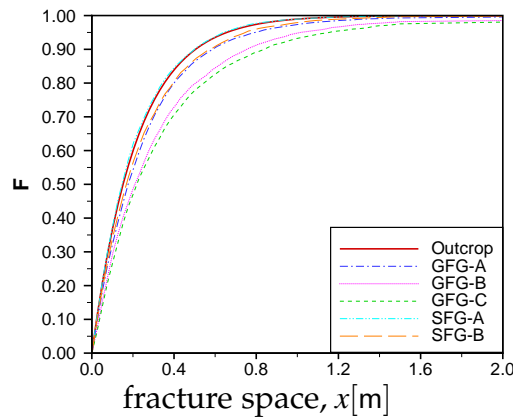


Figure 6.8: Comparison of cumulative distribution functions of the average fracture distance from the five study cases.

Spatial characteristics

The average value of the spatial characteristics such as the standardized experimental variogram (γ_s), the fracture neighborhood (N_f), the matrix neighborhood (N_m) and the fracture-cell density (H) discussed in Section 4.3 are compared with the data evaluated from the field block. These spatial characteristics are considered in GFG, however, not in SFG.

The standardized experimental variograms for the horizontal and vertical scanline directions from the three cases of GFG are closer to the field value than those from SFG-A and SFG-B (see Figure 6.9).

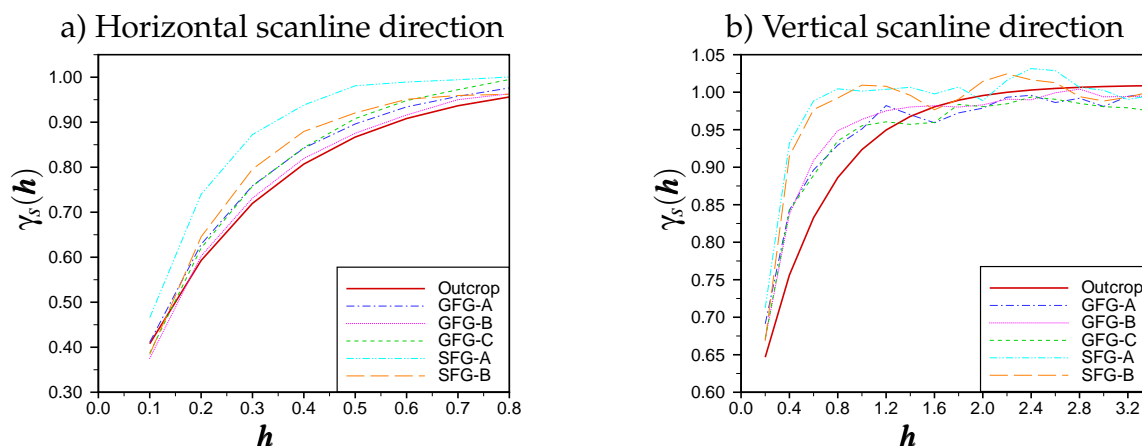


Figure 6.9: Comparison of the average standardized experimental variograms from the five study cases.

Additionally, the fracture and matrix neighborhoods for the horizontal scanline direction of GFG-A, GFG-B and GFG-C are closer to the field than SFG-A and SFG-B (see Figures 6.10a and 6.11a). However, the neighborhoods from the vertical scanline direction of GFG-A, GFG-B and GFG-C match closely only in the fracture direction ($k = 2, 3$) but not in the other directions, in which SFG-A and SFG-B show better results (see Figures 6.10b and 6.11b).

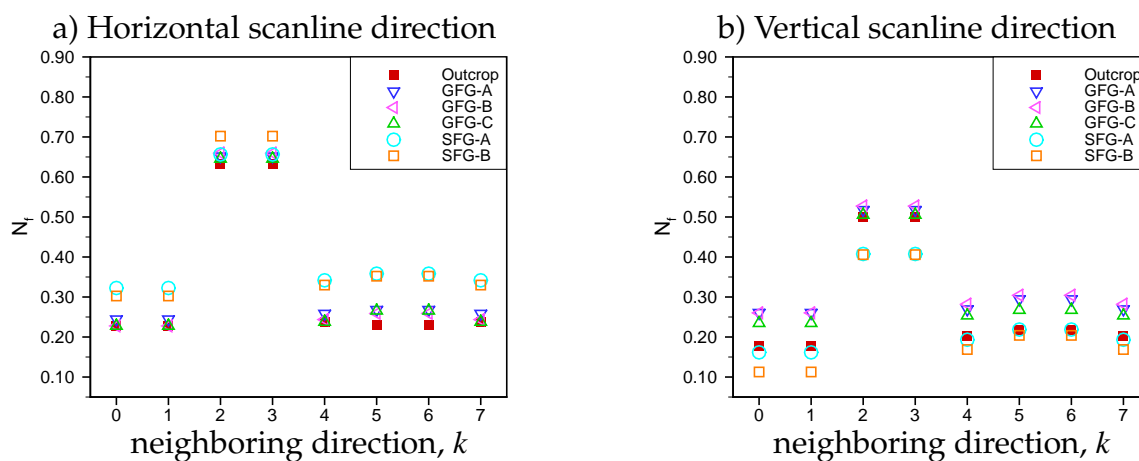


Figure 6.10: Comparison of the average fracture neighborhood from the five study cases.

The reason could be that the neighborhoods from the vertical scanline direction are varied in a range broader than from the horizontal scanline direction and tend to be directionally dependent on the south-west exposed walls (see Figures 4.11 and 4.12). Correctly representing the parameter which has this peculiarity might need a more complicated approach. The directional dependence of the neighborhoods

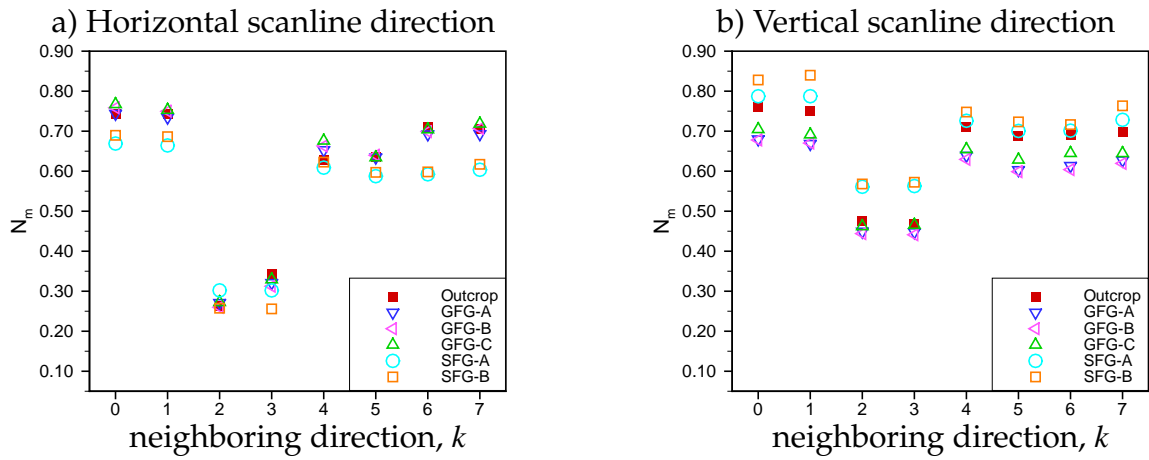


Figure 6.11: Comparison of the average matrix neighborhood from the five study cases.

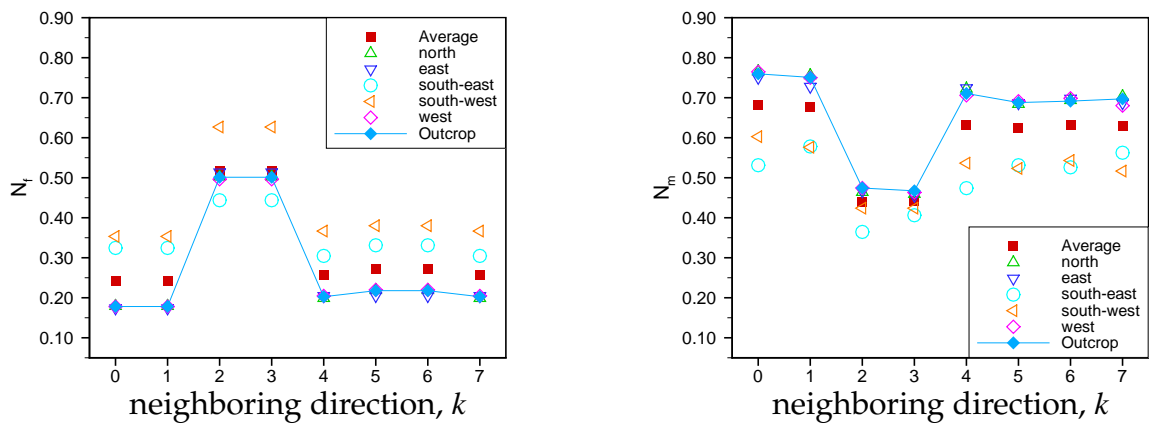


Figure 6.12: Neighborhoods of one realization of GFG-A from vertical-scanline indicator fields with a segment length of 0.10 m and a distance of 0.20 m.

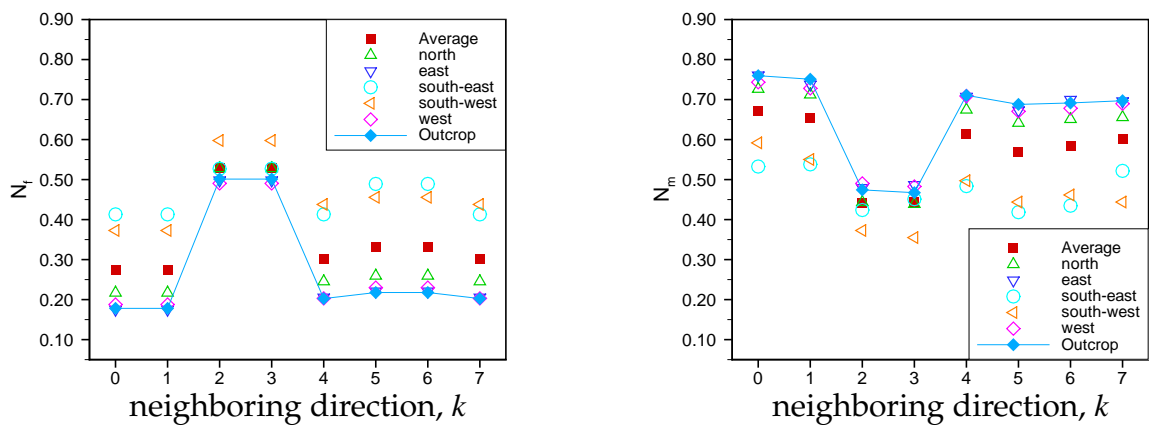


Figure 6.13: Neighborhoods of one realization of GFG-B from vertical-scanline indicator fields with a segment length of 0.10 m and a distance of 0.20 m.

is observed in all realizations generated by GFG-A, GFG-B and GFG-C. As shown in Figures 6.12 and 6.13 for the example of one realization from GFG-A and GFG-B respectively, N_{fr} and N_m from the field block are close to the values from the north, the east and the west exposed walls but not to the values from the south-east and the south-west exposed walls.

The fracture-cell density H evaluated from all cases is shown in Figure 6.14. The greater number of vertical fractures on the top as observed in the field outcrop is only noticed in GFG-A, GFG-B and GFG-C. SFG-A and SFG-B show relatively constant H due to randomly distributed fractures.

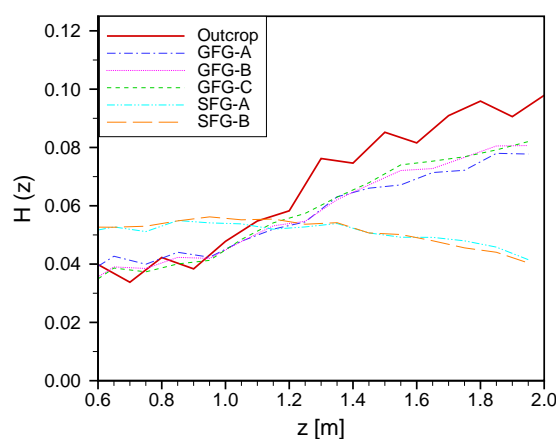


Figure 6.14: Comparison of average fracture-cell density from the five study cases.

Conclusion: fracture-network structure

Spatial structures of fracture networks of the five study cases such as the fracture-trace distribution, the fracture-space distribution and the spatial characteristics (standardized experimental variogram, neighborhoods and fracture-cell density) are compared with the target values obtained from the Pliezhausen block:

- The fracture size could be approximated from the fracture trace with careful consideration. The direct transfer of the fracture-trace distribution shows an underestimation of the fracture size (in SFG-A). The size of the fractures is approximated better by modifying the size until the fracture-trace distribution fits with the field value (in SFG-B). After the spatial characteristics in GFG-A and GFG-B have been optimized, the fracture-trace distribution changes slightly.
- The fracture distance is optimized in the statistical fracture generation (SFG), hence SFG-A and SFG-B show a good agreement with the field data. Even

though the distance is not considered in geostatistical fracture generation (GFG), the results from the three cases of GFG can still reproduce the cumulative distance fairly well.

- The spatial characteristics are taken into account in GFG, but not SFG. Therefore, the three cases of GFG can represent almost all the spatial characteristics, except the neighborhoods from the vertical scanline direction, which is directionally dependent. The two cases of SFG statistical show that they can reproduce only the neighborhoods in the fracture direction, but not the standardized variogram and the fracture-cell density.

6.3 Flow and Transport in Fracture-Matrix System

The flow and transport behavior of the fracture-matrix systems from the five study cases are investigated. Numerical simulations are performed on the south-west cross-sections of the generated three-dimensional fracture networks embedded in the porous matrix. The simulations are carried out in a two-dimensional problem because the results can be quantitatively compared with the simulation results from the scanned cross-section of the field block (see Figure 4.4). In addition, the south-west cross-section is selected for two main reasons. The spatial characteristics evaluated from this cross-section show the largest deviation from the observed values compared with the other exposed walls (see Figure 6.12 and 6.13), and the highest variation of the system behavior is expected due to its smallest size. This could imply that, if this cross-section represented the observed system, the other cross-section would possibly be able to represent it, too.

6.3.1 Model set-up

A single-phase flow of an incompressible fluid is simulated and the velocity field obtained from the flow simulation is later used in the transport simulation of a tracer. Boundary conditions are described in Figure 6.15. The top and the bottom boundaries are impermeable; hence, the boundaries are described by a Neumann no-flow for the flow and the transport simulations. On the left-hand side (the inflow boundary) and on the right-hand side (the outflow boundary), a Dirichlet boundary in terms of pressure is given for the flow simulation. For the transport simulation, the inflow boundary is described as a Neumann no-flow. A tracer is given at an inner boundary for a very short time instead of at the inflow boundary in order to avoid the loss of mass over the inflow boundary. The inner boundary is located a very small distance from the inflow boundary. For the outflow boundary, a free-flow

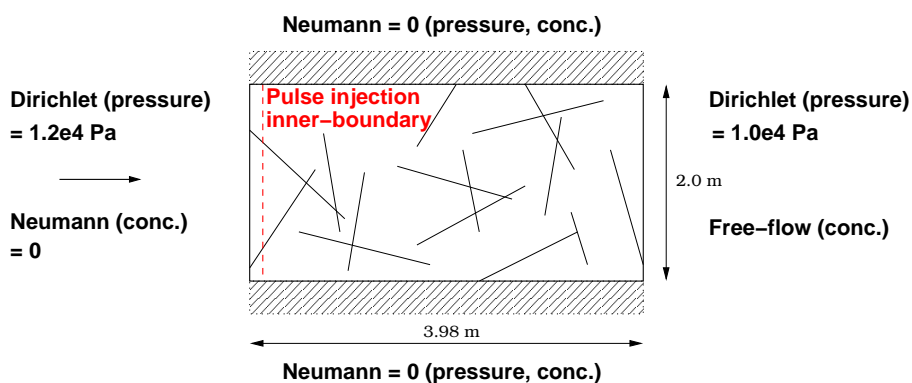


Figure 6.15: Boundary conditions for flow and transport simulations.

boundary is used for the transport simulation, which means that a tracer arriving at the boundary is allowed to leave freely.

A study domain is a two-dimensional cross-section 3.98 m long and 2.00 m high and consists of one-dimensional fractures embedded in the matrix. The domain is discretized by the mesh generator ART (Almost Regular Triangulation) (Fuchs [1999]). The properties of the domain (fractures and matrix) and of the fluid are presented in Table 6.2.

		Domain Properties	
		matrix	fracture
Permeability, K	$[m^2]$	$1.0e - 13$	$8.33e - 10$
Eff. porosity, ϕ	$[-]$	0.13	0.30
Long. dispersivity, α_l	$[m]$	$1.0e - 9$	0.0
Trans. dispersivity, α_t	$[m]$	$1.0e - 9$	0.0
Diffusion coeff., D_m	$[m^2 \cdot s^{-1}]$	$1.0e - 9$	$1.0e - 9$
Aperture, b	$[m]$	-	$1.0e - 4$
		Fluid Properties	
Viscosity, μ	$[kg \cdot m^{-1} \cdot s^{-1}]$	$1.814e - 5$	
Density, ρ	$[kg \cdot m^{-3}]$	1.21	

Table 6.2: Domain and fluid properties for all simulations.

6.3.2 Parameters characterizing system behavior

In order to quantitatively compare the flow and transport behavior of the fracture-matrix system, the characteristic variables such as total flux Q and characteristics of a breakthrough curve (initial breakthrough time t_{init} , peak mass flux \dot{m}_p , peak arrival time t_p , effective travel time \bar{t} , variance σ^2 and skewness γ) are evaluated from the simulations. The breakthrough curve (BTC) is defined as the rate of the mass leaving the domain at the outflow boundary in each time interval dt . The initial breakthrough time is defined as the time that the first 1% of the total tracer mass arrives at the outflow. The peak mass flux and peak arrival time are obtained directly from the BTC, whereas the effective travel time \bar{t} , the variance σ^2 and the skewness γ are evaluated from the moment μ_i and the central moment μ_i^c of the BTC as

$$\bar{t} = \frac{\mu_1}{\mu_0}, \quad (6.1)$$

$$\sigma^2 = \frac{\mu_2^c}{\mu_0}, \quad (6.2)$$

$$\gamma = \frac{\mu_3^c}{\mu_0 (\sigma^2)^{\frac{3}{2}}}, \quad (6.3)$$

where

$$\mu_i = \int_{t=0}^{t=\infty} t^i c(t) dt, \quad (6.4)$$

$$\mu_i^c = \int_{t=0}^{t=\infty} (t - \bar{t})^i c(t) dt. \quad (6.5)$$

Here, $c(t)$ is the total tracer mass concentration [kg/s] leaving the domain at time t .

The values of Q , \bar{t} and t_p reflect the bulk movement of fluid in the system, whereas the values of \dot{m}_p , σ^2 and γ depend highly on the distribution of tracer concentration in the system. The variance σ^2 of the BTC relates to the degree of spreading of the plume. The skewness γ shows the asymmetry of the spreading. As can be seen in Figure 6.16, zero skewness means a symmetrical distribution of the plume and a positive skewness indicates that a high concentration of tracer plume is transported to the outflow and then the rest of the plume arrives gradually; the reverse holds for a negative skewness.

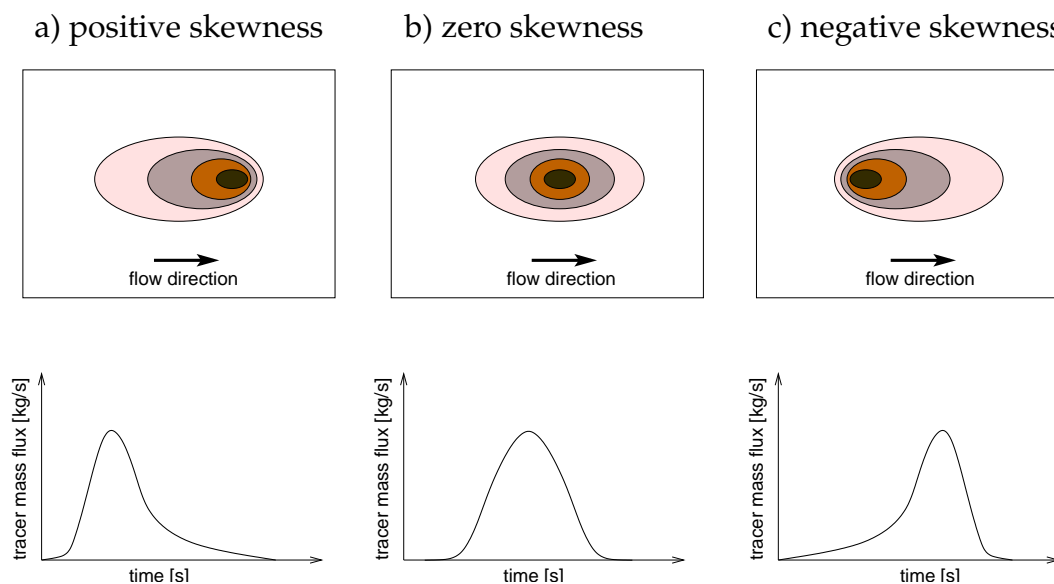


Figure 6.16: A schematic of concentration distributions related to the skewness evaluated from the breakthrough curves.

6.3.3 Mesh size analysis

Before the flow and the transport behavior of the five study cases is compared, a suitable mesh size for the problem of interest has to be identified by performing a convergence investigation on different mesh sizes. The numerical simulation is carried out on the scanned south-west wall of the Pliezhausen block using mesh sizes of approximately 0.01, 0.02, 0.05, 0.10 and 0.20 m. The discretized domains of approx. 0.02, 0.05, 0.10 and 0.20 m are illustrated in Figure 6.17. The fracture and matrix properties as well as the fluid properties refer to the values given in Table 6.2. The boundary conditions are described in Figure 6.15. However, the tracer is given at the inflow boundary using the Dirichlet boundary (at the initial time, $t = 0$) instead of assuming at the inner boundary to avoid the problem of a high variation of injected mass due to different discretized grid sizes.

The flux and the BTC characteristics from all mesh sizes are summarized in Table 6.3 and the BTCs are shown in Figure 6.18. As no analytical solution exists for such a complicated fracture-matrix system, the results from the finest mesh of 0.01 m are used as a reference result.

The effect of the grid size on the total flux Q , the effective travel time \bar{t} and the peak arrival time t_p is relatively small compared with its effect on the peak mass flux \dot{m}_p and the variance σ^2 (see Table 6.3). This is because Q , \bar{t} and t_p are related to the bulk movement of fluid in the system, which is not strongly grid dependent. Whereas the peak mass flux \dot{m}_p and the variance σ^2 are related to the distribution of tracer

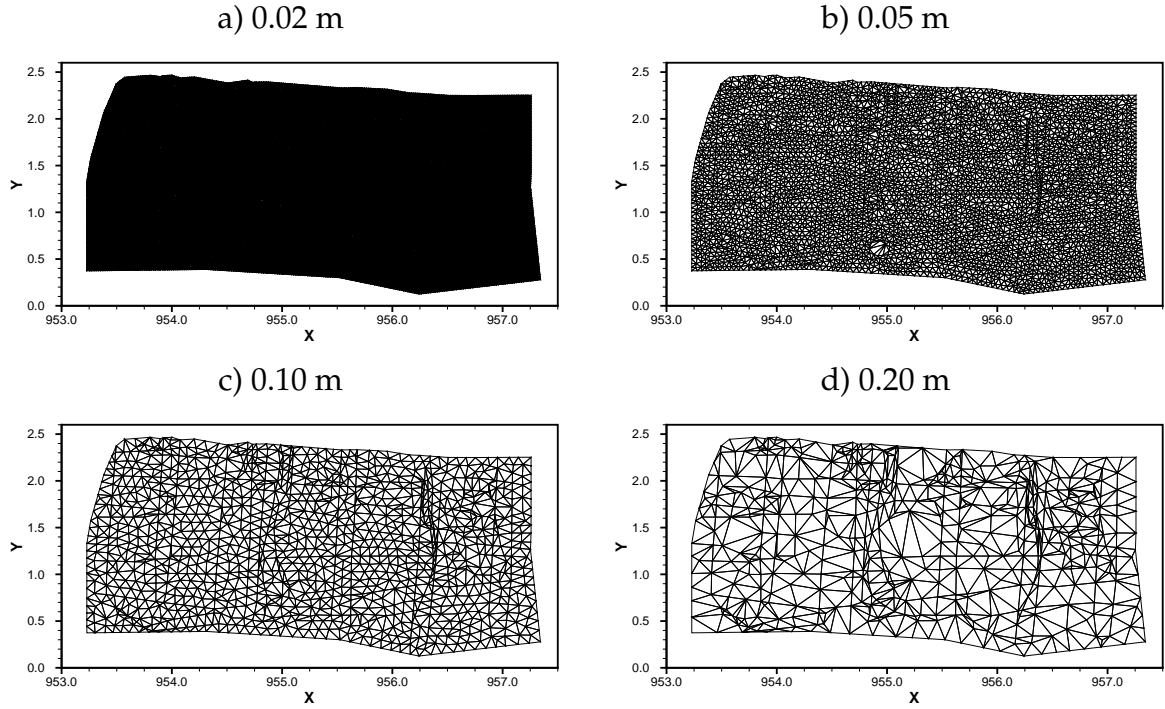


Figure 6.17: Discretized domain of different mesh sizes of a south-west exposed wall from a scanned outcrop.

	Q		\dot{m}_p		t_p		\bar{t}		σ^2	
	$[m^3 s^{-1}]$	$[\%]^1$	$[kg s^{-1}]$	$[\%]^1$	$[s]$	$[\%]^1$	$[s]$	$[\%]^1$	$[s^2]$	$[\%]^1$
0.01 m	1.71e-5	-	1.49e-5	-	5.22e+4	-	6.60e+4	-	9.78e+8	-
0.02 m	1.72e-5	0.59	1.54e-5	5.20	5.12e+4	1.90	6.64e+4	0.61	1.00e+9	2.25
0.05 m	1.75e-5	2.34	1.34e-5	18.33	5.02e+4	3.83	6.47e+4	1.97	7.93e+8	18.92
0.10 m	1.80e-5	5.10	1.72e-5	42.26	4.90e+4	6.13	6.24e+4	5.45	5.90e+8	39.67
0.20 m	1.84e-5	7.91	1.46e-5	73.26	5.08e+4	2.36	5.95e+4	9.85	3.84e+8	70.64

[1] percentage of the differences of parameters from the mesh size of 0.01 m

Table 6.3: Parameters characterized of flow and transport simulations of the scanned south-west wall of different mesh sizes.

plume in the system, which depends on the grid size and the discretization scheme (see Table 6.3). Applying a fully upwinding method on the advective term in the transport equation shown in Equation (5.42) introduces artificial diffusion, known as numerical diffusion. Due to this, the difference in the BTCs can be clearly observed in Figure 6.18. When a grid size becomes smaller, its variance σ^2 increases and its peak mass flux \dot{m}_p decreases. For a fine mesh, the result of a physical dispersion, which is the effect of fast flow in fractures and slow flow in the matrix arising from a large permeability difference between fractures and matrix, can be more accurately represented. As can be seen in Figures 6.19a and 6.19c for a fine mesh of

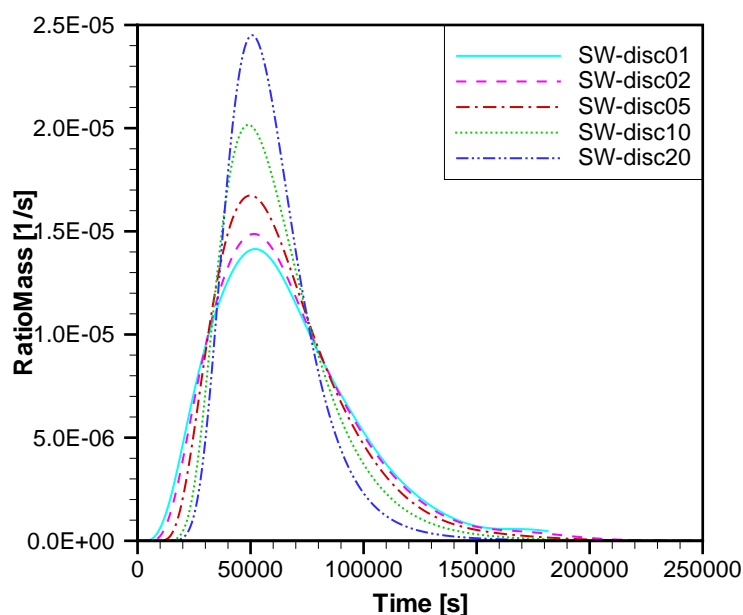


Figure 6.18: Comparison of breakthrough curves from different discretization meshes: 0.01, 0.02, 0.05, 0.10 and 0.20 m of a scanned south-west exposed wall.

0.02 m, when injected tracer arrives at the fractures, it is transported quickly along fractures which leads to a shorter initial breakthrough time of the tracer. Transporting a part of the tracer which remains in the matrix requires a longer time (see Figure 6.19e), which results in a long-tail behavior of the BTC (see Figure 6.18). In contrast, for the coarse mesh of 0.20 m shown in Figures 6.19b and 6.19d, the effect of fast flow in the fractures and slow flow in the matrix is smeared out, and the injected tracer remains together at a high concentration about the center of the plume. Hence, the high peak mass flux is observed when the center of the plume arrives at the outflow boundary. For a coarse mesh, numerical diffusion dominates the physical dispersion in the fracture-matrix system, and the system tends to behave more like a single-continuum system.

In the case of an advection-dominated problem like the transport in a fracture-matrix system, a small grid size is necessary to guarantee that the system behavior is represented correctly. However, this means a high computational demand. Therefore, a compromise should be made. The grid size of 0.02 m is selected for the study of the flow and transport in the fracture-matrix system because its total flux and BTC characteristics are close to a convergence to the fine mesh 0.01 m (only the peak mass flux is relatively different) and its computation time is practicable. The difference of the peak mass flux of the mesh size 0.02 m to the mesh size 0.01 m is still acceptable because the main focus of the flow and transport simulation is to study

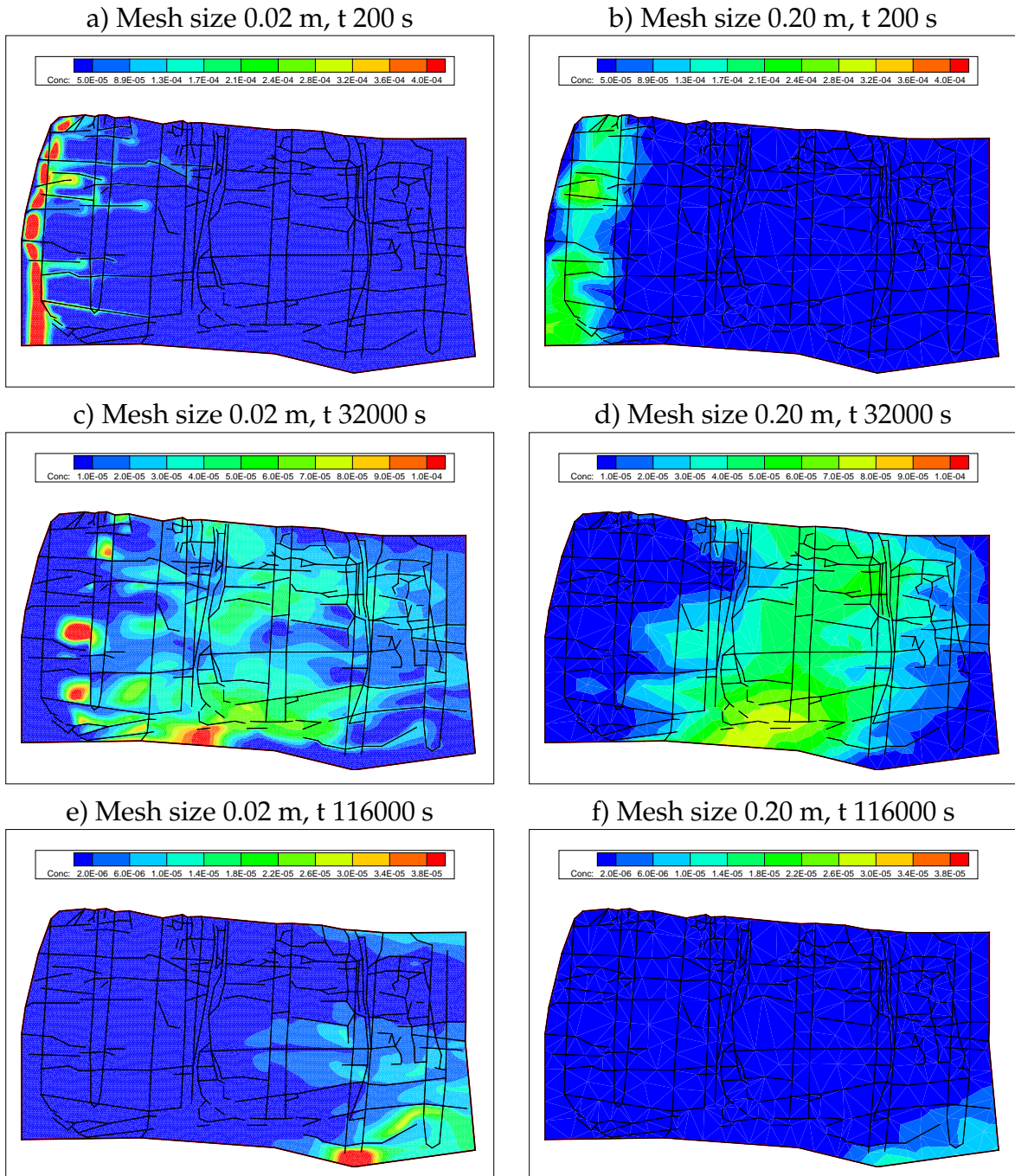


Figure 6.19: Concentration distribution of the south-west walls at times 200, 32000 and 116000 s from mesh sizes 0.02 and 0.20 m.

the behavior rather than to accurately predict the amount of the mass transported in the fracture-matrix system.

6.3.4 Comparison of study cases

The south-west cross-sections from a total of twenty-five realizations from five study cases are used as a study domain. The domain is discretized into triangular meshes of approx. 0.02 m; the boundary conditions and the domain properties as well as the fluid properties are described in Section 6.3.1. For each study case, the flow and transport behavior is quantified by the parameters described in Section 6.3.2. The values of the parameters from the scanned south-west wall and the average values of the parameters from all five study cases are summarized in Table 6.4. The deviation of the simulation results from the scanned wall is shown in Figure 6.20, where the standardized value (SV) is defined as

$$SV = \frac{P_r - P_{sw}}{P_{sw}}. \quad (6.6)$$

Here, P_r is the average of each investigated parameter of the realizations and P_{sw} is the parameter from the scanned south-west wall.

	Q [$m^3 s^{-1}$]	\dot{m}_p [$kg s^{-1}$]	t_p [s]	\bar{t} [s]	σ^2 [s^2]	γ [-]
Scanned wall	1.72e-5	1.49e-5	5.12e+4	6.64e+4	1.00e+9	1.115
SFG-A	1.03e-5	1.54e-5	1.00e+5	1.06e+5	7.09e+8	0.508
SFG-B	9.36e-6	1.29e-5	1.13e+5	1.15e+5	8.83e+8	0.294
GFG-A	1.73e-5	1.66e-5	5.97e+4	6.90e+4	6.27e+8	0.663
GFG-B	1.56e-5	1.41e-5	6.72e+4	7.74e+4	8.91e+8	0.697
GFG-C	1.51e-5	1.47e-5	5.99e+4	7.32e+4	8.05e+8	0.680

Table 6.4: Results of flow and transport simulations of the south-west wall obtained from the scanned wall and from average values of five study cases.

The breakthrough curves (BTCs) and the accumulated breakthrough curves (AccBTCs) evaluated from all realizations are presented in Figures 6.21 and 6.22 respectively. The abbreviations of the name in the graph legend $x - y - zn$ means

- x : "SW" south-west cross-section,
- y : "S" SFG and "G" GFG,
- z : "A,B,C" case of the SFG and GFG,
- n : "1,2,.. or 5" realization number.

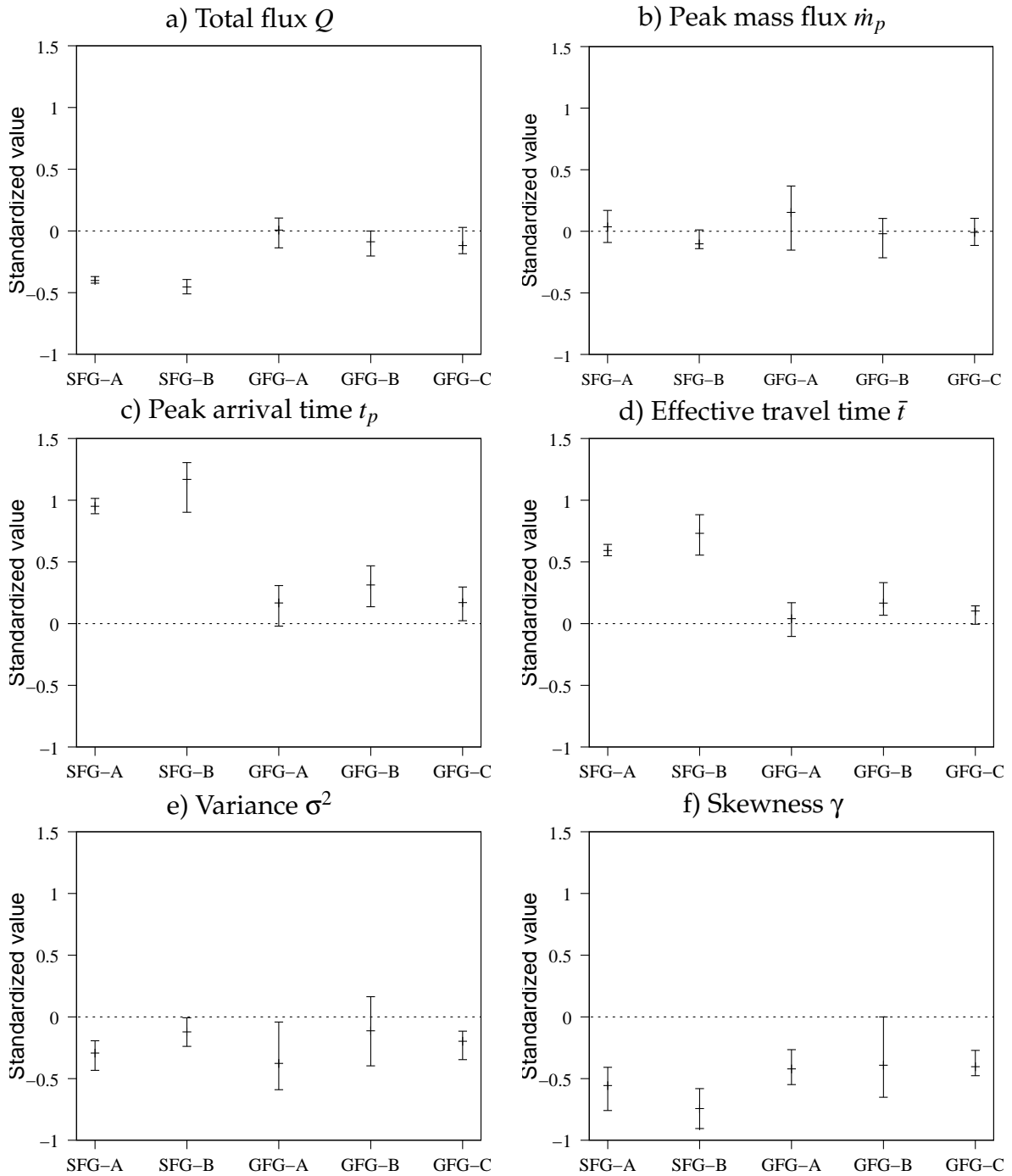


Figure 6.20: Average and extreme values (min./max.) of flow and transport simulations of the south-west wall of five study cases compared with the results obtained from the field outcrop simulation (dashed line).

The results of Q , \bar{t} and t_p obtained from the three study cases of the GFG are clearly closer to the numerical results of the scanned wall than the results obtained from the two cases of the SFG for both the average values (see Table 6.4) and the values from

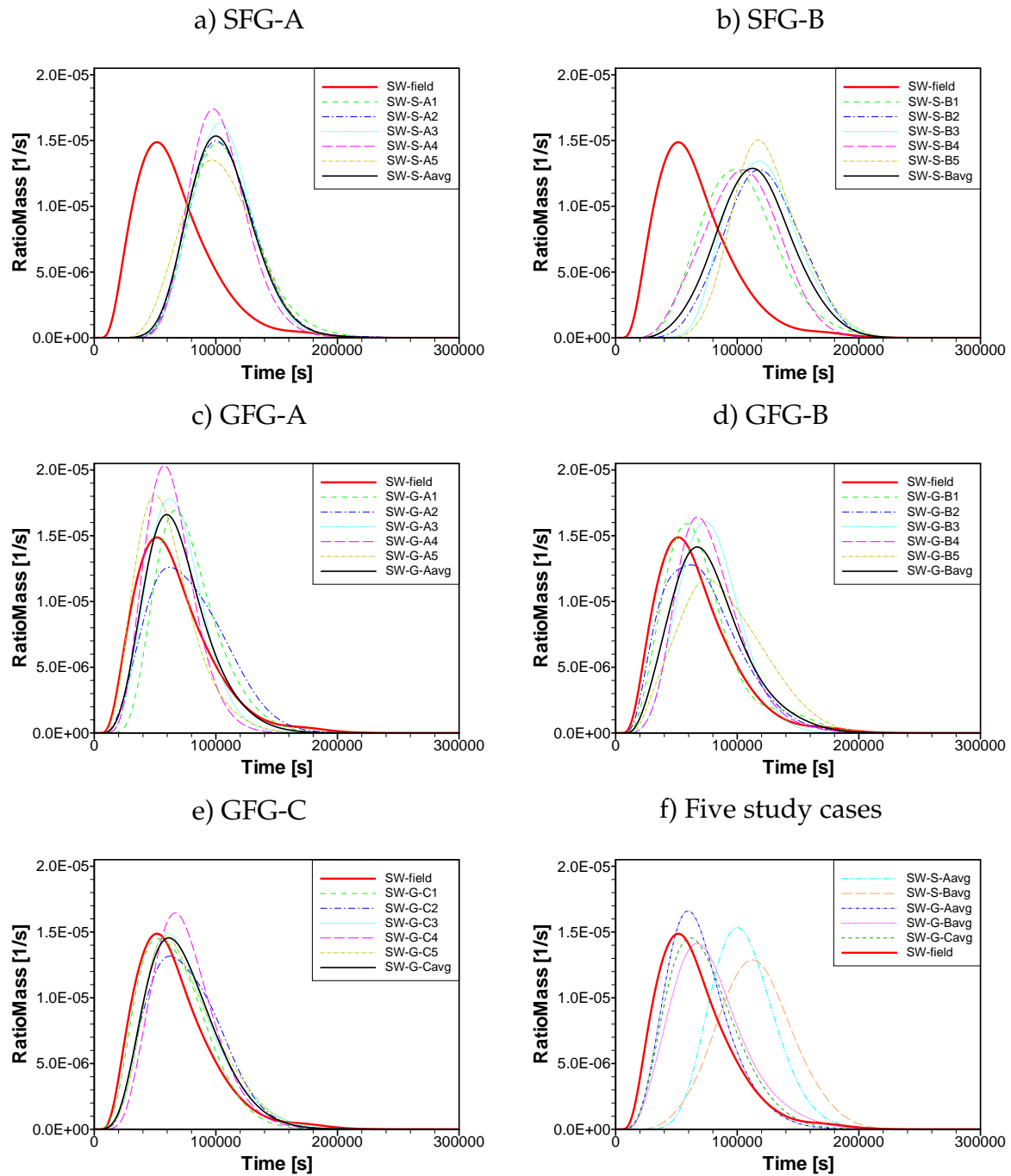


Figure 6.21: Comparison of breakthrough curves of the south-west walls from twenty-five realizations of five study cases.

all realizations (see Figures 6.20a, 6.20c and 6.20d). The smaller flux in SFG-A and SFG-B leads to a clear delay of the tracer transport in the fracture-matrix system, noticeable from the larger values of \bar{t} and t_p in Table 6.4 and the shifting of the BTCs and the AccBTCs in Figures 6.21 and 6.22 respectively. Connected flow paths of

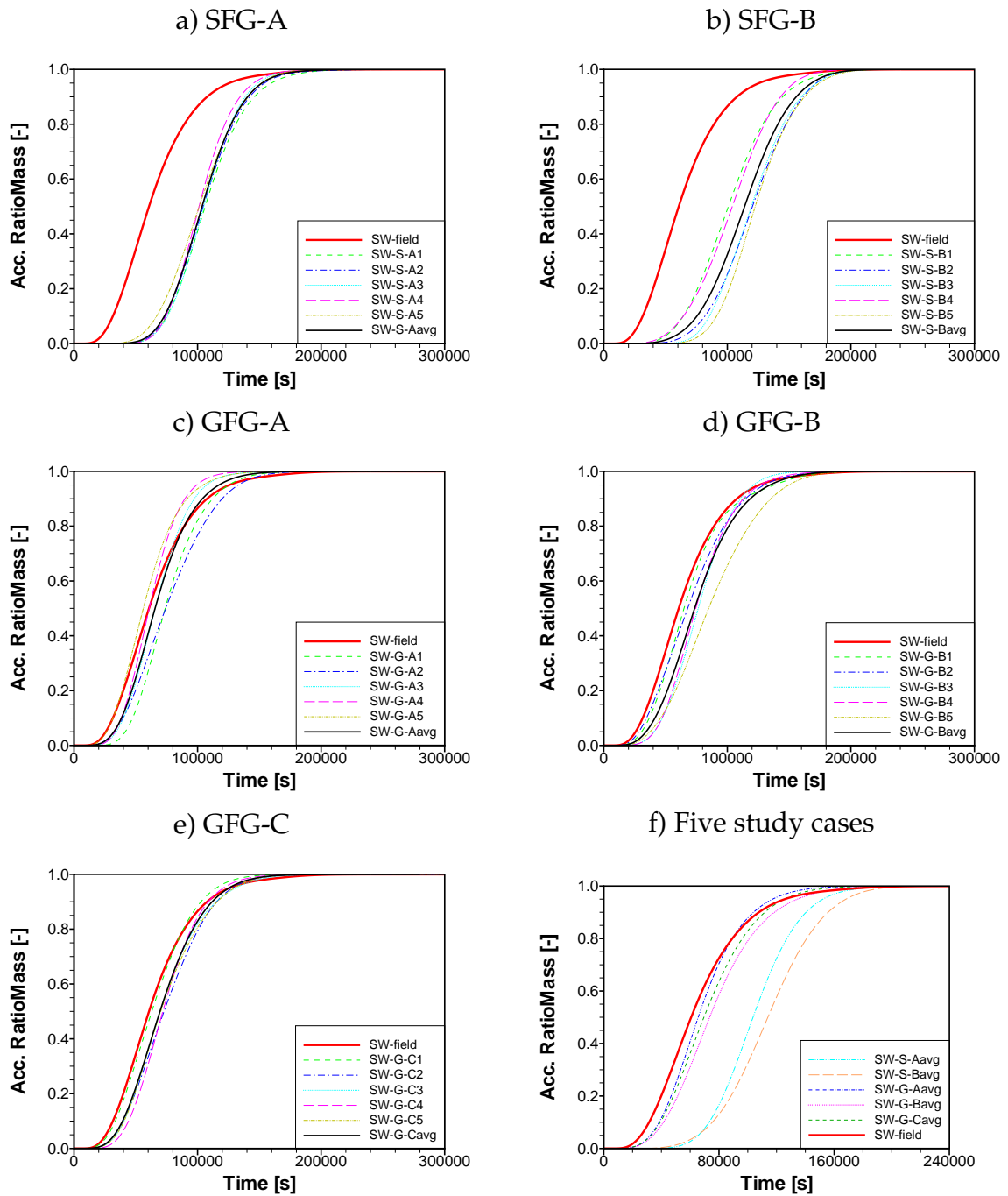


Figure 6.22: Comparison of accumulated breakthrough curves of the south-west walls from twenty-five realizations of five study cases.

fractures as observed from the scanned wall can be represented by the GFG because the spatial characteristics of a fracture network are considered. Therefore, the values of Q , \bar{t} and t_p from the three cases of the GFG are close to the scanned wall. However, when only the space distribution of fractures as spatial information in the SFG are

taken into account, connected flow paths of fractures cannot be reproduced.

Fast transport in connected fractures and a slow transport in the matrix can be noticed qualitatively from an asymmetry of a BTC with a long tail on the right side and quantitatively from a positive skewness γ of a BTC. A zero skewness means a symmetric distribution and a positive skewness indicates a long-tail behavior. As can be seen from Table 6.4 and Figure 6.21, this transport behavior is observed in the scanned south-west wall and the three cases of GFG, but not in the two cases of SFG. The BTCs from SFG are likely to be symmetric with a small skewness which means that fracture-matrix systems of SFG behave more like a single continuum. This is because connected and dominated flow paths cannot be reproduced in SFG. The results from SFG could lead to a misinterpretation of a system behavior as a single continuum.

The average values of the peak mass flux \dot{m}_p of GFG-B and GFG-C are closer to the scanned wall than SFG-A and SFG-B. However, the average \dot{m}_p of GFG-A shows the largest deviation from the scanned wall as well as the largest range of the extreme values (min. and max.) compared with the another four cases (see Figure 6.20). Its largest deviation could be because the average \dot{m}_p is evaluated from a too small number of realizations for this case where a large difference between extreme values is shown. In order to achieve a better average \dot{m}_p , more realizations are required. A large range of the extreme values is also observed for the variance σ^2 of GFG-A and GFG-B, which means more realizations are necessary to obtain a better average variance.

Conclusion: flow and transport behavior of a fracture-matrix system

For all five study cases, their flow and transport behavior characterized in terms of the average values of the total flux Q , the peak mass flux \dot{m}_p , the peak arrival time t_p , the effective travel time \bar{t} , the variance σ^2 and the skewness γ are compared with the values from the scanned south-west wall. The Q , t_p and \bar{t} obtained from the three cases of GFG are clearly closer to the field block than the two cases of SFG. This means that connected flow paths, which influence the bulk behavior of the fluid movement, can be represented in GFG, where the spatial characteristics are considered, but not in SFG. The distribution of the tracer plume is also effected by the preferential flow paths. Fast transport in connected paths and slow transport in the matrix result in a double-continuum behavior which can be observed from breakthrough curves with a long tail. This transport behavior is reproduced better by GFG than SFG. The variables which show a large range of extreme values (min. and max.), such as the peak mass flux \dot{m}_p and the variance σ^2 , require more realizations in order to obtain the acceptable average values of each study case.

The fracture networks generated by the geostatistical fracture generation obviously capture the flow and transport behavior of the fracture-matrix system better than those generated by statistical fracture generation. Integrating the spatial characteristics and the statistical geometries in GFG means that interconnected flow paths influencing flow and transport processes in fractured systems can be represented. None of the fracture networks from the three cases of GFG obviously captures the behavior of the field block better than another. This might be because the behavior of the fracture-matrix system is strongly influenced by the spatial characteristics rather than the fracture size, which is the difference between these three cases.

7 Comparison of Streamline Simulation and Advective-Diffusive Transport

A numerical study using a discrete fracture-matrix model for advective-dispersive transport (ADT) involves a high computational demand because several realizations of fracture networks are required to characterize the average behavior of a fracture-matrix system and, for each realization, a small grid size is necessary to overcome the numerical diffusion problem (see Section 6.3.3). Therefore, a streamline method for solving transport in a fracture-matrix system is considered since it requires much less computation time compared with ADT and shows no numerical diffusion. Classical streamline tracing (STR) accounts for the advective transport and neglects the dispersive transport. The comparison between ADT and STR is discussed in this chapter, with the aim of identifying the difference between the two approaches and the possibility of using STR in complex fracture-matrix systems instead of ADT. First, a comparison study is carried out for preliminary test cases in order to gain basic knowledge about the characteristics of STR compared with ADT. Then, STR is performed on the fracture-matrix systems of the five study cases generated in Section 6.1 and the results are compared with the results obtained from ADT shown in Section 6.3.4.

7.1 Mass Transport in Streamlines

After obtaining the velocity field from the flow simulation with the Box method, the flux recovery, which is a pre-process of streamline tracing, is carried out (see Section 5.4). Then streamlines are traced using the modified Pollock's method (see Section 5.3). In this study, a flow channel of each streamline is visualized as a streamtube. Each streamtube contains the same flux because streamlines are distributed equally according to the total flux along the inflow boundary. By definition, streamlines are lines that are tangential to the instantaneous velocity direction, and the velocity at any point has a single value; therefore, streamlines cannot cross. The mass transport in each streamtube is assumed to be only advective transport with no mass exchange between neighboring streamtubes (see Figure 7.1).

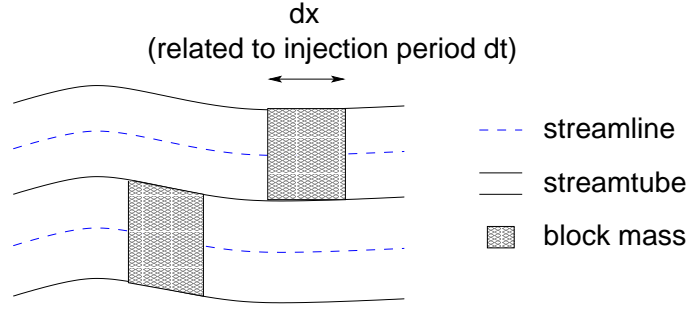


Figure 7.1: Mass transport in a streamtube as a block.

The transport behavior characterized from the results of the streamline tracing is described using the accumulated breakthrough curve $AccBTC$ and the breakthrough curve BTC . The accumulated breakthrough curve is the sum of the total mass leaving the domain at the outflow boundary until the time t and the breakthrough curve is the rate of change of the accumulated breakthrough curve during the time interval Δt :

$$BTC(t) = \frac{AccBTC(t) - AccBTC(t - \Delta t)}{\Delta t}, \quad (7.1)$$

$$AccBTC(t) = \sum_{i=1}^n \dot{m}_i^s \mathcal{T}_i, \quad (7.2)$$

where \dot{m}_i^s is the mass flux in the streamtube i , n is the total number of the streamtubes. The mass arrival time \mathcal{T}_i of the streamtube i is described as

$$\mathcal{T}_i = \begin{cases} 0 & ; t < TOF_i \\ t - TOF_i & ; TOF_i \leq t \leq TOF_i + dt \\ 0 & ; t > TOF_i + dt \end{cases} \quad (7.3)$$

where the time of flight TOF_i is the time that a block mass in a streamtube i travels until it reaches the outflow boundary and dt is the duration of mass injection.

The TOF of each streamtube is a discrete value, which can be the same for all streamtubes or highly varied depending on the geometries and structures of a domain. If equally distributed streamlines according to flux and no dispersion within and between streamtubes are assumed, the same mass is transported in each streamtube. The block mass arrives at the outflow boundary at a TOF and lasts for an injection period dt . A breakthrough curve evaluated exactly from the TOF is shown in Figure 7.2a. A short injection period dt leads to an exact BTC which is visualized as a discrete line of a mass flux at each point in time. Hence, the overall transport behavior of a system can hardly be interpreted from the exact BTC. For this reason, a histogram BTC is used to present the transport behavior. The histogram BTC evaluates a ratio mass flux over a specified interval of time rather than over the injection

period dt . The example of the exact BTC and the histogram BTC compared with the BTC from the ADT are shown in Figure 7.2.

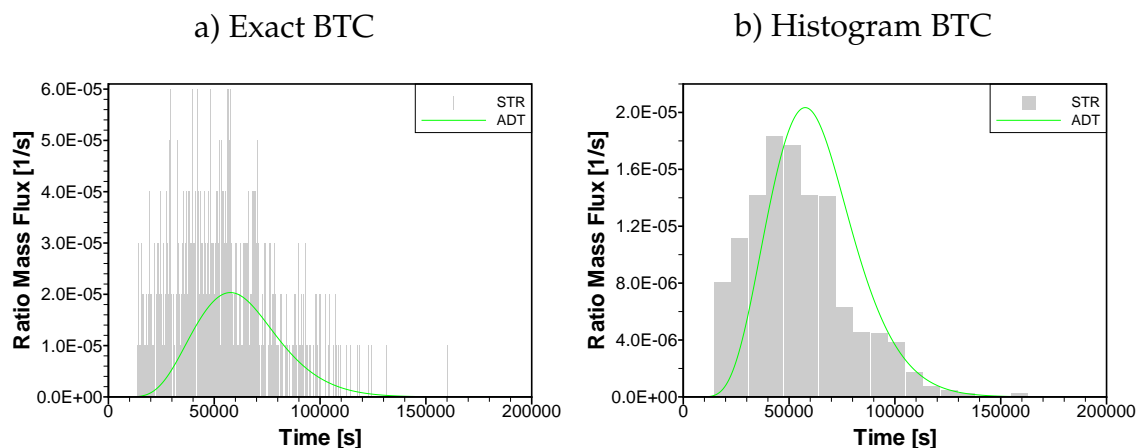


Figure 7.2: Breakthrough curve from STR and ADT.

7.2 Comparison Study in Preliminary Test Cases

In order to understand the difference arising from solving the transport process using ADT and STR, preliminary test cases are set up which consider a wide range of domain characteristics: Group A contains homogeneous and heterogeneous porous media, Group B concerns a single fracture in a porous matrix, and Group C focuses on systematically distributed fractures in a porous matrix. The qualitative comparison between ADT and STR is carried out by considering the breakthrough curve (BTC) and the accumulated breakthrough curve (AccBTC). For all test cases, a two-dimensional domain of $1.0 \text{ m} \times 1.0 \text{ m}$ is set up. The boundary conditions, the fluid properties and the domain properties correspond to the data presented in Section 6.3.1. The influence of numerical diffusion is observed by solving the ADT and the STR on different mesh sizes of approximately 0.01, 0.02 and 0.03 m.

7.2.1 Group A: Homogeneous and heterogeneous domains

The first group considers a homogeneous domain and a heterogeneous domain with a highly permeable lense of $0.60 \text{ m} \times 0.20 \text{ m}$ as shown in Figure 7.3. The inner boundary where tracer is defined at a distance of 0.03 m from the inflow boundary for both the homogeneous and the heterogeneous cases. The flow and transport simulations for both cases are performed on the same unstructured mesh. Figure 7.4 shows the discretized domain of the three different mesh sizes. The permeability of

the lense is equal to the surrounding material for the homogeneous case ($K_1 = K_2 = 1.0 \cdot 10^{-13} \text{ m}^2$) and four times higher than the matrix for the heterogeneous case ($K_1 = 4.0 \cdot 10^{-13} \text{ m}^2$ and $K_2 = 1.0 \cdot 10^{-13} \text{ m}^2$).

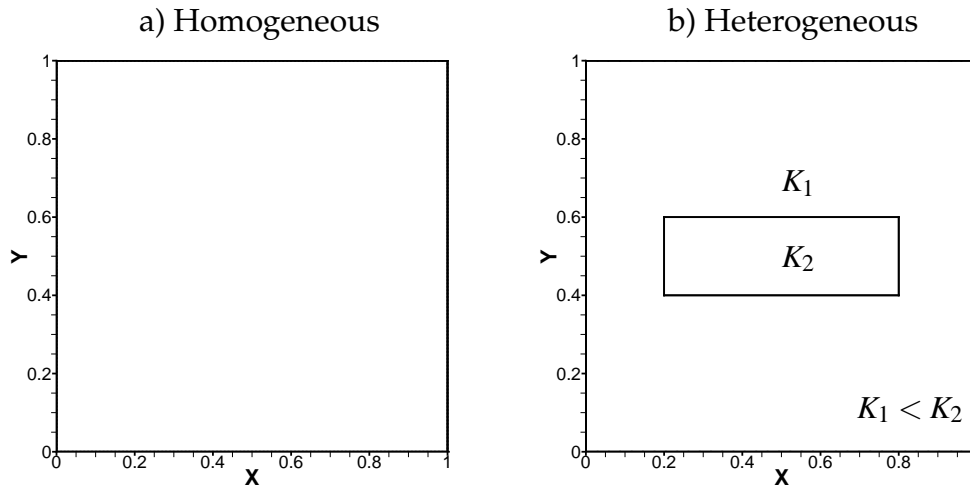


Figure 7.3: A domain of two cases of Group A.

The transport simulation using STR and ADT are performed for the homogeneous and the heterogeneous cases with different mesh sizes. The results of the accumulated breakthrough curves (AccBTCs) and the breakthrough curves (BTCs) are presented in Figure 7.5. As can be seen from the AccBTCs in Figures 7.5a1 and 7.5b1, the initial tracer breakthrough time of the ADT for both study cases is less for the larger mesh size. The BTCs of the ADT in Figures 7.5a2 and 7.5b2 show that using the larger mesh size results in a lower peak value and a higher variance. This indicates that the numerical diffusion smears out the concentration front and increases a spreading of the tracer plume. Additionally in the heterogeneous case, the effect of high- and low-permeable zones that results in distinct double continua is reduced. On the other hand, the AccBTCs from the STR are similar for all discretizations of the two study cases and this verifies the fact that the STR induces no numerical diffusion. Mass transport in the streamtubes of the homogeneous case arrives at the outflow boundary at the same time (see Figure 7.5a3), which corresponds to a sudden increase of the accumulated mass from 0 to 1 (see Figure 7.5a1). In the heterogeneous case, fast tracer transport in the highly permeable lense causes a first peak in the BTC and a first rise in the AccBTC, and a large part of the remaining tracer arrives and results in a second jump in the AccBTC as can be seen in Figures 7.5a2 and 7.5c2. The finer the mesh, the closer the AccBTC of the ADT to the STR. This indicates that the numerical diffusion leads to a divergence of the results of the ADT from those of the STR.

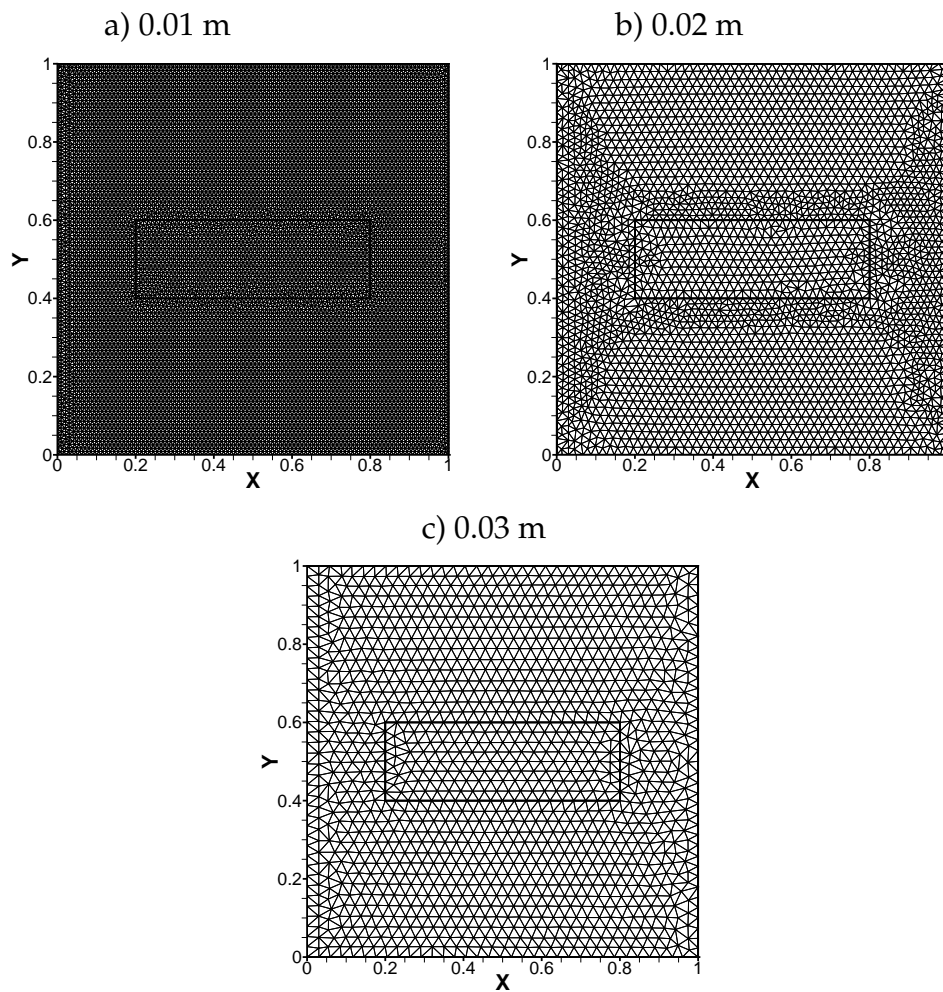
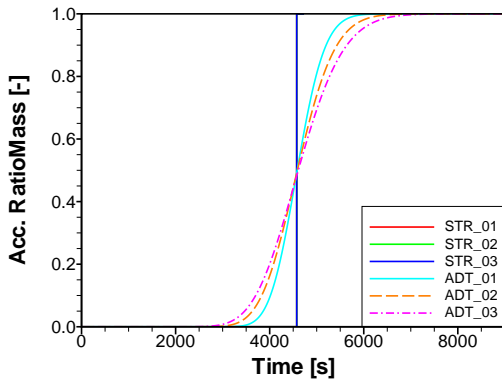


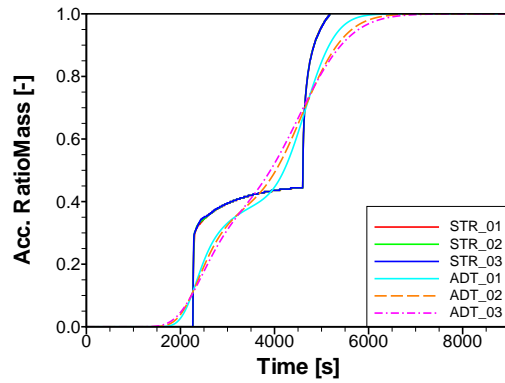
Figure 7.4: Discretized domain of different mesh sizes of homogeneous and heterogeneous domain.

Accumulated BTC of ADT and STR

a1)

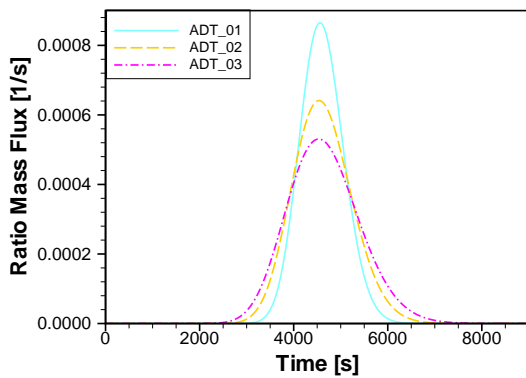


b1)

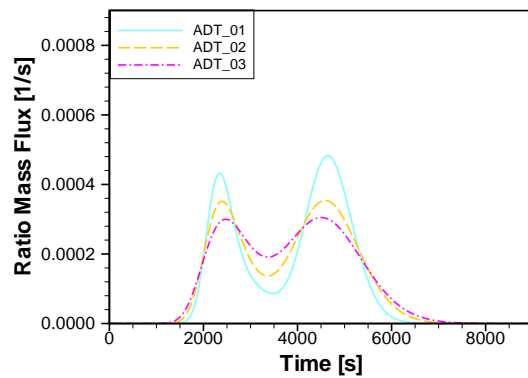


BTC of ADT for different mesh sizes

a2)

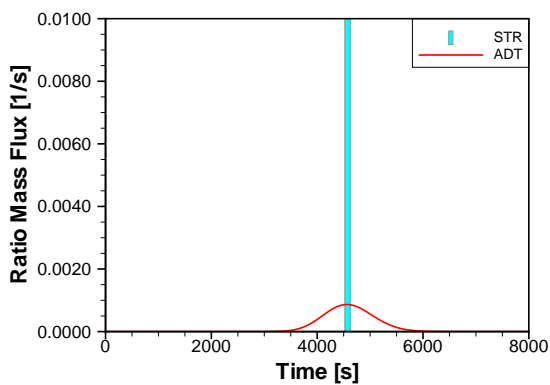


b2)



BTC of ADT and STR at a mesh size 0.01 m

a3)



b3)

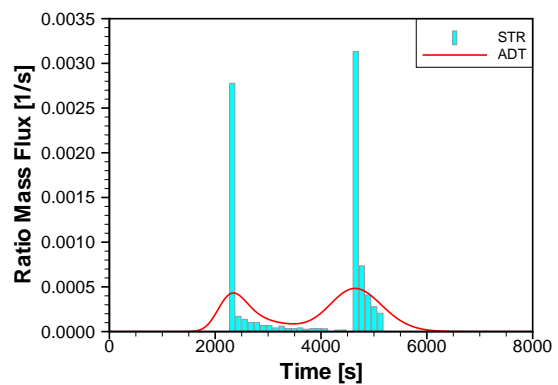


Figure 7.5: Numerical results of ADT and STR for two cases of Group A: a) homogeneous and b) heterogeneous.

7.2.2 Group B: Single fracture

Two different cases of a single fracture embedded in a homogeneous porous matrix are investigated: the case of a long fracture of 0.8 m and the case of a short fracture of 0.1 m (see Figure 7.6). The inner boundary is defined at a distance of 0.03 m from the inflow boundary for the two cases.

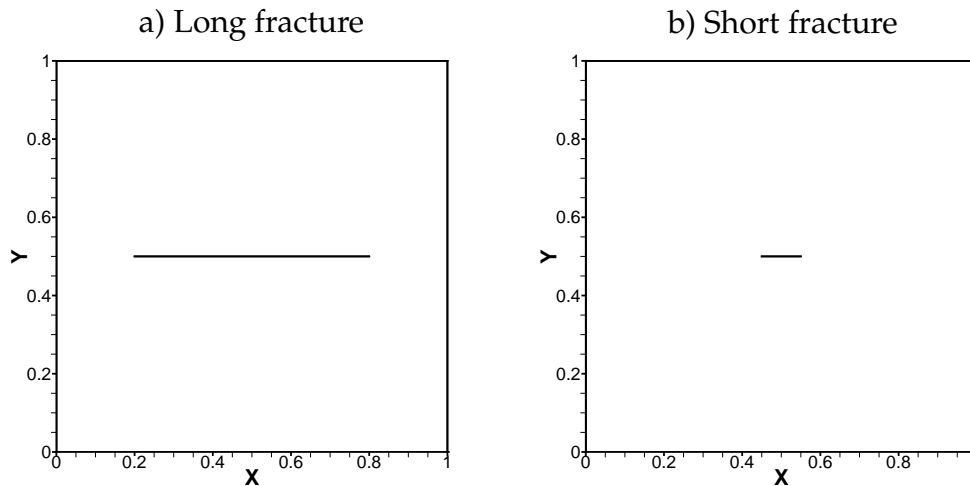


Figure 7.6: A domain of two cases of Group B.

The double-continuum behavior is clearly observed from the long-fracture case as in the heterogeneous case of Group A. In this case, fast transport in a long fracture results in the first peak of the BTCs; later, a part of the tracer plume transported in the matrix leads to the second peak (see Figure 7.7a2). The influence of the numerical diffusion of the ADT on a part of tracer transported in the long fracture results in a slightly lower first peak and a slightly longer arrival time of the first peak, and the influence on a part of the tracer transported through the porous matrix shows the same behavior as that observed in Group A. In the STR, where no numerical diffusion occurs, a tracer transported in a fracture remains at a high concentration and arrives at the outflow boundary shortly after the tracer plume observed from the ADT (see Figure 7.7a3). The numerical diffusion in the flow direction induces the spreading of the plume. Therefore, the results from the ADT show a lower initial breakthrough time and lower peak mass flux than those from the STR. In the short-fracture case, the numerical diffusion in the ADT dominates an effect of fast transport in a fracture as the BTCs only show a single-continuum behavior (see Figure 7.7b2). On the other hand, in the STR, the double-continuum effect is still observed from the two jumps of the AccBTCs and the two peaks of the BTCs (see Figures 7.7b1 and 7.7b3). Slightly different values of the AccBTCs of the STR at the first sudden rise can be seen in Figures 7.7a1 and 7.7b1. This is due to the fact that a velocity field obtained from a flow simulation is locally grid dependent (near a fracture).

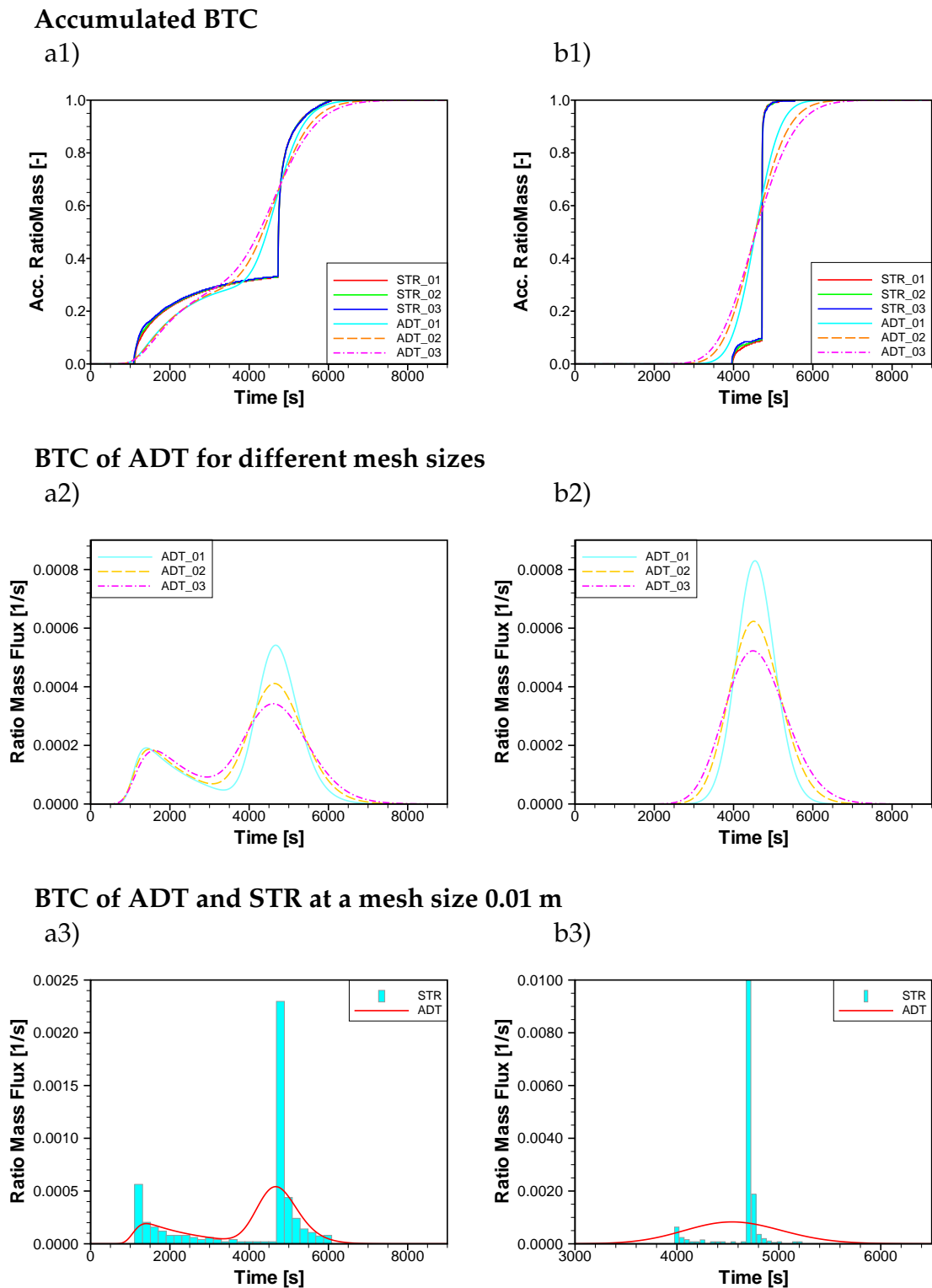


Figure 7.7: Numerical results of ADT and STR for two cases of Group B: a) long fracture and b) short fracture.

7.2.3 Group C: Systematically distributed fractures

In Group C, the influence of long and crossing fractures on the transport behavior are further studied by using systematically distributed fractures (see Figure 7.8). The horizontal fractures in both cases are 0.9 m long and parallel to the x-axis. A vertical fracture connecting all the horizontal fractures deviates slightly from the y-axis (by approx. 1.5°). The inner boundary in this case is shifted to a distance 0.01 m from the inflow boundary to avoid the strong influence of fractures on the injected tracer.

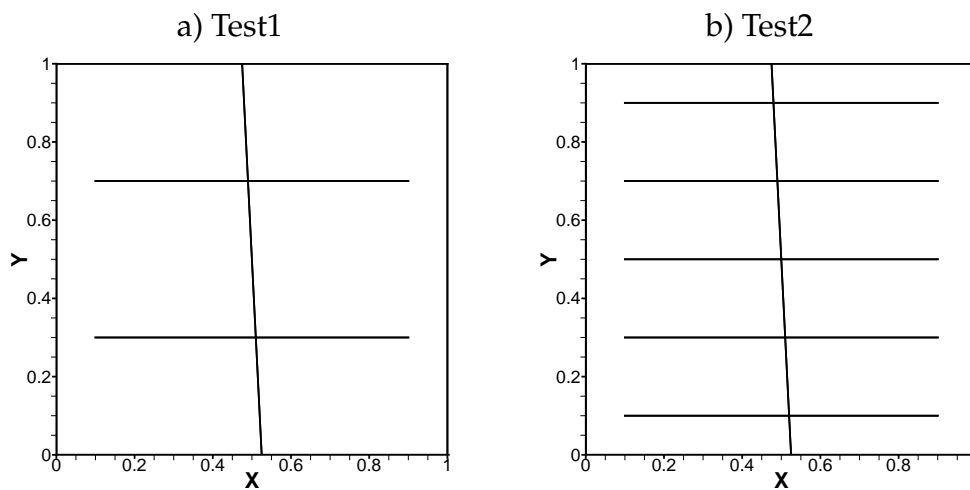
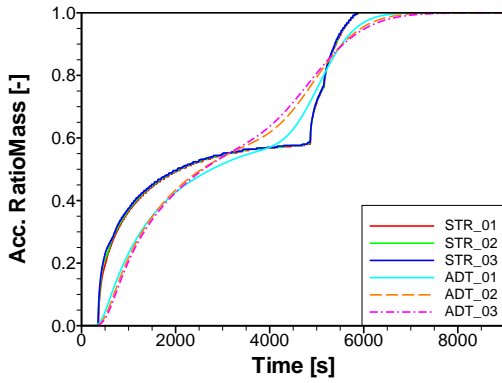


Figure 7.8: A domain of two cases of Group C.

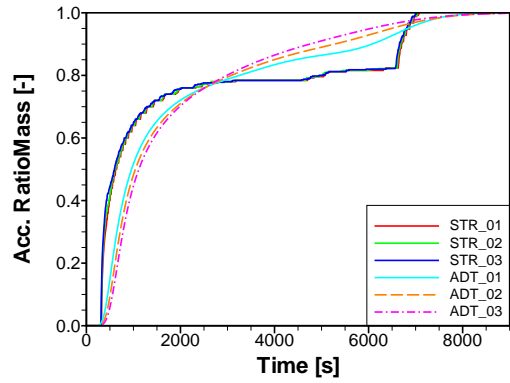
The double-peak BTCs indicating double-continuum behavior are clearly observed from the BTCs of the ADT and the STR of test1 (see Figures 7.7a2 and 7.7a3). Additionally, the same influence of the numerical diffusion as in the long fracture of Group-B is observed in test1. Increasing the number of horizontal fractures in test2 leads to an increase of the tracer transported in the fractures and a decrease of the tracer transported in the matrix. Therefore, the BTCs of the ADT from test2 show a high peak with a long-tail instead of a clear double-peak as from test1 (see Figure 7.7b2). Due to the influence of the numerical diffusion in the ADT in test2, the BTCs of the large mesh size of 0.03 and 0.02 m show only a long tail, whereas a BTC of the small mesh size of 0.01 m presents a small second peak, corresponding to the BTC of the STR (see Figure 7.7b3).

Accumulated BTC

a1)

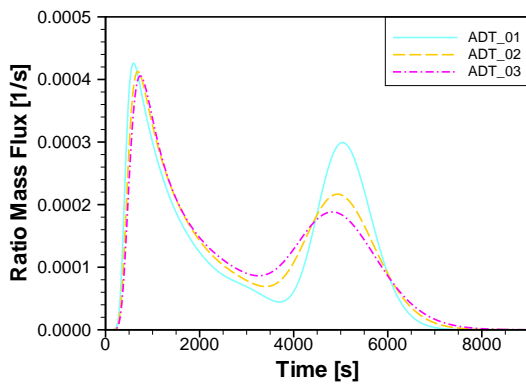


b1)

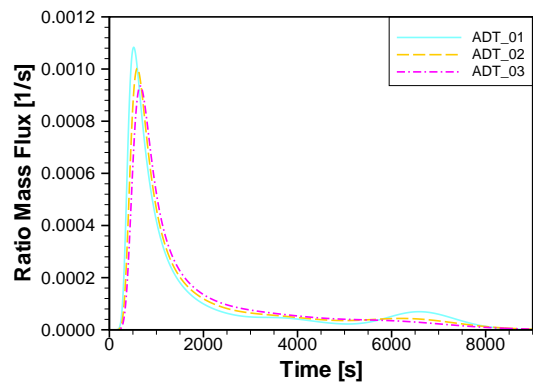


BTC of ADT for different mesh sizes

a2)

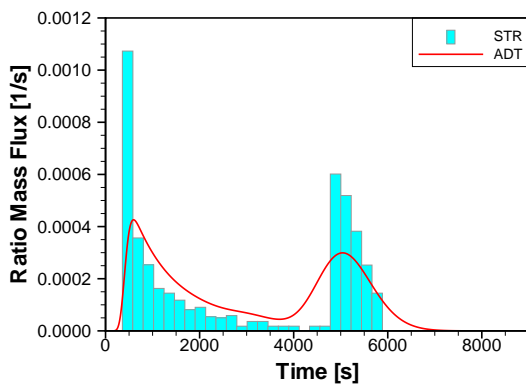


b2)



BTC of ADT and STR at a mesh size 0.01 m

a3)



b3)

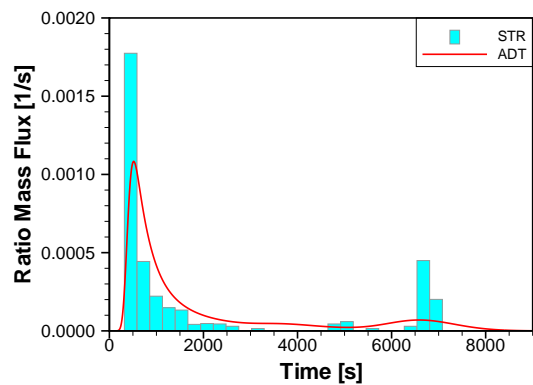


Figure 7.9: Numerical results of ADT and STR for two cases of Group C: a) test1 and b) test2.

7.3 Comparison Study in Complex Fracture Networks

After a basic understanding of the transport behavior using ADT and STR has been gained from the preliminary case study, the next step is to perform a comparison study between the two approaches in a complex fracture-matrix system. The domains obtained from the five study cases presented in Chapter 6, where the fracture networks are generated by geostatistical and statistical fracture generation, are investigated in this section. The boundary conditions, the fluid properties, and the domain properties described in Section 6.3.1 are applied for the numerical simulation of STR in this section. The flow and the STR transport simulation are performed on the discretization mesh of 0.02 m used in Section 6.3.4. The results of STR in terms of the BTCs and the AccBTCs are compared with the data from ADT presented in Section 6.3.4.

The average of the AccBTCs and the BTCs from the STR and the ADT of five realizations from each study case are shown in Figures 7.10 and 7.11 respectively. For all five study cases, the average AccBTCs from the STR shift to the left compared with the ADT which means that mass is transported faster in the cases from STR than from ADT. This corresponds to the average values of the effective travel time and the initial breakthrough time from the STR which are less than the values from the ADT presented in Figures 7.12a and 7.12b. This difference between STR and ADT can also be observed in Group C (systematically distributed fractures) in the preliminary test cases. However, a clear distinction between fast and slow transport resulting in two sudden rises in the AccBTCs of the STR shown in Group C is not noticed in the complex fracture-matrix systems. Increasing the number of fractures and varying their orientation lead to a high dispersion of tracer plume in the fracture-matrix system and no clearly separated fast and slow transport. Physical dispersion due to fast and slow transport can be identified from a slightly long-tail BTC of the STR and ADT in Figure 7.11 and from the result of the skewness from each realization in Figure 7.12d. Due to the purely advective transport and no numerical diffusion in the STR, its results for the skewness from the STR show larger values than the ADT, indicating a larger physical dispersion. On the other hand, the numerical diffusion in the ADT delays plume migration in the fracture-matrix system. As a result, the difference between AccBTCs and BTCs from the two approaches is clearly noticed in all study cases of the fracture-matrix system. Further investigations have to be carried out involving comparison with experimental or field studies to verify the results from the ADT and the STR.

Most of the values obtained from STR show a larger range of the extreme values (min. and max.) than ADT, particularly for the initial breakthrough time and the variance of the SFG-B. Hence, more realizations might be required to represent the transport behavior using STR.

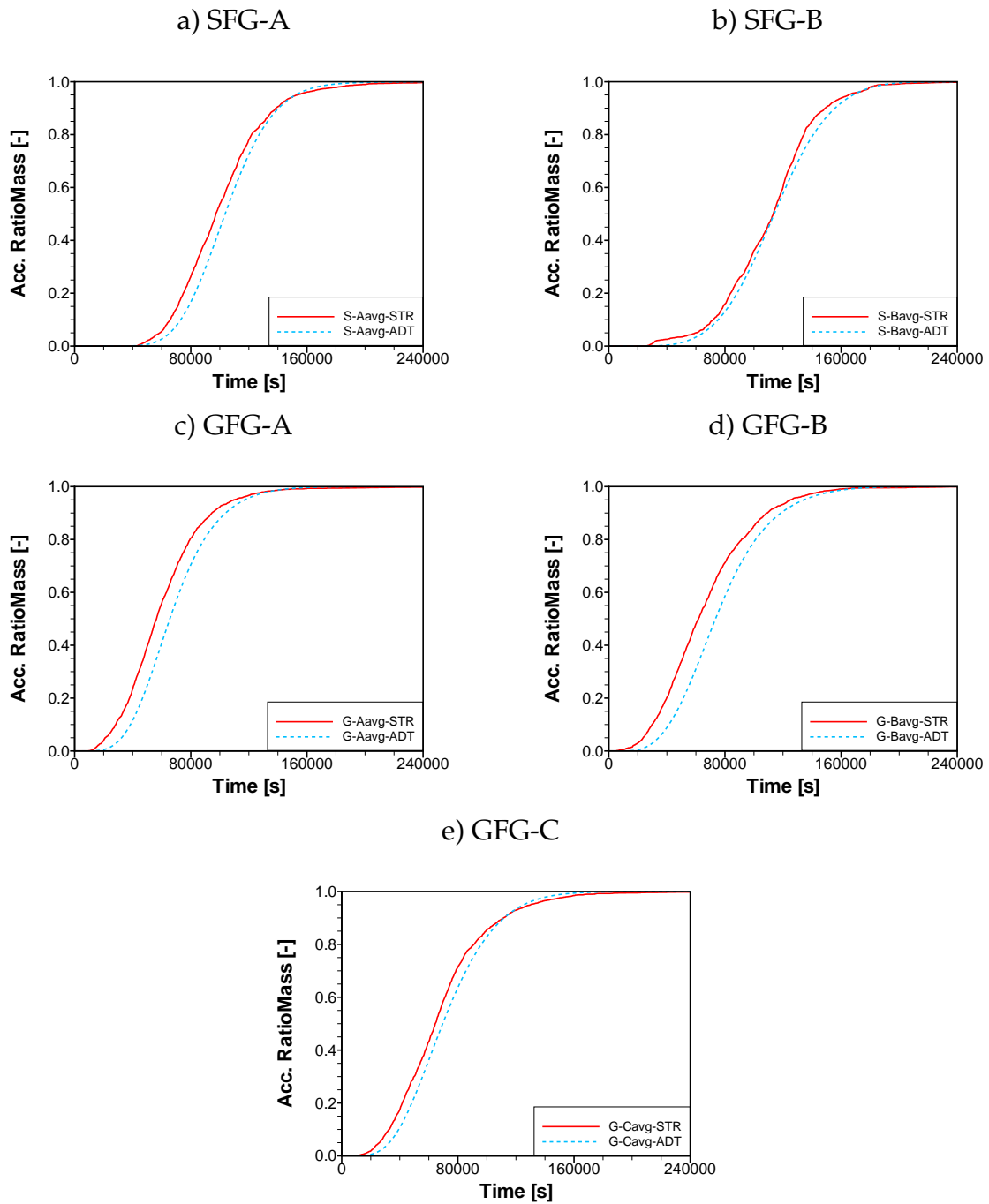


Figure 7.10: Comparison of average accumulated breakthrough curves of the southwest walls of five study cases.

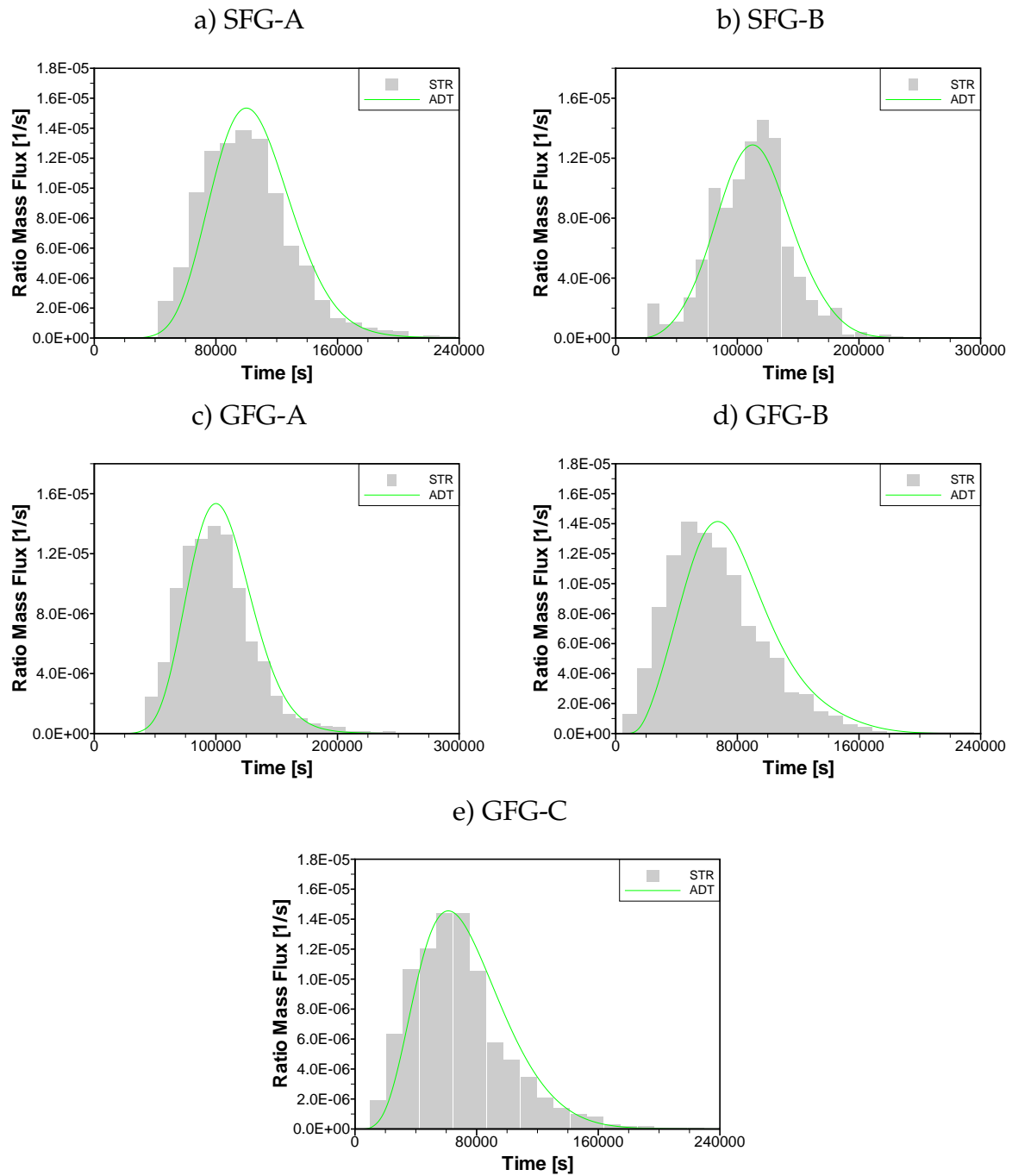


Figure 7.11: Comparison of average breakthrough curves of the south-west walls of five study cases.

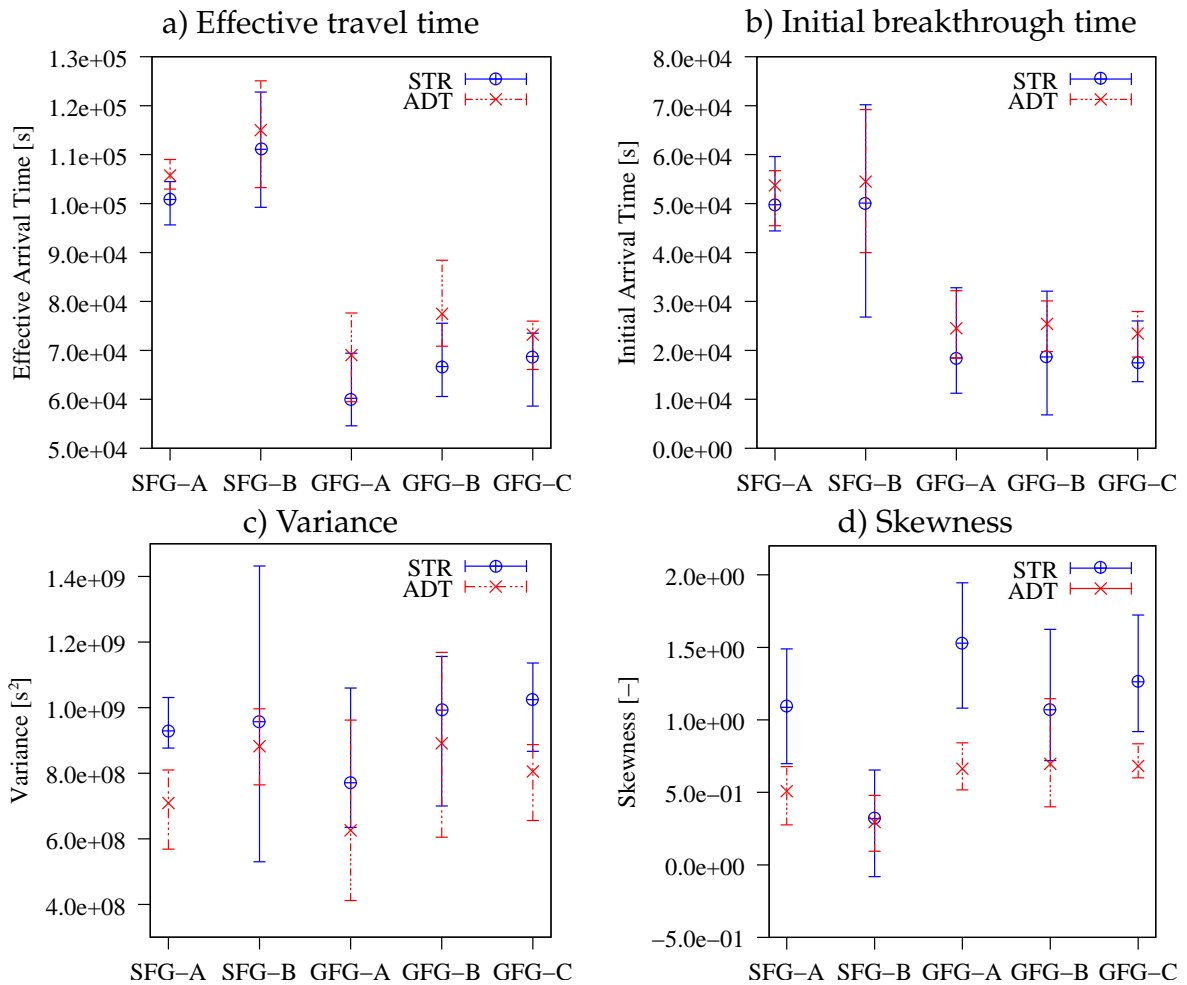


Figure 7.12: Average and extreme values (min./max.) obtained from the streamline tracing and the advective-dispersive transport of the south-west wall of five study cases.

8 Conclusion and Outlook

For many countries worldwide, fractured rock systems have provided important natural resources such as petroleum, gas, water and geothermal energy. During the last decades, the investigation for suitability of fractured systems as storage/disposal sites for high-level nuclear waste has been carried out. The resource exploitation and potential utilization have led to extensive studies with the aim of understanding, characterizing and ultimately predicting the behavior of fractured systems. Aquifer analogue studies have been widely used to characterize fractured aquifer systems. In the analogue studies, a detailed analysis of fractured systems such as borehole samplings, hydraulic measurements or exposed-wall investigations can be performed practically, and the flow and transport properties obtained on the analogue scale can be upscaled to the large field scale (Dietrich et al. [2005]).

On an analogue scale, a numerical study of a fractured rock system using a discrete fracture model is an attractive alternative to a continuum model since there is no a priori assumption of the fractured system as a Representative Elementary Volume (REV) and the effect of individual fractures can be explicitly investigated. Additionally, the increasing speed of computers nowadays makes even high computational demand, which is the main drawback of the discrete approach, feasible on this scale. The critical step for the discrete model approach is the generation of a “representative” fracture network (National Research Council [1996]). A fracture generator based on observed fracture geometries can be categorized as: deterministic fracture generation (DFG) and statistical fracture generation (SFG). The fracture geometries (e.g. size, aperture, orientation and location) are determined exactly for individual fractures in DFG, whereas they are defined by statistical distribution functions in SFG. Due to intensive data requirements in DFG, SFG is generally more practical. In the case where dominating fractures are known, a combination of SFG with DFG is required. However, SFG often fails to capture spatial variability and connectivity of the fracture networks, which is related to interconnected flow paths that may dominate flow and transport processes in fractured systems (Berkowitz [2002]).

This study aims to improve fracture generation by integrating the statistical geometries as well as the spatial variability. In addition to this, streamline tracing as an alternative to advective-dispersive transport for the study of a transport process in a fracture-matrix system is introduced. Basic knowledge on fracture geometries observed in nature and the different conceptual models used to study flow and trans-

port processes in a fractured system are presented in Chapter 2. In the following chapter, the application of statistics and geostatistics to describe the fracture geometries is reviewed. This information is required for generating a fracture network which has to be defined explicitly in a discrete model approach. Chapter 4 introduces the geostatistical fracture generation developed in this work by including statistical geometries and spatial characteristics. Next, the governing equations for flow and advective-dispersive transport processes in a fracture-matrix system are explained and discretized, and additionally equations describing streamline tracing in the system are presented in Chapter 5. The comparison of geostatistical fracture generation with statistical fracture generation is discussed by focusing on the flow and transport behavior of the fracture-matrix system in Chapter 6. The simulation results obtained from the transport model are compared with the results from the streamline tracing model in Chapter 7.

In the following, the main issues concerning geostatistical fracture generation (GFG) and the major results gained from streamline tracing (STR) in fracture-matrix systems are summarized.

Geostatistical generation of a fracture network: The geostatistical fracture generation based on spatial characteristics and statistical geometries of a fracture network is developed.

- The spatial characteristics of a fracture network (such as the standardized experimental variogram, the neighborhoods, the fracture-cell density and the variance) are analyzed from indicator fields, which are transformed from fracture trace maps by applying the modified scanline technique. The fracture trace maps are recorded from the surface of exposed walls by performing stereophotogrammetric shooting.
- The analysis of the spatial characteristics is carried out for the study object, the Pliezhausen block. For all five exposed walls of the field block, fairly similar spatial characteristics are identified for both vertical and horizontal fractures.
- In order to assess the spatial characteristics, the generation of indicator fields is conducted. As a result, the randomly distributed fracture cells in an initial indicator field are finally rearranged successively in the direction of the fracture traces, which is observed from the target indicator field.
- The generation of a three-dimensional fracture network using geostatistical fracture generation considering statistical geometries and spatial characteristics is presented. The initial state of a fracture network is generated by SFG based on the statistical geometries and later a global optimization Simulated Annealing (SA), which includes the spatial characteristics in the objective function, is carried out. For cases in which the reliable fracture size could not be obtained, geostatistical fracture generation is still able to generate a fracture

network by neglecting the explicitly defined fracture size and approximating it from the available fracture traces on the exposed walls.

Comparison of geostatistical and statistical fracture generation: The comparative study focuses on two different aspects: the structural characteristics of fracture networks and the flow and transport behavior of fracture-matrix systems. Based on the data obtained from the Pliezhausen block, a total of five different study cases including two from statistical fracture generation (SFG) and three from geostatistical fracture generation (GFG) are investigated. For each study case, five realizations are generated and the average results are evaluated by averaging over the five exposed walls of the fracture-matrix system of each realization and again over all five realizations.

- The fracture networks generated by GFG not only reproduce the spatial characteristics considered in the approach but also, to some extent, describe the fracture-distance distribution of the field which is not a priori assigned. On the other hand, the fracture networks created by SFG show the fracture-distance distribution, which is optimized in the generation scheme, close to the field data and reasonably good results for the neighborhoods, but not for the standardized variogram and the fracture-cell density.
- The strong influence of spatial characteristics is clearly noticed from the results of the two-dimensional flow and transport simulations in the south-west cross-section in terms of total flux and characteristics of the breakthrough curves. The study cases from GFG obviously capture the system behavior such as discharge, peak arrival time and mean effective time better than the study cases from SFG. By integrating spatial characteristics, spatial connectivity resulting in the preferential flow paths can be captured, and the behavior of the fractured system can thus be better represented. Considering only the fracture distance as a spatial structure in the SFG is not sufficient in this case to generate a “representative” fracture network.
- None of the fracture networks from the three GFG cases represents the behavior of the field block obviously better than the others. This might be because the behavior of the fracture-matrix system is strongly influenced by spatial characteristics rather than fracture size, which is the difference between these three cases.
- Convergence analysis with different mesh sizes of the fracture-matrix system shows that the effect of grid size on total flux, effective travel time and peak arrival time is relatively small compared with its effect on peak mass flux and variance. This is due to the fact that the parameters reflecting the bulk movement of the fluid in the fracture-matrix system such as total flux, effective travel time and peak arrival time are not strongly grid-dependent, whereas

peak mass flux and variance, which are highly depending on how the concentration distributes in the fracture-matrix system, relate closely to the grid size. By decreasing the grid size, which means less numerical diffusion, the effect of fast flow in fractures and slow flow in matrix arising from the large permeability difference between fractures and matrix can be more accurately represented. This can be clearly noticed from increasing variance and decreasing peak mass flux in the breakthrough curve of a small grid size.

Comparison of advective-dispersive transport (ADT) with streamline tracing (STR): The main advantages of streamline tracing are its fast computation time and no numerical diffusion; however, only advective transport is considered in this approach. The applicability of STR is investigated by comparing the results in terms of breakthrough curves (BTCs) and accumulated breakthrough curves (AccBTCs) with ADT qualitatively.

- In the preliminary test cases considering homogeneous and heterogeneous porous media, and a single fracture and systematically distributed fractures in a porous matrix, the effect of fast flow in fractures and slow flow in matrix is smeared out due to the numerical diffusion in the ADT. On the contrary, the preferential flow paths in the fracture-matrix system are obviously noticed in the STR from the double-peak BTCs and two sudden rises in the AccBTCs.
- In the complex fracture-matrix system of the five study cases, numerical diffusion in ADT delays plume migration, whereas purely advective transport in STR leads to fast solute transport. As a result, the difference between the AccBTCs and the BTCs from the two approaches are clearly distinguished in all study cases of the fracture-matrix system. Further investigations involving comparisons with experimental or field studies have to be carried out in order to validate the results of the two approaches.

A generated fracture network obtained from geostatistical fracture generation represents the spatial characteristics and the geometries of the fracture network of a field site; therefore, the flow and transport behavior of the fracture-matrix system can also be captured. Streamline tracing in a fracture-matrix system as introduced in this study is an attractive alternative to advective-dispersive transport since its small computational demand makes the numerical simulation of a transport process in several realizations and on a larger scale feasible. However, further studies in this field are required to answer several open questions:

- Flow and transport behavior of the two-dimensional cross-section of a fracture-matrix system can be captured for the case in which a fracture network is generated by geostatistical fracture generation. The investigation of the flow and transport process has to be extended to a three-dimensional fracture-matrix system, since the connectivity of fractures is more complex and

considering this effect might require additional effort to improve the geostatistical fracture generation. Moreover, a numerical study of flow and transport processes in a three-dimensional fracture-matrix system requires a mesh generator which should be robust and efficient for discretizing many stochastically generated fractures embedded in a matrix.

- In this work, streamline tracing performs well whereas advective-dispersive transport suffers from numerical diffusion, which in some cases even dominates physical dispersion. Since the application of streamline tracing is appropriate for a highly advective-dominated problem, the distinctive applicable range of streamline tracing has to be defined by comparing the results from streamline tracing and from advective-dispersive transport in a fracture-matrix system with an experimental set-up. A ratio between advection and dispersion (Peclet number) could be used as an indicator.
- Geostatistical fracture generation has shown promising results on an analogue and its concept tends to be scale independent. The applicability of geostatistical fracture generation on a large scale should be further investigated.

Bibliography

- E. Aarts and J. Korst. *Simulated annealing and Boltzmann machines*. John Wiley & Sons, New York, 1989.
- H. Abelin, L. Birgersson, J. Gidlung, and I. Neretnieks. A large-scale flow and tracer experiment in granite: 1. Experimental design and flow distribution. *Water Resources Research*, 27(12):3107 – 3117, 1991.
- A. Al-Huthali and A. Datta-Gupta. Streamline simulation of counter-current imbibition in naturally actured reservoirs. *Journal of Petroleum Science and Engineering*, 43(3 - 4):271 – 300, 2004.
- E. Baafi and N. Schofield. Simulation of Naturally Fractured Fields. In A. Soares, A. Brusco, and C. Guimaraes, editors, *Geostatistics Wollongong '96 (Quantitative Geology and Geostatistics)*. Kluwer Academic Publishers, 1997.
- G. Baecher. Statistical analysis of rock mass fracturing. *Mathematical Geology*, 15(2): 329 – 348, 1983.
- A. Bárdossy. Generating precipitation time series using Simulated Annealing. *Water Resources Research*, 34:1737 – 1744, 1998.
- G. Barenblatt, I. Zheltov, and I. Kochina. Basic concepts in the theory of seepage of homogeneous liquids in fissured rocks [strata]. *Journal of Applied Mathematics and Mechanics (PMM)*, 24(5):1286 – 1303, 1960.
- P. Bastian, K. Birken, S. Lang, K. Eckstein, N. Neuss, H. Rentz-Reichert, and C. Wieners. UG - A Flexible Software Toolbox for solving partial differential equations. *Computing and Visualization in Science*, 1997.
- J. Bear. *Dynamics of Fluids in Porous Media*. Academic Press, San Diego, California, 1972.
- J. Bear. *Hydraulics of groundwater*. McGraw-Hill, New York, 1979.
- J. Bear. Modeling Flow and Contaminant Transport in Fractured Rocks. In J. Bear, C. Tsang, and G. Marsily, editors, *Flow and Contaminant Transport in Fractured Rocks*, San Diego, California, 1993. Academic Press.

- B. Berkowitz. Characterizing flow and transport in fractured geological media: A review. *Advances in Water Resources*, 25:861 – 884, 2002.
- B. Berkowitz, J. Bear, and C. Braester. Continuum Models for Contaminant Transport in Fractured Porous Formations. *Water Resources Research*, 24(8):1225 – 1236, 1988.
- R. Bibby. Mass Transport of Solutes in Dual-Porosity Media. *Water Resources Research*, 17:1075 – 1081, 1981.
- D. Billaux, J. Chiles, K. Hestira, and J. Longa. Three-dimensional statistical modelling of a fractured rock mass—an example from the Fanay-Augères mine. *International Journal of Rock Mechanics and Mining Science & Geomechanics Abstracts*, 26(3,4):281 – 299, 1989.
- G. Bodvarsson and Y. Tsang. Special issue: Yucca mountain project. *Journal of Contaminant Hydrology*, 38:1 – 425, 1999.
- G. Bodvarsson, C. Ho, and B. Robinson. Special issue: Yucca mountain project. *Journal of Contaminant Hydrology*, 62-63:1 – 750, 2003.
- I. Bogdanov, V. Mourzenko, J.-F. Thovert, and P. Adler. Effective permeability of fractured porous media in steady state flow. *Water Resources Research*, 39(1):13–1 – 13–16, 2003.
- E. Bonnet, O. Bour, N. Odling, P. Davy, I. Main, P. Cowie, and B. Berkowitz. Scaling of fracture systems in geological media. *Reviews of Geophysics*, 39(3):347 – 384, 2001.
- S. Brown, A. Caprihan, and R. Hardy. Experimental observation of fluid flow channels in a single fracture. *Journal of Geophysical Research*, 103(B3), 1998.
- M. Cacas, E. Ledoux, G. de Marsily, A. Barbreau, P. Calmels, B. Gaillard, and R. Margritta. Modeling Fracture Flow With a Stochastic Discrete Fracture Network: Calibration and Validation 2. The Transport Model. *Water Resources Research*, 26(3):491 – 500, 1990a.
- M. Cacas, E. Ledoux, G. de Marsily, B. Tillie, A. Barbreau, E. Durand, B. Feuga, and P. Peaudecerf. Modeling Fracture Flow With a Stochastic Discrete Fracture Network: Calibration and Validation 1. The Flow Model. *Water Resources Research*, 26(3):479 – 489, 1990b.
- J. Chilès and G. de Marsily. Stochastic models of fracture systems and their use in flow and transport modeling. In J. Bear, C.-F. Tsang, and G. de Marsily, editors, *Flow and Contaminant Transport in Fractured Rock*, San Diego, California, 1993. Academic Press.

- C. Cordes and W. Kinzelbach. Continuous Groundwater Velocity Fields and Path Lines in Linear, Bilinear, and Trilinear Finite Elements. *Water Resources Research*, 28(11):2903–2911, 1992.
- M. Crane and M. Blunt. Streamline-based simulation of solute transport. *Water Resources Research*, 35(10):3061 – 3078, 1999.
- D. Cruden. Describing the size of discontinuities. *International Journal of Rock Mechanics and Mining Science & Geomechanics Abstracts*, 14(3):133 – 137, 1977.
- F. Day-Lewis, P. Hsieh, and S. Gorelick. Identifying fracture-zone geometry using simulated annealing and hydraulic-connection data. *Water Resources Research*, 36(7):1707 – 1721, 2000.
- A. Desbarats and S. Bachu. Geostatistical analysis of aquifer heterogeneity from the core scale to the basin scale, A case study. *Water Resources Research*, 30(3):673 – 684, 1994.
- C. Deutsch and P. Cockerham. Practical considerations in the application of simulated annealing to stochastic simulation. *Mathematical Geology*, 26(1):67 – 82, 1994.
- C. Deutsch and A. Journel. *GSLIB: Geostatistical Software Library and User's Guide*. Oxford University Press, New York, 1992.
- P. Dietrich, R. Helmig, M. Sauter, H. Hötzl, J. Köngeter, and G. Teutsch. *Flow and Transport in Fractured Porous Media*. Springer-Verlag, Berlin, 2005.
- B. Dverstorp and J. Andersson. Application of the Discrete Fracture Network Concept with Field Data: Possibilities of Model Calibration and Validation. *Water Resources Research*, 25(3):540 – 550, 1989.
- B. Dverstorp, J. Andersson, and W. Nordqvist. Discrete Fracture Network Interpretation of Field Tracer Migration in Sparsely Fractured Rock. *Water Resources Research*, 28:2327–2343, 1992.
- N. Fisher, T. Lewis, and B. Embleton. *Statistical analysis of spherical data*. Cambridge University Press, 1993.
- A. Fuchs. *Optimierte Delaunay-Triangulierungen zur Vernetzung getrimmter NURBS-Körper*. PhD thesis, Universität Stuttgart, 1999.
- H. Gerke and M. van Genuchten. A dual-porosity model for simulating the preferential movement of water and solutes in structured porous media. *Water Resources Research*, 29:305 – 319, 1993a.

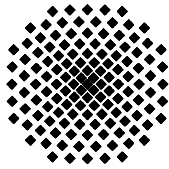
- H. Gerke and M. van Genuchten. Evaluation of a first-order water transfer term for variably saturated dual-porosity flow models. *Water Resources Research*, 29:1225 – 1238, 1993b.
- R. Glass, M. Nicholl, S. Pringle, and T. Wood. Unsaturated flow through a fracture-matrix network: Dynamic preferential pathways in mesoscale laboratory experiments. *Water Resources Research*, 38(12):17-1 – 17-17, 2002.
- H. Haegland, H. Dahle, G. Eigestad, K. Lie, and I. Aavatsmark. Improved streamlines and time-of-flight for streamline simulation on irregular grids. *Advances in Water Resources*, 30(4):1027 – 1045, 2007.
- H. Haegland, A. Assteerawatt, and R. Helmig. Simulation of Flow and Transport for a discrete fracture-matrix system II: Efficient and Accurate Streamline Approach. *Water Resources Research*, In preparation, 2008.
- E. Hakami and E. Larsson. Aperture Measurements and Flow Experiments on a Single Natural Fracture. *International Journal of Rock Mechanics and Mining Science & Geomechanics Abstracts*, 33(4,5):395 – 404, 1996.
- R. Helmig, H. Class, R. Huber, H. Sheta, R. H. R. Erwing, H. Jakobs, and P. Bastian. Architecture of modular program system MUFTE-UG for simulating Multiphase Flow and Transport Processes in Heterogeneous Porous Media. *Mathematische Geologie 2*, pages 123 – 231, 1998.
- R. Hinkelmann. *Efficient Numerical Methods and Information-Processing Techniques for Modeling Hydro-and Environmental Systems*. Springer, 2005.
- W. Huang, G. Donato, and M. Blunt. Comparison of streamline-based and grid-based dual porosity simulation. *Journal of Petroleum Science and Engineering*, 43(1 - 2):129 – 137, 2004.
- R. Huber. *Compositional Multiphase Flow and Transport in heterogeneous porous media*. Mitteilungen H. 102 , Institut für Wasserbau, Universität Stuttgart, 1999.
- O. Huseby, J. Thovert, and P. Adler. Dispersion in three-dimensional fracture networks. *Physics of Fluids*, 13:594 – 616, 2001.
- H. Jakobs. *Simulation nicht-isothermer Gas-Wasser-Prozesse in komplexen Kluft-Matrix-Systemen*. Mitteilungen H. 128 , Institut für Wasserbau, Universität Stuttgart, 2004.
- E. Jimenez, K. Sabir, and M. K. A. Datta-Gupta. Spatial error and convergence in streamline simulation. In *SPE Reservoir Simulation Symposium*, SPE 92873, Houston, TX, 2005.

- W. Kinzelbach. *Numerische Methoden zur Modellierung des Transports von Schadstoffen im Grundwasser*. R. Oldenburg Verlag, München Wien, 1992. 2. Auflage.
- S. Kirkpatrick, C. G. Jr., and M. Vecchi. Optimization by Simulated Annealing. *Science*, 220:671 – 680, 1983.
- P. Kitanidis. *Introduction to Geostatistics*. University of Cambridge, Cambridge, New York, Melbourne, 1997.
- K. Kobayashi. *Optimization methods for multiphase systems in the subsurface: application to methane migration in coal mining areas*. Mitteilungen H. 139 , Institut für Wasserbau, Universität Stuttgart, 2004.
- P. La Pointe and J. Hudson. Characterization and interpretation of rock mass joint patterns. Special paper 199, Geological Society of America, 1985.
- P. La Pointe, W. P.C., and D. W.S. Stochastic estimation of fracture size through simulated sampling. *International Journal of Rock Mechanics and Mining Science & Geomechanics Abstracts*, 30(7):1611 – 1617, 1993.
- P. Lapcevic, K. Novakowski, and E. Sudicky. The interpretation of a tracer experiment conducted in a single fracture under conditions of natural groundwater flow. *Water Resources Research*, 35(8):2301 – 2312, 1999.
- J. Lee, J. Kang, and J. Choe. Experimental analysis on the effects of variable apertures on tracer transport. *Water Resources Research*, 39(1):7–1 – 7–11, 2003.
- G. M. Lomize. *Flow in Fractured Rocks*. Gosenergoizdat, Moscow, 1951.
- J. Long. *Investigation of equivalent porous medium permeability in networks of discontinuous fractures*. PhD thesis, Berkley, 1983.
- J. Long and D. Billaux. From Field Data to Fracture Network Modeling: An Example Incorporating Spatial Structure. *Water Resources Research*, 23(7):1201 – 1216, 1987.
- J. Long, J. Remer, C. Wilson, and P. Witherspoon. Porous Media Equivalents for Networks of Discontinuous Fractures. *Water Resources Research*, 18(3):645 – 658, 1982.
- J. Maréchal, B. Dewandel, and K. Subrahmanyam. A critical review of data on field-scale dispersion in aquifers. *Water Resources Research*, 28(7):1955 – 1974, 1992.
- J. Marýšcaronka, O. Severýn, and M. Vohralík. Numerical simulation of fracture flow with a mixed-hybrid FEM stochastic discrete fracture network model. *Computational Geosciences*, 8(3):121 – 150, 2005.

- A. Mauldon, K. Karasaki, S. Martel, J. Long, M. Landsfeld, A. Mensch, and S. Vomvoris. An inverse technique for developing models for fluid flow in fracture systems using simulated annealing. *Water Resources Research*, 29(11):3775 – 3789, 1993.
- N. Metropolis, A. Rosenbluth, M. Rosenbluth, A. Teller, and E. Teller. Equations of state calculations by fast computing machines. *Journal of Chemical Physics*, 21:1087 – 1092, 1953.
- L. Moreno, Y. Tsang, C. Tsang, F. Hale, and I. Neretnieks. Flow and Tracer Transport in a Single Fracture: A Stochastic Model and Its Relation to Some Field Observations. *Water Resources Research*, 24(12):2033 – 2048, 1988.
- R. Munier. Statistical analysis of fracture data, adapted for modelling Discrete Fracture Networks-Version 2. Skb r-04-66, Svensk Kärnbränslehantering AB, 2004.
- National Research Council. *Rock Fractures and Fluid Flow*. National Academic Press, Washington, D.C., 1996.
- S. Neuman and J. Depner. Use of variable-scale pressure test data to estimate the log hydraulic conductivity covariance and dispersivity of fractured granites near Oracle, Arizona. *Journal of Hydrology*, 102:475 – 501, 1988.
- L. Neunhäuserer. *Diskretisierungsansätze zur Modellierung von Strömungs- und Transportprozessen in geklüftet-porösen Medien*. Mitteilungen H. 119, Institut für Wasserbau, Universität Stuttgart, 2003.
- A. Nordqvist, Y. Tsang, C. Tsang, B. Dverstorp, and J. Andersson. A Variable Aperture Fracture Network Model for Flow and Transport in Fractured Rocks. *Water Resources Research*, 28(6):1703 – 1713, 1992.
- N. Odling. Scaling and connectivity of joint systems in sandstones from western Norway. *Journal of Structural Geology*, 19(10):1257 – 1271, 1997.
- Y. Pannatier. *VARIOWIN: Software for spatial data analysis in 2D*. Springer-Verlag, Berlin, 1996.
- D. Pollock. Semi-Analytical Computation of Path Lines for Finite-Difference Models. *Ground Water*, 26(6):743 – 750, 1988.
- A. Poteri, D. Billaux, W. Dershowitz, J. Gómez-Hernández, V. Cvetkovic, A. Hautjärvi, D. Holton, A. Medina, and A. e. Winberg. Final report of the TRUE Block Scale project. 3. Modelling of flow and transport. Technical report, Swedish Nuclear Fuel and Waste Management Company (SKB), 2002. TR-02-15.

- M. Prévost, M. Edwards, and M. Blunt. Streamline Tracing on Curvilinear Structured and Unstructured Grids. *Society of Petroleum Engineers Journal*, 7(2):139 – 148, 2002.
- S. Priest and J. Hudson. Estimation of discontinuity spacing and trace length using scanline surveys. *International Journal of Rock Mechanics and Mining Science & Geomechanics Abstracts*, 18(3):183 – 197, 1981.
- S. D. Priest. *Discontinuity Analysis for Rock Engineering*. Chapman & Hall, Great Britain, 1993.
- K. Pruess, J. Wang, and Y. Tsang. On thermohydrologic conditions near high-level nuclear wastes emplaced in partially saturated fractured tuff. 2. Effective continuum approximation. *Water Resources Research*, 26:1249 – 1261, 1990.
- V. Reichenberger, H. Jakobs, P. Bastian, and R. Helmig. A mixed-dimensional finite volume method for two-phase flow in fractured porous media. *Advances in Water Resources*, 29(7):1020 – 1036, 2006.
- P. Reimus, M. Haga, A. Adams, T. Callahan, H. Turin, and D. Counce. Testing and parameterizing a conceptual solute transport model in saturated fractured tuff using sorbing and nonsorbing tracers in cross-hole tracer tests. *Journal of Contaminant Hydrology*, 62-63:613 – 636, 2003.
- A. Rouleau and J. Gale. Statistical characterization of the fracture system in the Stripa granite, Sweden. *International Journal of Rock Mechanics and Mining Science & Geomechanics Abstracts*, 22(6):353 – 367, 1985.
- T. Samardzioska and V. Popov. Numerical comparison of the equivalent continuum, non-homogeneous and dual porosity models for flow and transport in fractured porous media. *Advances in Water Resources*, 28:235 – 255, 2005.
- A. Silberhorn-Hemminger. *Modellierung von Kluftaquifersystemen: Geostatistische Analyse und deterministisch – stochastische Kluftgenerierung*. Mitteilungen H. 114, Institut für Wasserbau, Universität Stuttgart, 2002.
- D. Snow. The frequency and apertures of fractures in rock. *International Journal of Rock Mechanics and Mining Science & Geomechanics Abstracts*, 7(1):23 – 30, 1970.
- D. Tang, E. Frind, and E. Sudicky. Contaminant transport in fractured porous media: Analytical solution for a single fracture. *Water Resources Research*, 17(3):555 – 564, 1981.
- R. Therrien and E. Sudicky. Three-dimensional analysis of variably-saturated flow and solute transport in discretely-fractured porous media. *Journal of Contaminant Hydrology*, 23:1 – 44, 1996.

- N. Tran. Simulated annealing technique in discrete fracture network inversion: optimizing the optimization. *Computational Geosciences*, 11(3):249 – 260, 2007.
- N. Tran, Z. Chen, and S. Rahman. Integrated conditional global optimisation for discrete fracture network modelling. *Computer & Geosciences*, 32(1):17 – 27, 2006.
- Y. Tsang and C. Tsang. Chanel Flow Model through Fractured Media. *Water Resources Research*, 23(3):467 – 479, 1987.
- Y. Tsang, C. Tsang, I. Neretnieks, and L. Moreno. Flow and transport in fractured media: a variable aperture channel model and its properties. *Water Resources Research*, 24(12):2049 – 2060, 1988.
- Y. Tsang, C. Tsang, F. Hale, and B. Dverstorp. Tracer transport in a stochastic continuum model of fractured media. *Water Resources Research*, 32(10):3077 – 3092, 1996.
- P. Warburton. A stereological interpretation of joint trace data. *International Journal of Rock Mechanics and Mining Science & Geomechanics Abstracts*, 17(4):181 – 190, 1980.
- P. Witherspoon, J. Wang, K. Iwai, and J. Gale. Validity of cubic law for fluid flow in a deformable rock fracture. *Water Resources Research*, 16(6):1016 – 1024, 1980.
- J. Wollrath. Ein Strömungs- und Transportmodell für klüftiges Gestein und Untersuchungen zu homogenen Ersatzsystemen. Technical Report 28, Institut für Strömungsmechanik und Elektronisches Rechnen im Bauwesen, Universität Hannover, 1990.
- Y.-S. Wu, C. Haukwa, and G. Bodvarsson. A site-scale model for fluid and heat flow in the unsaturated zone of Yucca Mountain, Nevada. *Journal of Contaminant Hydrology*, 38:185 – 215, 1999.
- S. Yates. An analytical solution for one-dimensional transport in heterogeneous porous media. *Water Resources Research*, 26:2331 – 2338, 1990.
- S. Yates. An analytical solution for one-dimensional transport in porous media with an exponential dispersion function. *Water Resources Research*, 28:2149 – 2154, 1992.
- R. Zimmermann, T. H. G. Chen, and G. Bodvarsson. A numerical dual-porosity model with semianalytical treatment of fracture/matrix flow. *Water Resources Research*, 29:2127 – 2137, 1993.



Institut für Wasserbau Universität Stuttgart

Pfaffenwaldring 61
70569 Stuttgart (Vaihingen)
Telefon (0711) 685 - 64717/64749/64752/64679
Telefax (0711) 685 - 67020 o. 64746 o. 64681
E-Mail: iws@iws.uni-stuttgart.de
<http://www.iws.uni-stuttgart.de>

Direktoren

Prof. Dr. rer. nat. Dr.-Ing. András Bárdossy
Prof. Dr.-Ing. Rainer Helmig
Prof. Dr.-Ing. Silke Wieprecht

Vorstand (Stand 1.2.2008)

Prof. Dr. rer. nat. Dr.-Ing. A. Bárdossy
Prof. Dr.-Ing. R. Helmig
Prof. Dr.-Ing. S. Wieprecht
Prof. Dr.-Ing. habil. B. Westrich
Jürgen Braun, PhD
Dr.-Ing. H. Class
Dr.-Ing. S. Hartmann
Dr.-Ing. H.-P. Koschitzky
PD Dr.-Ing. W. Marx
Dr. rer. nat. J. Seidel

Emeriti

Prof. Dr.-Ing. habil. Dr.-Ing. E.h. Jürgen Giesecke
Prof. Dr.h.c. Dr.-Ing. E.h. Helmut Kobus, PhD

Lehrstuhl für Wasserbau und Wassermengenwirtschaft

Leiter: Prof. Dr.-Ing. Silke Wieprecht
Stellv.: PD Dr.-Ing. Walter Marx, AOR

Lehrstuhl für Hydromechanik und Hydrosystemmodellierung

Leiter: Prof. Dr.-Ing. Rainer Helmig
Stellv.: Dr.-Ing. Holger Class, AOR

Lehrstuhl für Hydrologie und Geohydrologie

Leiter: Prof. Dr. rer. nat. Dr.-Ing. András Bárdossy
Stellv.: Dr. rer. nat. Jochen Seidel

VEGAS, Versuchseinrichtung zur Grundwasser- und Altlastensanierung

Leitung: Jürgen Braun, PhD
Dr.-Ing. Hans-Peter Koschitzky, AD

Versuchsanstalt für Wasserbau

Leiter: apl. Prof. Dr.-Ing. habil. Bernhard Westrich

Verzeichnis der Mitteilungshefte

- 1 Röhnisch, Arthur: *Die Bemühungen um eine Wasserbauliche Versuchsanstalt an der Technischen Hochschule Stuttgart, und*
Fattah Abouleid, Abdel: *Beitrag zur Berechnung einer in lockeren Sand gerammten, zweifach verankerten Spundwand, 1963*
- 2 Marotz, Günter: *Beitrag zur Frage der Standfestigkeit von dichten Asphaltbelägen im Großwasserbau, 1964*
- 3 Gurr, Siegfried: *Beitrag zur Berechnung zusammengesetzter ebener Flächen-tragwerke unter besonderer Berücksichtigung ebener Stauwände, mit Hilfe von Randwert- und Lastwertmatrizen, 1965*
- 4 Plica, Peter: *Ein Beitrag zur Anwendung von Schalenkonstruktionen im Stahlwasserbau, und* Petrikat, Kurt: *Möglichkeiten und Grenzen des wasserbaulichen Versuchswesens, 1966*

- 5 Plate, Erich: *Beitrag zur Bestimmung der Windgeschwindigkeitsverteilung in der durch eine Wand gestörten bodennahen Luftschicht, und*
Röhnisch, Arthur; Marotz, Günter: *Neue Baustoffe und Bauausführungen für den Schutz der Böschungen und der Sohle von Kanälen, Flüssen und Häfen; Gesteigungskosten und jeweilige Vorteile, sowie Unny, T.E.: Schwingungsuntersuchungen am Kegelstrahlschieber, 1967*
- 6 Seiler, Erich: *Die Ermittlung des Anlagenwertes der bundeseigenen Binnenschiffahrtsstraßen und Talsperren und des Anteils der Binnenschifffahrt an diesem Wert, 1967*
- 7 *Sonderheft anlässlich des 65. Geburtstages von Prof. Arthur Röhnisch mit Beiträgen von* Benk, Dieter; Breitling, J.; Gurr, Siegfried; Haberhauer, Robert; Honekamp, Hermann; Kuz, Klaus Dieter; Marotz, Günter; Mayer-Vorfelder, Hans-Jörg; Miller, Rudolf; Plate, Erich J.; Radomski, Helge; Schwarz, Helmut; Vollmer, Ernst; Wildenhahn, Eberhard; 1967
- 8 Jumikis, Alfred: *Beitrag zur experimentellen Untersuchung des Wassernachschubs in einem gefrierenden Boden und die Beurteilung der Ergebnisse, 1968*
- 9 Marotz, Günter: *Technische Grundlagen einer Wasserspeicherung im natürlichen Untergrund, 1968*
- 10 Radomski, Helge: *Untersuchungen über den Einfluß der Querschnittsform wellenförmiger Spundwände auf die statischen und rammtechnischen Eigenschaften, 1968*
- 11 Schwarz, Helmut: *Die Grenztragfähigkeit des Baugrundes bei Einwirkung vertikal gezogener Ankerplatten als zweidimensionales Bruchproblem, 1969*
- 12 Erbel, Klaus: *Ein Beitrag zur Untersuchung der Metamorphose von Mittelgebirgsschneedecken unter besonderer Berücksichtigung eines Verfahrens zur Bestimmung der thermischen Schneequalität, 1969*
- 13 Westhaus, Karl-Heinz: *Der Strukturwandel in der Binnenschifffahrt und sein Einfluß auf den Ausbau der Binnenschiffskanäle, 1969*
- 14 Mayer-Vorfelder, Hans-Jörg: *Ein Beitrag zur Berechnung des Erdwiderstandes unter Ansatz der logarithmischen Spirale als Gleitflächenfunktion, 1970*
- 15 Schulz, Manfred: *Berechnung des räumlichen Erddruckes auf die Wandung kreiszylindrischer Körper, 1970*
- 16 Mobasseri, Manoutschehr: *Die Rippenstützmauer. Konstruktion und Grenzen ihrer Standsicherheit, 1970*
- 17 Benk, Dieter: *Ein Beitrag zum Betrieb und zur Bemessung von Hochwasserrückhaltebecken, 1970*

- 18 Gàl, Attila: *Bestimmung der mitschwingenden Wassermasse bei überströmten Fischbauchklappen mit kreiszylindrischem Staublech*, 1971, vergriffen
- 19 Kuz, Klaus Dieter: *Ein Beitrag zur Frage des Einsetzens von Kavitationserscheinungen in einer Düsenströmung bei Berücksichtigung der im Wasser gelösten Gase*, 1971, vergriffen
- 20 Schaak, Hartmut: *Verteilleitungen von Wasserkraftanlagen*, 1971
- 21 *Sonderheft zur Eröffnung der neuen Versuchsanstalt des Instituts für Wasserbau der Universität Stuttgart mit Beiträgen von* Brombach, Hansjörg; Dirksen, Wolfram; Gàl, Attila; Gerlach, Reinhard; Giesecke, Jürgen; Holthoff, Franz-Josef; Kuz, Klaus Dieter; Marotz, Günter; Minor, Hans-Erwin; Petrikat, Kurt; Röhnisch, Arthur; Rueff, Helge; Schwarz, Helmut; Vollmer, Ernst; Wildenhahn, Eberhard; 1972
- 22 Wang, Chung-su: *Ein Beitrag zur Berechnung der Schwingungen an Kegelstrahlschiebern*, 1972
- 23 Mayer-Vorfelder, Hans-Jörg: *Erdwiderstandsbeiwerte nach dem Ohde-Variationsverfahren*, 1972
- 24 Minor, Hans-Erwin: *Beitrag zur Bestimmung der Schwingungsanfachungsfunktionen überströmter Stauklappen*, 1972, vergriffen
- 25 Brombach, Hansjörg: *Untersuchung strömungsmechanischer Elemente (Fluidik) und die Möglichkeit der Anwendung von Wirbelkammerelementen im Wasserbau*, 1972, vergriffen
- 26 Wildenhahn, Eberhard: *Beitrag zur Berechnung von Horizontalfilterbrunnen*, 1972
- 27 Steinlein, Helmut: *Die Eliminierung der Schwebstoffe aus Flußwasser zum Zweck der unterirdischen Wasserspeicherung, gezeigt am Beispiel der Iller*, 1972
- 28 Holthoff, Franz Josef: *Die Überwindung großer Hubhöhen in der Binnenschifffahrt durch Schwimmerhebwerke*, 1973
- 29 Röder, Karl: *Einwirkungen aus Baugrundbewegungen auf trog- und kastenförmige Konstruktionen des Wasser- und Tunnelbaues*, 1973
- 30 Kretschmer, Heinz: *Die Bemessung von Bogenstaumauern in Abhängigkeit von der Talform*, 1973
- 31 Honekamp, Hermann: *Beitrag zur Berechnung der Montage von Unterwasserpipelines*, 1973
- 32 Giesecke, Jürgen: *Die Wirbelkammertriode als neuartiges Steuerorgan im Wasserbau*, und Brombach, Hansjörg: *Entwicklung, Bauformen, Wirkungsweise und Steuereigenschaften von Wirbelkammerverstärkern*, 1974

- 33 Rueff, Helge: *Untersuchung der schwingungserregenden Kräfte an zwei hintereinander angeordneten Tiefschützen unter besonderer Berücksichtigung von Kavitation*, 1974
- 34 Röhnisch, Arthur: *Einpreßversuche mit Zementmörtel für Spannbeton - Vergleich der Ergebnisse von Modellversuchen mit Ausführungen in Hüllwellrohren*, 1975
- 35 *Sonderheft anlässlich des 65. Geburtstages von Prof. Dr.-Ing. Kurt Petrikat mit Beiträgen von:* Brombach, Hansjörg; Erbel, Klaus; Flinspach, Dieter; Fischer jr., Richard; Gàl, Attila; Gerlach, Reinhard; Giesecke, Jürgen; Haberhauer, Robert; Hafner Edzard; Hausenblas, Bernhard; Horlacher, Hans-Burkhard; Hutarew, Andreas; Knoll, Manfred; Krummet, Ralph; Marotz, Günter; Merkle, Theodor; Miller, Christoph; Minor, Hans-Erwin; Neumayer, Hans; Rao, Syamala; Rath, Paul; Rueff, Helge; Ruppert, Jürgen; Schwarz, Wolfgang; Topal-Gökceli, Mehmet; Vollmer, Ernst; Wang, Chung-su; Weber, Hans-Georg; 1975
- 36 Berger, Jochum: *Beitrag zur Berechnung des Spannungszustandes in rotations-symmetrisch belasteten Kugelschalen veränderlicher Wandstärke unter Gas- und Flüssigkeitsdruck durch Integration schwach singulärer Differentialgleichungen*, 1975
- 37 Dirksen, Wolfram: *Berechnung instationärer Abflußvorgänge in gestauten Gerinnen mittels Differenzenverfahren und die Anwendung auf Hochwasserrückhaltebecken*, 1976
- 38 Horlacher, Hans-Burkhard: *Berechnung instationärer Temperatur- und Wärmespannungsfelder in langen mehrschichtigen Hohlzylindern*, 1976
- 39 Hafner, Edzard: *Untersuchung der hydrodynamischen Kräfte auf Baukörper im Tiefwasserbereich des Meeres*, 1977, ISBN 3-921694-39-6
- 40 Ruppert, Jürgen: *Über den Axialwirbelkammverstärker für den Einsatz im Wasserbau*, 1977, ISBN 3-921694-40-X
- 41 Hutarew, Andreas: *Beitrag zur Beeinflussbarkeit des Sauerstoffgehalts in Fließgewässern an Abstürzen und Wehren*, 1977, ISBN 3-921694-41-8, vergriffen
- 42 Miller, Christoph: *Ein Beitrag zur Bestimmung der schwingungserregenden Kräfte an unterströmten Wehren*, 1977, ISBN 3-921694-42-6
- 43 Schwarz, Wolfgang: *Druckstoßberechnung unter Berücksichtigung der Radial- und Längsverschiebungen der Rohrwandung*, 1978, ISBN 3-921694-43-4
- 44 Kinzelbach, Wolfgang: *Numerische Untersuchungen über den optimalen Einsatz variabler Kühlsysteme einer Kraftwerkskette am Beispiel Oberrhein*, 1978, ISBN 3-921694-44-2
- 45 Barczewski, Baldur: *Neue Meßmethoden für Wasser-Luftgemische und deren Anwendung auf zweiphasige Auftriebsstrahlen*, 1979, ISBN 3-921694-45-0

- 46 Neumayer, Hans: *Untersuchung der Strömungsvorgänge in radialen Wirbelkammerverstärkern*, 1979, ISBN 3-921694-46-9
- 47 Elalfy, Youssef-Elhassan: *Untersuchung der Strömungsvorgänge in Wirbelkammerdioden und -drosseln*, 1979, ISBN 3-921694-47-7
- 48 Brombach, Hansjörg: *Automatisierung der Bewirtschaftung von Wasserspeichern*, 1981, ISBN 3-921694-48-5
- 49 Geldner, Peter: *Deterministische und stochastische Methoden zur Bestimmung der Selbstdichtung von Gewässern*, 1981, ISBN 3-921694-49-3, vergriffen
- 50 Mehlhorn, Hans: *Temperaturveränderungen im Grundwasser durch Brauchwassereinleitungen*, 1982, ISBN 3-921694-50-7, vergriffen
- 51 Hafner, Edzard: *Rohrleitungen und Behälter im Meer*, 1983, ISBN 3-921694-51-5
- 52 Rinnert, Bernd: *Hydrodynamische Dispersion in porösen Medien: Einfluß von Dichteunterschieden auf die Vertikalvermischung in horizontaler Strömung*, 1983, ISBN 3-921694-52-3, vergriffen
- 53 Lindner, Wulf: *Steuerung von Grundwasserentnahmen unter Einhaltung ökologischer Kriterien*, 1983, ISBN 3-921694-53-1, vergriffen
- 54 Herr, Michael; Herzer, Jörg; Kinzelbach, Wolfgang; Kobus, Helmut; Rinnert, Bernd: *Methoden zur rechnerischen Erfassung und hydraulischen Sanierung von Grundwasserkontaminationen*, 1983, ISBN 3-921694-54-X
- 55 Schmitt, Paul: *Wege zur Automatisierung der Niederschlagsermittlung*, 1984, ISBN 3-921694-55-8, vergriffen
- 56 Müller, Peter: *Transport und selektive Sedimentation von Schwebstoffen bei gestautem Abfluß*, 1985, ISBN 3-921694-56-6
- 57 El-Qawasmeh, Fuad: *Möglichkeiten und Grenzen der Tropfbewässerung unter besonderer Berücksichtigung der Verstopfungsanfälligkeit der Tropfelemente*, 1985, ISBN 3-921694-57-4, vergriffen
- 58 Kirchenbaur, Klaus: *Mikroprozessorgesteuerte Erfassung instationärer Druckfelder am Beispiel seegangsbelasteter Baukörper*, 1985, ISBN 3-921694-58-2
- 59 Kobus, Helmut (Hrsg.): *Modellierung des großräumigen Wärme- und Schadstofftransports im Grundwasser*, Tätigkeitsbericht 1984/85 (DFG-Forschergruppe an den Universitäten Hohenheim, Karlsruhe und Stuttgart), 1985, ISBN 3-921694-59-0, vergriffen
- 60 Spitz, Karlheinz: *Dispersion in porösen Medien: Einfluß von Inhomogenitäten und Dichteunterschieden*, 1985, ISBN 3-921694-60-4, vergriffen
- 61 Kobus, Helmut: *An Introduction to Air-Water Flows in Hydraulics*, 1985, ISBN 3-921694-61-2

- 62 Kaleris, Vassilios: *Erfassung des Austausches von Oberflächen- und Grundwasser in horizontalebene Grundwassermodellen*, 1986, ISBN 3-921694-62-0
- 63 Herr, Michael: *Grundlagen der hydraulischen Sanierung verunreinigter Porengrundwasserleiter*, 1987, ISBN 3-921694-63-9
- 64 Marx, Walter: *Berechnung von Temperatur und Spannung in Massenbeton infolge Hydratation*, 1987, ISBN 3-921694-64-7
- 65 Koschitzky, Hans-Peter: *Dimensionierungskonzept für Sohlbelüfter in Schußbrinnen zur Vermeidung von Kavitationsschäden*, 1987, ISBN 3-921694-65-5
- 66 Kobus, Helmut (Hrsg.): *Modellierung des großräumigen Wärme- und Schadstofftransports im Grundwasser*, Tätigkeitsbericht 1986/87 (DFG-Forschergruppe an den Universitäten Hohenheim, Karlsruhe und Stuttgart) 1987, ISBN 3-921694-66-3
- 67 Söll, Thomas: *Berechnungsverfahren zur Abschätzung anthropogener Temperaturanomalien im Grundwasser*, 1988, ISBN 3-921694-67-1
- 68 Dittrich, Andreas; Westrich, Bernd: *Bodenseeufererosion, Bestandsaufnahme und Bewertung*, 1988, ISBN 3-921694-68-X, vergriffen
- 69 Huwe, Bernd; van der Ploeg, Rienk R.: *Modelle zur Simulation des Stickstoffhaushaltes von Standorten mit unterschiedlicher landwirtschaftlicher Nutzung*, 1988, ISBN 3-921694-69-8, vergriffen
- 70 Stephan, Karl: *Integration elliptischer Funktionen*, 1988, ISBN 3-921694-70-1
- 71 Kobus, Helmut; Zilliox, Lothaire (Hrsg.): *Nitratbelastung des Grundwassers, Auswirkungen der Landwirtschaft auf die Grundwasser- und Rohwasserbeschaffenheit und Maßnahmen zum Schutz des Grundwassers*. Vorträge des deutsch-französischen Kolloquiums am 6. Oktober 1988, Universitäten Stuttgart und Louis Pasteur Strasbourg (Vorträge in deutsch oder französisch, Kurzfassungen zweisprachig), 1988, ISBN 3-921694-71-X
- 72 Soyeaux, Renald: *Unterströmung von Stauanlagen auf klüftigem Untergrund unter Berücksichtigung laminarer und turbulenter Fließzustände*, 1991, ISBN 3-921694-72-8
- 73 Kohane, Roberto: *Berechnungsmethoden für Hochwasserabfluß in Fließgewässern mit überströmten Vorländern*, 1991, ISBN 3-921694-73-6
- 74 Hassinger, Reinhard: *Beitrag zur Hydraulik und Bemessung von Blocksteinrampen in flexibler Bauweise*, 1991, ISBN 3-921694-74-4, vergriffen
- 75 Schäfer, Gerhard: *Einfluß von Schichtenstrukturen und lokalen Einlagerungen auf die Längsdispersion in Porengrundwasserleitern*, 1991, ISBN 3-921694-75-2
- 76 Giesecke, Jürgen: *Vorträge, Wasserwirtschaft in stark besiedelten Regionen; Umweltforschung mit Schwerpunkt Wasserwirtschaft*, 1991, ISBN 3-921694-76-0

- 77 Huwe, Bernd: *Deterministische und stochastische Ansätze zur Modellierung des Stickstoffhaushalts landwirtschaftlich genutzter Flächen auf unterschiedlichem Skalenniveau*, 1992, ISBN 3-921694-77-9, vergriffen
- 78 Rommel, Michael: *Verwendung von Kluftdaten zur realitätsnahen Generierung von Kluftnetzen mit anschließender laminar-turbulenter Strömungsberechnung*, 1993, ISBN 3-92 1694-78-7
- 79 Marschall, Paul: *Die Ermittlung lokaler Stofffrachten im Grundwasser mit Hilfe von Einbohrloch-Meßverfahren*, 1993, ISBN 3-921694-79-5, vergriffen
- 80 Ptak, Thomas: *Stofftransport in heterogenen Porenaquiferen: Felduntersuchungen und stochastische Modellierung*, 1993, ISBN 3-921694-80-9, vergriffen
- 81 Haakh, Frieder: *Transientes Strömungsverhalten in Wirbelkammern*, 1993, ISBN 3-921694-81-7
- 82 Kobus, Helmut; Cirpka, Olaf; Barczewski, Baldur; Koschitzky, Hans-Peter: *Versucheinrichtung zur Grundwasser und Altlastensanierung VEGAS, Konzeption und Programmrahmen*, 1993, ISBN 3-921694-82-5
- 83 Zang, Weidong: *Optimaler Echtzeit-Betrieb eines Speichers mit aktueller Abflußregenerierung*, 1994, ISBN 3-921694-83-3, vergriffen
- 84 Franke, Hans-Jörg: *Stochastische Modellierung eines flächenhaften Stoffeintrages und Transports in Grundwasser am Beispiel der Pflanzenschutzmittelproblematik*, 1995, ISBN 3-921694-84-1
- 85 Lang, Ulrich: *Simulation regionaler Strömungs- und Transportvorgänge in Karst-aquiferen mit Hilfe des Doppelkontinuum-Ansatzes: Methodenentwicklung und Parameteridentifikation*, 1995, ISBN 3-921694-85-X, vergriffen
- 86 Helmig, Rainer: *Einführung in die Numerischen Methoden der Hydromechanik*, 1996, ISBN 3-921694-86-8, vergriffen
- 87 Cirpka, Olaf: *CONTRACT: A Numerical Tool for Contaminant Transport and Chemical Transformations - Theory and Program Documentation -*, 1996, ISBN 3-921694-87-6
- 88 Haberlandt, Uwe: *Stochastische Synthese und Regionalisierung des Niederschlages für Schmutzfrachtberechnungen*, 1996, ISBN 3-921694-88-4
- 89 Croisé, Jean: *Extraktion von flüchtigen Chemikalien aus natürlichen Lockergesteinen mittels erzwungener Luftströmung*, 1996, ISBN 3-921694-89-2, vergriffen
- 90 Jorde, Klaus: *Ökologisch begründete, dynamische Mindestwasserregelungen bei Ausleitungskraftwerken*, 1997, ISBN 3-921694-90-6, vergriffen
- 91 Helmig, Rainer: *Gekoppelte Strömungs- und Transportprozesse im Untergrund - Ein Beitrag zur Hydrosystemmodellierung-*, 1998, ISBN 3-921694-91-4

- 92 Emmert, Martin: *Numerische Modellierung nichtisothermer Gas-Wasser Systeme in porösen Medien*, 1997, ISBN 3-921694-92-2
- 93 Kern, Ulrich: *Transport von Schweb- und Schadstoffen in staugeregelten Fließgewässern am Beispiel des Neckars*, 1997, ISBN 3-921694-93-0, vergriffen
- 94 Förster, Georg: *Druckstoßdämpfung durch große Luftblasen in Hochpunkten von Rohrleitungen* 1997, ISBN 3-921694-94-9
- 95 Cirpka, Olaf: *Numerische Methoden zur Simulation des reaktiven Mehrkomponententransports im Grundwasser*, 1997, ISBN 3-921694-95-7, vergriffen
- 96 Färber, Arne: *Wärmetransport in der ungesättigten Bodenzone: Entwicklung einer thermischen In-situ-Sanierungstechnologie*, 1997, ISBN 3-921694-96-5
- 97 Betz, Christoph: *Wasserdampfdestillation von Schadstoffen im porösen Medium: Entwicklung einer thermischen In-situ-Sanierungstechnologie*, 1998, ISBN 3-921694-97-3
- 98 Xu, Yichun: *Numerical Modeling of Suspended Sediment Transport in Rivers*, 1998, ISBN 3-921694-98-1, vergriffen
- 99 Wüst, Wolfgang: *Geochemische Untersuchungen zur Sanierung CKW-kontaminierter Aquifere mit Fe(0)-Reaktionswänden*, 2000, ISBN 3-933761-02-2
- 100 Sheta, Hussam: *Simulation von Mehrphasenvorgängen in porösen Medien unter Einbeziehung von Hysterese-Effekten*, 2000, ISBN 3-933761-03-4
- 101 Ayros, Edwin: *Regionalisierung extremer Abflüsse auf der Grundlage statistischer Verfahren*, 2000, ISBN 3-933761-04-2, vergriffen
- 102 Huber, Ralf: *Compositional Multiphase Flow and Transport in Heterogeneous Porous Media*, 2000, ISBN 3-933761-05-0
- 103 Braun, Christopherus: *Ein Upscaling-Verfahren für Mehrphasenströmungen in porösen Medien*, 2000, ISBN 3-933761-06-9
- 104 Hofmann, Bernd: *Entwicklung eines rechnergestützten Managementsystems zur Beurteilung von Grundwasserschadensfällen*, 2000, ISBN 3-933761-07-7
- 105 Class, Holger: *Theorie und numerische Modellierung nichtisothermer Mehrphasenprozesse in NAPL-kontaminierten porösen Medien*, 2001, ISBN 3-933761-08-5
- 106 Schmidt, Reinhard: *Wasserdampf- und Heißluftinjektion zur thermischen Sanierung kontaminierter Standorte*, 2001, ISBN 3-933761-09-3
- 107 Josef, Reinhold: *Schadstoffextraktion mit hydraulischen Sanierungsverfahren unter Anwendung von grenzflächenaktiven Stoffen*, 2001, ISBN 3-933761-10-7

- 108 Schneider, Matthias: *Habitat- und Abflussmodellierung für Fließgewässer mit unscharfen Berechnungsansätzen*, 2001, ISBN 3-933761-11-5
- 109 Rathgeb, Andreas: *Hydrodynamische Bemessungsgrundlagen für Lockerdeckwerke an überströmbaren Erddämmen*, 2001, ISBN 3-933761-12-3
- 110 Lang, Stefan: *Parallele numerische Simulation instationärer Probleme mit adaptiven Methoden auf unstrukturierten Gittern*, 2001, ISBN 3-933761-13-1
- 111 Appt, Jochen; Stumpp Simone: *Die Bodensee-Messkampagne 2001, IWS/CWR Lake Constance Measurement Program 2001*, 2002, ISBN 3-933761-14-X
- 112 Heimerl, Stephan: *Systematische Beurteilung von Wasserkraftprojekten*, 2002, ISBN 3-933761-15-8
- 113 Iqbal, Amin: *On the Management and Salinity Control of Drip Irrigation*, 2002, ISBN 3-933761-16-6
- 114 Silberhorn-Hemminger, Annette: *Modellierung von Kluftaquifersystemen: Geostatistische Analyse und deterministisch-stochastische Kluftgenerierung*, 2002, ISBN 3-933761-17-4
- 115 Winkler, Angela: *Prozesse des Wärme- und Stofftransports bei der In-situ-Sanierung mit festen Wärmequellen*, 2003, ISBN 3-933761-18-2
- 116 Marx, Walter: *Wasserkraft, Bewässerung, Umwelt - Planungs- und Bewertungsschwerpunkte der Wasserbewirtschaftung*, 2003, ISBN 3-933761-19-0
- 117 Hinkelmann, Reinhard: *Efficient Numerical Methods and Information-Processing Techniques in Environment Water*, 2003, ISBN 3-933761-20-4
- 118 Samaniego-Eguiguren, Luis Eduardo: *Hydrological Consequences of Land Use / Land Cover and Climatic Changes in Mesoscale Catchments*, 2003, ISBN 3-933761-21-2
- 119 Neunhäuserer, Lina: *Diskretisierungsansätze zur Modellierung von Strömungs- und Transportprozessen in geklüftet-porösen Medien*, 2003, ISBN 3-933761-22-0
- 120 Paul, Maren: *Simulation of Two-Phase Flow in Heterogeneous Poros Media with Adaptive Methods*, 2003, ISBN 3-933761-23-9
- 121 Ehret, Uwe: *Rainfall and Flood Nowcasting in Small Catchments using Weather Radar*, 2003, ISBN 3-933761-24-7
- 122 Haag, Ingo: *Der Sauerstoffhaushalt staugeregelter Flüsse am Beispiel des Neckars - Analysen, Experimente, Simulationen -*, 2003, ISBN 3-933761-25-5
- 123 Appt, Jochen: *Analysis of Basin-Scale Internal Waves in Upper Lake Constance*, 2003, ISBN 3-933761-26-3

- 124 Hrsg.: Schrenk, Volker; Batereau, Katrin; Barczewski, Baldur; Weber, Karolin und Koschitzky, Hans-Peter: *Symposium Ressource Fläche und VEGAS - Statuskolloquium 2003, 30. September und 1. Oktober 2003*, 2003, ISBN 3-933761-27-1
- 125 Omar Khalil Ouda: *Optimisation of Agricultural Water Use: A Decision Support System for the Gaza Strip*, 2003, ISBN 3-933761-28-0
- 126 Batereau, Katrin: *Sensorbasierte Bodenluftmessung zur Vor-Ort-Erkundung von Schadensherden im Untergrund*, 2004, ISBN 3-933761-29-8
- 127 Witt, Oliver: *Erosionsstabilität von Gewässersedimenten mit Auswirkung auf den Stofftransport bei Hochwasser am Beispiel ausgewählter Stauhaltungen des Oberrheins*, 2004, ISBN 3-933761-30-1
- 128 Jakobs, Hartmut: *Simulation nicht-isothermer Gas-Wasser-Prozesse in komplexen Kluft-Matrix-Systemen*, 2004, ISBN 3-933761-31-X
- 129 Li, Chen-Chien: *Deterministisch-stochastisches Berechnungskonzept zur Beurteilung der Auswirkungen erosiver Hochwasserereignisse in Flusstauhaltungen*, 2004, ISBN 3-933761-32-8
- 130 Reichenberger, Volker; Helmig, Rainer; Jakobs, Hartmut; Bastian, Peter; Niessner, Jennifer: *Complex Gas-Water Processes in Discrete Fracture-Matrix Systems: Upscaling, Mass-Conservative Discretization and Efficient Multilevel Solution*, 2004, ISBN 3-933761-33-6
- 131 Hrsg.: Barczewski, Baldur; Koschitzky, Hans-Peter; Weber, Karolin; Wege, Ralf: *VEGAS - Statuskolloquium 2004*, Tagungsband zur Veranstaltung am 05. Oktober 2004 an der Universität Stuttgart, Campus Stuttgart-Vaihingen, 2004, ISBN 3-933761-34-4
- 132 Asie, Kemal Jabir: *Finite Volume Models for Multiphase Multicomponent Flow through Porous Media*. 2005, ISBN 3-933761-35-2
- 133 Jacoub, George: *Development of a 2-D Numerical Module for Particulate Contaminant Transport in Flood Retention Reservoirs and Impounded Rivers*, 2004, ISBN 3-933761-36-0
- 134 Nowak, Wolfgang: *Geostatistical Methods for the Identification of Flow and Transport Parameters in the Subsurface*, 2005, ISBN 3-933761-37-9
- 135 Süß, Mia: *Analysis of the influence of structures and boundaries on flow and transport processes in fractured porous media*, 2005, ISBN 3-933761-38-7
- 136 Jose, Surabhin Chackiath: *Experimental Investigations on Longitudinal Dispersive Mixing in Heterogeneous Aquifers*, 2005, ISBN: 3-933761-39-5
- 137 Filiz, Fulya: *Linking Large-Scale Meteorological Conditions to Floods in Mesoscale Catchments*, 2005, ISBN 3-933761-40-9

- 138 Qin, Minghao: *Wirklichkeitsnahe und recheneffiziente Ermittlung von Temperatur und Spannungen bei großen RCC-Staumauern*, 2005, ISBN 3-933761-41-7
- 139 Kobayashi, Kenichiro: *Optimization Methods for Multiphase Systems in the Sub-surface - Application to Methane Migration in Coal Mining Areas*, 2005, ISBN 3-933761-42-5
- 140 Rahman, Md. Arifur: *Experimental Investigations on Transverse Dispersive Mixing in Heterogeneous Porous Media*, 2005, ISBN 3-933761-43-3
- 141 Schrenk, Volker: *Ökobilanzen zur Bewertung von Altlastensanierungsmaßnahmen*, 2005, ISBN 3-933761-44-1
- 142 Hundecha, Hirpa Yeshewatersa: *Regionalization of Parameters of a Conceptual Rainfall-Runoff Model*, 2005, ISBN: 3-933761-45-X
- 143 Wege, Ralf: *Untersuchungs- und Überwachungsmethoden für die Beurteilung natürlicher Selbstreinigungsprozesse im Grundwasser*, 2005, ISBN 3-933761-46-8
- 144 Breiting, Thomas: *Techniken und Methoden der Hydroinformatik - Modellierung von komplexen Hydrosystemen im Untergrund*, 2006, 3-933761-47-6
- 145 Hrsg.: Braun, Jürgen; Koschitzky, Hans-Peter; Müller, Martin: *Ressource Untergrund: 10 Jahre VEGAS: Forschung und Technologieentwicklung zum Schutz von Grundwasser und Boden*, Tagungsband zur Veranstaltung am 28. und 29. September 2005 an der Universität Stuttgart, Campus Stuttgart-Vaihingen, 2005, ISBN 3-933761-48-4
- 146 Rojanschi, Vlad: *Abflusskonzentration in mesoskaligen Einzugsgebieten unter Berücksichtigung des Sickerraumes*, 2006, ISBN 3-933761-49-2
- 147 Winkler, Nina Simone: *Optimierung der Steuerung von Hochwasserrückhaltebecken-systemen*, 2006, ISBN 3-933761-50-6
- 148 Wolf, Jens: *Räumlich differenzierte Modellierung der Grundwasserströmung alluvialer Aquifere für mesoskalige Einzugsgebiete*, 2006, ISBN: 3-933761-51-4
- 149 Kohler, Beate: *Externe Effekte der Laufwasserkraftnutzung*, 2006, ISBN 3-933761-52-2
- 150 Hrsg.: Braun, Jürgen; Koschitzky, Hans-Peter; Stuhmann, Matthias: *VEGAS-Statuskolloquium 2006*, Tagungsband zur Veranstaltung am 28. September 2006 an der Universität Stuttgart, Campus Stuttgart-Vaihingen, 2006, ISBN 3-933761-53-0
- 151 Niessner, Jennifer: *Multi-Scale Modeling of Multi-Phase - Multi-Component Processes in Heterogeneous Porous Media*, 2006, ISBN 3-933761-54-9
- 152 Fischer, Markus: *Beanspruchung eingeeerdeter Rohrleitungen infolge Austrocknung bindiger Böden*, 2006, ISBN 3-933761-55-7

- 153 Schneck, Alexander: *Optimierung der Grundwasserbewirtschaftung unter Berücksichtigung der Belange der Wasserversorgung, der Landwirtschaft und des Naturschutzes*, 2006, ISBN 3-933761-56-5
- 154 Das, Tapash: *The Impact of Spatial Variability of Precipitation on the Predictive Uncertainty of Hydrological Models*, 2006, ISBN 3-933761-57-3
- 155 Bielinski, Andreas: *Numerical Simulation of CO₂ sequestration in geological formations*, 2007, ISBN 3-933761-58-1
- 156 Mödinger, Jens: *Entwicklung eines Bewertungs- und Entscheidungsunterstützungssystems für eine nachhaltige regionale Grundwasserbewirtschaftung*, 2006, ISBN 3-933761-60-3
- 157 Manthey, Sabine: *Two-phase flow processes with dynamic effects in porous media - parameter estimation and simulation*, 2007, ISBN 3-933761-61-1
- 158 Pozos Estrada, Oscar: *Investigation on the Effects of Entrained Air in Pipelines*, 2007, ISBN 3-933761-62-X
- 159 Ochs, Steffen Oliver: *Steam injection into saturated porous media – process analysis including experimental and numerical investigations*, 2007, ISBN 3-933761-63-8
- 160 Marx, Andreas: *Einsatz gekoppelter Modelle und Wetterradar zur Abschätzung von Niederschlagsintensitäten und zur Abflussvorhersage*, 2007, ISBN 3-933761-64-6
- 161 Hartmann, Gabriele Maria: *Investigation of Evapotranspiration Concepts in Hydrological Modelling for Climate Change Impact Assessment*, 2007, ISBN 3-933761-65-4
- 162 Kebede Gurmessa, Tesfaye: *Numerical Investigation on Flow and Transport Characteristics to Improve Long-Term Simulation of Reservoir Sedimentation*, 2007, ISBN 3-933761-66-2
- 163 Trifković, Aleksandar: *Multi-objective and Risk-based Modelling Methodology for Planning, Design and Operation of Water Supply Systems*, 2007, ISBN 3-933761-67-0
- 164 Götzinger, Jens: *Distributed Conceptual Hydrological Modelling - Simulation of Climate, Land Use Change Impact and Uncertainty Analysis*, 2007, ISBN 3-933761-68-9
- 165 Hrsg.: Braun, Jürgen; Koschitzky, Hans-Peter; Stuhmann, Matthias: *VEGAS – Kolloquium 2007*, Tagungsband zur Veranstaltung am 26. September 2007 an der Universität Stuttgart, Campus Stuttgart-Vaihingen, 2007, ISBN 3-933761-69-7
- 166 Freeman, Beau: *Modernization Criteria Assessment for Water Resources Planning; Klamath Irrigation Project, U.S.*, 2008, ISBN 3-933761-70-0

- 167 Dreher, Thomas: *Selektive Sedimentation von Feinstschwebstoffen in Wechselwirkung mit wandnahen turbulenten Strömungsbedingungen*, 2008, ISBN 3-933761-71-9
- 168 Yang, Wei: *Discrete-Continuous Downscaling Model for Generating Daily Precipitation Time Series*, 2008, ISBN 3-933761-72-7
- 169 Kopecki, Ianina: *Calculational Approach to FST-Hemispheres for Multiparametrical Benthos Habitat Modelling*, 2008, ISBN 3-933761-73-5
- 170 Brommundt, Jürgen: *Stochastische Generierung räumlich zusammenhängender Niederschlagszeitreihen*, 2008, ISBN 3-933761-74-3
- 171 Papafotiou, Alexandros: *Numerical Investigations of the Role of Hysteresis in Heterogeneous Two-Phase Flow Systems*, 2008, ISBN 3-933761-75-1
- 172 He, Yi: *Application of a Non-Parametric Classification Scheme to Catchment Hydrology*, 2008, ISBN 978-3-933761-76-7
- 173 Wagner, Sven: *Water Balance in a Poorly Gauged Basin in West Africa Using Atmospheric Modelling and Remote Sensing Information*, 2008, ISBN 978-3-933761-77-4
- 174 Hrsg.: Braun, Jürgen; Koschitzky, Hans-Peter; Stuhmann, Matthias; Schrenk, Volker: *VEGAS-Kolloquium 2008 Ressource Fläche III*, Tagungsband zur Veranstaltung am 01. Oktober 2008 an der Universität Stuttgart, Campus Stuttgart-Vaihingen, 2008, ISBN 978-3-933761-78-1
- 175 Patil, Sachin: *Regionalization of an Event Based Nash Cascade Model for Flood Predictions in Ungauged Basins*, 2008, ISBN 978-3-933761-79-8
- 176 Assteerawatt, Anongnart: *Flow and Transport Modelling of Fractured Aquifers based on a Geostatistical Approach*, 2008, ISBN 978-3-933761-80-4

Die Mitteilungshefte ab der Nr. 134 (Jg. 2005) stehen als pdf-Datei über die Homepage des Instituts: www.iws.uni-stuttgart.de zur Verfügung.